

The University of Nottingham

UNITED KINGDOM · CHINA · MALAYSIA

Department of Electrical and Electronic Engineering

Faculty of Engineering

Design of High Speed Synchronous Reluctance Machine

Mauro Di Nardo

Submitted to the University of Nottingham for the degree of Doctor of Philosophy,

January 2017

This thesis describes the work done during the several stages of the design, analyse, manufacture and test of a high speed synchronous reluctance machine capable of delivering 5 kW at 80 krpm. In order to meet such demanding speed requirement, several multi-disciplinary design exercises have been carried out having different aims. First the influences of the speed-dependent limiting factors on the machine performance have been investigated by analytical methodologies. After the preliminary analytical design, the main challenges related with the structural and electromagnetic FE-based design refinements have been identified. A comparative study has been then presented with the purpose of identify the most effective rotor design approach in terms of performance of the final design and computational effort related for its achievement. Once the design strategy has been chosen, the advantages of considering rotor parametrization of increasing complexity are evaluated via a comparative study showing the results of several structural optimizations. With this study, the optimal geometry to manufacture has been identified. Prior to the machine prototyping, the influence of the rotor manufacturing tolerance as well as the thermal limitations on the machine performance have been deeply analysed. Tests carried out on the prototype have essentially validated the proposed design approach. In addition, an investigative study aimed at identifying and understanding the reasons of the found discrepancy between the measured and expected performance is also reported.

Ad Enrica

senza la cui fiducia

questo non sarebbe mai stato possibile

Grazie

Quanno 'o vico è stuorto c'è cchiù sfizio

(Edoardo De Filippo)

ACKNOWLEDGEMENTS

I would like to start thanking my supervisors Prof. Chris Gerada and Dr. Michael Galea for accepting me as a student and let me freely work in the multi-cultural and intellectually exciting PEMC group. It is opportune to recognize the contributions of Prof. Francesco Cupertino and Dr. Vincenzo Trovato; without their supports the PhD experience would have never seen the end. It is difficult to list the conspicuous number of people who through the course of the PhD have helped me with fruitful discussions and a lot of laughs; therefore I will try to be as much concise as possible. I would like to deeply thank Dr. James Borg Bartolo for the countless technical and friendly conversations and his help during the prototyping stage of the project. Without his assistance and the expertise of the technicians (Kevin, Guy, Ian and John) the manufacturing of the prototypes would have not been possible. With the same importance I express my gratitude to Giovanni Lo Calzo for his support during the testing stage of the machine and for the moment of laughs and real friendship we shared together. I also hope that Andrea Formentini, Alessandro Galassini and Giampaolo Buticchi will forgive me for having extorted them some help during the control algorithm implementation in the DSP. Similarly I would like to acknowledge Gaurang Vakil for the magnetic material characterization and for frequently sharing technical opinions. A special gratitude has to be dedicated to Dr. Michele Degano and Dr. Liliana De Lillo for all the moral encouragements (and not only). Finally, thanks to my dear friends Lorenzo Marinelli and Antonio Papagni for supporting me throughout the whole PhD.

TABLE OF CONTENTS

Abstract iii

Acknowledgements v

Table of Contents vi

List of Figures xi

List of Tables xx

Chapter 1 Introduction ..... - 1 -

1.1 Background and enabling factors ..... - 2 -

1.2 Design challenges and limits ..... - 4 -

1.3 Overview of high speed applications ..... - 12 -

1.4 Overview of high speed electrical machine topologies ..... - 20 -

1.5 High speed synchronous reluctance machine: a possible alternative? - 24 -

1.6 Goals and organization of the thesis ..... - 28 -

Chapter 2 SyR machine design ..... - 31 -

2.1 Historical background ..... - 32 -

2.2 SyR modelling and design: an overview ..... - 35 -

2.3 Analytical design of SyR machine ..... - 39 -

2.3.1 Rotor modelling and design considerations ..... - 40 -

2.3.1.1 Inductances calculation ..... - 40 -

2.3.1.2 Torque ripple considerations ..... - 47 -

2.3.1.3 Other design considerations ..... - 51 -

2.3.2 Stator-rotor design equations ..... - 54 -

2.4 Low speed SyR machine design ..... - 63 -

2.4.1 Inductances and torque ..... - 65 -

2.4.2 Internal power factor and saliency ratio ..... - 68 -
2.4.3 Torque and internal power factor compromise ..... - 70 -
2.5 High speed SyR machine design ..... - 71 -
2.5.1 Inclusion of the structural limitation in the design equations ..... - 71 -
2.5.2 Influence of the high speed limiting factors ..... - 76 -
2.5.3 Subdivision of the high speed limiting factor influence ..... - 80 -
2.5.3.1 Iron losses influence ..... - 82 -
2.5.3.2 Structural rib influence ..... - 85 -
2.5.4 Final consideration ..... - 87 -
2.6 Conclusion ..... - 89 -
Chapter 3 Multi-physics rotor design of HS-SyR machine ..... - 91 -
3.1 Design challenges ..... - 92 -
3.1.1 Parametric study or optimization? ..... - 92 -
3.1.2 Physically coupled or de-coupled design? ..... - 97 -
3.1.3 Proposed comparative study ..... - 100 -
3.2 Preliminary design choices ..... - 101 -
3.3 Standard design procedure ..... - 105 -
3.3.1 Performance evaluation ..... - 105 -
3.3.2 Optimization results ..... - 109 -
3.3.3 Structural FE parametric study ..... - 111 -
3.4 Proposed design procedures ..... - 123 -
3.4.1 Introduction ..... - 123 -
3.4.2 Selection of the structural objective function ..... - 125 -
3.4.3 Physically decoupled design ..... - 126 -
3.4.4 Physically coupled design ..... - 127 -

3.4.5 Optimization results ..... - 129 -
3.4.6 Analysis of the optimized machines ..... - 132 -
3.4.7 Design strategy comparison ..... - 139 -
3.5 Conclusion ..... - 142 -
Chapter 4 Structural design optimization of HS-SyR machine ..... - 144 -
4.1 Alternative structural performance indexes ..... - 145 -
4.2 Proposed comparative study ..... - 149 -
4.3 Optimization results ..... - 154 -
4.4 Analysis of the optimized rotor geometries ..... - 156 -
4.5 Rotor-shaft coupling influence ..... - 161 -
4.6 Conclusion ..... - 167 -
Chapter 5 Manufacturing tolerance influences on the machine performance .....- 170 -
5.1 Introduction ..... - 171 -
5.2 Proposed sensitivity analysis ..... - 174 -
5.3 Sensitivity analysis carried out by a simplified parametric study... - 175 -
5.4 Sensitivity analysis carried out on the multi-physics optimization results ..... - 180 -
5.5 Conclusion ..... - 188 -
Chapter 6 Performance of the optimized machine ..... - 190 -
6.1 Power losses calculation ..... - 191 -
6.1.1 Copper losses ..... - 191 -
6.1.2 Iron losses ..... - 195 -
6.1.3 Airgap friction losses ..... - 199 -
6.2 Thermal modelling ..... - 201 -

6.2.1 Lumped parameters network ..... - 202 -
6.2.1.1 Model description ..... - 202 -
6.2.1.2 Adopted heat transfer correlations ..... - 205 -
6.2.2 Thermal performance ..... - 211 -
6.3 Overall performance ..... - 215 -
6.4 Conclusion ..... - 221 -
Chapter 7 Experimental results ..... - 224 -
7.1 The built prototype ..... - 225 -
7.2 Experimental rig layout ..... - 229 -
7.3 Magnetic model identification at constant speed ..... - 233 -
7.3.1 Vector control scheme ..... - 233 -
7.3.2 Magnetic model identification procedure ..... - 234 -
7.3.2 Comparison between the measured and the FE magnetic model - 238 -
7.4 Magnetic material properties characterizations ..... - 243 -
7.4.1 Introduction ..... - 243 -
7.4.2 Stator material ..... - 245 -
7.4.3 Rotor material ..... - 248 -
7.4.4 Considerations on the discrepancy between the expected and measured performance ..... - 251 -
7.5 Motoring no load test ..... - 253 -
7.6 Generating load test ..... - 256 -
7.6.1 Comparison between the measured and estimated temperatures. - 259 -
7.6.2 Comparison between the measured and estimated efficiency and power factor ..... - 262 -
7.7 Conclusion ..... - 264 -

Chapter 8 Conclusion ..... - 266 -
8.1 Summary of the undertaken work ..... - 267 -
8.2 Scientific contributions ..... - 271 -
8.2.1 Specific conclusion ..... - 271 -
8.2.2 General conclusion ..... - 273 -
8.3 List of published papers ..... - 273 -
8.4 Possible future works ..... - 275 -
References ..... - 278 -

LIST OF FIGURES

Figure 1: General design flow chart of a high speed electrical machine ..... - 6 -

Figure 2: Applications of high speed electrical machines in conjunction with an internal combustion engine (ICE) ..... - 13 -

Figure 3: High speed spindle for drilling application (Air bearing) ..... - 16 -

Figure 4: Rotor of a micro turbine (Ansaldo) ..... - 18 -

Figure 5: Turbo-molecular pump (Agilent) ..... - 19 -

Figure 6: Cross section sketch of a SyR machine with a zoom on the central iron bridge ... - 25 -

Figure 7: Simplified 2 poles SyR rotor geometries, a) salient, b) segmented pole configuration - 32 -

Figure 8: a) Transversally and b) axially laminated SyR rotor structures ..... - 34 -

Figure 9: An example of FE calculated d- and q-axis fluxes vs d- and q-axis currents for a SyR machine (3.5 Nm rated at 2500 rpm) ..... - 36 -

Figure 10: Examples of FE calculated flux density distributions and main flux trajectories with only a) D-axis current, b) Q-axis current without iron bridges, c) Q-axis current with relevant tangential and radial iron bridge thicknesses ..... - 41 -

Figure 11: Simple SyR rotor structure parametrization ..... - 42 -

Figure 12: Subdivision of the q-axis m.m.f. and rotor reaction distribution (here supposed proportional to $f\alpha$) expressed in per unit ..... - 43 -

Figure 13: Per unit q-axis m.m.f components for a rotor having 3 (left) and 5 (right) flux barriers equally distributed along the airgap periphery ..... - 44 -

Figure 14: Simplified per unit q-axis equivalent magnetic circuit ..... - 45 -

Figure 15: Flux density distribution at MTPA condition for a) a SyR rotor having flux barrier with constant thickness and b) a SyR rotor with the improved flux barrier profile - 53 -

Figure 16: Stator and rotor parametrizations ..... - 55 -

Figure 17: Vector diagram of a SyR machine (with vectors not in scale) ..... - 56 -

Figure 18: Constant locus of the magnetizing inductances in the design plane $sr - mr$ ..... - 65 -

Figure 19: Constant locus of the magnetic anisotropy and torque in the design plane $sr - mr$. - 66 -

Figure 20: Constant locus of the d- and q-axis current component in the design plane $sr - mr$ - 67 -

Figure 21: Constant locus of the slots area in the design plane $sr - mr$ ..... - 67 -

Figure 22: Constant locus of the maximum internal power factor and the one relative to the maximum torque per ampere operating condition in the design plane $sr - mr$ .... - 68 -

Figure 23: Constant locus of leakage inductance, saliency ratio and saliency ratio without considering the leakage in the design plane $sr - mr$ ..... - 69 -

Figure 24: Constant locus of torque and internal power factor in the design plane $sr - mr$; the position of the maximum torque is represented with a black cross while a possible design solution with a higher power factor is represented with a blue circle ..... - 70 -

Figure 25: a) Simple SyR rotor geometry with equal tangential bridge, b) Rotor sketches highlighting the mass that each set of iron bridge per flux barrier has to hold up .. - 74 -

Figure 26: Maximum torque and internal power factor as function of the speed..... - 77 -

Figure 27: Maximum power and its derivative (in %) as function of the speed ..... - 77 -

Figure 28: Maximum power capabilities curve of 4 different lamination materials ..... - 78 -

Figure 29: Trend of the optimum magnetic and split ratio (i.e. corresponding to the maximum torque design) as the speed increases ..... - 80 -

Figure 30: Trends of the optimum magnetic and split ratio as function of the speed considering only the iron losses or the iron ribs effect or both of them ..... - 81 -

Figure 31: Maximum torque and internal power factor as function of the speed obtained considering only the iron losses or the iron ribs effect or both of them ..... - 81 -

Figure 32: Constant toque loci in the design plane $sr - mr$ obtained considering only the iron losses effect for three different speeds ..... - 83 -

Figure 33: Constant q-axis current loci in the design plane $sr - mr$ obtained considering only the iron losses effect for three different speeds ..... - 83 -

Figure 34: Contour plot of the stator surface and iron losses for two different speed ..... - 84 -

Figure 35 Constant ipf loci in the design plane $sr - mr$ obtained considering only the iron losses effect for three different speeds ..... - 84 -

Figure 36: Constant toque loci in the design plane $sr - mr$ obtained considering only the iron ribs effect for three different speeds ..... - 85 -

Figure 37: Constant locus in the design plane $sr - mr$ obtained considering only the iron ribs effect of the average total bridge per flux barrier, torque loss and q-axis inductance increment ..... - 86 -

Figure 38: Constant ipf loci in the design plane $sr - mr$ obtained considering only the iron ribs effect for three different speeds ..... - 87 -

Figure 39: Trends of the internal power factor related to the maximum torque design and to the maximum ipf achievable for a 5% torque de-rating respect to the maximum torque .. - 89 -

Figure 40: a) Parametrization of the main part of the flux barrier, b) parametrization of the iron bridge thicknesses, c) parametrization of the position and bending angle of the lateral iron ribs ..... - 104 -

Figure 41: Rotor parametrization of the standard design procedure ..... - 107 -

Figure 42: Pareto front torque-ripple of the standard design procedure..... - 109 -

Figure 43:Airgap angular positions $\Delta\alpha i$ and heights hi of the flux barriers and current phase angle $\gamma$of the optimal machines..... - 110 -

Figure 44: Average torque and torque ripple as function of current phase angle for two current level (150% and 50% of the rated value) ..... - 111 -

Figure 45: von Mises stress distribution of the rotor number 8 of the Pareto front shown in Figure 42 evaluated at 80 krpm and shown with a deformation scale of 1:30 ..... - 112 -

Figure 46: radial ribs distributions: 1rib (a), 2ribs (b), 3ribs (c), fillet radius variation (d) - 114 -

Figure 47: Influence of the fillet radius on the maximum stress for three different subdivisions of the radial iron bridges ..... - 115 -

Figure 48: Influence of the fillet radius on the torque performance for three different subdivisions of the radial iron bridges..... - 115 -

Figure 49: Limit of the linear and angular positions ($ALBmax = 60\ [deg]$) of the lateral ribs . - 116 -

Figure 50: Influence of the position of the lateral ribs on the maximum stress ..... - 117 -

Figure 51: Influence of the position of the lateral ribs on the average torque and torque ripple.. - 117 -

Figure 52: von Mises stress distribution of the rotor having the best positions of the lateral ribs - 117 -

Figure 53: Influence of the position of the lateral ribs on the maximum stress for a rotor having $TB = 0.2$ mm. The black bars corresponds to rotor having $ALB2{,}3 = 0$ while the coloured bars to the best solution in terms of $ALB2$ and $ALB3$ ..... - 119 -

Figure 54: Combinations of the bending angles $ALB2{,}3$ that minimize the maximum stress..... - 120 -

Figure 55: von Mises stress distributions of the rotors with TB=0.2 mm and related details of the stress on the radial rib of the solutions having: c,d) the lowest maximum stress (i.e. with $PLB2 = 0.8\,pu, PLB3 = 0.6\,pu, ALB2 = 60\,[deg.], ALB3 = 60\,[deg.]$), and a,b) the same combination of $PLBs$ and $ALBs = 0\,[deg.]$..... - 120 -

Figure 56: Influence of the angular positions of the lateral ribs on the torque performance for a rotor having $TB = 0.2$ mm and the best combinations of $PLB2$ and $PLB3$ ..... - 122 -

Figure 57: Flux density distributions at MTPA condition of b) the best rotor structural wise (with $TB = 0.2\,mm$) and a) the rotor with the same $PLBs$ and $ALBs = 0\,deg.$.. - 122 -

Figure 58: a) Rotor parameters optimized during the proposed two design approaches, b) critical rotor's regions considered for the calculation of the stress factor..... - 124 -

Figure 59: Optimization results: physically decoupled approach (black dots is the Pareto front of the electromagnetic optimization while the colored dot is the final solution after the structural optimization), physically coupled approach (colored stars is the Pareto front of the 3-objective optimization while the black crosses is the front of the 2-objective optimization) ..... - 130 -

Figure 60: Stress factor evolutions during the structural optimization (i.e. second stage of the physically decoupled approach). The best and the worst runs are reported. ..... - 130 -

Figure 61: Stress factors of the optimal solutions of the two design strategies, i.e. the multi-physics approach (2 and 3 objective optimizations) and physically decoupled approach ..... - 131 -

Figure 62: Airgap angular positions $\Delta\alpha i$ and heights hi of the flux barriers and current phase angle $\gamma$of the Pareto optimal solutions of the two multi-physics design approaches a) 2-objective, b) 3-objective optimization. The solutions are numbered from the one showing the smallest torque ripple to the highest. ..... - 133 -

Figure 63: Total iron bridge thickness distributions per barrier of the Pareto optimal solutions of the two multi-physics design approaches a) 2-objective, b) 3-objective optimization. The solutions are numbered from the one showing the smallest torque ripple to the highest. ..... - 134 -

Figure 64: Selected rotor optimized with the physically decoupled design approach (*PDD*), the multi-physics approach carried out with a 3-objective (*PCD3*) and 2-objective (*PCD2*) optimization ..... - 135 -

Figure 65: a) Airgap angular positions $\Delta\alpha i$ and heights hi of the flux barriers and b) total iron bridge thickness distributions per barrier of the selected rotors ..... - 136 -

Figure 66: von Mises stress distribution of the selected rotors with a 1:30 scale for the deformation optimized with the a) physically decoupled design approach and the

multi-physics design approach carried out with b) a 3–objective and c) a 2-objective optimization ..... - 137 -

Figure 67: Flux density distributions (at MTPA with 150% the rated current) of the selected rotors optimized with the PDD) physically decoupled design approach and the multi-physics design approach carried out with PCD3) a 3–objective and PCD2) a 2-objective optimization ..... - 139 -

Figure 68: Analysis of the results of 10 structural optimization runs carried out with a DE algorithm (80 elements per population for 150 generations) minimizing the stress factor. a) torque – stress factor, b) average total bridge (*ATB*) – stress factor, c) torque – *ATB* ..... - 148 -

Figure 69: a) iron bridge parameterization, b) upper and lower limits of the position and bending angle of the lateral rib ..... - 151 -

Figure 70: Average total bridge evolutions during the structural optimizations of the 5 considered rotor geometries ..... - 155 -

Figure 71: Average total bridge and average torque as function of the geometrical degrees of freedom (*GDOF*) for the best (continuous line) and worst (dashed line) optimization runs ..... - 157 -

Figure 72: von Mises stress distributions of the optimized rotor geometries with a 1:30 scale for the deformation ..... - 159 -

Figure 73: von Mises stress distribution of the optimal rotor geometry with *8 GDOF* obtained with b) without a) considering the interference pressure ..... - 163 -

Figure 74: von Mises stress distribution of the rotor geometry with a) *8 GDOF* and b) 12 *GDOF* optimized considering the interference pressure ..... - 165 -

Figure 75: Maximum Von Mises stress, average torque and torque ripple variations (respect to the optimized machine performance) due to positive and negative deviations of the iron bridge dimensions ..... - 176 -

Figure 76: d- and q-axis flux linkage variations (respect to the optimized machine performance) due to positive and negative deviations of the iron bridge dimensions ... - 177 -

Figure 77: Maximum Von Mises stress, average torque and torque ripple variations (respect to the optimized machine performance) due to positive and negative deviations of the barrier thicknesses ..... - 178 -

Figure 78: d- and q-axis flux linkage variations (respect to the optimized machine performance) due to positive and negative deviations of the barrier thicknesses . - 179 -

Figure 79: Objective functions of all the evaluated candidates during the multi-physics optimization of the rotor geometry (in which average torque and oscillation are optimized with the upper constraint on the FE calculated maximum Von Mises stress) ..... - 181 -

Figure 80: Torque ripple sensitivity a) in the average torque - torque ripple plane and b) its distribution for discrete range of torque ripple ..... - 184 -

Figure 81: Average torque sensitivity a) in the average torque - torque ripple plane and b) its distribution for discrete range of average torque ..... - 185 -

Figure 82: Maximum stress sensitivity a) in the average torque - torque ripple plane and b) its distribution for discrete range of average torque ..... - 186 -

Figure 83: Sensitivity of the torque ripple, average torque and maximum stress as the limit of the standardized Euclidean distance defining the neighbours of each solution increases. The most frequent and worst cases are reported in the lowest torque ripple range. The previous three figures correspond to a $SEDlim = 0.5\ [pu]$ ..... - 187 -

Figure 84: a) FE model implemented to estimate the AC copper losses, b) current density distribution with a phase current of 12 A_{pk} and 2500Hz, c) detailed current density distribution within the conductor of one slot, d) placement of the bundles ..... - 193 -

Figure 85: Resistance factors components as function of the frequency: related to a) winding portion included in the lamination stack (active length) and b) the whole phase winding (i.e. including the end winding part) ..... - 194 -

Figure 86: Constant copper loss loci [W] in the speed-torque plane ..... - 195 -

Figure 87: a) Constant total iron losses loci [W] at 80 krpm in the d-q current plane, b) constant loci of the ratio between stator and total losses in the d-q current plane ..... - 197 -

Figure 88: Constant iron losses loci [W] at MTPA condition in the speed-torque plane .... - 198 -

Figure 89: Friction losses in the airgap as function of the speed. ..... - 200 -

Figure 90: Lumped parameters thermal network ..... - 204 -

Figure 91: maximum winding temperature rise as function of the coolant flow rate for the rated current (17Apk) and the maximum speed (80 krpm) ..... - 212 -

Figure 92: Estimated bulk temperatures with coolant flow rate of 15 l/min in the rated current condition (19Apk) and maximum speed (80 krpm) ..... - 212 -

Figure 93: Radial temperatures rise with coolant flow rate of 15 l/min in the rated current condition (19Apk) and maximum speed (80 krpm) estimated with MotorCAD .. - 214 -

Figure 94: Radial temperatures distribution in the rotor (b) and in the slot (a) with coolant flow rate of 15 l/min in the rated current condition (19Apk) and maximum speed (80 krpm) estimated with the FE tool of MotorCAD ..... - 214 -

Figure 95: q- and d-axis flux linkage as function of the respective axis current..... - 215 -

Figure 96: Constant loci in the d-q axis current plane of the maximum flux densities in t5he salient points of the machine: a) stator tooth, b) stator yoke, c) central rotor flux guide; d) flux density distribution of the optimal machine in the rated condition.. - 216 -

Figure 97: Average torque and torque ripple constant loci in the d-q axis current plane.... - 217 -

Figure 98: a) Internal power factor and b) saliency ratio constant loci in the d-q axis current plane ..... - 218 -

Figure 99: Average torque, torque ripple and internal power factor at the MTPA condition as function of the current amplitude ..... - 219 -

Figure 100: Constant efficiency loci a) in the d-q axis current plane at the maximum speed (80 krpm) and b) in the speed-torque plane at MTPA condition. ..... - 220 -

Figure 101: Constant loci of a) the maximum winding temperature rise and b) the electromagnetic loss distribution in the speed-torque plane at MTPA condition. - 221 -

Figure 102: Section view of the built prototype showing the most important components - 226 -

Figure 103: a) Prototyped rotor lamination (the one on the right), b) rotor stack before shaft insertion, c) shaft insertion phase and d) complete rotor assembly. ..... - 227 -

Figure 104: a) Stator lamination stack before winding, b) Stator with windings before the insertion in the housing. ..... - 228 -

Figure 105: Complete machine mounted on the bracket of the test rig: a) rear view, b) top view. ..... - 229 -

Figure 106: Layout of the loading rig ..... - 230 -

Figure 107: a) power electronic converter, b) control platform ..... - 231 -

Figure 108: a) top view of the experimental layout, b) view of some of the measurement instrumentations (power analyser and oscilloscope), power electronic converter with its cooling, and dc power supply ..... - 232 -

Figure 109: Example of the salient variables time-behaviour during the identification test of one point of the d-q current plane: a) reference and measured currents, b) shaft speed transient, c) reference voltages, d) torque transient. ..... - 237 -

Figure 110: Example of the two current phase behaviours during the experimental magnetic model identification of one point of the d-q current plane. ..... - 238 -

Figure 111: FE-calculated and experimental estimated flux linkages a) q-axis and b) d-axis ..... - 239 -

Figure 112: Relative difference between the FE-calculated and experimental estimated flux linkages a) q-axis and b) d-axis ..... - 240 -

Figure 113: Measured and FE-calculated d- and q-axis fluxes as function of current module at the MTPA condition. ..... - 241 -

Figure 114: a) Torque as function of the current phase angle: FE-evaluated, measured by the torquemeter and calculated from the estimated flux; b) torque at MTPA as function of the current estimated from flux and FE-evaluated and their percentage difference. ..... - 242 -

Figure 115: Control rack of the magnetic properties characterization facility available in-house and single sheet tester used for measurements under tension and compression ... - 244 -

Figure 116: Datasheet and measured characteristics of the JNHF600 a) DC magnetization curves and their percentage difference and b) specific iron losses ..... - 246 -

Figure 117: Measured characteristics of the JNHF600 material when subject to different compressive stress: a) DC magnetization curves and their differences respect to the unstressed condition, b) specific iron losses with the material unstressed and subject to the compressive stress of 150 MPa, c) percentage variations of the specific iron losses as function of the compressive stress for different frequencies and flux densities ..... - 248 -

Figure 118: Datasheet and measured characteristics of the 35HXT780T a) DC magnetization curves and their percentage difference and b) specific iron losses ..... - 249 -

Figure 119: Measured characteristics of the 35HXT780T material when subject to different tensile stress: a) DC magnetization curves, b) specific iron losses with the material unstressed and subject to the tensile stress of 150 MPa, c) percentage variations of the specific iron losses as function of the tensile stress for different frequencies and flux densities ..... - 250 -

Figure 120: Measured torque, q- and d-axis apparent inductances contours with the MTPA locus used to build the look-up tables needed for the vector control ..... - 253 -

Figure 121: a) Transient and steady state acquisitions during the no-load motoring tests in which the speed increases from 28 to 30 krpm, b) snapshot of two phase currents measured by the oscilloscope at 30 krpm ..... - 255 -

Figure 122: Measurements during a transient motoring no-load speed test up to 35krpm: a) Reference and measured mechanical speed, b) reference d/q voltage/current and measured current ..... - 256 -

Figure 123: Transient and steady state acquisitions during the load generating test at 30krpm in which the current module increases from 14 to 21 A_{pk}, b) snapshot of two phase currents and two phase to phase voltages measured by the oscilloscope at steady state at 30 krpm and with a current module of 21 $A_{pk,}$ c) measured minimum and maximum winding temperatures during the load test at 30 krpm ..... - 258 -

Figure 124: a) Measured and estimated maximum winding temperatures as function the current amplitude for different speeds, b) percentage error between the estimated and the measured temperature..... - 261 -

Figure 125: a) Measured efficiency constant loci in the torque-speed plane, b) Coloured contour of the initial estimated efficiency in the current-speed plane and error between the estimated and the measured efficiencies ..... - 262 -

Figure 126: measured and FE-estimated power factor as function of the current amplitude - 264 -

LIST OF TABLES

Table 1: Iron losses and yield strength for conventional and high strength electrical steels [3] .. - 11 -

Table 2: Initial geometrical constraints and preliminary design assumptions..... - 64 -

Table 3: Additional assumptions needed for the parametric analysis for different speeds ... - 76 -

Table 4: Materials properties used for the comparative analysis shown in Figure 28 ..... - 78 -

Table 5: Requirements of the target machine and its main parameters..... - 103 -

Table 6: Standard deviation (in percentage) of each parameter (calculated excluding the solutions 1 and 2) ..... - 111 -

Table 7: Structural performance (critical von Mises stresses, stress factor, mean and standard deviation of the critical stresses) and electromagnetic performance (torque and ripple) of the selected rotors ..... - 138 -

Table 8: Final results and evaluated generations of 10 structural optimizations carried out with the same setting, i.e. 80 elements per population for 100 maximum generations. - 141 -

Table 9: Analysis of the results of 10 structural optimizations performed with GA and DE with 80 element per population and 100 (or 150) generations: std(SF) standard deviations of the final stress factors, max(ED) – min(ED) difference between the maximum and minimum Euclidean distances calculated respect to the average solution and std(ED) standard deviation of the same set of distances. In round bracket the same figures of merit are reported calculated respect to the best solution. The column marked with the asterisk (*) reports the results obtained calculating the stress factor considering the average of the stress for each critical region and not its maximum value ..... - 146 -

Table 10: Analysis of the results of 10 structural optimizations both performed with the DE algorithm (with 80 element per population and 150 generations) minimizing the stress factor or the average total bridge per barrier: *std(SF)* standard deviations of the final stress factors, *max(ED) – min(ED)* difference between the maximum and minimum Euclidean distances calculated respect to the average solution and *std(ED)* standard deviation of the same set of distances. In round bracket the same figures of merit are reported calculated respect to the best solution. ..... - 149 -

Table 11: Boundaries of the research space of the structural optimizations ..... - 153 -

Table 12: Geometrical parameters and electromagnetic performance of the optimal rotors. - 158 -

Table 13: Analysis of the results of 10 structural optimizations performed on the 5different rotor geometries minimizing the average total bridge per barrier: *mean(ATB)* mean of

the final *ATBs*, *std(ATB)* standard deviations of the optimal *ATBs*, *max(ED) – min(ED)* difference between the maximum and minimum Euclidean distances calculated respect to the average solution and *std(ED)* standard deviation of the same set of distances. ..... - 160 -

Table 14: Geometrical parameters and electromagnetic performance of the rotors with 8 and 12 *GDOF* optimized with and without considering the interference pressure ..... - 164 -

Table 15: Analysis of the results of 10 structural optimizations performed on the rotor geometries featuring 8 and 12 *GDOF* minimizing the average total bridge per barrier: *mean(ATB)* mean of the final *ATBs*, *std(ATB)* standard deviations of the optimal *ATBs*, *max(ED) – min(ED)* difference between the maximum and minimum Euclidean distances calculated respect to the average solution and *std(ED)* standard deviation of the same set of distances. ..... - 166 -

Chapter 1
Introduction

In this chapter, a concise literature review on high speed electrical machines and their main applications is presented. Starting from the advantages and disadvantages of direct drive solutions, the requirements of considered application are outlined as well as the issues related to the design of most common high speed electrical machine topologies. The aims of the thesis are then described with its structure and main contributions.

1.1 Background and enabling factors

High speed rotating mechanical machines have been investigated and industrially employed for a wide range of applications since the middle of the last century. Traditionally such systems are made up of low speed electrical motors coupled with gear, turbines or belt driven configuration. These mechanically-enhanced systems usually have low efficiency, limited controllability and reliability and require high maintenance [1, 2]. In a bid to overcome these challenges in the last two decades the research community and the main market players have spent an ever-increasing effort in investigating the possibility of applying direct drive solutions [3]. Direct drive solutions allow for improvements in terms of efficiency, reliability, maintenance and mechanical stiffness mainly due to the elimination of the gearbox. Another clear advantage is the reduction of overall system volume and weight due to the higher power density obtained by increasing the rotational speed of the electrical machine (therefore reduction in machine size) and to the elimination of the gear unit [4]. The high speed operation can also lead to enhancement of the process such as improvement of the milling and cutting performance due to the higher speed, and reduction of the compressor, or turbine size, etc. The interest in high speed electrical machine is also strongly correlated to the more restrictive efficiency standards [5] which translate the effort of some countries in covering the energy demand in the most efficient way possible due to environmental considerations.

This increased interest in applications of high speed electrical machine has been only possible due to improvement in methodologies of manufacturing, bearing technologies, and the availability of high specifications materials [6] and new power electronic devices [7]. In particular the last two enabling factors are briefly described in the following.

- The high speed operation of an electrical machine is only possible if a multiple phase current system with a high fundamental frequency can be synthetized. This needs to be as clean as possible in terms of harmonic content in order to minimize the harmonic induced losses such as eddy current and hysteretic in the magnetic components and skin effect in the conductors. With pulse width modulation (PWM) techniques, the switching frequency has to be at least 15-20 times higher than the fundamental frequency in order to limit the current harmonic content; therefore a high switching frequency of several tens of kHz is required for converter supplying a high speed electrical machine (e-g- a 4 poles machine at 50krpm has a fundamental frequency of 1.6kHz, therefore a switching frequency of 25-30kHz is required). The introduction of wide gap materials (SiC and GaN) and their use in power electronic devices has allowed coping easier these requirements respect to standard power electronic devices. Such technologies also permit a better level of controllability and reduce, or completely eliminate, the dimensions of the output and input filters traditionally used to respectively minimize the total harmonic distortion of the input voltage and the output current ripple.

- Soft magnetic materials have been traditionally designed to reach certain electromagnetic characteristics in terms of saturation flux density and specific iron losses, while the mechanical properties have played a minor role in the material development. High speed electrical machine research have received a consistent boost due to the development of new electrical steel materials specifically designed to reach really low specific iron losses or to cope the higher demand in terms of mechanical features (i.e. yield strength and elongation) [3, 7].

1.2 Design challenges and limits

The advantages of having a reduced weight and volume and higher system reliability due to elimination of the gear unit come at the price of a more complex design approach. In fact at higher speeds, the thermal and the mechanical behaviours of the machine become the dominant aspects of the machine performance; therefore the design of a high speed machine is a combined thermal-mechanic-electromagnetic problem [8, 9]. The high speed operation pushes the materials to operate to their mechanical and thermal limit; furthermore some applications require a wide field-weakening capability which is a constraint from the electromagnetic standpoint. The maximum operating range of an electrical drive is not easy to describe since it depends on several physic phenomena. The concept of high speed is quite controversial since there is no clear definition of what high speed means. Several attempts have been

presented in literature in order to find semi-empirical formulations which numerically define with an index what high speed means [10, 11]. An interesting explanation of physical limits incurring in different speed range in the power-speed plane (or power*speed-speed plane) is presented in [4]. The tangential speed of the outer rotor radius is often taken as a criterion when defining high speed because it also takes into account the size of the machine [2, 7]. In fact considering a rotating cylinder the tangential stress σ is proportional to the square of the tangential speed v through the mass density of ρ:

$$\sigma = \rho v^2 \tag{1}$$

Considering an electrical steel which exhibits a yield strength of 460 [MPa] and a mass density of 7600 [kg⁄m^3], the maximum tangential speed is 246 [m⁄s] which corresponds to a rotational speed of 4700 rpm if the rotor diameter is 1 m and 47000 rpm if the rotor diameter is 100 mm. Thus, it is evident that the definition of high speed is strongly dependent on the tangential speed and it is not a matter of the rotational speed. However this criterion represents the degree of the mechanical utilization of the machine, which is not the only critical factor. Nevertheless the factors which limit the speed and the power density can be grouped in four families: mechanical, thermal, electromagnetic and the power electronic limits. The choice of the machine materials is a crucial factor that influences all the aforementioned limits. Considering all the above, the design procedure should try to put equal weight to the three main aspects (mechanical, electromagnetic, thermal) using a multi-physics approach.

In fact, differently from conventional speed, where the electromagnetic design is carried out starting from certain mechanical and thermal assumptions that are verified in a second design stage, when the speed increases, the mechanical and thermal constraints becomes so stringent to make indispensable deal with all the design aspects simultaneously. A generic flow chart for a high speed machine design is shown in Figure 1, where starting from the requirement of the application a preliminary analytical design is usually performed after which a multi-physics design procedure is applied.

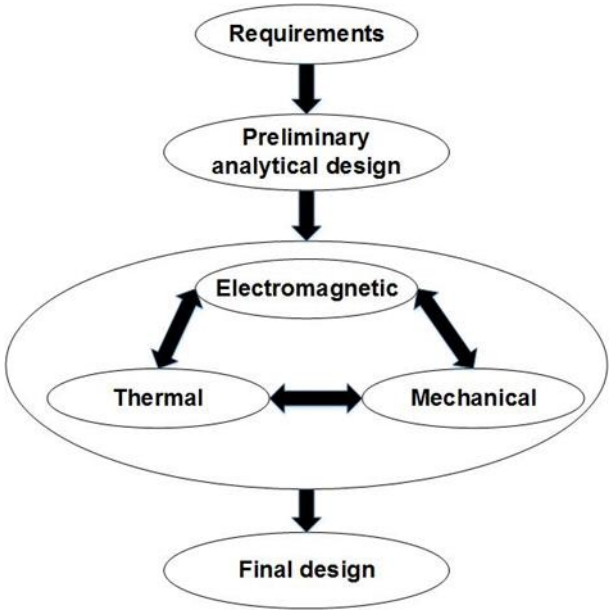


Figure 1: General design flow chart of a high speed electrical machine

The choices which have to be taken during the design concern also the methods with which the electro-magnetic, mechanical and thermal behaviour are evaluated. These depend on the particular machine under study that is the complexity of the structure. Usually an analytical approach is adopted for the electromagnetic part and a finite element tool is applied as a refinement stage. The thermal behaviour is commonly investigated by means of lumped

parameter networks and finite element or computational fluid dynamic methods are only used respectively to verify the temperature distribution or to calculate the convection heat transfer coefficients for complicated geometries. For the mechanical design as well, some analytical calculations are possible, both for structural and rotor dynamic assessments, but according to the complexity of the rotor structure and to the needed accuracy, a finite element method is employed to validate the initial performance estimation. Another important challenge is how to coordinate all the different aspects mentioned above and achieve a design procedure that balances their relative importance. In the following the most important design aspects of a high speed drive are briefly described and the correlations among them are highlighted.

- *Mechanical aspect*

The mechanical design mainly comprises the stress analysis in the rotor components as well as the rotor dynamic analysis. The first one involves keeping the maximum stress induced in the rotor parts well below the yield strength of the material in order to avoid that part of the structure coming close to the elasticity/plasticity limit [12]. This constraint becomes of fundamental importance during the selection of the rotor material. A rotor dynamic analysis is needed to calculate the critical frequencies of the rotor and be sure that the first one is above the maximum operated speed. By doing so, it is avoided that low external perturbation at that particular speed leads to resonant effects with a consequent destruction of the motor [13]. Operation above the first critical frequency is possible; however it is usually avoided since particular attention

needs to be cared when crossing such critical speed. It is well-know that in order to reduce the induced stress in the rotor, its diameter should be as low as possible and consequently the length has to be incremented in order to achieve the same desired power. However, by doing so the first critical frequency decreases, therefore there is a clear trade-off during the selection of the diameter and the length of the rotor between structural and rotor dynamic performances. The rotor dynamic analysis involves the study of the vibrations at different speed as well as the selection of bearing type, bearing stiffness and the shaft diameter. Regarding the bearings, they have to offer higher performances in terms of maximum rotational speed, working temperature, precision and stiffness compared to the one used in low speed applications. For these reasons, bearings composed by steel rings and low density rolling balls with a really high stiffness (e.g. ceramic ball bearing) are often used in high speed application. The lubrication of the bearing is the most important factor which defines its maximum speed and life time. The most common lubrication methods employed for high speed ball bearing are the oil mist and oil jet; both of them require additional components and this increases the complexity of the overall system [14]. The use of magnetic or air foil bearings allow the reduction of the bearing failure for fatigue, and avoid the need of any lubrication system making the overall system oil-free.

- *Electromagnetic aspect*

From the electromagnetic point of view the design of a high speed motor is not so much different from the low-medium speed range considering the same type

of electrical machine. As in the low-medium speed range, special care must be taken if a wide constant speed range is required, i.e. the coordination between values of the inductances (therefore winding topology) and permanent magnet flux becomes fundamental [15, 16]. The most important electromagnetic limitations arise from the extra losses generation due to the higher fundamental frequency. The extra copper losses in the stator winding due to the non-uniform distribution of the current density within the slot and the increment of the iron losses due to the higher fundamental frequency need to be carefully considered during the design. The AC copper losses are usually mitigated employing winding realized with Litz wires when it is feasible; for all other cases when this solution is not possible, these extra losses can be compensated by a reduction of the current density. With the aim of reducing the iron losses, two approaches can be adopted: employ a low specific iron losses lamination material and/or decrease the flux density values in the teeth and in the stator back iron. The reduction of the magnetic and/or the current loading in order to keep constant the temperature rise is the main electromagnetic reason which limits the torque production as the speed increases [2, 4].

- *Thermal aspect*

The loss density is higher in high speed machines than for machines designed for the same power but lower rated speed, therefore the loss dissipation becomes more problematic due to the reduced heat exchange surfaces and paths. Considering that the thermal behaviour of the machine is dependant both on the electro-magnetic and mechanical losses and the last two mechanisms

depend on the temperature distribution, then an appropriate thermal modelling is fundamental to correctly correlate all the design aspects. A proper thermal management allows designing the cooling system (which can also depend on the specific application) in order to ensure that all the different motor components are within their safe operating limits and to model the material properties at the right temperature. As previously explained the thermal model allows the designer to choose the appropriate electric and magnetic loadings and thus select the optimum distribution of losses, as well as choose the most appropriate materials (i.e. conductor insulation, lamination insulation and permanent magnet technology). A good thermal analysis can also help to minimize the rotor losses and maintain a low enough operating temperature for the rotor components. This is very important since rotor cooling is in general more difficult and care needs to be taken to ensure that temperature sensitive components such as the magnets do not demagnetize. For rotors that comprise a retaining sleeve, one must also consider that the sleeve is usually a bad thermal conductor making the cooling of the magnets more difficult.

- *Material selection aspect*

The choice of the stator and rotor materials deals with the trade-off between the electromagnetic and the structural performances. In particular, there is a clear compromise between saturation flux density, specific iron losses and yield strength [17]. Table 1 reports the iron losses and the yield strength for conventional and high strength electrical steel showing the clear trade-off between the electromagnetic and the structural characteristic.

Table 1: Iron losses and yield strength for conventional and high strength electrical steels [3]

Lamination grade	***Loss (W/Kg), 1T/50Hz***	***Yield strength (MPa)***
M270-35A	1.2	380
35HXT780T	6.15	822

- *Power electronic aspect*

The role played by the power electronic circuit with which the electrical machine is fed is as important as the others that concern only the electrical machine. Therefore the correct design of a high speed drive must not overlook the effect that the converter has on the performance of the whole system. The design, the rating and therefore the cost of the converter is strongly related with the characteristics of the electrical machine. In order to minimize the converter rating, the efficiency and the power factor of the machine needs to be as high as possible as well as the capability of the latter to operate in field weakening. The amplitude of the current ripple is proportional to the harmonic voltage, and inverse proportional to the switching frequency and machine inductance. High speed machines usually require low number of turns, which means a quite low phase inductance therefore the current ripple is high. In order to reduce such current harmonic content which cause additional losses, torque oscillation and vibration in the electrical machine, two approaches can be pursed: further increment the switching frequency or introduce output filter. The first possibility is limited by the adopted power electronic device technologies while the second could be limited by envelope/weight constraint. The higher switching frequency, required by the high fundamental frequency, demands

also a higher computational power needed to acquire the measurements, elaborate the control algorithm and generate the output commands.

1.3 Overview of high speed applications

The general design challenges and limits have been briefly described in previous section; however the specific design choices depend on the considered application. In the following, the most important applications of high speed electrical machines are described along with their specific requirements.

- *Internal combustion engines*

Internal combustion engines (ICE) are both employed in automotive and small-medium power generation applications. The exploitation of the waste heat energy sources of such systems through the use of high speed electrical machines can potentially lead to the improvement of both efficiency and performance. This concept is not new both in automotive and industrial applications and it has been driven by the more restrictive efficiency and emissions standards [3]. The applications of high speed electrical machines in conjunction with an ICE are depicted in Figure 2 where some of the more known technologies related to the more electric engine (MEE) includes:

- ✓ an electrically assisted turbocharger,
- ✓ an electrically driven air compressor,
- ✓ a generator driven by a turbine,

✓ an exhaust gas recirculation system (EGR).

The function of the first one is twofold because the machine operates in different ways according to the engine load. In fact during low loads, when there is a lack of energy in the exhaust gas flow, the electrical machine operates as a motor to drive the compressor thus reducing the so-called turbo-lag [18].

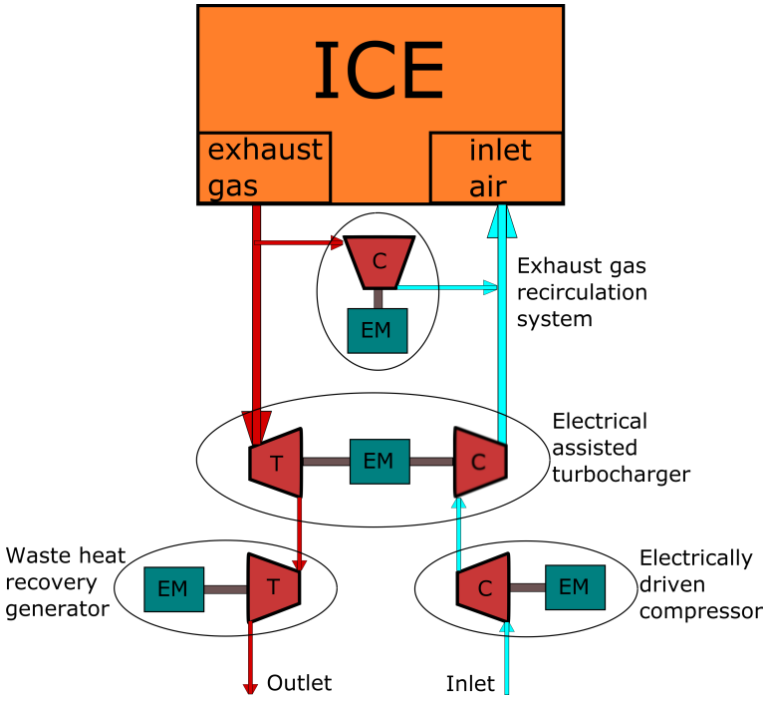


Figure 2: Applications of high speed electrical machines in conjunction with an internal combustion engine (ICE)

This delay occurs between the request of the air inlet pressure rise and the actual increment that is common in direct turbo-compressor solution. By reducing such a delay improves the driveability and therefore the performance of the overall system. During a high load condition, there is an excess of energy in the exhaust gas and in order to prevent dangerous shaft over speed, part of this gas is usually wasted via opening a valve positioned before the

turbine inlet. During this regime, the electrical machine can operate as generator and the excess of energy in the exhaust gas can thus be recovered and used to supply the auxiliary service of the system or the main load. The most challenging task during the integration of the electrical machine in such system is due to the huge axial thermal gradient between the compressor and the turbine. Two interesting approaches have been proposed in order to avoid such aggressive environment. The first one consists in placing the electrical machine in front of the compressor and not in the middle (i.e. much less thermally aggressive); however this solution needs an additional bearing to support the machine. The second approach is the so-called fully electric turbocharger, where turbine and compressor are mechanically decoupled and each of them is connected to a separate high-speed electrical machine. By having such a decoupled configuration the turbine and the compressor can run independently and at different speeds enabling the performance and so the efficiency of each to be optimized, at the cost of a higher component count and therefore financial cost. A further improvement in efficiency can be achieved by installing 1) an additional turbine and a high speed machine at the outlet of the exhaust gas in order to extract the remaining wasted energy and 2) an additional high speed electrically-driven compressor to further increment the air inlet pressure. The exhaust gas recirculation system can be adopted in order to reduce the NO_x emissions by mean of the recirculation of a percentage of the exhausted gas into the ICE. The electrical driven high speed compressor is needed to cover the differential pressure between the inlet and the outlet of the engine.

- *Spindle*

Conventional low cost high speed spindles have been historically implemented with belt drives configurations, which are limited in maximum speed. In these applications, high speeds are needed in order to guarantee high volumetric material removal rates, therefore spindles applications have traditionally driven and pushed the research community and industry towards high speed direct drive solutions. Spindle applications can be mainly divided in three areas: milling, grinding and drilling [19]. The maximum rotational speed needed during each of this operation depends on the material under process. Therefore the power range and speed limits in spindle applications are very wide, going from 6000 rpm up to 300000 rpm, with a power approximately from 24 kW down to 200 W. Figure 3 shows a high speed spindle of 470W at 300000 rpm commercially available for drilling applications. Among the new applications that require very high speed spindles, it is worth to mention the ever increasing speed (up to 1 million rpm) needed for printed-circuit-board (PCB) drilling and dental surgery tools (up to 400000 rpm, with a power of 10/20 W). The latter are commonly implemented through turbines fed by compressed air; therefore each tool operates at a single speed and several tools with different speeds are needed. By replacing the traditional air turbine tools with an electrical drive could reduce the number of tools and add the benefit of having an accurate speed and torque control [20]. Spindle motors typically operate in non-aggressive thermal environments and the main design constraints are high power density, low vibration limit, high dynamic stiffness, the possibility of withstand high axial loads and a wide constant power-speed range.



Figure 3: High speed spindle for drilling application (Air bearing)

- *Gas compressor and air blowers*

Industrial gas compression applications have been traditionally implemented driving the compressor by a high speed gas turbine or by a low-speed electric motor coupled with a gearbox. In certain applications, the restricted environmental standards are limiting the use of compressor driven by gas turbines. Direct coupling of a high speed electric motor with the compressor allows the integration of the motor-compressor system, the elimination of the ancillary system (gearbox, seals and lubrication system) therefore an improvement of the reliability and maintenance and the enhancement of the performance due to the possibility of variable speed operation [21]. The implementation of magnetic bearings allows eliminating the need of any oil lubrication system. The requirement of an oil free system which completely avoids the risk of oil contamination of the process is becoming fundamental in some industrial air compressor and blower applications such as food and beverage, pharmaceutical and electronic industries and waste water treatment plants. Regarding small compressors employed in commercial and light industrial applications such as in air conditioning and refrigeration systems, they are usually implemented by means of reciprocating pistons or screw type

compressor which are inefficient and physically large. The use of a high speed centrifugal compressor in this market area would allow the reduction of the size of the system and the improvements of the efficiency; however such solutions have to be implemented with a cost comparable with commercial compressor and this constitutes the main design challenge [22].

- *Distributed and renewable energy sources*

Mini or micro turbines are small gas turbines directly coupled with a high speed electric generator (typically in the range of 30-400 kW, 15-120 krpm) that can be used for power generation in locations with space limitation, remote access or in countries where such distributed power generation is incentivized by specific government policy [23]. They can be run with a wide range of fuels (natural gas, diesel, etc.) and allows low emission, high efficiency and the possibility of waste heat utilization by means of combined heat and power systems. Another application of high speed electrical machines in the renewable energy market is related with the Organic Rankine Cycle (ORC) based power generation plants. The ORC allows the extraction of low grade heat and for this reason it can be implemented in waste heat recovery system employed in medium-small internal combustion engine for industrial application, and for biomass, geothermal or solar thermal power plants characterized by having a low temperature heat source [24].



Figure 4: Rotor of a micro turbine (Ansaldo)

The full exploitation of the renewable energy sources is only possible if an energy storage system is available and connected to the grid. A flywheel based system is a possible form of energy storage [25]. In the past, electrical machine designed for flywheel applications had large diameters, low speed, low power and low energy density. The use of high speed machines directly connected to a smaller flywheel allows the improvements of the power density, overall size, and dynamic response. They are usually used to cover the peak power demand and for the frequency regulation of the grid thanks to their fast response time. It is worth to mention that high speed flywheels have gained attention also in automotive applications mainly to assist the power management of hybrid vehicles [26, 27].

- *Turbo-molecular pumps*

Turbo-molecular pumps are used to obtain a really high vacuum (up to 10^{-10} mbar). Such low vacuum environment is crucial in manufacturing processes of semiconductors, dye chemical, and solar cells [3]. This particular type of pump requires electrical machine with very low power and high speed (up to 90 krpm). The operation of the electrical machine in deep vacuum environment is the main design challenge since it restricts the heat dissipation to only to

radiation phenomena. Figure 5 shows a commercially available product with a maximum speed of 80000 rpm.



Figure 5: Turbo-molecular pump (Agilent)

- *Starter/generator for aero engine applications*

The concepts within the aerospace research community today of more electric aircraft and more electric engine with which there is a clear tendency to replace critical functions traditionally covered by mechanical systems with electrical system are pushing the generation capacity always to higher and higher level. This augmented electric power demand in turn requires the increment of the auxiliary power unit and/or the main engine generator capacities. Light-weighting and compactness are the most important features in air transportation along with a higher level of reliability respect to land based applications. The use of a high speed electrical machine as a generator (sometimes also with motoring function) allows to achieve a high level of power density. The reliability constitutes the main design challenge along with the capability to work in really harsh environment [28].

1.4 Overview of high speed electrical machine topologies

Regarding the high speed machine topology choice, several options have been proposed in literature and adopted in industry, mainly surface mounted permanent magnet synchronous machine (PMSM), induction machine (IM) and switched reluctance (SR) machine. Each of them has its own advantages and disadvantages, and the choice strongly depends on the considered application. In the following the main features of the aforementioned machine topologies are described.

- *PMSM*

PMSMs are a very popular machine topology employed in high speed applications mainly due to the higher power density, efficiency and power factor respect to the other machine candidates [29-31]. These advantages are strictly related to the use of high energy density permanent magnet (based on rare-earth materials), the lack of a magnetizing current component and the absence of the rotor joule losses. The major challenge when dealing with this machine topology for high speed applications is associated with the design and the manufacturing of the magnets retention system. Several configurations of shaft, magnets and sleeve geometries and materials have been investigated and presented in literature. Most of them feature the absence of the rotor back iron, a hollow parallel magnetized ring magnet (or a more complicated Halbach array configuration) fitted on a permeable shaft and retained with a sleeve. The three high strength retention materials that are commonly adopted are: Inconel 718, Ti6A14V (titanic alloy) and a carbon fibre composite. The first one

features a yield strength of 1100MPa with a good thermal conductivity. The second one is much lighter than the first one (4.4 respect to 8.19 kg/m^3) and provides a yield strength of 950 MPa. Carbone fibre composites material can exhibit impressive tensile strength (up to 1800 MPa) with the lowest mass density (1.79 kg/m^3). The selection of the sleeve material has to be based on both structural and electromagnetic considerations. On one hand from the structural point of view, the interference fit between the magnets and the sleeve has to be designed in order to provide a positive contact pressure between the two mating components at the maximum operating speed and the worst temperature condition (which depends on the thermal expansion coefficients of the materials). On the other hand, the sleeve material and thickness has a huge influence on the rotor losses; several papers have presented comparative study showing the effectiveness of using carbon fibre composites sleeve, which have a lower conductivity respect to Inconel or titanium alloys, with the aim of minimizing the rotor losses. The flux weakening capability of PMSMs with distributed winding configuration is traditionally one of the limits of such machine topology due to the low value of the d-axis inductance. The latter is further lowered in high speed design by the increased effective airgap (physical clearance, sleeve and magnet thickness). The low inductance value also results in very high short circuit currents. In order to wider the constant power speed range, two design strategies can be adopted. The first one simply consists in oversizing the converter rating and therefore increases the associated cost. The second one involves the use of concentrated winding configuration. The latter naturally leads to higher value of the inductance and therefore both flux

weakening capability and short circuit current are improved. However such winding configuration increases the harmonic content of the magneto motive force which causes the rise of the eddy current losses in the magnets and sleeve. In a bid to reduce such loss component, which can lead to excessive rotor temperature, several authors have proposed slot-less stator configurations [30, 32]. Another inherit drawback of this machine topology related with the use of PMs is the uncontrolled voltage operation which occurs in case of inverter fault and can lead to dangerous overvoltage at high speed.

- IM

High speed IMs can be built using both laminated and solid rotor construction. The solid rotor structure allows achieving a higher peripheral speed and mechanical stiffness compared to the laminated rotor structure as well as compared with PMSM [33]. Solid rotor IMs with a peripheral speed of 360 m/s have been reported in literature while PMSM usually reach 200-250 m/s [3]. These advantages come at the price of a reduced efficiency and power factor. Several design attempts have been proposed in literature in order to enhance the electromagnetic performance of the solid rotor IM such as axial slitting [34], surface copper coating, etc. However these workarounds tend to make the rotor structurally weaker or complicate the manufacture. It has to be underlined that for high speed applications, the IM rotor construction (solid or laminated) is much easier and its manufacturing is industrially mature respect to the PMSM rotor construction. It is common practice to prefer laminated rotor IM when mechanically possible since they provide better efficiency and power

factor respect to the solid rotor solutions [35]. Regarding the electromagnetic features, its natural flux weakening capability is one of the main advantages of this machine topology along with the higher rotor robustness respect to the PMSMs. The large rotor losses and so low efficiency and the low power factor are however its main disadvantages.

- SRM

The switched reluctance machine is the most robust solution respect to the above-mentioned machine families. Its simple and robust rotor construction permits higher speed and therefore high power density operation, while the absence of any magnets in the rotor enables it to operate safely in harsh environments such as in aerospace applications [36]. Its inherent fault tolerance capability and reliability are also related with the use of concentrated winding configuration and the consequent magnetic and electrical insulation between phases. The lack of active components and containment system on the rotor simplifies the manufacturing and involves that the maximum operating temperature is only limited by the adopted stator winding insulation. Although switched reluctance motors have many merits, there are some drawbacks that are not easy to overcome. The double salient structure can cause significant torque ripple and acoustic noise; several design strategies have been presented in literature with the aim of minimizing such torque oscillation such as proper stator and rotor pole shaping for a given combination of stator phases and number of poles. The high rotor iron losses in high speed operation due to the pulsating fields are another factor that must be considered during the design of

a SRM especially during the selection of the lamination material and the combination between phases and poles. The need for a dedicated power electronic converter topology (asymmetric bridge) as opposed to the standard symmetric three phase converters is another clear disadvantage of this machine topology.

1.5 High speed synchronous reluctance machine: a possible alternative?

Several electrical machine topologies have not been described in the last section because they have been traditionally considered unsuitable for high speed applications for their inherent limits; one of these is the synchronous reluctance machine (SyR). The latter is currently experiencing a revamped industrial interest in the low-medium speed application market mainly because when compared to the more common IM, they can achieve a volume reduction and/or an improvement of the operational efficiency [37, 38]. Along with the higher efficiency, its simple rotor construction and no need of permanent magnets (PM) are the other main advantages. The absence of rare earth based material and the possibility of manufacturing the rotor with standard methods make SyR machines a low cost alternative. High torque ripple and low power factor are the most important disadvantages of this particular machine topology. For this reason, a consistent amount of literature can be found addressing the above mentioned issues. In particular, several design techniques have been proposed in order to mitigate the high torque oscillations while the low power factor can be easily overcame introducing small amount of

permanent magnets inside the rotor structure. The insertion of the permanent magnets (also based on ferrite) allows also improving the constant power speed range. Such machine is usually called permanent magnet assisted reluctance machine (PMaSyR). Although these machine topologies can be considered a valuable alternative to the more common IM and PMSM in the low-medium speed range, as the speed increases the conflict requirements between electromagnetic torque and structural integrity can potentially compromise its overall performances. In fact the rotor integrity is practically dependant on the so-called iron bridges (also known as ribs or posts) shown in Figure 6.

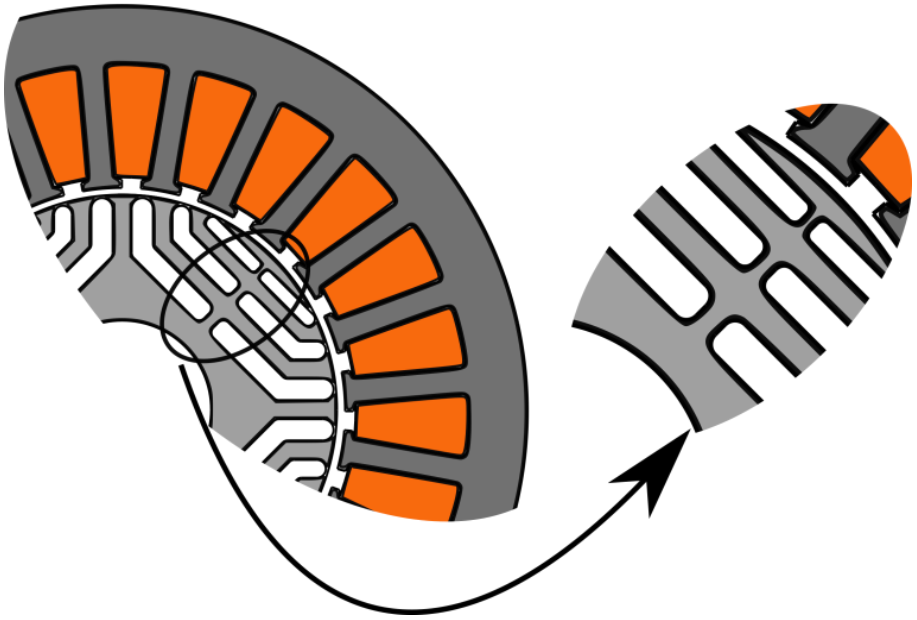


Figure 6: Cross section sketch of a SyR machine with a zoom on the central iron bridge

If these bridges are made to be wider for the sake of the rotor robustness at high speed, then this comes at the cost of a reduction in torque and power factor. The poor structural behaviour of SyR and PMaSyR machines have historically discouraged their uses in high speed applications and limited their adoption to low-medium speed ranges. Three design philosophies have been

recently proposed in literature aimed at overcoming the structural limitations of SyR and PMaSyR machines when applied in high speed applications. The first makes use of solid rotor structure; the second involves the use of high strength soft magnetic material while the third one encompasses the design of a SyR machine with a rotor featuring an external sleeve. The first one, which involves the use of a solid rotor structures [39-41], requires particular manufacturing process; in addition the machine performances (especially in terms of efficiency) are deeply limited by the high rotor losses. The second approach makes use of novel laminated material specifically designed to meet the higher demand in yield strength with minimum effect on electro-magnetic characteristics. The development of such materials has lately encouraged the research community to invest more in the concept of applying SyR and PMaSyR machines in very high speed applications as recently reported in [42, 43]. It is worth to mention another new soft magnetic material recently presented which has been used to push the speed limit of this class of electrical machine. In particular, in [44, 45] the author makes use of this new material whose magnetic permeability (normally high) can be locally reduced by means of heat treatments. This feature has been exploited to selectively reduce the permeability of the iron bridge regions present within a SyR rotor lamination. The use of this dual-state material allows overcoming all the structural speed-dependent limitations of SyR and PMaSyR machines; however such material is not available on the market. A SyR machine with a rotor having an external sleeve has been recently presented in [46] with the aim of relieving the stresses experienced in the iron bridges and so increases the speed limit of the machine.

The main challenge when designing such rotor structure is to achieve the optimum compromise between the torque improvement due to the reduced iron bridge thickness possible by the insertion of the sleeve and the reduction of the torque due to the increased physical airgap (always due to the introduction of the sleeve); the sleeve material, magnetic or non-magnetic, obviously plays an important role in deciding such trade-off. However, its introduction undoubtedly complicates the rotor manufacturing.

The advantages of HS-SyR machines with respect to other machine topologies usually adopted in high speed applications, which justify the increased interest of the research community on this topic, are summarized in the following.

- They do not require any rotor retaining system which makes the rotor construction more complex; such advantage would be lost adopting the sleeved SyR rotor configuration.
- The absence of PMs implies that SyR machines are not susceptible to price variability of the rare-earth materials.
- In addition, the PM absence essentially nullifies the risk of uncontrolled voltage operation in case of inverter fault and all the concerns about the PM demagnetization.
- The maximum temperature is dictated only by the winding insulation system and not also by the PMs characteristic.
- Despite the absence of the PMs, this machine topology allows achieving a good efficiency and, with a proper design, a low torque ripple.

In spite of these advantages, particular care must be devoted to the rotor design of HS-SyR machines since structural and electromagnetic aspects have to be

considered with equal importance. In addition, being the power density and power factor of a HS-SyR machine lower than the SPMSM, its design has to focus on their maximization.

1.6 Goals and organization of the thesis

The main aim of this thesis is to explore the potentials advantages of the SyR for high speed applications (described in the previous paragraph) and investigate its practical feasibility using the best available off-the-shelf soft magnetic materials. As a vessel to investigate the above mentioned design challenge, this work aims at developing a HS-SyR machine capable of delivering 5 kW at 80 krpm. In order to meet such demanding speed requirement, several multi-disciplinary design exercises have been carried out mainly having the following objectives.

1. Evaluate the influence of the speed-dependent limiting factors on the machine performance.
2. Identify the most effective design strategy which correctly balances the final performance and the design effort.
3. Investigate the compromise between rotor geometrical complexity and structural and electromagnetic performances.

With the purpose of achieving these objectives, the thesis has been organized as follows.

- Chapter 2 presents an introduction on the historical background and most relevant works related with the analytical design of SyR machines. In particular, the analytical design formulation first introduced by prof. Vagati is analyzed in details. This set of design equations is then extended with the aim of including the most important performance limitations as the speed increases.
- Chapter 3 faces the issues related with the electromagnetic and structural design of the rotor geometry of a HS-SyR. Since these two problems involve a relevant number of geometrical parameters to be identified and the optimization of several competitive performance indexes, different design approaches are implemented and compared in terms of final geometries, performance and computational effort.
- Chapter 4 investigates in detail the rotor structural design and the trade-off between the rotor geometrical complexity and the final machine performance. According to the comparative analysis presented in this chapter the best rotor geometry electromagnetic and structural wise is selected for prototyping.
- Chapter 5 aims at analyzing the structural and electromagnetic performance modification due to aspects related with the real manufacturing and assembling processes. In particular the influence of the geometrical manufacturing tolerances on the overall performance is addressed implementing two different approaches with the aim of evaluating the entities of such performance deviations.

- Chapter 6 first details the calculation of all loss components and then describes the lumped parameter thermal model used to evaluate the thermal performance of the designed machine and to identify the minimal coolant flow rate required to keep all the temperature within safe limits. Then the complete thermal and electromagnetic analysis of the final design is presented.
- Chapter 7. The manufacturing and assembling of the critical components are first outlined along with the experimental rig layout. Then the carried out tests are described and their results compared with the FE-predicted ones. In particular, first a magnetic model identification approach is implemented in order to estimate the flux-current behaviors of the built machine. With the aim of explaining the discrepancy between the estimated and measured performance, the influence on the magnetic characteristics of the constituent materials when subject to different mechanical stress conditions is measured by means of a specially designed test setup. Finally the results of several no-load and load tests are presented with the aim of validating the proposed design.
- Chapter 8 draws some conclusions by summarizing the key observations and describing possible related future works and developments.

Chapter 2
SyR machine design

This chapter, after a brief introduction on the historical background and possible design strategies, presents the salient works related with the analytical design of SyR machines. In particular the analytical formulation presented by prof. Vagati in [47-49], which allows writing a set of design equations of a low speed SyR machine under certain assumptions, is analysed in detail and extended with the aim of considering the most important limitations related to the increasing speed. Such formulation is then used to evaluate the influence of each limiting factor as the speed increases and to draw general conclusions about the design of a HS-SyR machine.

2.1 Historical background

The concept of the reluctance torque production is known since the development of the two axis theory of Blondel [50] which was first applied to synchronous machine. In principle, a SyR machine is a classic salient pole synchronous machine without any excitation winding on the rotor. This kind of rotor structure, in which the outer profile is suitable shaped, can be considered the first attempt to analyse and realize a SyR machine [51, 52]. The inherent limitations of SyR machines with salient pole rotor structure, shown in Figure 7a, was first recognized by Kostko in 1923 [53]. The main limitation is related to the fact that if the interpolar space region is widened (in order to decrease the q-axis inductance), the pole space is consequently narrowed, producing an unwanted reduction of the d-axis inductance. The poor performance in terms of efficiency and power factor is due to the low saliency ratio obtainable with such rotor construction. In the same paper, Kostko proposed a solution to overcome this limit which consists in subdividing the rotor into several iron sections magnetically insulated from each other as depicted in Figure 7b.

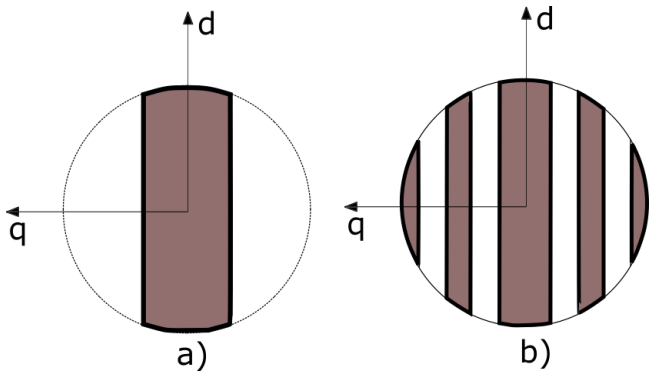


Figure 7: Simplified 2 poles SyR rotor geometries, a) salient, b) segmented pole configuration

This rotor structure allows obtaining a higher magnetic saliency because:

- the portion of the pole pitch used to conduct the d-axis flux is widened respect to the salient pole construction, (only a part of it is used for this purpose) with a consequent increment of the d-axis inductance;
- the insertion of magnetic insulated layers (also called flux barriers) along the q-axis flux path increases its reluctance and thus the q-axis inductance decreases.

Despite the promising and improved performance as described above, however in practice, the SyR machine in its early days was still a challenging system to implement when connected directly online. Thus SyR machines only started attracting, 'real' interest from the research community, when solid state inverter tecnology matured in the 1960s and 1970s. The 'traditional' drawbacks of this machine under direct supply, i.e. stabilty issues and start up torque (previously achieved by using rotor cage windings), could then be overcome [54, 55]. In fact, during subsequent years, research regarding SyR machines led to more accurate analysis, design guidelines and real implementations all intended to be applied to variable-frequency drives [56]. In those years (1960-1980), two methods of rotor constructions were of main interest, namely the transversally and axially laminated rotor geometries, both shown in Figure 8. Theoretically, the most interesting solution is the axially laminated one in which the laminations are properly shaped at each pole, insulated from each other and kept together with radially placed bolts. This rotor structure gives the opportunity to increase the achievable saliency ratio by increasing the number of iron sections.

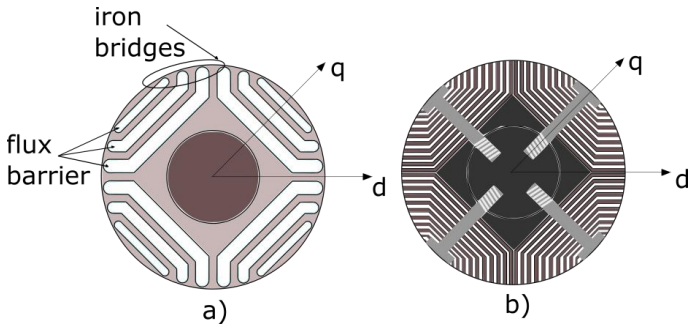


Figure 8: a) Transversally and b) axially laminated SyR rotor structures

The expected higher efficiency is however lowered by the high rotor iron losses concentrated near the airgap [57]. This rotor construction never faced a real commercialization phase since its manufacturing is more difficult respect to the conventional machine [58]. On the other hand, the transversally laminated SyR rotor structure is obviously easier to manufacture and consists in a multiple air flux barriers geometry which makes the structure electromagneticaly anisotropic. The iron and air layers are kept together by small iron bridges, also called ribs, as highlighted in Figure 8a. These structural supports, whose dimensions need to increase as the speed increases, worsen the q-axis inductance and therefore have a negative effect on the overall performance. As mentioned in Chapter 1, historically, this has limited the application of SyR machines in high speed applications. Another relative advantage of the transversal laminated rotor is related to its torque ripple performance. The latter is due to the rotor magnetic reaction to the stator m.m.f harmonics [59] and one of the method that can be adopted to reduce such drawbacks is the rotor skewing. The latter, although does not gaurantee the complete elimination of the torque ripple [60], can be only applied to transversal laminated rotor structure. Considering all the above, it is therefore

clear why the majority of published literature and research efforts in the last three decades has been focused on the transversal laminated SyR rotor configuration.

2.2 SyR modelling and design: an overview

High torque ripple, low power factor and efficiency and not standardized design procedure constitute the main disadvantages and challenges of SyR machines. Consequently, a lot of research effort has been dedicated to these aspects. Since its introduction, the SyR machine was seen as a possible replacement for the vector controlled induction motor drive. Subsequently a common design practice consists in replacing the squirrel cage rotor by a SyR one; therefore a considerable amount of literature has focused only on the rotor design. For a SyR machine, the rotor design is always very challenging, as it involves many degrees of freedom and complex phenomenas. In particular, the influence of the number of flux barriers, their angular positions at the airgap and their shape on the average torque, power factor and torque ripple, have consituted the core topics of research [61-63]. Regarding the design procedure which include both stator and rotor laminations, the most relevant work has been reported through the years by prof. Vagati in [47, 49, 64]. Under certain assumptions, a set of design equations, which allows the clear identification of the several trade-offs involved during the design of such machine topology, has been developed. Further important contributions to the analytical modelling of

SyR machine is related to the work published by Bianchi [63, 65-67] and Reza [68]. Such analytical methods based on the magnetic equivalent circuits have in general the clear advantage of fast prediction of the machine performances. Despite being fast they are obviously based on hypotesis which make possible the modelling itself. Such assumptions usually involve the linearity of the iron and the simplification of the rotor geometry. However neglecting the high non linear relation betweeen flux and current could lead to imprecise results [69]. An example of a relationship between the d- and q-axis fluxes and the d- and q-axis current components is shown in Figure 9. The iron saturation essentially limits the d-axis flux at high current levels, while the q-axis flux is almost linear except at extremely low current values where the saturation of the iron bridges cause the peculiar change of the slope of the q-axis flux-current curve. The same graph shows the so-called cross-coupling effect, which consists in the magnetic interaction between the d- and q-axis caused by the saturation.

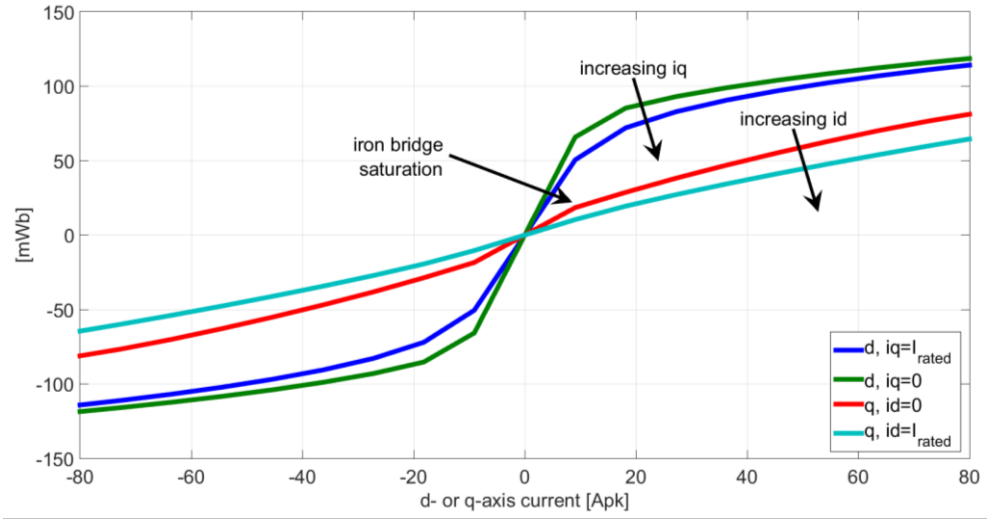


Figure 9: An example of FE calculated d- and q-axis fluxes vs d- and q-axis currents for a SyR machine (3.5 Nm rated at 2500 rpm)

In fact both axis fluxes share part of the magnetic circuit and its saturation due to a certain flux influences the other flux-current relation. As a consequence the d- and q-axis fluxes are a function of both current components. This phenomena is of particular relevance in SyR machine and its modelling, mainly possible by a detailed FEA, is fundamental if an accurate prediction of the torque has to be achieved for design or control purpose [49, 70, 71]. The accuracy of linear analytical models obviously fails in the prediction of the main torque in the non linear region which usually corresponds to overload conditions and in the prediction of the cross-saturation influence. While the iron saturation along the d-axis can be easily considered with classical methods, the influence of the cross-saturation is more difficult to include in the analysis. The simplification of the rotor geometry, mainly of the flux barrier geometry, usually adopted with the aim of making the analytical modelling possible, is not only another source of inaccuracy but it could also lead to sub-optimal designs if the model is used as a design tool (the hypotesis of constant flux barrier thickness is a clear example). It is worth to mention that analytical models of outstanding accuracy have been recently reported in [72, 73] which allow a quite accurate prediction of the torque profile. The first one is able to precisly consider the saturation of both stator and rotor iron by means of an iterative procedure while the second estimates the reluctance of a complex flux barrier shape through the use of conformal mapping. However such analytical models (which anyway do not consider the influence of the local saturations on the machine performance) are difficult to set up and their use oriented to the design can be considered the next challenge of the research on SyR machines

[74]. The above considerations constitute the main reasons for which the design procedure of SyR machine is usually divided in two steps: first an analytical model is used to carry out a preliminary design and then a Finite Element Analysis (FEA) is employed to fine-tune the design and evaluate the design aspects disgregarded in the first stage. During the FE refinement stage, several iterations can be needed and the time required for this stage mainly depends on the level of accuracy of the analytical model used for the preliminary design. In recent works [75-78], automated design procedures assisted by stochastic optimization algorithms and coupled with FEA have been presented as an alternative of the aforementioned two steps design strategy. In principle this design approach does not make use of any hypothesis and therefore has the clear advantage of considering all the design aspects during the performance evaluations such as iron non-linearities and all the geometrical parameters. However, also in this case particular attentions have to be paid to the preliminary design choices and constraints imposed during the definition of the optimization problem. In fact erroneous choices during the problem statement can heavily influence the results of the optimization and in extreme cases it can completely nullify the advantages related with the adoption of this design approach. The bottleneck of this design methodology lies on the computational burden required to carry out the optimization. The latter depends on two factors: the computational time required to evaluate the performance of a single machine candidate and the high number of functional evaluation required by the optimization algorithm (OA) to converge. The first depends on which performance indexes are being optimized (in fact torque,

torque ripple and iron losses for example require different computational time for their FE determination) and consequently this factor is strictly related with the trade-off between the required accuracy and the single FE simulation time (which mainly depends on the FE mesh setting). The second one depends on a multitude of aspects related with the selected OA, its settings, the number and type of objective functions and the number of input variables which defines the research space dimension.

In the following paragraphs the salient works related with the analytical design of SyR machines are reported. In particular the set of design equations reported in [47] is analysed in detail in order to highlight the several trade-offs involved in the design of a low speed SyR machine. Then such formulation is extended with the aim of considering the limiting phenomena which incurs as the operating speed increases such as iron losses and structural restrictions. Using this set of equations some considerations about the capability of SyR machine to be applied in high speed applications are presented.

2.3 Analytical design of SyR machine

This section reports first the calculation of the d- and q-axis inductance of a SyR machine neglecting the stator slots presence and then some design considerations regarding the torque ripple reduction.

2.3.1 Rotor modelling and design considerations

Two main objectives have to be pursued when designing a transversal laminated SyR rotor structure: the maximization of the torque and the minimization of the torque ripple. Considering only the rotor design, therefore keeping the rotor diameter constant, the maximization of the torque simply corresponds to the maximization of the difference between the axis inductances. With the aim of obtaining a SyR rotor structure with the maximum anisotropy, let's first consider a sinusoidal stator m.m.f.. As the torque ripple is caused by the interaction between the stator m.m.f. harmonics and the harmonic of the m.m.f. rotor reaction [59], the assumption of a purely sinusoidal stator m.m.f leads to a SyR machine without torque oscillation. In a later stage the influence of the stator m.m.f discretization will be introduced and some design considerations, aiming to the minimization of the torque ripple, will be reported.

2.3.1.1 Inductances calculation

Whatever is the relative position between the stator m.m.f and the rotor, the stator m.m.f. can be subdivided in d- and q-axis component. An example of these two operating condition is reported for sake of clarity in Figure 10 in which the main flux paths are highlighted.

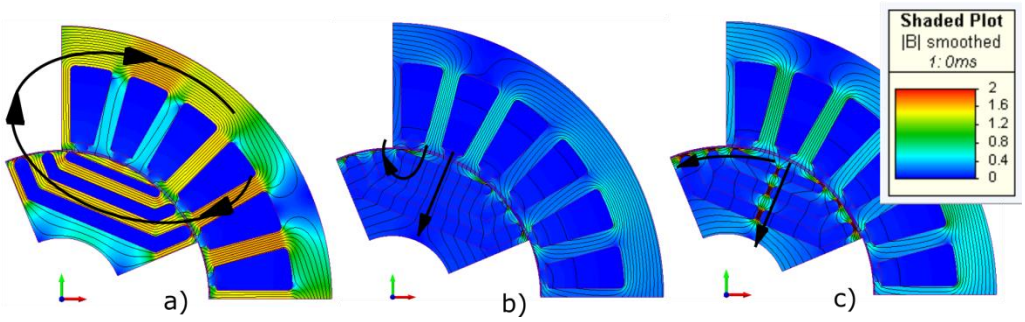


Figure 10: Examples of FE calculated flux density distributions and main flux trajectories with only a) D-axis current, b) Q-axis current without iron bridges, c) Q-axis current with relevant tangential and radial iron bridge thicknesses

Considering only the d-axis component and disregarding the iron m.m.f drops, the rotor magnetic potentials are zero, which means that the rotor segments (also called flux guides or rotor islands) do not react to the stator m.m.f, and the magnetizing d-axis inductance can be simply written [79] as:

$$L_{dm} = \frac{\pi}{2}\mu_0 k_w \left(\frac{N}{p}\right)^2 \frac{R_r \cdot L}{k_c \cdot g} \tag{2}$$

where k_w is the winding factor, N the number of turns is series per phase, p the pole pairs, R_r the rotor radius, L the stack length, k_c the carter coefficient (which takes into account the slots presence) and g the geometrical airgap length. All the following discussion refers to the simple rotor structure shown in Figure 11. It is clear that small values of airgap length and low pole pairs have to be adopted if a high d-axis magnetizing inductance is desired. If only the q-axis component of the stator m.m.f. is considered, the rotor iron segments assume different magnetic potentials r_i. In other words the rotor magnetically reacts to the applied stator m.m.f..

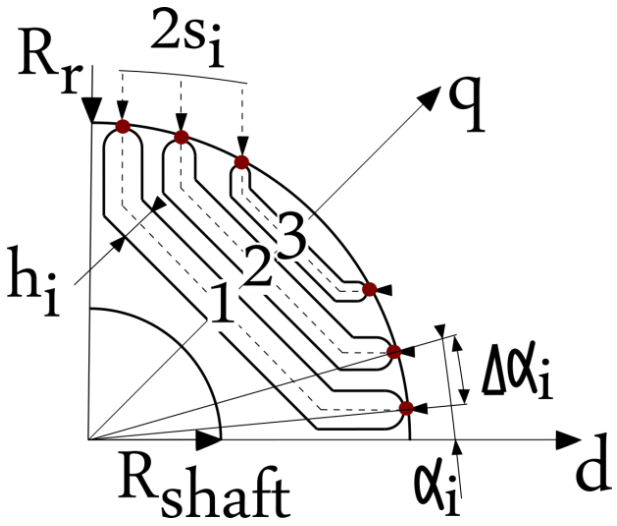


Figure 11: Simple SyR rotor structure parametrization

With the aim of calculating the magnetizing q-axis inductance, the applied q-axis m.m.f can be considered as made up of two components. In fact, if the m.m.f. is averaged along the periphery of the rotor with intervals equal to the rotor pitches, i.e. the angular distance between each flux barrier $\Delta\alpha_i$, a staircase function $f(\alpha)$ is obtained where the i-th step can be calculated as:

$$f_i = \frac{1}{\Delta\alpha_i}\int_{\alpha_i}^{\alpha_{i+1}} \sin\alpha \, d\alpha = \frac{\cos\alpha_i - \cos\alpha_{i+1}}{\alpha_{i+1} - \alpha_i} \qquad (3a)$$

The other component $c(\alpha)$ of the stator m.m.f. is the remaining part of the sinusoidal stator m.m.f. as depicted in Figure 12. The staircase-shaped component of the stator m.m.f causes the flowing of the q-axis flux from one flux guide to the other by means of the air flux barriers and for this reason it has been called flow-through component. The other component generates the so-called circulating flux which is the q-axis flux that does not enter any flux barrier and circulate only in the most external part of the rotor as shown also in Figure 10.

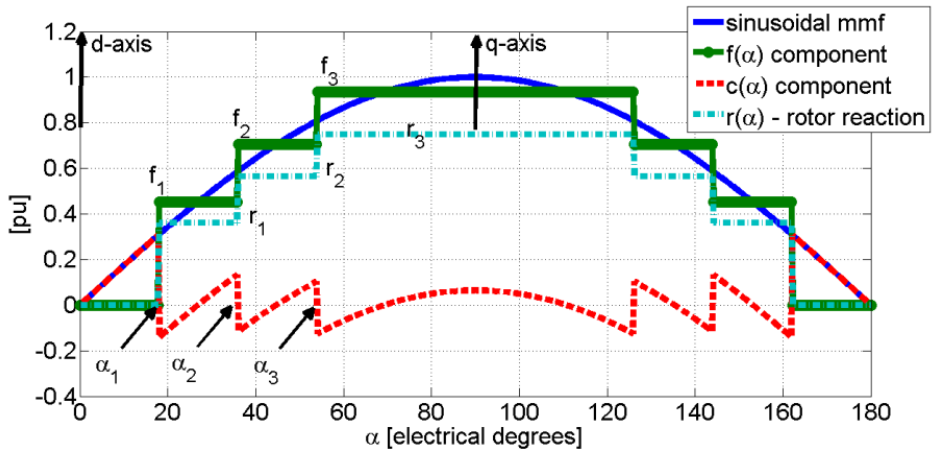


Figure 12: Subdivision of the q-axis m.m.f. and rotor reaction distribution (here supposed proportional to $f(\alpha)$) expressed in per unit

It can be proved that the circulating q-axis component of the inductance can be expressed [48, 49, 80] as:

$$L_{qm\_c}/L_{dm} = 1 - \frac{4}{\pi} \cdot \sum_{i=1}^{n} f_i^2 \Delta\alpha_i \qquad (3b)$$

where f_i are the step values of the staircase function (shown in Figure 12) and $\Delta\alpha_i$ are the rotor angular pitches as depicted in Figure 11. As the number of flux barriers n increases, the area between the m.m.f. component $c(\alpha)$ and the α-axis rapidly decreases. This area is proportional to the circulating q-axis flux, therefore also L_{qm_c} decreases as the number of flux barrier increases as shown in Figure 13. In general 3 flux barriers per pole are enough to obtain a low value the circulating q-axis flux component. The calculation of the flow-through component of the q-axis inductance requires the knowledge of the rotor magnetic potential r_i of each flux guide; the latter can be determined by

means of the equivalent magnetic circuit related with such operating condition as reported in Figure 14 (for a rotor with 3 flux barriers).

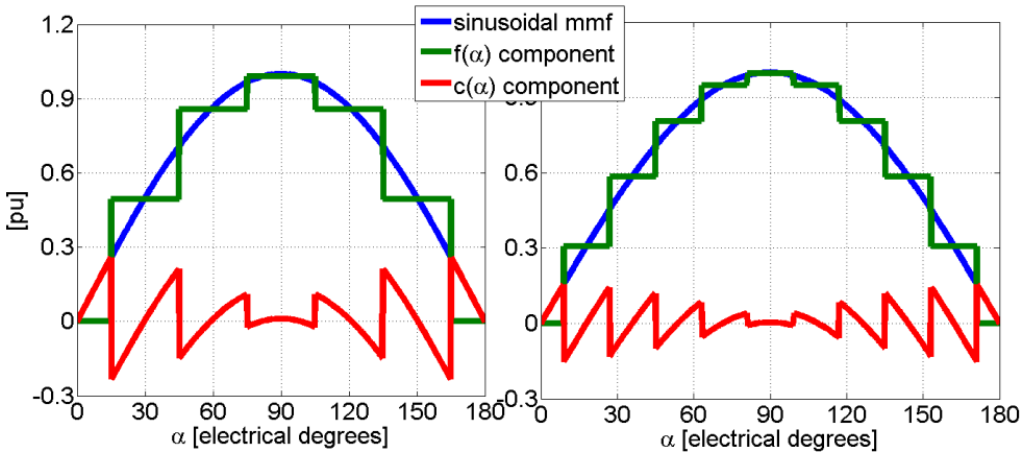


Figure 13: Per unit q-axis m.m.f components for a rotor having 3 (left) and 5 (right) flux barriers equally distributed along the airgap periphery

The m.m.f. steps f_i and the permeances (airgap p_{gi} and barrier p_{bi}) shown in this circuit are expressed in per unit considering as base values respectively the maximum m.m.f. and the product $\mu_0 \cdot L$. In fact the flow-through component of the q-axis inductance can be expressed as [49]:

$$L_{qm\_f}/L_{dm} = \frac{4}{\pi} \cdot \sum_{i=1}^{n} f_i(f_i - r_i)\Delta\alpha_i \qquad (4)$$

The magnetic equivalent circuit reported in Figure 14 neglects the effect of the iron bridges. However this can be taken into account adding an extra branch in parallel to the flux barrier permeance [81] containing the iron rib permeance and its m.m.f. drop (calculated imposing a certain rib iron saturation level). Such equivalent magnetic circuit can be obviously solved in a general way applying the nodal-voltage method as reported in [82].

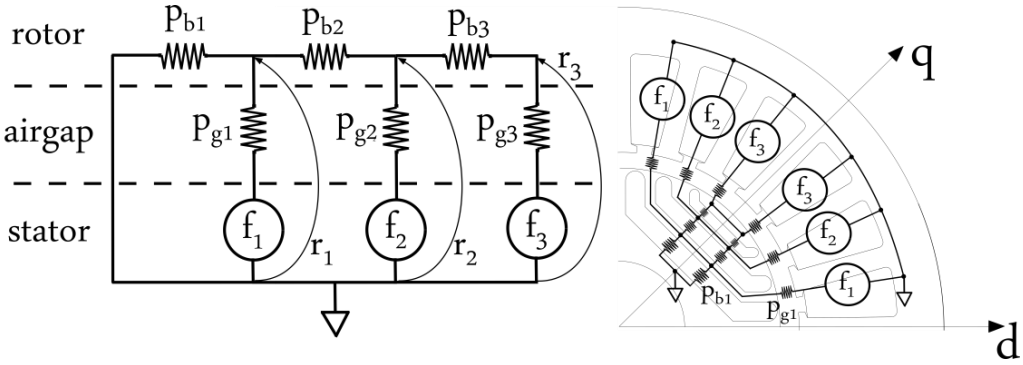


Figure 14: Simplified per unit q-axis equivalent magnetic circuit

However if the airgap m.m.f. drops is neglected, which is equivalent to consider $f_i \cong r_i$, the following approximate relation can be written which avoids solving the equivalent magnetic circuit [48]:

$$L_{qm\_f}/L_{dm} \cong \frac{4}{\pi} \cdot \frac{p \cdot k_c \cdot g}{R_r} \sum_{i=1}^{n} \frac{s_i}{h_i} \Delta f_i^2 \qquad (5)$$

where all the geometric symbols are shown in Figure 11. Neglecting the secondary influence of the pole pairs on the surface of the flux barrier s_i (which depends on the adopted flux barrier profile), it can be stated that the flow-through component of the magnetizing q-axis inductance worsen as the pole pairs increases. The same behaviour can be noted when considering an increment of the airgap length g. The most significant parameter affecting L_{qm_f} is the total amount of air along the q-axis h_{air}, which is obviously the sum of the flux barrier thickness h_i; the influence of the flux barrier number n can be instead considered negligible as proven in [49]. Considering all the above, a clever design consideration is to increase the number of flux barriers n until L_{qm_c} becomes a small portion of the total q-axis inductance and then

increase as much as possible the air-layer along the q-axis, i.e. increase the barrier thickness in order to achieve a small value of L_{qm_f}. This is why the SyR rotor with 3 flux barrier per pole is the most adopted configuration in literature. Obviously the sum of the flux barrier thicknesses h_{air} has an upper limit imposed by the minimum amount of rotor iron measured on the same axis needed to conduct the d-axis flux without reaching a high level of saturation. In other words, if the amount of air h_{air} along the q-axis is excessively incremented, to the expected decrement of L_{qm_f} is also related an unwanted decrement of the d-axis inductance due to the high saturation of the rotor flux guides. Therefore it can be stated that also with segmented SyR rotor configurations a trade-off needs to be achieved between the competitive goals of increasing the d-axis inductance and decreasing the q-axis one. Considering the equation (5), it is easily possible to obtain the relation between the flux barrier thicknesses h_i, their surface s_i and the m.m.f. steps Δf_i which leads to the minimization of L_{qm_f}, simply imposing the partial derivatives of (5) with respect to each h_i equal to zero:

$$\frac{h_k}{h_i} = \frac{\Delta f_k}{\Delta f_i}\sqrt{\frac{s_k}{s_i}} \Leftrightarrow \frac{p_i}{p_k} = \frac{\Delta f_k}{\Delta f_i}\sqrt{\frac{s_i}{s_k}} \tag{6}$$

for each k and i flux barrier and where p_i is the per unit barrier permeance (i.e. s_i/h_i). Since for a generic angular position at the airgap of the barriers α_i, and for any barrier shape, both barrier surface s_i and m.m.f. step Δf_i decrease going from the innermost to the outermost barrier, equation (6) mathematically

expresses the optimum decrement of the barrier thicknesses going from the innermost to the outermost barrier in order to achieve the minimum q-axis inductance component L_{qm_f}. The latter can be obtained substituting equation (6) into (5):

$$L_{qm\_f}/L_{dm} \cong \frac{4}{\pi} \cdot \frac{p \cdot k_c \cdot g}{R_r \cdot h_{air}} \left(\sum_{i=1}^{n} \Delta f_i \sqrt{s_i} \right)^2 \qquad (7)$$

The discussion regarding the inductances calculation so far reported remain still valid also when a slotted stator is considered, even if some approximations need to be accepted [48]. This is not the only method with which is possible to calculate the axis inductances; in fact, other works [49] make use of a more complex equivalent magnetic circuit in order to compute the overall performance. However such methods of analysis do not allow drawing general design guidelines such the ones that has been reported in this section.

2.3.1.2 Torque ripple considerations

The main influence of the slot presence is related to its impact on the torque oscillations. In order to minimize the torque ripple, the harmonic contents of the stator m.m.f. and the rotor reaction $r(\alpha)$ have to be as different as possible since the main cause of the torque oscillation is their interaction [59]. The rotor reaction $r(\alpha)$ can be derived from the equivalent magnetic circuit as shown in Figure 14, whose parameters depend on the rotor geometry which is in turn

defined by a considerable amount of geometrical degrees of freedom. In order to simplify the design considerations aimed at the torque ripple minimization and to achieve general guidelines, only the stator slots spatial harmonics are considered along with a regular displacement of the rotor flux barriers at the airgap [59]. By doing so, the stator m.m.f harmonic order can be expressed as $h \cdot n_s \pm 1$ with h any positive integer and n_s the number of stator slot per pole pair; while the staircase component of the q-axis m.m.f $f(\alpha)$ will contain harmonics of order $k \cdot n_r \pm 1$ with k any positive integer and n_r the number of equivalent rotor slots (which ideally correspond to the number of iron bridge at the airgap). If the rotor geometry is designed such as the rotor reaction $r(\alpha)$ has a harmonic content similar to the staircase component of the q-axis m.m.f $f(\alpha)$ then the consideration on the torque ripple minimization, (i.e. the minimization of the harmonic interaction between the stator m.m.f and the rotor reaction), can be done by considering only the number of the stator and equivalent rotor slots. Despite the evidence, which would lead to choose n_r as much different as possible from n_s, in [59] it has been proved that the best strategy is to choose n_r the closest possible to n_s, but avoiding n_s and $n_s \pm 2$, as this would lead to the direct interaction between the stator and the rotor harmonics. As a consequence the same author suggests that rotor designs with

$$n_r = n_s \pm 4 \tag{8}$$

leads to the minimization of the torque ripple; when n_s is high, the solution with $n_r = n_s - 4$ is preferred since it is easier to manufacture. The relation between the number of stator and rotor slots aiming to reduce the torque ripple

requires that the rotor magnetic reaction $r(\alpha)$ has the same harmonic content of the staircase component of the q-axis m.m.f $f(\alpha)$, which means that it has to assume a staircase shape. In order to achieve this condition, since the airgap permeance p_{gi} for the different rotor flux guide are equal (as a consequent of the fact that the barrier are regularly displaced at the airgap), the permeance of all flux barriers p_{bi} must be the same as also elegantly explained in [82]. The condition of constant flux barrier permeance that leads to the minimization of the torque ripple is however different from the condition described by the equation (6) which allows the minimization of the q-axis inductance (in particular of the flow-through component) and so the maximization of the rotor anisotropy. It can be therefore stated that the maximization of the rotor anisotropy and the minimization of the torque ripple require slightly different rotor design, especially in terms of distribution of flux barrier thicknesses. In fact, for a given number of stator slots, the optimum number of rotor slots and their angular positions at the airgap are determined following the previous explained rule, and once the barrier profile is chosen also the surface of the flux barrier is defined from their angular positions; therefore the remaining geometrical degrees of freedom are the distribution of the barrier thicknesses. Once the number of equivalent rotor slots is defined, the number of flux barriers n can be chosen according to the following relations which considers only complete positive rotor structure as defined in [59, 83]:

$$n = \frac{n_r - 2}{4} \quad \text{if } \frac{n_r}{2} \text{ is odd} \tag{9}$$

$$n = \frac{n_r}{4} \qquad \text{if } \frac{n_r}{2} \text{ is even}$$

The differentiation between rotor having $n_r/2$ odd or even is due to the introduction of a virtual rotor slot along the q-axis. When the optimum number of flux barrier is high according to (9), a smaller number can be selected to make the manufacturing easier. In particular, one or more flux barriers nearest to the q-axis can be omitted since they are the smallest and so more difficult to realize. However in this case, even considering flux barriers with equal permeance, the distribution of the magnetic rotor reaction $r(\alpha)$ does not strictly follow anymore the shape of the staircase component of the q-axis m.m.f. $f(\alpha)$, therefore another criteria needs to be identify in order to minimize the torque ripple. The most rigorous solution to this problem has been proposed in [49] which suggests solving the matrix equation related to the equivalent magnetic circuit of the q-axis and imposing the proportionality between $f(\alpha)$ and the rotor reaction $r(\alpha)$ and some other geometrical constraints; by doing so the optimal permeances of the flux barriers are not equal anymore. A clever solution to this problem is reported in [83] and consists in keeping a regular displacement at the airgap of all flux barriers except the one nearest to the q-axis. The position of the latter can be then calculated in such a way that the rotor magnetic reaction $r(\alpha)$ is as much similar as possible to the staircase component of the stator m.m.f $f(\alpha)$. Another really interesting idea on how to minimize the torque ripple of SyR machine is reported in [68]. The author states that the torque ripple can be minimized without following the relation between number of stator and equivalent rotor slots suggested by Vagati. In

particular, [68] states that whatever number of stator slots and flux barriers are selected, the torque ripple can be minimized without affecting the main torque by means of a fast FE sensitivity analysis which acts only on one parameter, which is proportional to the angular rotor pitch (still considered constant) and keeping fixed the amount of air along the q-axis. Although the constant rotor slot pitch is a general accepted rule for all conventional electrical machine in order to minimize the torque ripple, this is not the only one that can be applied to mitigate this drawback of SyR machines. For example, [84] considers unequal rotor slot pitches, [85, 86]] make use of asymmetrical barrier arrangement, [87] considers different rotor slot pitches in different poles, [88] subdivides the stack length in two parts having SyR rotor with different slot pitches.

2.3.1.3 Other design considerations

It is clear that the wide variety of rotor design solutions, which can be found in literature, is mainly ascribed to the huge number of degrees of freedom that SyR rotor geometry offers during its design. Although the previous design guidelines can be considered the most important and general, there are no clear suggestions on the optimum flux barrier shape The choice of the latter affects the dependence of the barrier permeance from its angular position at the airgap. In particular, different barrier profiles assume different surface s_i for the same α_i and the same s_i changes differently as α_i varies. Since the analysis of the

flux barrier profile on the performance of SyR machine involves many geometrical degrees of freedom, almost all authors make use of FE simulation to carry out sensitivity analysis studies. An interesting attempt to obtain a further improvement in terms of torque capability of SyR machine is reported in [68]. In particular the author suggests adopting a flux barrier profile which follows the flux lines that the stator winding would produce in a solid rotor (i.e. laminated rotor without flux barriers). Fortunately a closed form expression of such flux lines can be deduced from the conformal mapping theory and the Jaukowski air-flow potential formulation. This flux barrier profile has been implemented also by other authors [89, 90] and an accurate comparison among different barrier shape is reported in [91, 92]. All of them agree that this flux barrier shape allows achieving the best torque performance. The main reasons behind this improved performance lies on the not-constant thickness of the flux barrier which guarantee a more uniform exploitation of the rotor iron. This concept is depicted in Figure 15 which shows the flux density distribution at maximum torque per ampere (MTPA) condition of two SyR machines having a flux barrier with constant thickness (a) and the barrier profile (b) proposed in [68]. The maximization of the torque and the minimization of the torque ripple have been the key topics among researchers in SyR machine design during the last 30 years and the most important of them have been here summarized. However, a considerable amount of works which address the problem related with the iron losses in SyR machines can be also found.

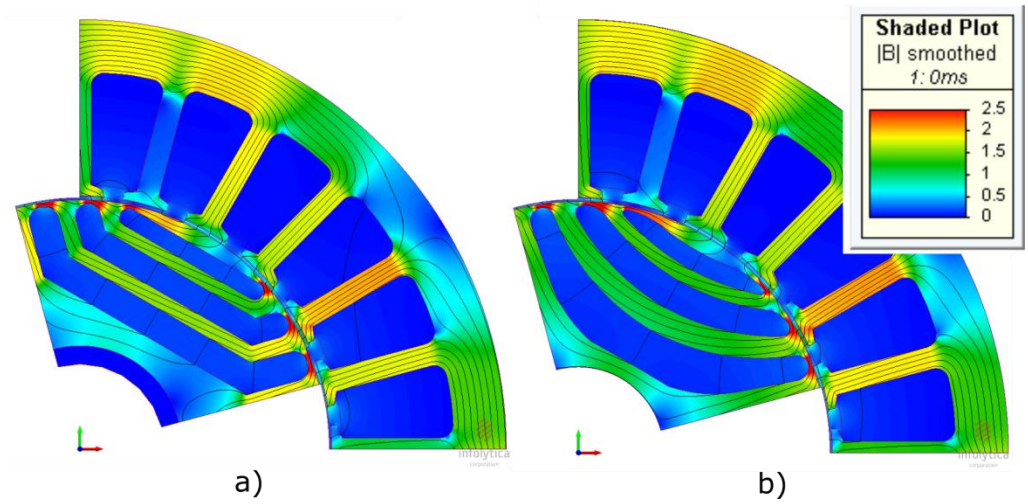


Figure 15: Flux density distribution at MTPA condition for a) a SyR rotor having flux barrier with constant thickness and b) a SyR rotor with the improved flux barrier profile

Also in this case an analytical investigation comparing SyR machines having different stator and rotor slot combinations is presented in [93]. In the latter it is proved that n_r, n_s combinations that lead to the maximum torque ripple (i.e. $n_r = n_s$), minimize the iron losses, therefore there is a trade-off to accomplish between iron losses and torque ripple when n_r has to be chosen. Other analytical studies has focused only on the rotor or stator iron losses [94, 95] achieving the same conclusion regarding the parameters which most affect the loss component (i.e. stator and rotor slots numbers, and in general the airgap positions of the flux barriers) but they proposed different design approaches in order to reduce them (i.e. proper angular positioning of the flux barriers at the airgap, adopting an odd number of stator slots per pole pair, etc.).

2.3.2 Stator-rotor design equations

In the following torque and power factor will be expressed as function of two independent design variables, i.e. the split ratio sr and the magnetic ratio mr. The first one is the classic ratio between the outer rotor to stator radius ($sr = R_r/R_s$), while the second is the ratio between the airgap flux density and the iron flux density ($mr = B_g/B_{fe}$). The remaining geometrical parameters (all depicted in Figure 16) will be expressed in terms of these two via physical and geometrical constrain equations. Both torque and power factor are considered because in general the combinations of mr, sr which optimize the torque does not necessarily coincide with the one maximizing the power factor. In fact the maximum power factor depends only on the inductances L_d and L_q while the torque depends both on inductances and capability of the machine to produce the stator m.m.f and flux, which in turn depends on the geometry and on the constraints imposed during the design, e.g. which variables are considered constant (e.g. external radius, electrical loading, current density, losses, etc.). The hypotheses on which this set of design equations is based are:

- the outer diameter and length of the stator laminations are considered fixed,
- the iron is considered linear with an infinite permeability, which in turn implies that the iron m.m.f drops are disregarded;
- the characteristic of the cooling system is preliminary chosen, which mainly means that the maximum ratio k_{cool} between total machine power losses and external surface available for the heat exchange is given;

- the operating flux densities B_{fe} within each part of stator and rotor is preliminary chosen and the main dimensions will be identified (also imposing such constraint) as function of both design variables mr and sr.

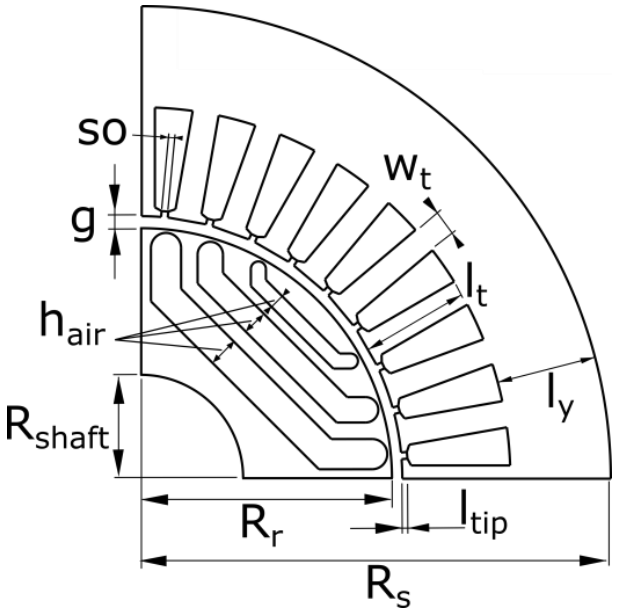


Figure 16: Stator and rotor parametrizations

The hypothesis of linear behaviour of the magnetic material is obviously a limit of this design approach if the flux density in the iron imposed during the design is too near or above the knee of the B-H curve of the selected magnetic material. The electromagnetic torque produced by a SyR machine is expressed in the d-q reference frame with the well-known equation [96]:

$$T = \frac{3}{2} \cdot p \cdot \left(L_d - L_q\right) \cdot i_d \cdot i_q \tag{10}$$

Knowing that both total inductances L_q, L_d are the sum of the respective magnetizing inductances L_{mq}, L_{md} and the leakage inductance L_{leak} (equal for both axis) and being the q-axis magnetizing inductance composed by two

components as explained in the previous section, equation (10) can also be easily written in the form:

$$T = \frac{3}{2} \cdot p \cdot L_{dm} \cdot \left(1 - \frac{L_{qm\_c} + L_{qm\_f}}{L_{dm}}\right) \cdot i_d \cdot i_q \qquad (11)$$

From the vector diagram at steady state depicted in Figure 17 is possible to deduce the power factor relation.

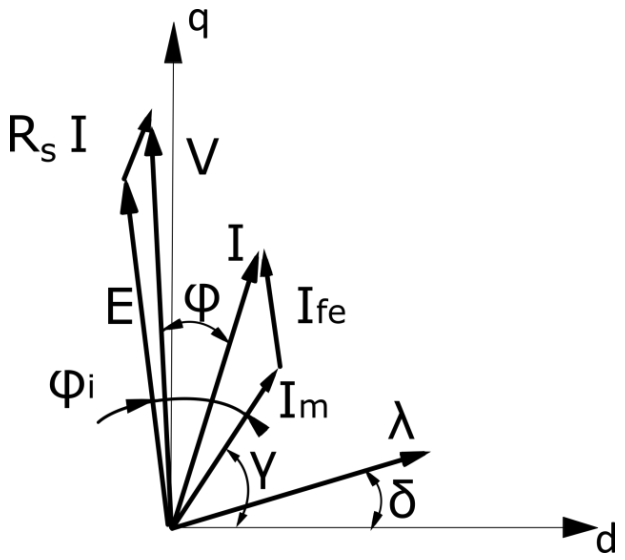


Figure 17: Vector diagram of a SyR machine (with vectors not in scale)

In particular, if the influence of the stator resistance R_s and iron losses resistance R_{fe} are neglected, the power factor pf coincides with the so-called internal power factor ipf, i.e. the cosine of the angle between the current vector I and the induced voltage E. The internal power factor can be obviously expressed as:

$$ipf = cos(\varphi_i) = cos(\pi/2 - (\gamma - \delta)) = \sin(\gamma - \delta) \qquad (12)$$

where γ and δ are respectively the current and the flux phase angle. The second can be expressed in function of the first one ($tg(\delta) = \lambda_q/\lambda_d = \left(L_q i_q\right)/(L_d i_d) = L_q/L_d \cdot tg(\gamma)$), therefore the following relation can be deduced:

$$ipf = \sin(\gamma - \delta) = \sin\left(\gamma - arctg\left(L_q/L_d \cdot tg\gamma\right)\right) \qquad (13)$$

Imposing the derivative of (13) equal to zero it is possible to determine the maximum value of internal power factor which occurs when $tg(\gamma) = \sqrt{L_d/L_q}$:

$$ipf_{max} = \frac{L_d - L_q}{L_d + L_q} = \frac{L_d/L_q - 1}{L_d/L_q + 1} = \frac{L_{dm} - L_{qm}}{L_{dm} + L_{mq} + 2 \cdot L_{leak}} \qquad (14)$$

It is evident that the calculation of the maximum internal power factor (as well as all ipf and pf) requires also the knowledge of the leakage inductance, while the torque depends only on the magnetizing inductances. Analyzing the vector diagram it is clear that neglecting the stator resistance and the equivalent iron losses resistance leads to a lower value of ipf respect to pf. In the following the dependence of the parameters and variables present in the equations of the torque (11) and ipf (12) from the two design variables mr and sr will be analysed in details. The d-axis magnetizing inductance expressed in (2) is a function of the split ratio sr (because $R_r = sr \cdot R_s$) and does not depend on the magnetic ratio mr. The per unit circulating component of the q-axis inductance, i.e. L_{qm_c}/L_{dm}, expressed by the equation (3) does not depend neither from sr or mr and depends only on the rotor barrier angles α_i and barrier number n. The per unit flow-through component of the q-axis

inductance L_{qm_f}/L_{dm} expressed by the equation (7) depends on the split ratio sr (directly through R_r and indirectly by s_i which depends also on α_i and the selected flux barrier profile) and on the total amount of air along the q-axis h_{air} which is a function of both design variables mr and sr as it will be shown later. The d-axis current component can be deduced from the correlation between the maximum airgap flux density B_g and the stator m.m.f [48] leading to:

$$i_d = \frac{2}{\sqrt{3}} \frac{g \cdot k_c}{\mu_0} \frac{p}{N \cdot k_w} \cdot B_g \tag{15}$$

where N is the number of turns is series per phase. This current component is function of both design variables since the airgap flux density depends on the magnetic ratio ($B_g = mr \cdot B_{fe}$) while the Carter coefficient k_c, which account for the slot presence, is a complex function [79] of the slot pitch ($\tau_s = (sr \cdot R_s \cdot \pi)/(3 \cdot p \cdot q)$ where q is the number of slots per pole per phase), slot opening ($so = so_{pu} \cdot \tau_s$) and airgap length ($g$) and so depends on the split ratio. The q-axis current component can be calculated simply from the knowledge of the maximum current I_{max} i.e. $i_q = \sqrt{I_{max}^2 - i_d^2}$. The latter depends on the cooling capability k_{cool} and other geometrical parameters. In fact, starting from the total losses P_{tot}, sum of the joule and iron losses and the definition of k_{cool}, equation (16) is written:

$$\begin{aligned} P_{tot} &= 2 * \pi \cdot R_s \cdot L \cdot k_{cool} = P_j + P_{fe} \\ &= 3 \cdot R_{ph} \cdot I_{max}^2 + P_{fe} \end{aligned} \tag{16}$$

Since the stator phase resistance can be expressed as function of the total slots area A_{slots}, the slot fill factor k_{ff} and the end winding length L_{ew}, such as:

$$R_{ph} = N \cdot \frac{2 \cdot \rho_{cu} \cdot (L + L_{ew})}{A_{1cond}} = 3 \cdot N^2 \cdot \frac{2 \cdot \rho_{cu} \cdot (L + L_{ew})}{k_{ff} \cdot A_{slots}} \tag{17}$$

then the following relation of the maximum current can be deduced:

$$I_{max} = \frac{1}{3 \cdot N} \sqrt{\frac{k_{fill} \cdot A_{slots}}{2 \cdot \rho (L + L_{ew})} \left(2 \cdot \pi \cdot R_s \cdot L \cdot k_{cool} - P_{fe}\right)} \tag{18}$$

In the last equation, 3 parameters depends on the two design variables sr and mr, i.e. the total slot area A_{slots}, the end winding length L_{ew} and the iron losses P_{fe}. The first one can be determined by simple geometrical consideration:

$$\begin{aligned} A_{slots} = \frac{6 \cdot q \cdot p \cdot l_t}{2} \\ \cdot \left[\frac{2 \cdot \pi \cdot \left(sr \cdot R_s + g + l_{tip_{pu}} \cdot w_t\right)}{6 \cdot q \cdot p} \right. \\ \left. + \frac{2 \cdot \pi \cdot (sr \cdot R_s + g + l_t)}{6 \cdot q \cdot p} - 2 \cdot w_t \right] \end{aligned} \tag{19}$$

where all the geometrical parameters are depicted in the Figure 16. The end winding length can be assumed to be proportional to the split ratio and tooth length l_t through the equation:

$$L_{ew} = k_{ew} \cdot \frac{2 \cdot \pi \cdot (sr \cdot R_s + g + l_t/2)}{2 \cdot p} \tag{20}$$

where k_{ew} is an empirical coefficient. Neglecting the rotor iron losses, the stator iron losses (21) are the product of the loss per kg (21) calculated according to the Steinmetz equations (whose coefficients depends on the selected magnetic material) and the mass of the stator iron (23), i.e.:

$$P_{fe} = k_{fe} \cdot p_{fe} \cdot M_{fe} \tag{21}$$

$$p_{fe} = k_h \cdot f^{\alpha} \cdot B_{fe}^{\beta} + k_e \cdot \left(f \cdot B_{fe}\right)^2 \tag{22}$$

$$M_{fe} = \rho_{fe} \cdot L \cdot \left\{\pi \cdot [R_s^2 - (sr \cdot R_s + g)^2] - A_{slots} - l_{tip_{pu}} \cdot w_t \cdot so \cdot 6 \cdot p \cdot q\right\} \tag{23}$$

where k_{fe} is a correction coefficient (usually between 1.5-2). Considering all above equations and analyzing the machine sketch reported in Figure 16, the following geometrical parameters needs still to be identified: tooth length l_t, tooth width w_t, total amount of rotor air along the q-axis h_{air} and stator yoke length l_y. The yoke and tooth thicknesses can be calculated equating the pole flux to the flux flowing in the stator yoke or in the tooth imposing the flux density B_{fe}:

$$l_y = \frac{\pi}{2}\frac{R_s}{p} \cdot mr \cdot sr \tag{24}$$

$$w_t = \frac{2 \cdot \pi \cdot R_s}{6 \cdot q \cdot p} \cdot mr \cdot sr \tag{25}$$

The tooth length follows from simple geometrical consideration:

$$\begin{gathered} R_s = sr \cdot R_s + g + l_t + l_y \Rightarrow \\ l_t = R_s \cdot \left[1 - sr \cdot \left(1 + \frac{\pi}{2}\frac{mr}{p}\right)\right] - g \end{gathered} \tag{26}$$

Also the sum of the rotor flux barrier thickness h_{air} follows from geometrical consideration supposing that the total rotor iron thickness l_{ferot} along the q-axis is equal to the stator yoke length l_y:

$$\begin{gathered} sr \cdot R_s = R_{shaft} + h_{air} + l_{ferot} \Rightarrow \\ h_{air} = sr \cdot R_s - R_{shaft} - \frac{\pi}{2}\frac{R_s}{p} \cdot mr \cdot sr \end{gathered} \tag{27}$$

Although different and more complicated approaches are possible when calculating the total rotor iron thickness l_{ferot} and its distribution [68] (here not considered), the adopted approach is the simplest but still effective considering that all the written equations are used to carry out a preliminary design and a FE refinement stage is always needed. As previously mentioned, the leakage inductance L_{leak} is needed to determine the total inductances and so all the power factors. It is mainly the sum of the slot, tooth tip and end winding leakage inductances, which can be expressed in terms of geometrical

parameters (and so mr and sr) by means of classic formulations reported in [79]. The maximum internal power factor requires only the knowledge of the total inductances, while the ipf (at maximum torque per ampere condition) can be determined from the current phase angle with equation (13). The power factor in the same operating point can be derived from the vector diagram, the stator phase resistance (17) and the equivalent iron loss resistance:

$$R_{fe} = \frac{E^2}{P_{fe}} = \frac{(\omega \cdot \lambda)^2}{P_{fe}} = \frac{(2 \cdot \pi \cdot f \cdot)^2 \left[(L_d i_d)^2 + \left(L_q i_q\right)^2\right]}{P_{fe}} \qquad (28)$$

All the equations reported up to now along with a set of initial assumptions and design choices allow to carry out a parametric study of the torque and the power factors (ipf, ipf_{max} and pf) as function of the split and magnetic ratio. The preliminary design choices include: outer envelope (R_s, L), cooling capability (k_{cool}), slot fill factor (k_{ff}), per unit slot opening (so_{pu}, normalized respect to the slot pitch τ_s), per unit tooth tip ($l_{tip_{pu}}$, normalized respect to the tooth width w_t), number and angular position at the airgap of the flux barriers (n, α_i chosen in order to minimize the torque ripple), number of poles ($2 \cdot p$) , airgap length (g) and iron flux density (B_{fe}, chosen according to the B-H curve of the selected magnetic material).

2.4 Low speed SyR machine design

Design a low speed SyR machine essentially means that it is acceptable to neglect the influence of the speed-dependent phenomena during the electromagnetic design, i.e. the reduced torque and power factor due to the structural rotor iron ribs, and the maximum current decrement due to the presence of the iron losses (as expressed in the equation 18) for a given total losses (or k_{cool} coefficient for a certain outer surface). Considering the set of assumptions and constraints, reported in Table 2, and using the design equations described in the last subsection, the dependences of the torque and power factor from the split and magnetic ratio are analysed by constant locus plot in the design plane $sr - mr$. Their behaviours are also studied by investigating the dependence of the most important parameters affecting these two performance indexes. The rotor geometry considered for this study is depicted in Figure 11; this choice obviously affects the function $s_i = f(R_r, \alpha_i)$, which describes the barrier surface (as function of the rotor radius and barrier angle), needed to calculate the q-axis inductance (equation (7)). Let's underline that the outer envelope considered in this design exercise (along with some other assumptions such as k_{cool}) coincides with the one of the machine that has been designed, analysed, prototyped and tested through all this thesis.

Table 2: Initial geometrical constraints and preliminary design assumptions

Description	***Symbol***	***Value***	***Unit***
Outer stator radius	R_s	30	mm
Stack length	L	30	mm
Cooling capability	k_{cool}	50000	W/m^2
Fill factor	k_{ff}	0.45	-
Stator slots per pole pair	n_s	12	-
Pole pair	p	2	-
Airgap length	g	0.3	mm
Per unit slot opening	so_{pu}	0.3	-
Per unit tooth tip	$l_{tip_{pu}}$	0.25	-
Equivalent rotor slots per pole pair	n_r	16	-
Number of flux barriers	n	3	-
Barrier angle at the airgap	α_i	16.87, 28.12, 39.38	$deg.$
Iron flux density	B_{fe}	1.4	T
Specific iron losses at 50 Hz, 1T (lamination material 10JNHF600)	-	1.17	W/kg

2.4.1 Inductances and torque

Figure 18 shows the constant L_{md} and L_{mq} loci in the design plane $sr - mr$, while Figure 19 depicts the contour of the inductances difference ($L_d - L_q = L_{md} - L_{mq}$) and of the electromagnetic torque T.

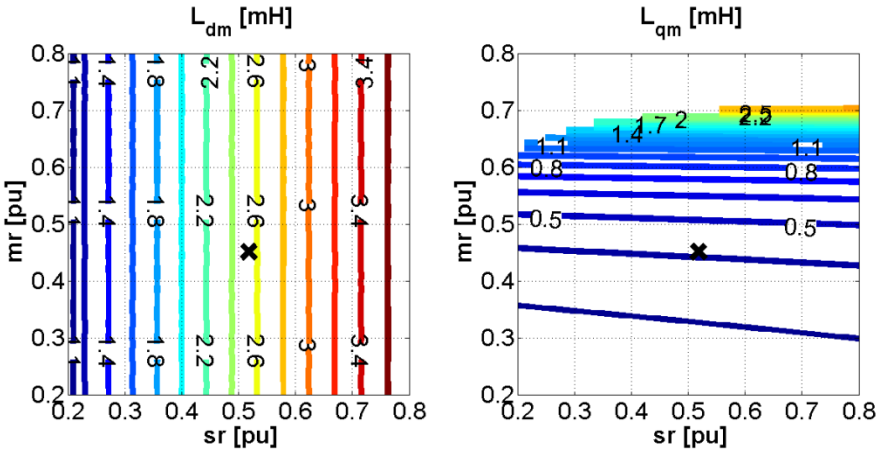


Figure 18: Constant locus of the magnetizing inductances in the design plane $sr - mr$

The magnetizing d-axis inductance depends only on the split ratio, as explained in the previous sub-section and in the equation (2), while the q-axis magnetizing inductance mainly depends on the magnetic ratio. In fact, being the circulating component a small portion of L_{mq}, and considering the product of equation (7) and (2) which gives $L_{mq\_f} \cong L_{mq}$, the strong dependence from the split ratio is eliminated; increasing the magnetic ratio decreases the total amount rotor air along the q-axis h_{air} as shown in the equation (27), therefore L_{mq} increases as depicted in Figure 18.

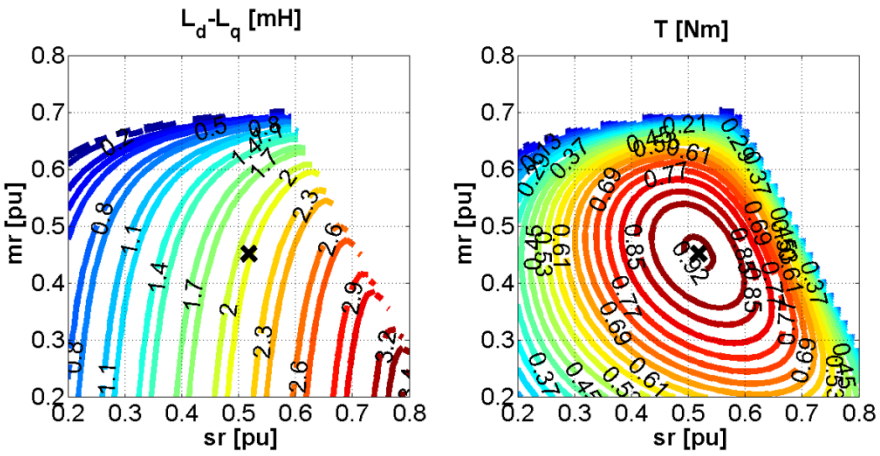


Figure 19: Constant locus of the magnetic anisotropy and torque in the design plane $sr - mr$

While high magnetic anisotropy (i.e. $L_d - L_q$) can be achieved with high split ratio and low magnetic ratio, the maximum torque can be obtained with lower split ratio and higher magnetic ratio as reported in Figure 19. It can be then concluded that the maximization of the magnetic anisotropy does not lead to the maximum torque [47, 48]. The iron saturation will obviously change the behaviour of the magnetic anisotropy in the design plane $sr - mr$ as well as the one of the torque. In fact, at low value of the magnetic ratio, the magnetizing d-axis inductance would decrease (as a consequence of rotor saturation due to the reduced iron along the q-axis), therefore the maximum value of $L_d - L_q$ would be located to higher magnetic ratio. The shape of the constant torque locus can be easily understood from Figure 20 which shows the contour of the current components.

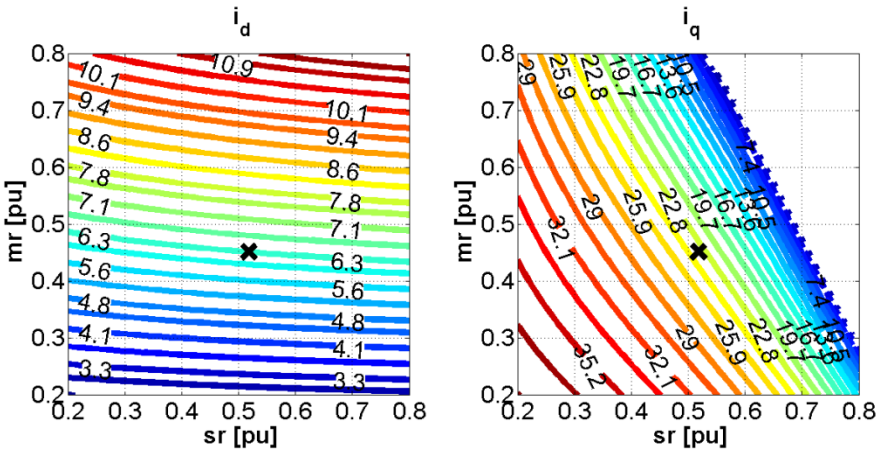


Figure 20: Constant locus of the d- and q-axis current component in the design plane $sr - mr$

The d-axis current component mainly depends on the magnetic ratio while the q-axis component is function of both design variables. This dependence is easily explained if the contour of the slot area is analysed (Figure 21). In fact, A_{slots} is the parameter which most affects the maximum current and so i_q as shown in the equations (18). The available area for the slots increases as both split and magnetic ratios decrease because the tooth length increases and tooth thickness decreases as respectively proved with the equations (25) and (26).

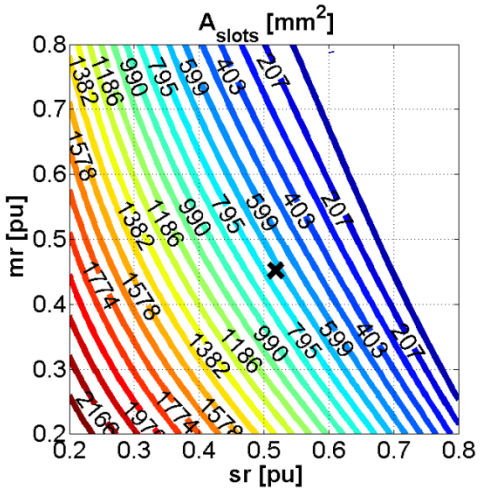


Figure 21: Constant locus of the slots area in the design plane $sr - mr$

Considering all the above, it can be stated that the torque behaviour in the design plane $sr - mr$ and so its maximum value is the results of the compromise among the competitive needs of maximizing the magnetic anisotropy ($L_d - L_q$), the slots area A_{slots} and the magnetizing current (i_d).

2.4.2 Internal power factor and saliency ratio

Figure 22 reports the internal power factors, i.e. its maximum value and its value at the maximum torque per ampere operating condition.

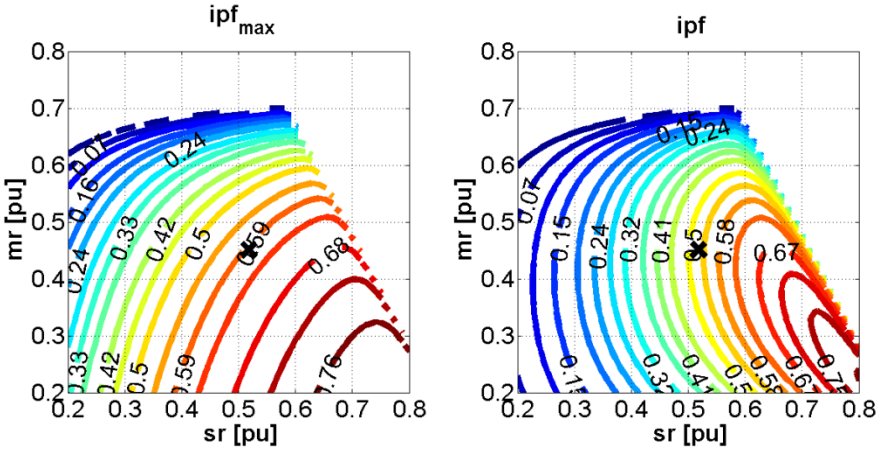


Figure 22: Constant locus of the maximum internal power factor and the one relative to the maximum torque per ampere operating condition in the design plane $sr - mr$

The maximum internal power factor ipf_{max} follows the same behaviour of the magnetic anisotropy $L_d - L_q$ (Figure 19); in fact it shows high values at high split ratios and low magnetic ratios but the shape of the iso-curves are slightly different compared to $L_d - L_q$. This difference is due to the fact that the ipf_{max} depends on the saliency ratio L_d/L_q (as shown with the equation (14))

which is different from $L_d - L_q$ for two reasons: its definition is different and both L_d and L_q include the leakage inductance L_{leak}. Figure 23 show 3 contour plots: the leakage inductance and the saliency ratios obtained with and without considering the L_{leak}. The behavior of the iso-saliency ratio (L_d/L_q) curves are the same as the maximum internal power factor ones as just mentioned. The saliency ratio is obviously lower than the one calculated without the leakage inductance (i.e. L_{dm}/L_{qm}) and it has a slightly different shape due to the influence of L_{leak}. The latter obviously impacts more the q-axis inductance than the d-axis one and it is mainly inversely proportional to the split ratio because low rotor radius implies big tooth lengths and so higher slot leakage inductances [79]. The internal power factor at the maximum torque per ampere condition is a complex function; it depends on both saliency ratio and current phase angle γ as proven in the equation (13). In general it follows the same trends, i.e. higher values are obtained with high sr and low mr as depicted in Figure 22

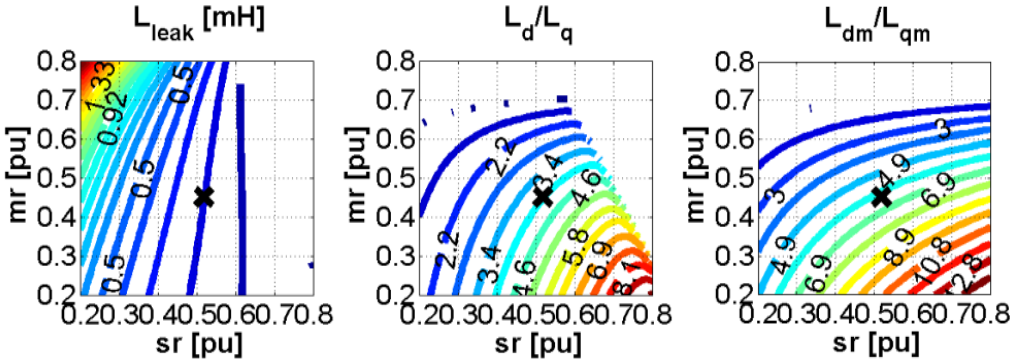


Figure 23: Constant locus of leakage inductance, saliency ratio and saliency ratio without considering the leakage in the design plane $sr - mr$

2.4.3 Torque and internal power factor compromise

Comparing the constant torque and internal power factor loci, both shown in Figure 24, it is clear that when choosing the magnetic and the split ratios, a trade-off between these two performance indexes needs to be accomplished being their maximum values located in different positions of the design plane.

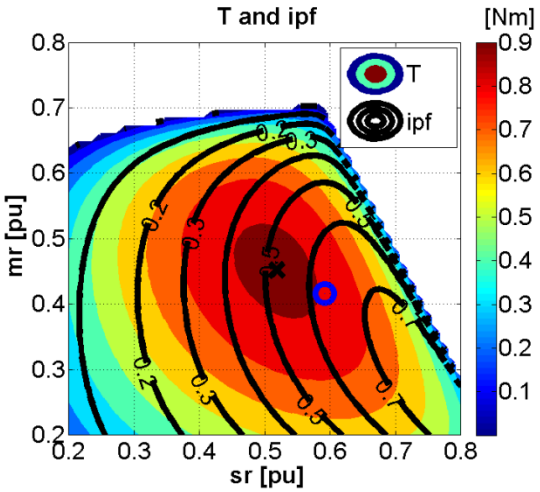


Figure 24: Constant locus of torque and internal power factor in the design plane $sr - mr$; the position of the maximum torque is represented with a black cross while a possible design solution with a higher power factor is represented with a blue circle

In general the choice of the design variables sr and mr depends on the requirements of the specific application. Although several design choices are possible [49], if the torque is the most important performance index and the power factor has still to be considered (even if with less importance), then a torque de-rating can be accepted with the aim of increasing the power factor. As an example (shown in Figure 24), accepting a torque decrement of 5% respect to the maximum torque (black cross) would improve the power factor of almost 20% (blue circle). The new split ratio is obviously higher than the

one related with the maximum torque design while the magnetic ratio is smaller. The considerations carried out analysing the constant loci of the most influencing parameters and performance indexes starting from a specific set of initial assumptions (reported in Table 2) can be considered general even though the shape of the contours change when the preliminary design choices change (e.g. the number of poles).

2.5 High speed SyR machine design

In the following the limitations incurring as the speed increases during the design of a SyR machine will be analysed in details expressing the reduction of the performance as function of the geometry and the speed. For a given total losses or for a given cooling capability coefficient k_{cool} and outer surface $L \cdot R_s$, the maximum current decreases as the speed increases due to the not-negligible rise of the iron losses P_{fe} as already shown by the equation (18). This current decrement causes a reduction of the torque and an increment of the power factor as it will be proved later.

2.5.1 Inclusion of the structural limitation in the design equations

The other source of performance reduction proportional to the speed is the increment of the q-axis inductance due to the not-negligible rise of the

thickness of the structural iron bridges. A bigger L_q, caused by the shunted flux flowing in the iron ribs (an example is shown in Figure 10), obviously implies a loss of torque and power factor. The influence of the structural iron bridge on the q-axis inductance can be analysed adding an additional branch in parallel to the each barrier permeance in the q-axis equivalent magnetic circuit shown in Figure 14. Such additional branch contains the series of the rib permeance and its m.m.f. drop calculated imposing an a-priori saturation flux density [83]. By doing so the rotor magnetic potentials r_i can be exactly determined and then the flow-through component of L_{qm} follows using the equation (4). This approach allows considering iron ribs of different thickness and with different saturation level for each flux barrier. However if all the iron bridges assume the same radial dimension and all of them are considered saturated at the same flux density B_{sat} then the q-axis flux linkage shunted by the ribs can be calculated as [48]:

$$\lambda_{rib} = \frac{4}{\sqrt{3}} \cdot N \cdot k_w \cdot TB \cdot L \cdot B_{sat} \tag{29}$$

where TB is the thickness of the tangential iron bridge shown in Figure 25a. This relationship supposes that each flux barrier is sustained by means of only two tangential iron bridges per flux barrier. Such iron ribs can be divided into several pieces along the flux barrier in order to increase the mechanical load that each of them can withstand. In particular they are more effective when placed along the q-axis as shown also in Figure 25b; the optimal position and distribution of the iron ribs along the flux barrier will be analysed in details in

the next two chapters. Wherever the iron ribs are located along the flux barrier, it can be assumed that they electromagnetically act in the same way. The increment of the q-axis inductance and the decrement of the torque can be then easily calculated by the following two relations:

$$\Delta Lq_{rib} = \frac{\lambda_{rib}}{i_q} \tag{30}$$

$$\Delta T_{rib} = \frac{3}{2} \cdot p \cdot \lambda_{rib} \cdot i_d \tag{31}$$

The thickness of the iron bridge for each flux barrier is a complex function of rotor geometry and speed. A simplified mechanical analytical formulation, which considers only the steady state centrifugal force at the maximum speed and neglects any other force (of rotor-dynamic and electromagnetic origin), has been presented in [97]. This formulation allows estimating the total thickness of iron bridge for each flux barrier ($TotB_i = 2 \cdot TB_i + CB_i$) from the static stress analysis of the flux guides. Considering a rotor shown in Figure 25b, the force acting on the i-th iron bridge can be expressed as:

$$F_i = m_i \cdot R_i \cdot {\omega_m}^2 \tag{32}$$

where m_i is the sum of the flux guide masses mfg_k which has to be sustained by the i-th iron bridge:

$$m_i = \sum_{k=i}^{n} mfg_k \tag{33}$$

while R_i is the centre of gravity of the mass m_i which can be calculated as:

$$R_i = \frac{Sx_i}{A_i} \tag{34}$$

being Sx_i the first moment of area A_i (which is the surface of the mass m_i). The total thickness of the iron bridge for each flux barrier can be then estimated as:

$$TotB_i = k_s \cdot \frac{F_i}{\sigma_s \cdot L} \tag{35}$$

where k_s is a safety factor (usually between 2 and 4) and σ_s is the yield strength of the rotor material.

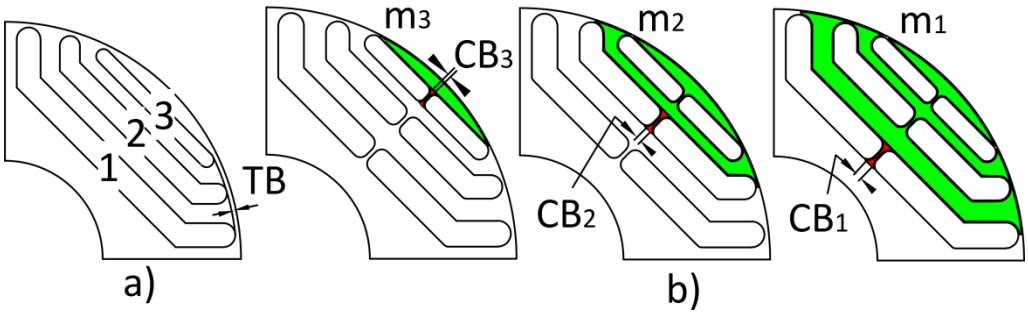


Figure 25: a) Simple SyR rotor geometry with equal tangential bridge, b) Rotor sketches highlighting the mass that each set of iron bridge per flux barrier has to hold up

The calculated total iron bridge obviously increases going from the outermost to the innermost flux barrier because the mass that each rib has to sustain increases in the same direction. As a consequence in order to determine the variation of the q-axis inductance the equivalent magnetic circuit approach has to be adopted because equation (29) assumes that all flux barriers have the same iron bridge thickness. However supposing that the worsening of the

electromagnetic performance is proportional to the average of the total bridge thicknesses per flux barrier ATB calculated as:

$$ATB = \frac{1}{n}\sum_{i=1}^{n} TotB_i \tag{36}$$

then equations (29), (30) and (31) can be still used (adopting $ATB/2$ instead of TB) to estimate the torque and the q-axis inductance losses due to the ribs presence even though the latter are not the same for all barriers. This approximation allows a fast estimation of the performance reduction due to the speed rise once the rotor geometry is defined without solving the q-axis equivalent magnetic circuit. In fact, for each point of the design plane $sr - mr$ corresponds a value of the total amount of air along the q-axis and consequently a different rotor geometry (for a given set of α_i and subdivision of h_{air} into several h_i) from which is possible to calculate the total bridge thickness of each flux barrier by equation (35) and their average ATB. Once the latter is known for each couple of the split and magnetic ratio is possible to determine the torque and q-axis inductance losses with the equations (29), (30) and (31).

2.5.2 Influence of the high speed limiting factors

Table 3 reports the additional assumptions needed to carry out a parametric study of torque and power factor in the design plane $sr - mr$ for different speed going from 1 to 160 krpm.

Table 3: Additional assumptions needed for the parametric analysis for different speeds

Description	***Symbol***	***Value***	***Unit***
Mechanical safety factor	k_s	3	-
Yield strength rotor material (35HXT780T)	σ_s	822	MPa
Correction coefficient iron losses	k_{fe}	2	-

Figure 26 depicts the maximum torque and the internal power factor in the same operating condition as function of the speed. The torque reduction from the lowest to highest speed is about 60% while the ipf drop is approximately 30%. As the reduction of the torque is less than the increment of the speed, the mechanical power, shown in Figure 27, greatly increases until a certain speed after which it remains at the same level. It is clear that beyond a threshold speed the power improvement is negligible (in this case after 120krpm, the power gain is less than 10%), therefore it is not convenient to further increase the operating speed.

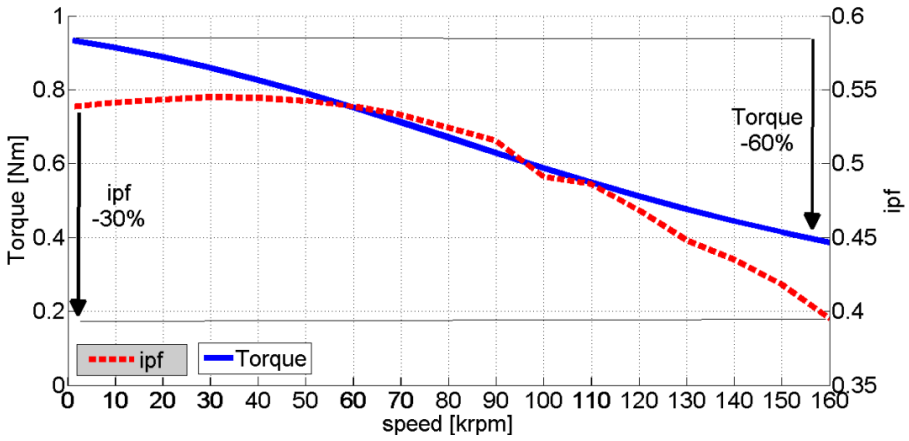


Figure 26: Maximum torque and internal power factor as function of the speed

The trend of the maximum power respect to the speed obviously depends on the set of initial design assumptions. In particular the most relevant preliminary choice which affects this trend is the selection of the lamination material. In fact, specific iron losses p_{fe} and yield strength σ_s are intrinsic characteristics of the material and both of them heavily influence the decrement of the performance as the speed increases. It is obvious that the best electromagnetic performance can be achieved adopting a material with low specific iron losses and high yield strength.

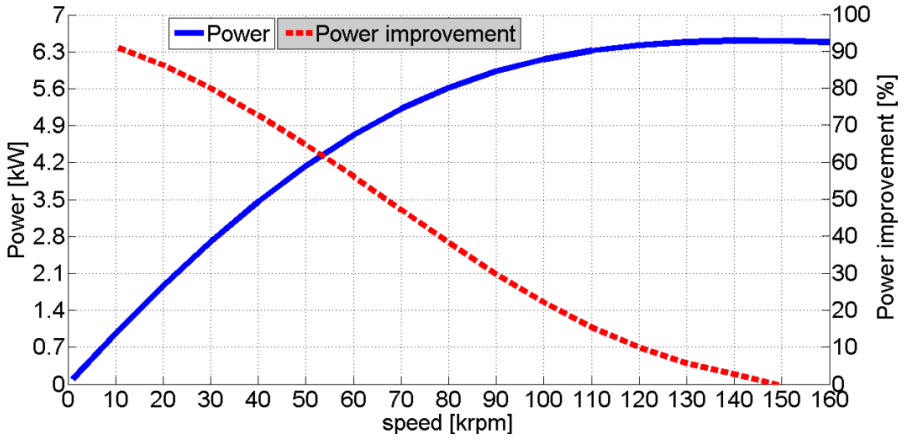


Figure 27: Maximum power and its derivative (in %) as function of the speed

Unfortunately mechanical strength is in general inversely proportional to the specific iron losses [7] therefore the choice of the lamination material is the result of a trade-off study in which materials with different properties are analyzed and compared. Figure 28 shows the maximum power capabilities as function of speed associated with different lamination materials listed in Table 4. Although the considered materials have different BH curves, the parametric analysis have been carried out with the same iron flux density B_{fe}.

Table 4: Materials properties used for the comparative analysis shown in Figure 28

Legend name plot figure 28	***Material***	***Specific iron losses at 1T and 50Hz***	***Yield strength [MPa]***	***Saturation flux density at 5000 A/m***
M1	35HXT780T	6.15	822	1.68
M2	10JNHF600	1.17	546	1.6
M3	M270-35A	1.2	380	1.65
M4	Stator: 10JNHF600 Rotor: 35HXT780T	1.17	822	1.6

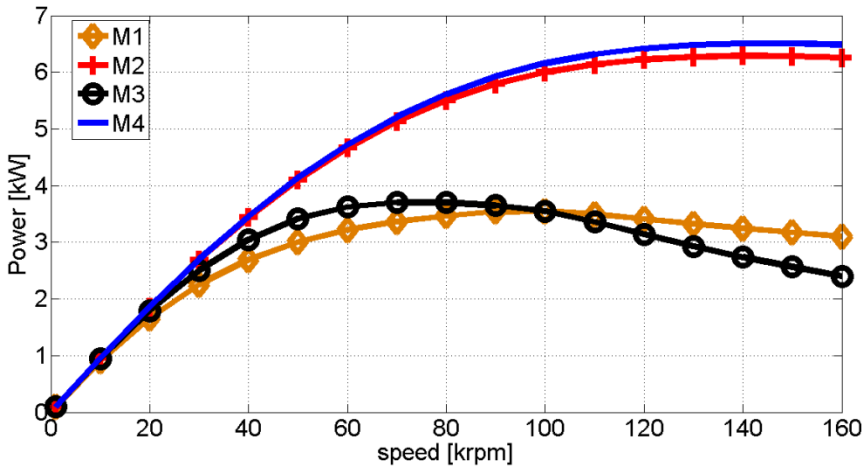


Figure 28: Maximum power capabilities curve of 4 different lamination materials

The power capability obtained with the material having the highest yield strength and also the highest specific iron losses (M1) is comparable with the one obtained with a standard material (M3, i.e. much lower p_{fe} and σ_s). Both materials present two speed ranges, during the first one the power increases while in the second the power slowly decreases. Above a certain speed (90krpm in this case) the material with better mechanical feature (M1) performs better while under this speed the material with standard properties (M3) has to be preferred. Therefore the choice between these two materials depends on which is the maximum speed of the considered application. The material (M2) featuring low iron losses with a quite high yield strength clearly performs much better (+100%) than the ones (M1 and M3) that respectively excels only mechanically or electromagnetically. The best power capability is obviously obtained if two different materials for stator and rotor are adopted as shown with the curve (M4). In particular the stator material has the lowest specific iron losses while the rotor material features the highest yield strength. Despite the low torque improvement achievable adopting two different materials for stator and rotor (compared with the solution M2), this choice has been preferred during the following of the thesis. Figure 29 reports the trends of the split and magnetic ratio corresponding to the maximum torque design (shown in Figure 26) as the speed increases. The split ratio sr remains almost constant with a light reduction above a certain speed while the magnetic ratio mr monotonically decreases as the speed increases.

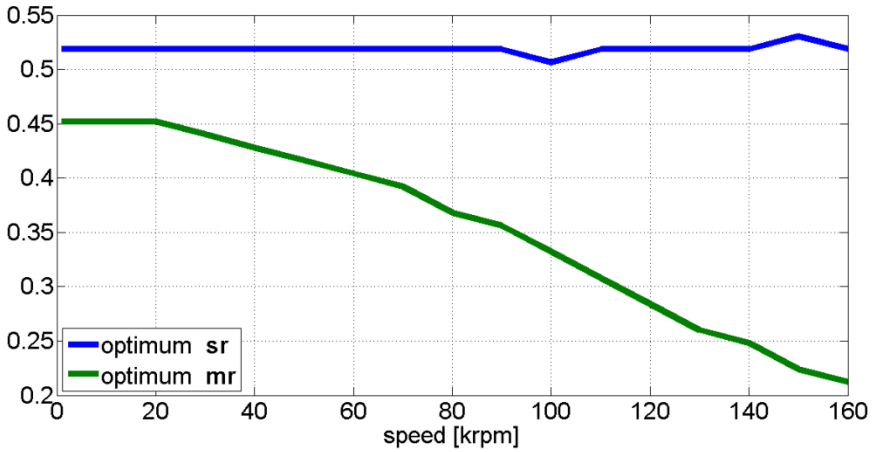


Figure 29: Trend of the optimum magnetic and split ratio (i.e. corresponding to the maximum torque design) as the speed increases

2.5.3 Subdivision of the high speed limiting factor influence

The rates of such reductions depend on the considered material (but it is always a reduction) since their trends is the result of the compromise between the iron losses and iron ribs effects. On one hand, the rise of the iron losses causes an increment of the optimum split ratio and a decrement of the magnetic ratio, as reported in Figure 30. On the other hand, the presence of the iron ribs determines a reduction of the optimum split ratio as well as of the magnetic ratio. Consequently the combination of these two effects makes the split ratio almost constant (or reducing if a different material is selected) and the magnetic ratio surely decreasing as the speed increases.

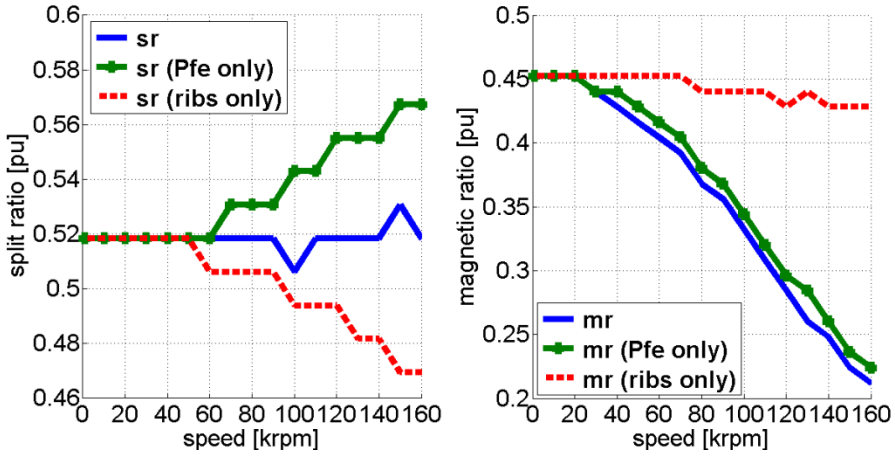


Figure 30: Trends of the optimum magnetic and split ratio as function of the speed considering only the iron losses or the iron ribs effect or both of them

In Figure 31 the effect of the iron losses and iron ribs as the speed increases on the maximum torque and internal power factor are separately analysed. As previously mentioned both factors negatively affect the torque; however the internal power factor is improved by the effect of the iron losses while is worsen by the iron bridge presence which prevails on the first one.

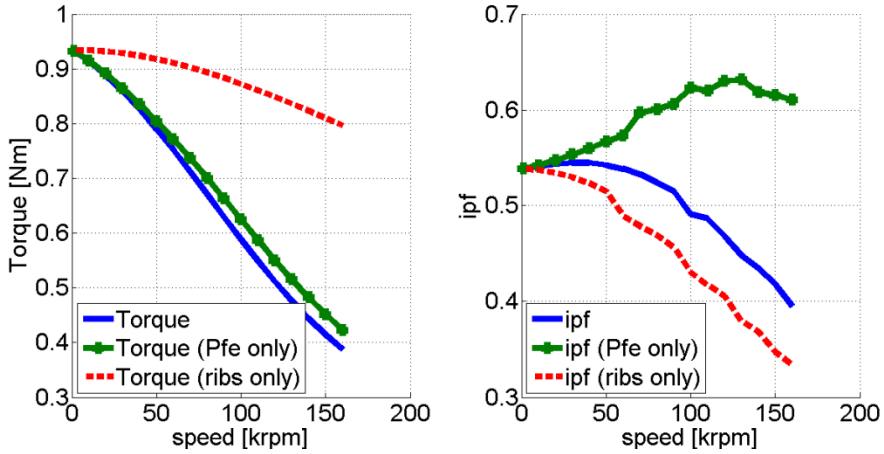


Figure 31: Maximum torque and internal power factor as function of the speed obtained considering only the iron losses or the iron ribs effect or both of them

In order to investigate in details the several trends contained in the Figure 30 and 31, let's analyse the torque and internal power factor loci in the design

plane $sr - mr$ for three different speeds (1, 60 and 120 krpm) obtained considering only the influence of the iron losses or the iron ribs presence.

2.5.3.1 Iron losses influence

Figure 32 shows three constant torque loci calculated considering only the effect of the iron losses. It is clear that the maximum torque design moves towards the bottom-right side of the design plane and so the optimum (torque wise) split and magnetic ratios respectively increases and decreases as shown also in Figure 30. This trend is caused by the reduction of the q-axis current, reported in Figure 33. In fact the maximum torque location is the results of the compromise among the competitive needs of maximizing the magnetic anisotropy ($L_d - L_q$), the magnetizing current (i_d) and the q-axis current i_q. The first two, i.e. $L_d - L_q$ and i_d, do not depends on the speed (if the iron ribs effect is neglected) while the third one depends on the slots area (unaffected by the speed) and the iron losses. As the speed increases, the iron losses rises and the influence of the q-axis current component weaken and the maximum torque design moves towards the maximum magnetic anisotropy, i.e. higher split ratio and low magnetic ratio as also shown in Figure 19.

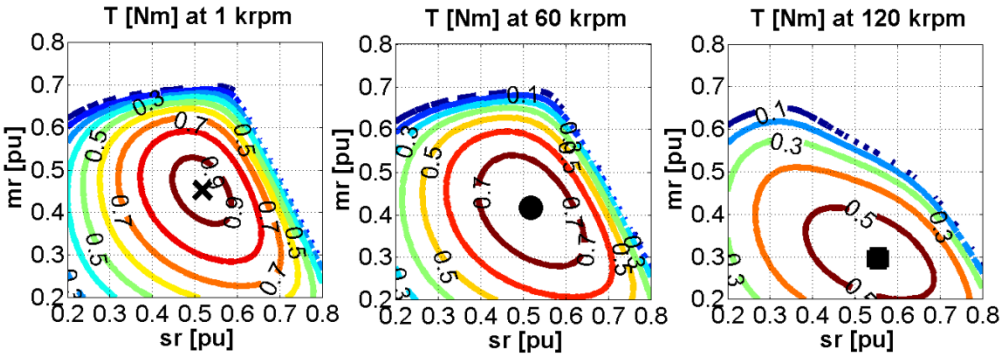


Figure 32: Constant toque loci in the design plane $sr - mr$ obtained considering only the iron losses effect for three different speeds

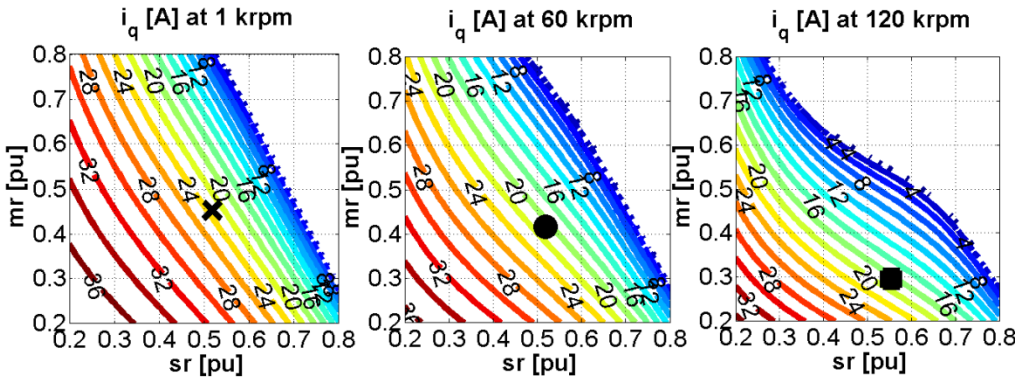


Figure 33: Constant q-axis current loci in the design plane $sr - mr$ obtained considering only the iron losses effect for three different speeds

The iron losses contours for 60 and 120 krpm along with the stator surface contour are reported in Figure 34. It is clear that the maximum torque design moves towards the zone of the design plane with lower stator surface and so lower iron losses which in turn means higher q-axis current and bigger slots area. The increment of the internal power factor corresponding to the maximum torque design can be easily explained looking the Figure 35. The ipf loci are slightly affected by the iron losses, and since the direction of the

maximum torque designs corresponds to the direction towards higher magnetic anisotropies, also the internal power factor increases.

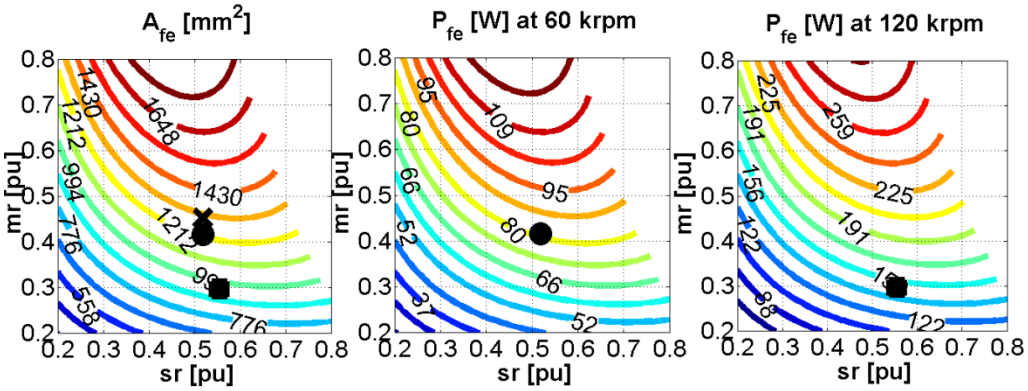


Figure 34: Contour plot of the stator surface and iron losses for two different speed

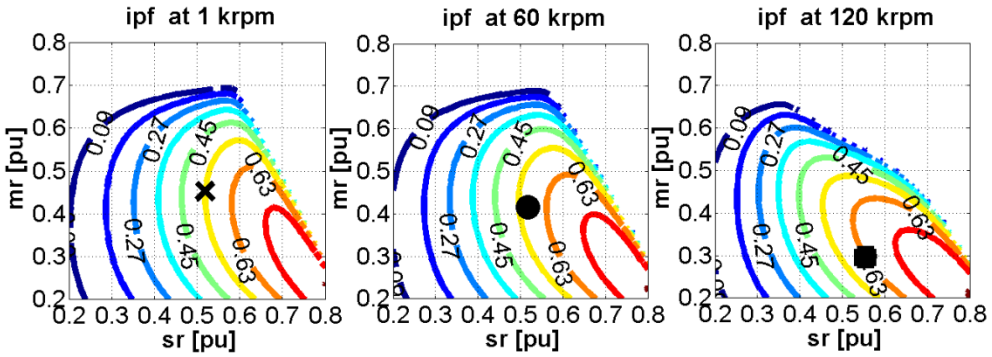


Figure 35 Constant ipf loci in the design plane $sr - mr$ obtained considering only the iron losses effect for three different speeds

2.5.3.2 Structural rib influence

Figure 36 reports the constant torque loci obtained considering only the iron rib effect for three different speeds (1, 60 and 120 krpm). The maximum torque designs slightly moves towards the bottom left corner of the design plane $sr - mr$, i.e. lower split and magnetic ratios, because in the same direction decreases the average total bridge per flux barrier ATB and so the loss of torque. In fact, the ATB, whose contour is shown in Figure 37 (for 120 krpm), decreases as the split (sr) and magnetic (mr) ratios decreases because: 1) lower sr implies lower rotor radius so lower centrifugal forces and consequently reduced $ATBs$, 2) lower mr implies lower amount of rotor iron along the q-axis (i.e. higher h_{air}) and so smaller mass of the flux guides and consequently smaller centrifugal forces and ATB.

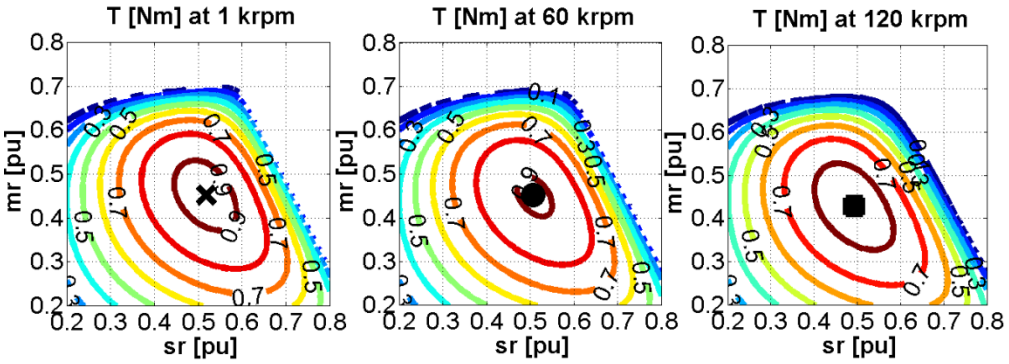


Figure 36: Constant toque loci in the design plane $sr - mr$ obtained considering only the iron ribs effect for three different speeds

Figure 37 also reports the contours of the percentile variations of torque and q-axis inductance due to the iron ribs presence. It is worth to notice that the

influence of the iron bridge thickness is much heavier on the q-axis inductance than on the torque; in fact for a given couple of design variables sr, mr, $\Delta Lq_{rib}\%$ is higher than $\Delta T_{rib}\%$. The higher variation of the q-axis inductance can be justified analysing the equation (30). In fact ΔLq_{rib} is proportional to ATB through λ_{rib} and is inversely proportional to i_q; while the average total bridge increases going from the bottom-left to the upper-right corner of the design plane, the q-axis current increases in the opposite direction, therefore i_q exacerbates the effect of ATB in the genesis of ΔLq_{rib}. The higher reduction of the q-axis inductance cause a significant drop of the internal power factor as reported in Figure 38. Although the shape of the constant ipf locus does not change much with the speed, its value is greatly reduced as also shown in Figure 31.

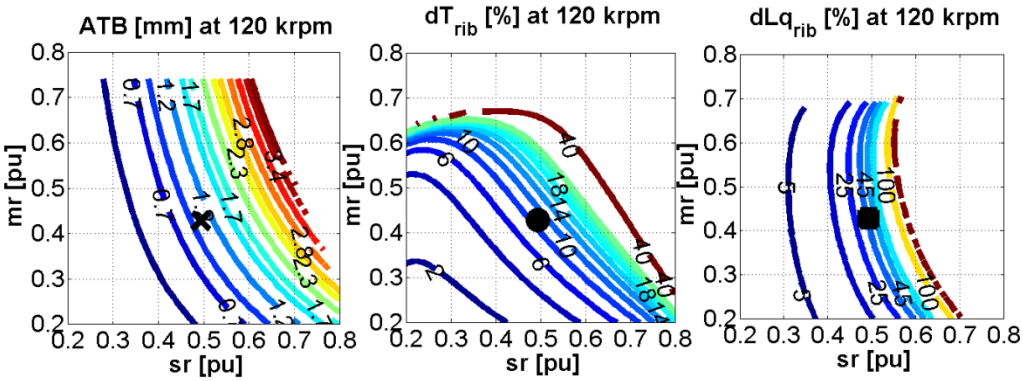


Figure 37: Constant locus in the design plane $sr - mr$ obtained considering only the iron ribs effect of the average total bridge per flux barrier, torque loss and q-axis inductance increment

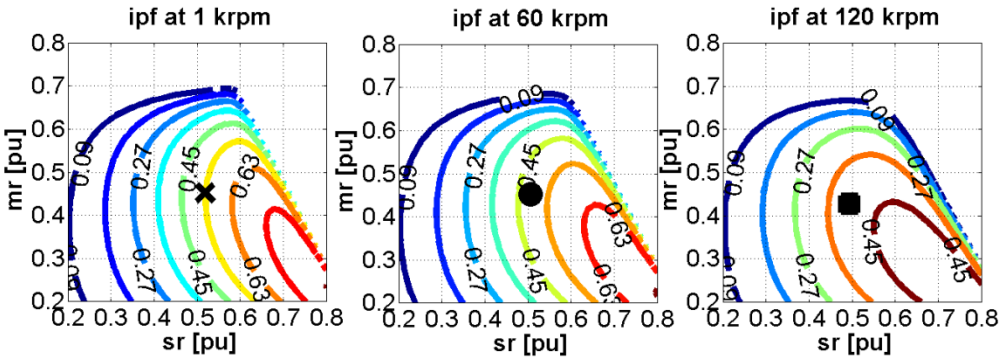


Figure 38: Constant ipf loci in the design plane $sr - mr$ obtained considering only the iron ribs effect for three different speeds

2.5.4 Final consideration

Considering the maximum torque solution in the plane $sr - mr$, the behaviours of torque, internal power factor and optimum split and magnetic ratio described up to now can be considered general although their rate of change depends on the selected lamination material. Therefore several general conclusions regarding the speed dependent worsening of the maximum torque design solution can be drawn.

- The iron ribs growth affects more the q-axis inductance and so the power factor rather than the torque.
- The iron losses rise heavily influences the maximum current and so the torque capability for a certain level of total losses and lightly improves the power factor.

- The rate of decrement of the optimum split ratio is smaller than the one of the magnetic ratio. In fact, the increment of both iron losses and iron bridge dimensions tends to decreases the optimal magnetic ratio. While the optimum split ratio tends to increases with the speed and decreases with the iron losses.

In conclusion the last remark that it is worth to underline regards a possible different design choice in the plane $sr - mr$ with respect to the maximum torque solution. As mentioned in the previous paragraph, several combinations of the design variables sr and mr can be selected and the choice depends on the specific application requirements. If a certain torque de-rating (respect to the maximum torque) is accepted in order to improve the power factor then a different design is achieved for each speed. Figure 39 illustrates the internal power factors as function of the speed obtained considering the maximum torque design and a solution allowing 5% decrement of the torque. It can be deduced that for a given torque de-rating the ipf improvement drastically reduces as the speed increases.

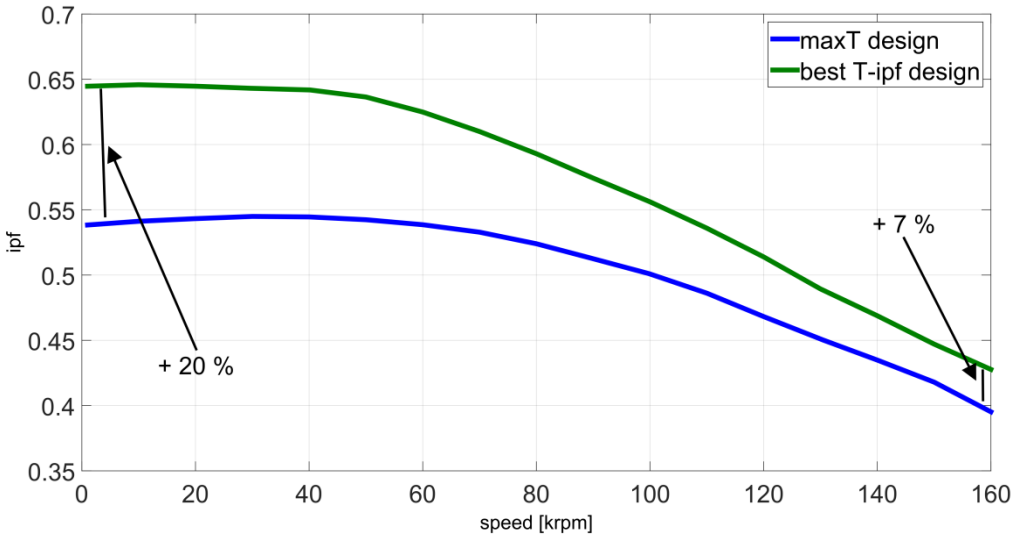


Figure 39: Trends of the internal power factor related to the maximum torque design and to the maximum ipf achievable for a 5% torque de-rating respect to the maximum torque

2.6 Conclusion

In this chapter the set of design equation of a low speed SyR machine first introduced by Vagati has been deeply analyzed in order to highlight the most important trade-offs involved during the design of a low speed SyR machine. The effect of the not-negligible iron losses and thickness of the structural ribs have been included in the design equations in order to apply such formulation to the design of a high speed SyR machine. A parametric analysis is then carried out with the aim of evaluating the influence of each speed-dependent limiting factor on torque and power factor as the speed increases. This set of design equation has been used to carry out the preliminary analytical design of the target machine (5kW at 80krpm) including some considerations regarding the lamination material selection. This preliminary design constitutes the base

for the further design refinements which will be presented in the following chapters. As mentioned at the beginning of this chapter, from the electromagnetic point of view, a FE design refinement stage is needed to evaluate the influence of the saturation and cross-saturation on the machine performance and to further minimize the torque ripple. Regarding the mechanical performance, the simplified analytical model used in the previous paragraph allows only the estimation of the total iron bridge for each flux barrier, therefore a structural FE analysis is needed to verify such design and further optimize the positions of the iron ribs. The following two chapters deeply address the rotor design issues related with the torque maximization, torque ripple reduction and structural optimization.

Chapter 3
Multi-physics rotor design of HS-SyR machine

This chapter aims at facing three issues which characterize the rotor design of a high speed SyR machine.

1. From the electromagnetic point of view, a refinement stage of the torque profile has to be performed taking into account the magnetic non-linearity and the influence of the geometrical parameters disregarded during the preliminary design stage.
2. Considering the structural performance, the analytical model presented in the last chapter only is able to calculate the total iron bridge per flux barrier and not its associated distribution. Therefore, if such an analytical model is used, a structural verification and re-distribution of the total iron rib per barrier is needed, otherwise a complete design has to be performed.
3. The influence of the electromagnetic design choices on the mechanical performance and vice versa has to be analysed in details in order to identify the most effective design strategy.

3.1 Design challenges

The difficulty of solving the first two problems is strictly related with the high number of geometrical parameters that need to be considered while the third problem is more related to the need of performing or not a truly multi-physics rotor design, i.e. a design involving the evaluation of both structural and electromagnetic performance at each design step.

3.1.1 Parametric study or optimization?

The first two objectives of this chapter are common issues in the field of electrical and mechanical engineering and they can be faced carrying out a parametric study or applying an optimization algorithm both based on FEA. A parametric study can be generically defined as a discrete mapping of the function $p(x)$ where x is the vector of geometrical parameters (also called factors) while p is the vector of the considered performance indexes. The complexity of the function $p(x)$ defines the number of points needed to obtain a faithful discrete description of $p(x)$. For example, a linear function would require two points for each factor in order to be completely defined while a non-linear function in general requires more points for each factor and the number of points depends also on the part of the research space under investigation (the research space is obviously the domain of the function $p(x)$). When the number of design factors is not too high as well as the complexity of

the function $p(x)$, a parametric study is the easiest and most effective method to characterize the function $p(x)$ and therefore to obtain a clear understanding of the effect of each design factor (and their joint influences) on the performance indexes. However, when the number of geometrical parameters becomes relevant, an exhaustive parametric study would involve an excessive number of points and so a massive number of FE simulations. For example, considering only the refinement of the torque profile, a parametric study on 7 factors (3 barrier angles, 3 barrier heights and the current phase angle) evaluated with 5 steps each would necessitate $5^7 = 78125$ FE simulations (which corresponding to 325 hours with only 15 seconds per FE simulation). In this case, a complete parametric study would become unreasonably long, therefore the most influencing factors on the performance indexes need to be recognized. By doing so, the design/analysis can focus only on the most influencing subset of variables. Such identification can be done implementing the theory of the design of experiment [98] or making assumptions based on physical/engineering considerations which are peculiar of the problem under investigation. The first one essentially consists in carrying out a statistic analysis of the results of a parametric study evaluated on a certain subset of combinations of design variables; this method is de facto preferred when there are no information about the problem under examination or when the complexity of the function $p(x)$ is really high. It is however much more common to identify the most important design factors by means of physical considerations and so hypothesis; the full validation of such assumptions is almost impossible, therefore this method in most cases provides results having

a limited generality. Another peculiarity of the considered problems, common in all engineer fields, is the competitive nature of some performance indexes (such as torque, torque ripple, structural integrity and so on) that is, one can't be improved without worsening another one. Therefore the designer is usually asked to find the optimum trade-offs among these goals. The structural and electromagnetic FE design refinements can be obviously seen as optimization problems consequently they can be faced by means of optimization algorithm (OA). There are different ways to solve a multi-objective optimization problem. One of the strategies is to define an aggregated cost function expressed as a weighted sum of the various goals and then implement a single objective OA. This approach is simple but the formulation of the cost function requires a-priori knowledge of the trade-off among the optimization goals and it heavily affects the result of the optimization. An alternative approach could be the use of a multi-objective OA that it is able to search for a set of possible solutions according to the well-known Pareto dominance criterion. A solution is called non-dominated, Pareto optimal, or Pareto efficient if it cannot be eliminated from the set of solutions by replacing it with another solution which improves an objective without worsening the others. Finding such non-dominated solutions, called Pareto front, is the goal of a multi-objective optimization algorithm. Once the best-known Pareto front is identified, the designer can select the preferred solution clearly knowing how much the improvement of one objective worsen another one. Optimization algorithms can be divided into two categories: deterministic methods that find the optima algorithmically and stochastic methods, which explore the solution space

quasi-randomly. All the deterministic methods require the calculation of the gradient of the cost function and this is computationally expensive and sometimes impossible. Stochastic OAs do not need any knowledge of the gradient of the cost function and do not require a good initial point to start the procedure. Several stochastic OAs have been proposed in literature and applied to practical engineering problems [99]; each of them is suitable for a particular class of problem. In fact it has been proved that there is no algorithm which is the best for any class of optimization problem [100] and can avoid the risk of premature convergence to suboptimal solutions (with the so-called no free-lunch theorem). Among the wide variety of available stochastic OAs, the ones that mimic the natural evolutionary principles are becoming more and more popular. This class of algorithm makes use of a set of potential solutions (population) that are iteratively modified according to probabilistic rules (inspired by the concepts of natural operators) with the aim of minimizing a set of objective functions for each solution (also called individual or candidate). Genetic algorithms (GA) are one of the most popular classes of stochastic population-based OAs which is inspired by the natural evolution mechanisms, i.e. selection, crossover and mutation. A more detailed description of the concepts related with stochastic OAs is behind the scope of this work (interested reader may refer to [101]) and in the following only the essential information are reported. Almost all stochastic population-based algorithms are mainly based on two operators, one that tends to focus on the most promising region of the research space (i.e. the one that show the best fitness) and one that try to explore new part of the research space. The right balance between

these two mechanisms (respectively crossover and mutation for GA) determines the effectiveness of an OA [102, 103]. One of the main advantages of the stochastic population-based OAs lies in their parallelism, i.e. the ability to travel in a search space with more individuals, so they are less likely to get stuck in local optimum like some other methods. On the other hand, the main disadvantage of such class of OAs is in their computational time, in fact they can be slower than some other methods. The convergence of stochastic population-based OAs is tightly related with the population size and maximum number of generations along with other parameters characteristic of the selected OA. These settings must be tuned accordingly to the optimization problem; however the exact knowledge of the objective functions would require a preliminary study longer than the optimization itself. Therefore these settings are usually the results of some preliminary optimizations tests carried out starting from parameters identified with generic rule of thumb (i.e. population size roughly 10 times the dimension of the research space and maximum number of generations higher than the population size). In practical optimization problem, which require a long computational time in order to calculate the objective functions of a single candidate solution, the number of functional evaluations (product of population size and generations) is essentially limited by the overall time dedicated to the optimization. In addition, the stochastic nature of such algorithms leads to the need of performing several optimization runs in order to verify the repeatability of the results and so increase its reliability; such necessity further increases the global computational burden. In conclusion both parametric study and optimization

algorithm are methodology commonly used in engineer fields and both suffer in general from long computational time when coupled with FEA. When the number of design factor is limited, a parametric study is the most effective approach since it allows obtaining a clear understanding of the effect of each design factor on the performance indexes with a limited computational cost. However, when the number of design variables is high, the adoption of an OA could drastically cut the computational burden of the overall design at the cost of a reduced understanding of the effect of each design factor on the performance indexes. For example, considering the electromagnetic design refinement aimed at identifying 7 factors, it can be easily carry out adopting a multi-objective stochastic OA performing only 21000 FE simulations (considering 3 optimization runs with population size 70 and 100 as number of generations). Unfortunately when the complexity of the problem is really high also adopting an OA could lead to unreasonable computational time. Therefore also in this case could become necessary to individuate the most influencing design variables on a certain performance index or subdivide the research space into several subspaces where each of them influence most a certain figure of merit.

3.1.2 Physically coupled or de-coupled design?

Traditionally, SyR machine design is performed by doing the electromagnetic design (by analytical or FE methods or both of them), followed by a FE

structural verification at the maximum operating speed. This approach does not perform a proper rotor structural design and does not consider all the interaction between mechanical and electromagnetic aspects. In fact both electromagnetic and mechanical performances of a SyR machine strongly depend on the rotor geometry. In particular, from the electromagnetic point of view the iron bridge dimensions have to be minimized while from the mechanical perspective they need to be thick enough so to guarantee the structural integrity at the maximum speed. The sum of the thicknesses of all the iron bridges of each flux barrier depends on the mass of the flux guides; therefore it depends on the angular position at the airgap and on the radial thickness of the barriers. Since such parameters also influence electromagnetic performance, it is mandatory to design the rotor structure taking into account mechanic and electromagnetic design aspects, which are strongly coupled. In the previous chapter it has been described the trade-off between the needs of minimizing the q-axis inductance and maximizing the d-axis inductance when choosing the amount of air along the q-axis h_{air} (with reference to Figure 11 and 16). In fact, considering a low speed SyR machine, incrementing the total flux barrier thickness, the q-axis inductance decreases; however above a certain value the flux guides become too narrow and a premature saturation is reached with a consequent unwanted reduction of the d-axis inductance. Considering also the presence of the iron ribs, i.e. considering a high speed SyR machine, if the total flux barrier thickness is increased, obviously the thickness of the flux guide decreases as well as their volume and mass. Consequently as h_{air} increases, the total iron bridge of each flux barrier decreases being the latter

proportional to the mass of the respective set of flux guides to be sustained. It can be then deduced that the optimum value of the total amount of air along the q-axis is not constant as the speed increases. Figure 29, reported in the last chapter, shows the trend of the optimum magnetic ratio as function of the speed; this trend along with equation (27) describing the total barrier length h_{air} allows achieving the same conclusion, i.e. for a given split ratio, the optimal total barrier thickness increases as the speed increases. Such increment is limited by the iron saturation which has not been considered in the analytical formulation. It is clear that in order to properly address the interaction between the electromagnetic and structural design aspects, a FE-based multi-physics design should be adopted considering all the rotor parameters simultaneously and both electromagnetic and structural performances during each design step. Both physics (structural and electromagnetic) need to be evaluated by means of FEA in order to take into account the magnetic and structural non-linearities and geometrical complexity impossible to consider with analytical means. In addition, even if only the rotor design is considered, a high number of geometrical parameters is involved during the design. It can be then concluded that whatever design method is adopted (parametric study or optimization algorithm), the main practical problem that the designer has to face deals with the impressive computational burden required to carry out the design. The advantage and disadvantages of performing a truly multi-physics rotor design or performing a two-steps design (i.e. an electromagnetic design followed by a structural one) have to be analyzed in details both in terms of computational burden and performance of the final optimal machines.

3.1.3 Proposed comparative study

In the following paragraphs, both electromagnetic and structural FE design refinement stages will be carry out by means of a multi-objective stochastic OA. This choice is the direct consequence of the high number of geometrical parameters to be identified and the unreasonable long computational time required to carry out a meaningful parametric study. Considering what it has been said in the last two paragraphs, it is clear that the practical trade-off between performance of the final design and the overall time dedicated to the FE-based optimization refinement stage needs to be clearly identified. In order to evaluate such compromise, two design approaches are presented. The two design strategies differ from each other according to how the electromagnetic and structural designs are coupled. The first and simpler design procedure consists of an electromagnetic design followed by a proper mechanical design. The set of parameters describing the rotor geometry is divided into two sub-sets, with the first being mainly concerned with the electromagnetic performance and the other addressing the structural aspects. Such subdivision of the research space is based only on simple hypothesis although more sophisticated and correct approaches can be applied as mentioned in the first paragraph. Each subset of parameters is separately optimized with the aid of an OA. In the second design procedure a truly multi-physics approach is adopted by addressing all the rotor parameters simultaneously in a single optimization run that evaluates both electromagnetic and structural performances of each

considered machine. The latter approach is computationally more intensive but considers the interaction of magnetic and structural issues and allows a deeper optimization of machine performance. Before showing the details and the results of these two design approaches, the procedure presented in [43, 104] will be reported (which will be called standard design procedure) with the aim of highlight its advantages and limitations. This approach consists in performing the electromagnetic FE optimization of the rotor structure followed by a structural FE parametric study. For each rotor considered during the electromagnetic optimization, the total bridge per flux barrier will be estimated using the simple structural analytical model presented in the last chapter. Once the electromagnetic optimization is performed, a structural FE parametric study is needed in order to carry out the re-distribution of the estimated total bridge per flux barrier. In the next paragraph the reasons behind the design assumptions used for both preliminary analytical design and electromagnetic and structural FE refinements are described in details.

3.2 Preliminary design choices

The set of design equations presented in the previous chapter has been used to carry out the preliminary analytical design of the target machine (5kW at 80krpm). With the same model, it has been confirmed that adopting a stator lamination material with a low specific iron losses and a rotor material with a high yield strength, it is possible to achieve better performances. It has to be

underlined that such model provides approximate results not only because of the disregarded magnetic non-linearity and inaccuracy of the structural model but also because both rotor iron losses and addition AC copper losses are completely neglected. The last two sources of losses will be analyzed in Chapter 6 along with the thermal performance. The latter is needed to design a cooling system which has to satisfy the assumption imposed during the preliminary analytical design through the coefficient k_{cool} with the constraint of the maximum winding temperature. The stator axial length and external diameter assumed at the beginning of the preliminary analytical design are fixed by the given space envelope along with the airgap length. The latter has been chosen equal to the minimum required by the adopted bearing system. Bigger airgap thickness (g) would be safer from the mechanical point of view; however it is well-known that the electromagnetic performance of SyR machines rapidly decrease when a bigger value is considered (in fact the magnetizing d-axis inductance is inversely proportional to g while the q-axis one is directly proportional to g). The selection of the number of pole pairs is related not only to electromagnetic consideration but also to power electronic and control system related issues. In fact also to limit as much as possible such issues, a two pole pair rotor configuration has been selected. The choice of the flux barrier numbers heavily affects not only the electromagnetic performance but also the real rotor manufacturability. This is really important for SyR machines having a particularly small rotor diameter such as the machine considered in this study. In fact, adopting a high number of flux barriers improves the magnetic anisotropy but increases the construction complexity

because the thickness of the smallest flux barrier falls in the order of few millimetres. After some simple manufacturing considerations, and bearing in mind that the number of flux barrier is correlated with the number of stator slots if a good trade-off between torque ripple and iron losses has to be achieved, a stator with 24 slots and a rotor having three flux barriers per pole is considered. The most important specifications and assumptions used to carry out the preliminary analytical design are reported in Table 5.

Table 5: Requirements of the target machine and its main parameters

Description	***Value***	***Unit***
Rated power	5	kW
Maximum speed	80000	rpm
Stator diameter	60	mm
Stack length	30	mm
Stator slots	24	-
Airgap length	0.3	mm
Pole pair	2	-
Number of flux barriers	3	-

Concerning the flux barrier geometry, several options have been proposed in literature and a complete comparison is shown in [91, 92]. In the last works it has been proved that flux barriers with complex geometries improve the torque production at the expense of an increased computational burden if a FE-based design assisted by stochastic OA is adopted. The latter statement is obvious,

complex geometries require more parameters to be identified and so more time is needed by the OA to converge. However the same work shows that the performance obtainable with simpler flux barrier geometry is not drastically different when compared to the more complicated structure. All these considerations have led to the adoption of a simple barrier shape described by a reduced number of parameters and shown in Figure 40a. Each flux barrier is made by straight segments and is univocally identified by the barrier thickness h_i, and the angular displacement at the airgap $\Delta\alpha_i$. With the aim of making the rotor lamination suitable for high rotational speed, additional radial iron bridges are introduced in the geometry as shown in Figure 40b. In particular, for all the flux barriers, central and lateral strengthening iron bridges (CB_i, LB_i) are inserted. The latter are placed to the most external side of the respective straight part of the flux barrier although a different choice in terms of position and angle could be possible as shown in Figure 40c.

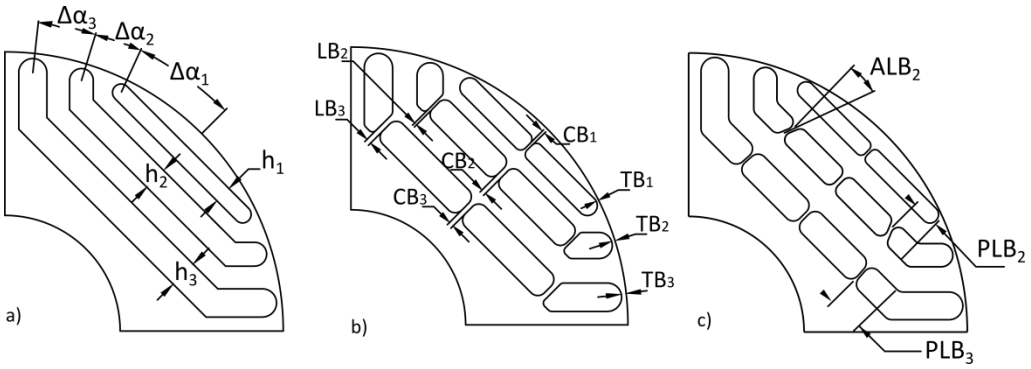


Figure 40: a) Parametrization of the main part of the flux barrier, b) parametrization of the iron bridge thicknesses, c) parametrization of the position and bending angle of the lateral iron ribs

3.3 Standard design procedure

3.3.1 Performance evaluation

The aim of the electromagnetic optimization is to improve the quality of the torque profile, i.e. maximize the average torque and minimize the torque ripple. The evaluation of the torque performance requires the execution of several FE simulations for different amplitudes and phases of the current vector. In fact the current phase angle corresponding to the maximum torque per ampere condition (MTPA) depends on the rotor geometry and current amplitude therefore is not a-priori known. Although it is possible to carry out an electromagnetic optimization evaluating the torque performance at different current levels, the natural choice would be to perform the optimization only at the rated current condition in order to decrease the computational effort. However it has been shown in [77] that if the torque profile of a SyR machine is optimized for the rated current, then the machine will provide a higher torque ripple when the current amplitude is increased. On the other hand, optimizing the torque performance at an extremely high current level would lead to oversize the amount of rotor iron along the q-axis; reducing the sum of the flux barrier thicknesses implies a decrement of the average torque in the rated condition. Consequently a good compromise between the torque performance at rated and overload condition can be reached carrying out the optimization at a current amplitude intermediate between these two loads. The inclusion of the

current phase angle within the vector parameters to be optimize by the algorithm [105] allows avoiding the detection of the MTPA angle via several FE simulations. Despite the increment of the number of parameters to be optimized, this ploy, obviously valid only when the average torque is one the objective to be maximized, allows a great reduction of the computational time. The accuracy of the evaluation of the torque profile mostly depends on two FE settings: the number of samples over one sixth of the electrical period adopted to assess the torque behaviour and the dimensions of the FE mesh. Using a high steps number and a fine FE mesh improve the quality of the results but increases the computational time therefore such settings have to be the results of a preliminary trade-off study. In particular, the steps number depends on the maximum harmonic order to be detected in the torque profile (order defined by the Nyquist–Shannon sampling theorem); regarding the FE mesh, particular attention needs to be paid when choosing the airgap mesh size since it definitely plays the most important role in defining the results accuracy. A real interesting attempt aimed at reducing the number of steps needed to sample the torque profile has been proposed in [106]; the author proposes always to sample the torque profile with equally spaced steps but the position of the first step can randomly vary. By doing so, it has been empirically proven that a good estimation of the torque ripple can be achieved if a sufficiently large number of functional evaluations is performed in order to compensate the noise introduced in the objective function by the random positioning of the samples. Consequently the effectiveness of such stratagem relies on the high number of performed functional evaluations which in turns depends on the research space

dimension and so on the specific optimization problem. During the optimization process, the average torque and the torque ripple are evaluated adopting all the conclusions deduced by the literature described so far (except the random positioning of the simulation steps), while angular positions and heights of the flux barrier (as shown in Figure 41) along with the current phase angle constitute the vector parameters to be identified (for a total of 7 variables).

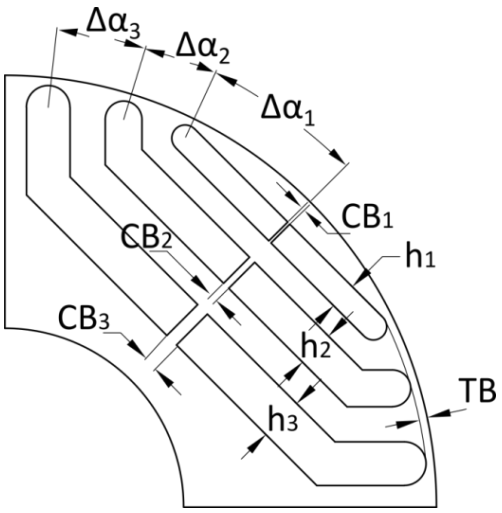


Figure 41: Rotor parametrization of the standard design procedure

For each rotor candidate, the radial iron ribs' thicknesses CB_i are automatically calculated using the simple mechanical analytical model presented in the previous chapter. In fact, once the positions at the airgap and heights of the flux barriers are defined, the centrifugal stress acting on each flux guide can be easily calculated and so applying (35) an estimation of the radial ribs can be obtained. Once the central iron bridge is known for each barrier, if it is bigger than a certain value, it is included in the corresponding barriers, otherwise it is neglected and the rotor integrity is ascribed to tangential bridges (TB). The

minimum iron thickness depends on the technology used to manufacture the machine, i.e. how stator and rotor laminations are cut. In fact, different manufacturing methods provide different geometrical tolerances and so the minimum iron thicknesses are possible (here considered 50 μm). By doing so, only rotor structures which can be easily manufactured are considered during the optimization. The choice of the tangential iron bridge thickness TB (considered equal for all flux barriers) and the safety factor k_s used in the equation (35) to calculate the radial ribs require some considerations regarding the structural analytical formulation. In fact, it has to be underlined that the latter is only able to estimate the thicknesses of the radial iron bridges; however it is not capable to assess the notch effect which characterizes all the iron ribs. Such effect depends on the barrier geometry, in particular it is heavily influenced by the end barrier shape (the ones close to the airgap) and the fillet radius of the barrier corners. Although it is possible to estimate such concentration stress factors for simple notch geometries [107], the complexity of the SyR rotor structure does not allow implementing any of these formulations. Consequently the values of TB and k_s have to be identified by some preliminary FE structural analysis or by utilising the designer experience. In the following a quite conservative assumption is made, i.e. tangential bridges equal to 0.3 mm are imposed, while the considered maximum stress is the 80% of the yield strength of the rotor material (i.e. 822 MPa). Some other considerations regarding the assumption of the tangential bridge thickness and the safety factor will be proposed at the end of the structural FE parametric study reported in the paragraph 3.3.3.

3.3.2 Optimization results

A multi-objective genetic algorithm (NSGA-II implemented in Matlab) has been adopted to estimate the Pareto front. Three different optimization runs have been performed in order to validate the repeatability of the results. Each run has been executed with a population of 60 elements iterated for 100 generations. The evaluation of the electromagnetic performance requires 14 seconds per rotor candidate leading to a total computational time per run of 23 hours (on an Intel Core i7 3.6 GHz, 16 GB RAM). Figure 42 reports the Pareto front average torque – torque ripple obtained evaluating the performance at 150% the rated load. All the machines of the front have similar average torque except for two solutions, while the torque ripple (measured in percentage standard deviation) varies from 1 to 5 %. Except for the solutions having the lowest average torque, the optimal parameters of the machine of the front are practically very similar as shown in Figure 43.

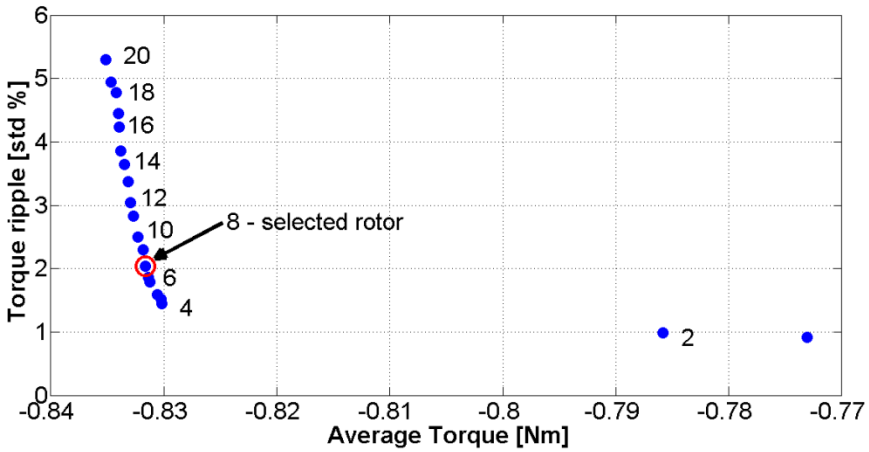


Figure 42: Pareto front torque-ripple of the standard design procedure

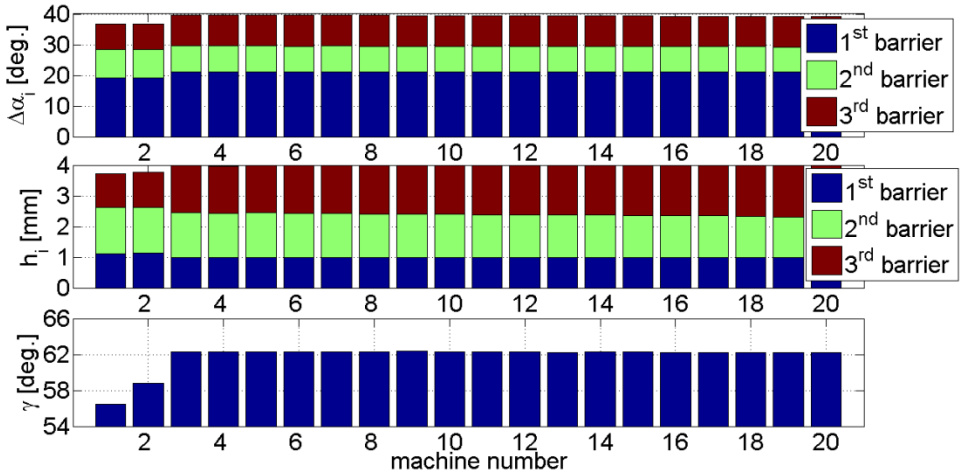


Figure 43:Airgap angular positions $\Delta\alpha_i$ and heights h_i of the flux barriers and current phase angle $\gamma$of the optimal machines

The large variation of the torque ripple on the Pareto front is probably due to the slightly different heights of the second and third flux barrier as can be deduced from Table 6 that reports the standard deviation of each optimized parameter for all the machine of the front. The optimal airgap angular positions of the flux barriers respect quite well the constant rotor slot pitch rule explained in the previous chapter, except for the most external flux barrier. Figure 44 reports the average torque and torque ripple as function of the current phase angle γ for 2 current levels of the selected machine (number 8 in the Pareto front). Analysing this graph and the value of the optimal current phase angle reported in Figure 43, it can be observed that the OA is clearly able to calculate the performance corresponding to the MTPA condition even if the angle γ is included in the vector of the parameters to be optimized. In addition the torque ripple evaluated at a lower current (50% of the rated current) with respect to the value used for the optimization (150%) is not drastically different at the respective MTPA conditions.

Table 6: Standard deviation (in percentage) of each parameter (calculated excluding the solutions 1 and 2)

$\Delta\alpha_1$	$\Delta\alpha_2$	$\Delta\alpha_3$	h_1	h_2	h_3	γ
0.02	1.32	0.67	0.01	3.48	4.22	0.07

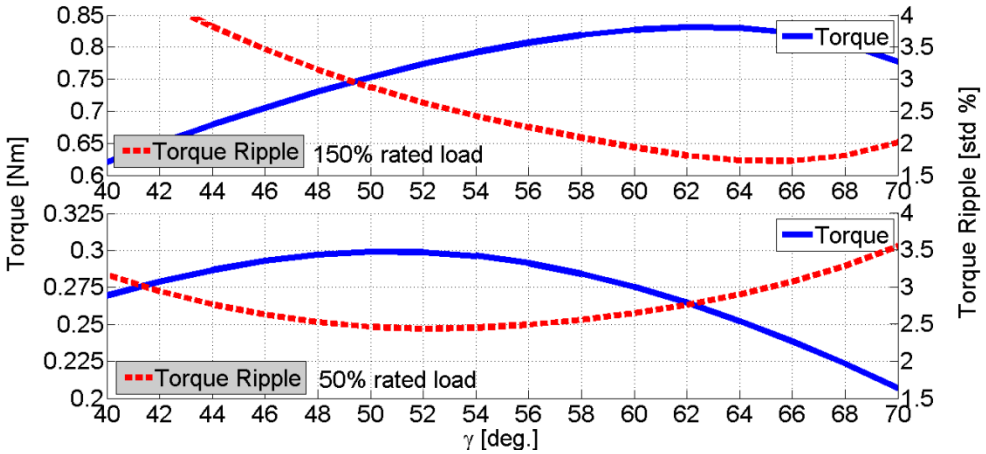


Figure 44: Average torque and torque ripple as function of current phase angle for two current level (150% and 50% of the rated value)

3.3.3 Structural FE parametric study

Figure 45 reports the von Mises stress distribution of the solution (number 8) selected from the Pareto front of Figure 42. Even though the maximum stress in the radial ribs area is well below the imposed limit, the tangential iron bridge of the innermost barrier experiences a maximum stress over the 80% of the yield point, i.e. 657 MPa. Subsequently, a structural refinement stage becomes mandatory.

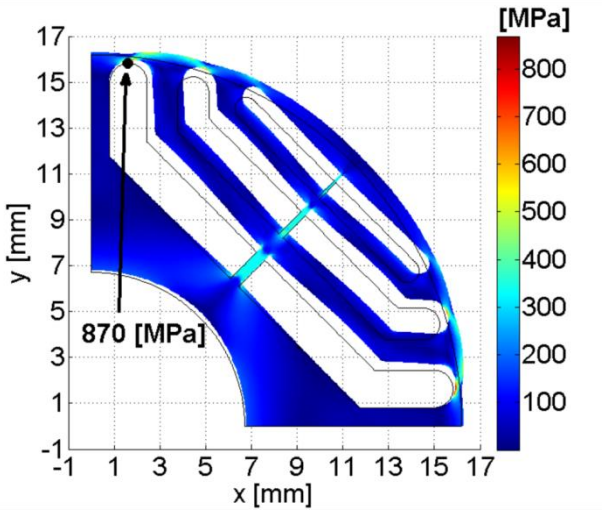


Figure 45: von Mises stress distribution of the rotor number 8 of the Pareto front shown in Figure 42 evaluated at 80 krpm and shown with a deformation scale of 1:30

As mentioned in section 3.1.1, a complete parametric study would be impossible to evaluate due to enormous number of degrees of freedom that the rotor geometry can offer. For example, even if the total iron bridge thickness per flux barrier are considered constant and equal to the estimated values by the analytical formulation, the iron bridge dimensions of each flux barrier (except the most external that requires only one variable) can be described by 4 parameters, i.e. 2 independent variables among TB, CB, LB, and the position and bending angle of the lateral bridge, PLB and ALB) as depicted clearly in Figure 40. Consequently the total number of parameters involved in the analysis would be 9. If it was required to evaluate for each factor 5 values, this would lead to an unreasonable number of combinations (5^9= 1953125). It is clear that, whatever parametric study has to lie on a certain set of assumptions and so limitations. In the following, the tangential bridge thickness is kept constant (to 0.3 mm) along with the total length of iron bridge for each flux barrier (calculated by the analytical model) in order to try keeping the

electromagnetic performance as much as possible similar to the one of the electromagnetically optimized solution. Then a nested parametric study will be carried out in order to decrease the number of combinations to assess; that is, the influences on the structural and electromagnetic performances of one or two parameters at a time will be evaluated. In the next two sub-paragraphs, the influence of the fillet radius, the subdivision of the radial ribs into several parts, and the position of the lateral bridges are independently analyzed. Finally, in the third sub-paragraph, a less conservative assumption about tangential bridges width will be explored as well as the influence of bending the lateral bridge on the overall performance.

A. Subdivision of the radial iron ribs and fillet radii influences

The influence of the radial ribs fillet radius (expressed in per unit of half of the corresponding barriers' height) has been investigated on three different iron bridges distributions of the two innermost flux barriers, as shown below:

- rotor with one central bridge per barrier (CB_i) placed in the middle of each barrier (referred to as *1 rib* in Figure 46);
- rotor with the central bridge equally split in two lateral ribs (LB_i) placed at the end of the straight part of each barrier (referred to as *2 ribs*);
- rotor with the central bridge equally split in three parts, two lateral ribs placed at the end of the straight part of each barrier and one in the middle (referred to as *3 ribs*).

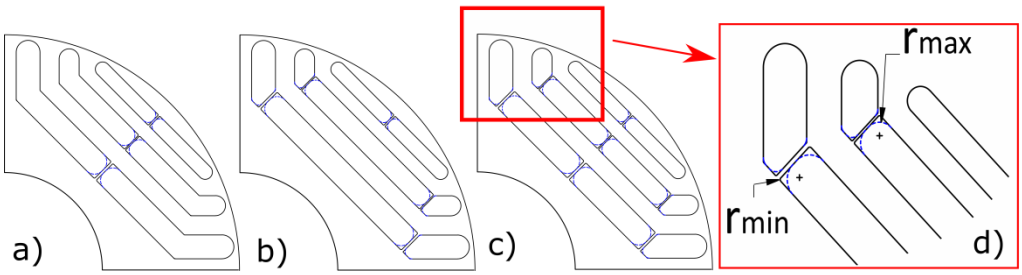


Figure 46: radial ribs distributions: 1rib (a), 2ribs (b), 3ribs (c), fillet radius variation (d)

Figure 47 and 48 show the variations of the maximum stress, average torque and torque ripple with respect to the initial machine. The latter has one central rib per barrier with a fillet radius of 0.1 p.u. and produces an average torque of 0.83 Nm with a 3% ripple and experiences a maximum stress about 870 MPa. The fillet radii have an impact on the maximum stress in the range of 10-20% according to the considered radial bridge subdivision; for all three distributions of iron ribs, the maximum stress does not decrease monotonically as the fillet radii increase. It is worth noticing that rotors having the central rib show a much lower maximum stress with respect to rotors without it. The best stress improvement can be achieved by splitting the central rib into three parts, however such decrement it is not enough to bring the stress below the considered limit. The impact on average torque of the fillet radii is quite low as depicted in Figure 48 while the torque ripple changes more significantly. Both of them worsen almost monotonically as the fillet radii increase.

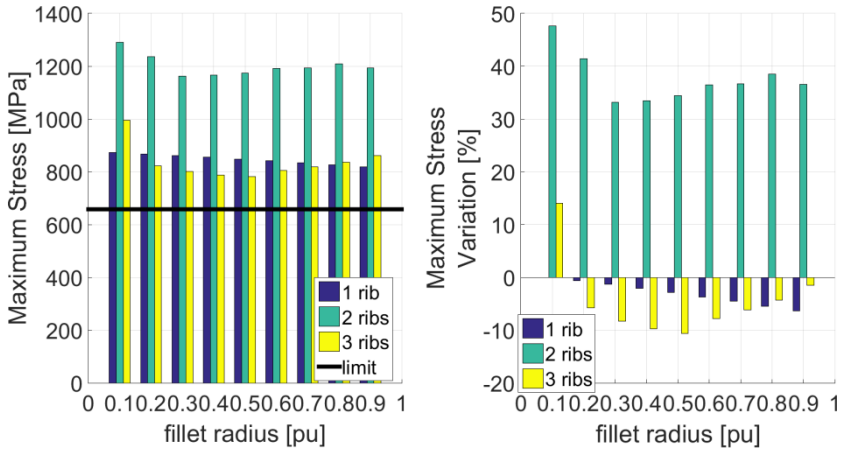


Figure 47: Influence of the fillet radius on the maximum stress for three different subdivisions of the radial iron bridges

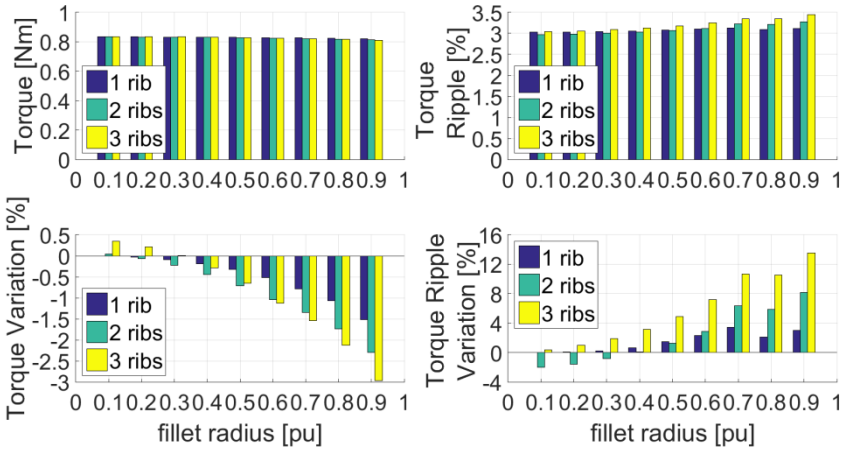


Figure 48: Influence of the fillet radius on the torque performance for three different subdivisions of the radial iron bridges

B. Lateral iron bridge influence

According to the previous analysis the best iron bridges distribution would be the one with three radial ribs per barrier. However from the manufacturing point of view, a rotor with two thicker bridges is preferable to a rotor with three thinner ribs. For this reason, the best two ribs rotor has been chosen to

investigate the influence of lateral bridges positions (PLB) on the overall machine performance. For simplicity, the position of the lateral bridges is expressed in per unit of half of the length of the straight part of each barrier as shown in Figure 49 while the thickness of the central bridge of the outer barrier is kept constant.

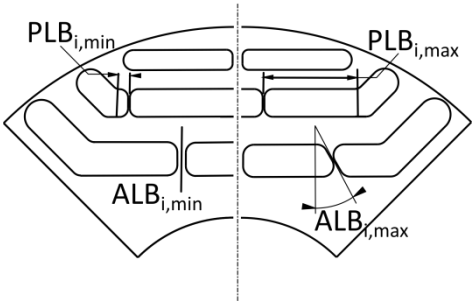


Figure 49: Limit of the linear and angular positions ($ALB_{max} = 60\ [deg]$) of the lateral ribs

Figure 50 highlights that the positions of the lateral iron bridge $PLB_{2,3}$ have a heavy influence on the maximum stress experienced in the rotor lamination. In particular, several combinations of $PLB_{2,3}$ lead to a maximum stress value below the stress limit (shown by the black line). Despite the average torque does not practically change, the torque ripple is quite affected by the position of the lateral iron ribs as reported in Figure 51. The von Mises stress of the best solution obtained with this parametric analysis is shown in Figure 52, i.e. the one with $PLB_2 = PLB_3 = 0.8$ p.u. The optimal positioning of the lateral iron bridges along the respective flux barrier allows a reduction of 30% of the maximum stress without affecting the electromagnetic performances respect to the initial solution (only because the selected solution shown a negligible worsening of the torque ripple, as it is for all combinations with equal $PLBs$).

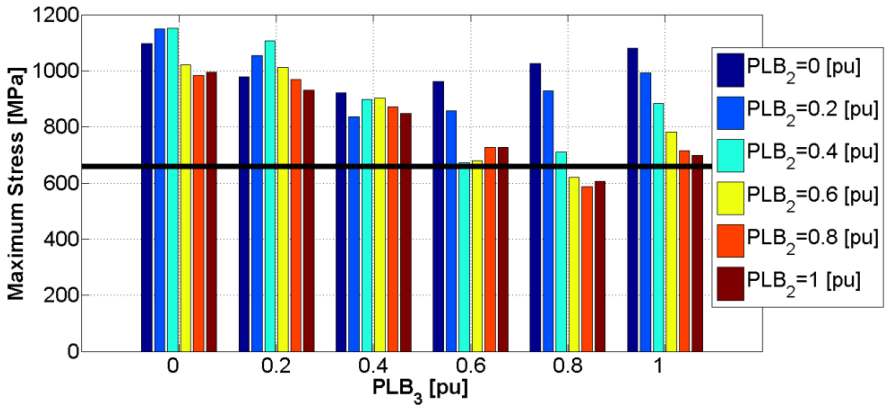


Figure 50: Influence of the position of the lateral ribs on the maximum stress

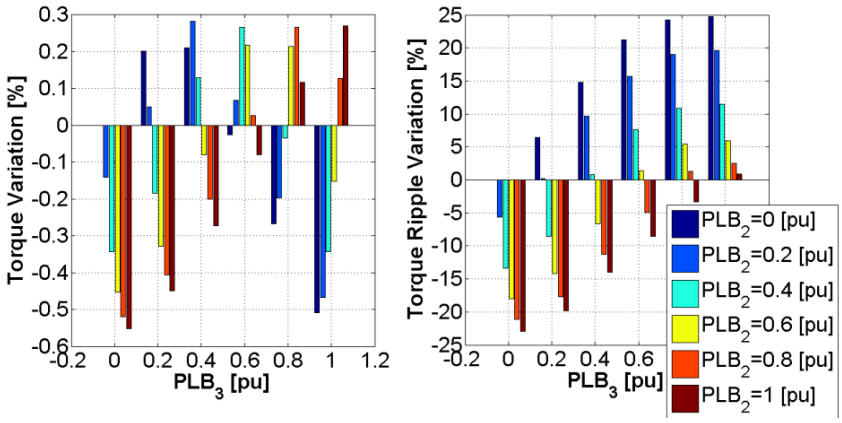


Figure 51: Influence of the position of the lateral ribs on the average torque and torque ripple

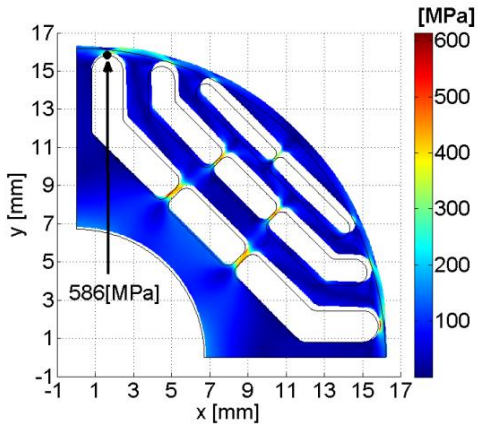


Figure 52: von Mises stress distribution of the rotor having the best positions of the lateral ribs

C. Different assumption of the tangential bridge thickness and influence of the angular orientation of the lateral iron bridge

With the previous two simple parametric analyses it has been demonstrated that adopting the simplified mechanical formulation to estimate the total iron rib per flux barrier with a proper assumption of the tangential bridge thickness is possible to obtain a rotor geometry showing a maximum stress lower than the limit. However if a less conservative choice regarding the tangential bridge thickness is made (i.e. a value lower than 0.3 mm), performing the same parametric analysis it is not possible to obtain a rotor geometry that satisfy the maximum stress constraint. It can be then concluded that if the tangential bridge thicknesses were considered equal to the minimum iron thickness (e.g. 0.05 mm), then the mechanical analytical formulation would underestimate the required iron bridge size of the most external flux barrier of about 80% and respectively 65 and 50% for the two innermost barriers. In other words, if TB is imposed to the minimum, then safety factors of 5, 3 and 2 (going from the outermost to the innermost barrier) have to be adopted. It is worth to underline that the above considerations regarding the safety factors to be used in conjunction with the mechanical analytical model are not general, i.e. it cannot be stated that the above safety coefficients are valid whatever are the parameters describing the rotor geometry (rotor radius, airgap angular position and heights of the flux barrier, etc.). In addition, the above considerations can slightly change if a further geometrical degree of freedom is considered during the parametric analysis. In fact, if the lateral iron bridges are allowed to assume

a direction not parallel to the q-axis, as shown in Figure 49, then also considering a tangential bridge thickness of 0.2 mm, it is possible to obtain rotor geometries showing a maximum stress lower than the limit. Figure 53 shows the results of two parametric studies carried out with a tangential bridge equal to 0.2 mm. In particular for each couple of positions of the lateral ribs, two bars are presented: the black one corresponds to the geometry having the radial ribs parallel to the q-axis (i.e. $ALB_2 = ALB_3 = 0$) while the coloured one corresponds to the best solutions in terms of both bending angles $ALB_{2,3}$. The combinations of bending angles that minimize the maximum stress depend on the positions of the lateral bridge as shown in Figure 54. However, it can be stated that rotating the radial ribs results in a reduction of the maximum stress. Figure 55 reports the von Mises stress distribution of the rotor showing the lowest maximum stress (i.e. the solution with $PLB_2 = 0.8\,[pu], PLB_3 = 0.6\,[pu], ALB_2 = ALB_3 = 60\,[deg.]$) and the rotor with both ribs in the same position but parallel to the q-axis.

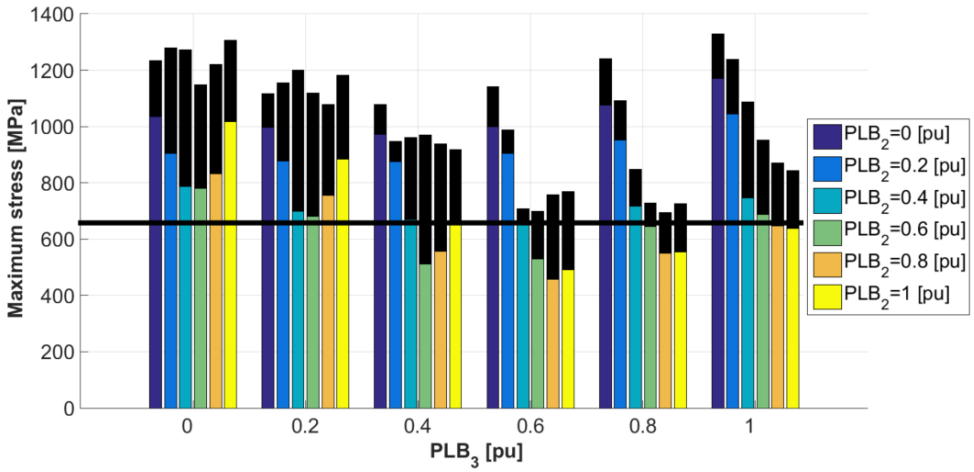


Figure 53: Influence of the position of the lateral ribs on the maximum stress for a rotor having $TB = 0.2$ mm. The black bars corresponds to rotor having $ALB_{2,3} = 0$ while the coloured bars to the best solution in terms of ALB_2 and ALB_3

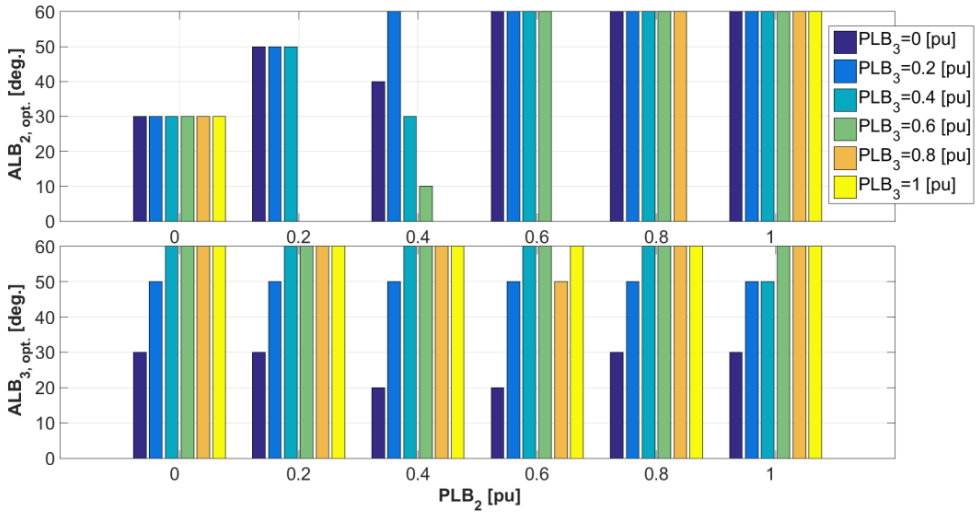


Figure 54: Combinations of the bending angles $ALB_{2,3}$ that minimize the maximum stress.

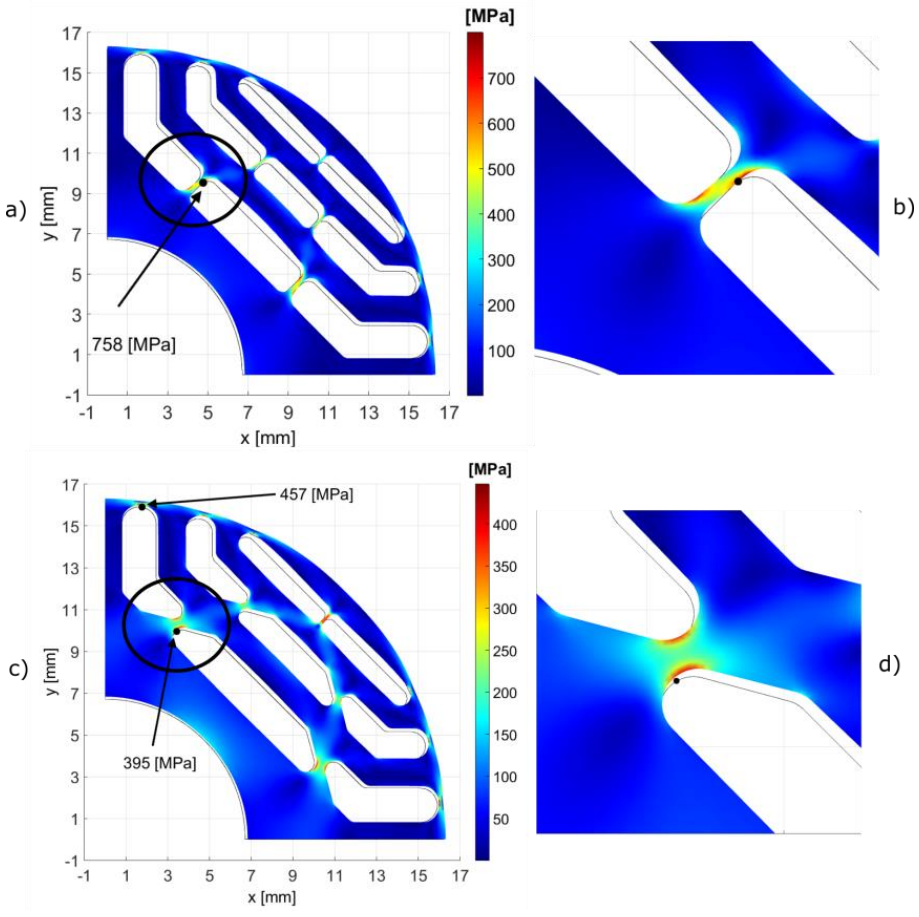


Figure 55: von Mises stress distributions of the rotors with TB=0.2 mm and related details of the stress on the radial rib of the solutions having: c,d) the lowest maximum stress (i.e. with $PLB_2 = 0.8\ [pu], PLB_3 = 0.6\ [pu], ALB_2 = 60\ [deg.], ALB_3 = 60\ [deg.]$), and a,b) the same combination of $PLBs$ and $ALBs = 0\ [deg.]$.

Analysing this figure, it is clear that the reduction of the maximum stress can be ascribed to two reasons:

- rotating the radial ribs clockwise (with reference to the ones on the left of the q-axis and anticlockwise the right ones) corresponds to follow the direction of the maximum stress;
- the effective length of the radial ribs decrease as $ALBs$ increase; that is the part of the rib that actually has a small thickness is reduced.

While acting on the angular positions of the radial ribs can have a beneficial impact on the structural performance, the torque profile is heavily and negatively affected by this additional geometrical degree of freedom This aspect is clearly shown in Figure 56 which reports the trends of average torque and torque ripple as function of the angles $ALBs$ calculated for the best combination of the positions of the lateral ribs ($PLB_2 = 0.8\,[pu], PLB_3 = 0.6\,[pu]$). Although such trends are not general, since they differ according to the combinations of *PLBs*, it is interesting to note that the average torque decreases as both bending angles increase. This behavior can be explained analyzing the Figure 57 in which the electromagnetic field distributions at the MTPA condition of the best rotor (best structural wise) is compared with the rotor having the lateral bridges parallel to the q-axis and in the same optimal linear positions. It is clear that the reduction of the average torque is due to the shorter length of saturated area of the ribs which essentially cause an increase of the q-axis inductance (in fact the leakage flux is higher when the radial ribs are rotated). It has to be underlined that both linear (*PLB*) and angular (*ALB*)

positions of the lateral iron bridge heavily and negatively influence the torque ripple as reported in Figure 51 and 56.

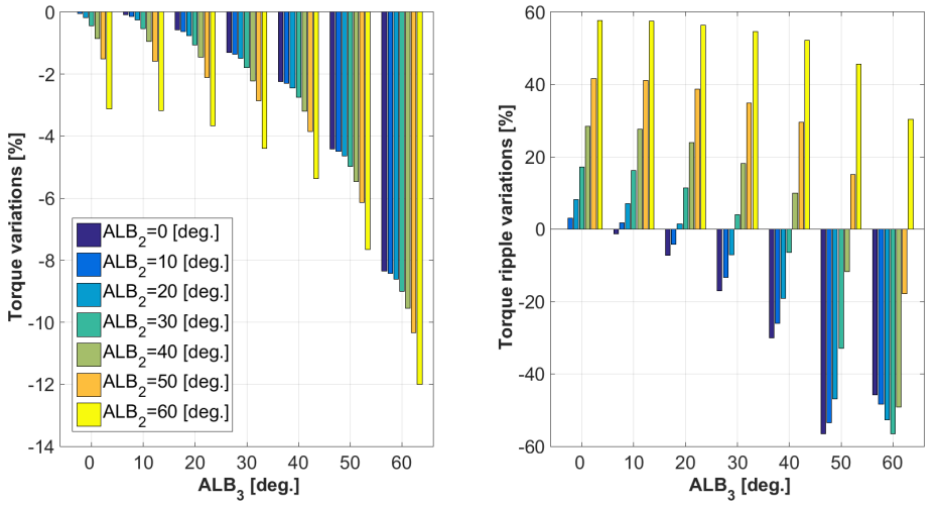


Figure 56: Influence of the angular positions of the lateral ribs on the torque performance for a rotor having $TB = 0.2$ mm and the best combinations of PLB_2 and PLB_3

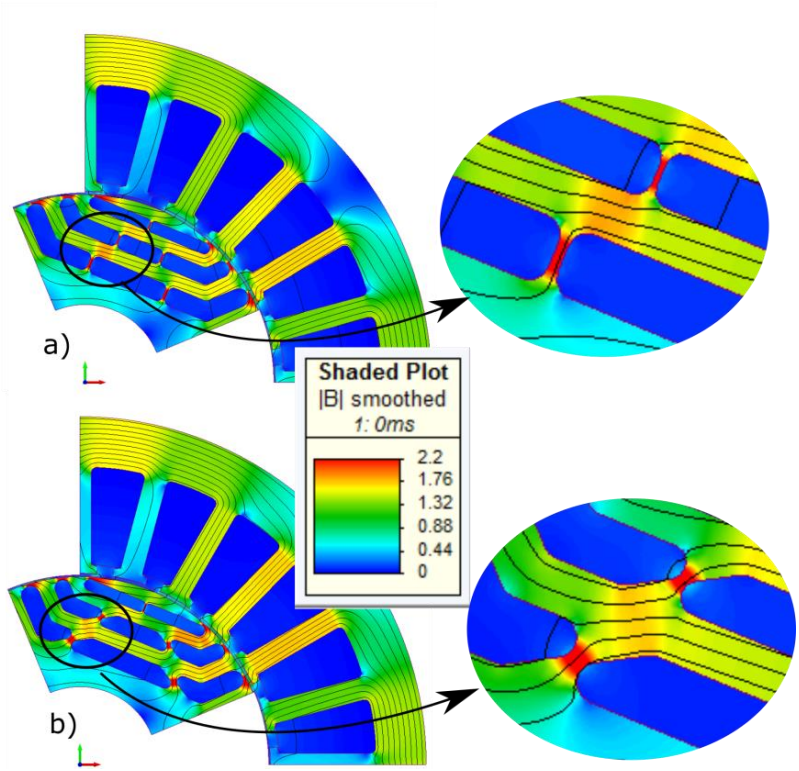


Figure 57: Flux density distributions at MTPA condition of b) the best rotor structural wise (with $TB = 0.2\ mm$) and a) the rotor with the same $PLBs$ and $ALBs = 0\ deg$.

3.4 Proposed design procedures

3.4.1 Introduction

The standard design procedure presented in the previous paragraph could lead to sub-optimal design solutions for the following two reasons:

- during the first stage, i.e. the electromagnetic optimization in which the central ribs are analytically estimated, the interaction between the magnetic and structural design aspect are not fully exploited due to the low accuracy of the evaluation of the mechanical performance;
- during the second stage, i.e. the structural FE parametric analysis, not all the possible combinations of the geometrical parameters have been explored.

Aiming at overcoming the limitations mentioned above, a truly multi-physics rotor design will be performed evaluating both electromagnetic and structural performance at each design step and considering all the geometrical degrees of freedom in the vector of parameters to be optimized. Even though this design approach is implemented with the aid of a multi-objective stochastic optimization algorithm, the high number of parameters to be identified lead to a relevant computational burden. Therefore, with the purpose of evaluating the advantages and disadvantages of performing a truly physically coupled rotor design, in terms of computational time and quality of the final optimal solutions, another design approach is presented. The latter consists in a

physically decoupled approach, i.e. an electromagnetic optimization followed by a proper mechanical optimization; each step addresses a sub-set of parameters and it is always carried out with a multi-objective stochastic OA. The rotor parameters considered in both design approaches are depicted in Figure 58a. The positions and the bending angle of the lateral iron bridges are not included in the vector of variables to be optimized by the OA. The possible advantage and disadvantage of considering also these parameters during the rotor design will be analysed in detail in the next chapter. It is worth noticing that, differently from the standard design procedure, all the tangential iron bridges can independently vary within an assigned range (0÷1 mm, equal for all ribs) and they are not preliminary imposed equal to each other.

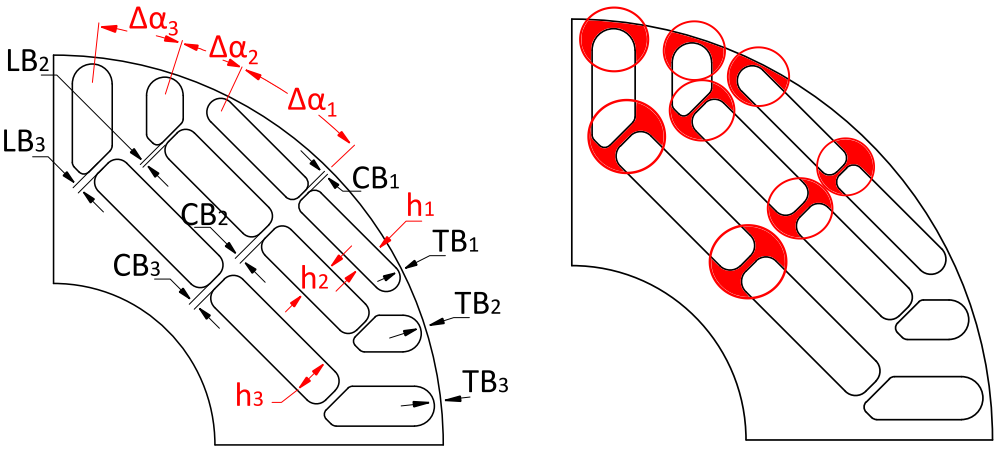


Figure 58: a) Rotor parameters optimized during the proposed two design approaches, b) critical rotor's regions considered for the calculation of the stress factor

The electromagnetic performance FE evaluation will be carried out implementing the same settings adopted for the standard design procedure described in the paragraph 3.3.1. Regarding the mechanical design aspect, the

rotor integrity is obviously guaranteed if the maximum Von Mises stress induced in the rotor lamination lies within a certain percentage of the yield strength. However this condition can be used as a constraint during the rotor design optimizations (for both design approaches) but not as a proper structural cost function. In fact, this condition can be satisfied by several rotor geometries, therefore another design criteria needs to be identified if a proper structural optimization has to be performed. In the next subparagraphs, first a new structural design criteria is introduced, then the details of both design approaches are presented and finally the optimization results are outlined.

3.4.2 Selection of the structural objective function

During the following two design processes, if the maximum von Mises stress exceeds the stress limit (80% of the yield strength), the rotor candidate is penalized, i.e. the objective functions are multiplied by a constant factor. In order to mechanically distinguish the rotor geometries showing the same maximum stress but different torque performance and von Mises stress distribution another structural design criteria needs to be introduced. In particular, with the aim to fully exploit the iron bridges, possibly minimizing their thicknesses (and so maximizing the torque), the same maximum stress should be measured in each structural rib area. To this aim, the following mechanical objective, called stress factor SF, can be considered:

$$SF = \sum_{i=1}^{n_{ribs}} \left| \sigma_{max,i} - \sigma_{target} \right| \quad (37)$$

where $\sigma_{max,i}$ is the maximum von Mises stress value induced in the area which surrounds the i-th iron bridge as depicted in Figure 58b, σ_{target} is the stress target (here considered equal to the stress limit, 658 MPa) and n_{ribs} is the number of bridges (8). Minimizing such structural objective implies that even the bridge's area which experiences a von Mises stress lower than the stress target is penalized since it contributes to increase the stress factor.

3.4.3 Physically decoupled design

This procedure is based on the assumption that the design variables can be divided into two subsets. The first subset contains 7 parameters, shown in red in Figure 58a, mainly influencing the electromagnetic performances, i.e. the airgap angular positions and height of each barrier ($\Delta\alpha_i, h_i$) and the current phase angle (γ). The second subset includes 8 variables, shown in black in Figure 58a, primarily affecting the von Mises stress distribution of the rotor structure, i.e. all the bridge sizes (TB_i, CB_i and LB_i). The hypothesis on which this subdivision is based is the negligible impact of the first subset of parameters on structural performances and of the second subset on electromagnetic performance. Based on this assumption the following two-steps strategy is adopted.

1. First an electromagnetic optimization is carried out, having as objectives the minimization of the torque ripple and the maximization of the average torque. During this step the first set of 7 variables ($\Delta\alpha_i, h_i, \gamma$) are optimized imposing all the tangential bridges (TB_i) equal to a certain value (0.3 mm) and the lateral and central ribs (CB_i, LB_i) equal to zero. Once the electromagnetic optimization is carried out, from the Pareto front average torque – torque ripple, one machine is selected.
2. A mechanical optimization is then performed on the chosen solution having as objective the minimization of the stress factor defined in (37). During this second design stage the first set of 7 variables are kept equal to the optimum values obtained with the first design stage while all the bridges' dimensions are optimized.

The electromagnetic and mechanical optimizations are both carried out with 80 elements per population iterated for 100 generations, leading to a total computation time of 36 hours (23 hours for the electromagnetic design and 13 for the structural one).

3.4.4 Physically coupled design

The physically coupled design strategy assumes that all geometric rotor parameters have a certain influence on both electromagnetic and structural performance. This is mainly motivated by the following two obvious considerations.

1. As already mentioned, the total bridge width per flux barrier is related to the mass of the flux guide, which in turn depends on the angular position at the airgap and on the radial thickness of the flux barriers. Therefore the parameters $\Delta\alpha_i$ and h_i, which mainly influence the electromagnetic behavior, also have a side effect on the structural performance.
2. On the other hand, the electromagnetic performances are affected by the bridge dimensions, because:
    - increasing the total bridge width per flux barrier leads to a loss of average torque at constant stator current;
    - changing the tangential bridge widths modify their saturation level at the air-gap, therefore also the torque ripple is affected.

With these statements in mind, two types of multi-physics optimizations addressing all the geometrical parameters (15) are carried out. These two families of optimizations differ to each other according to the number of objectives. Both of them optimize average torque and torque ripple with the constraint on the maximum stress while only one of them minimizes also the stress factor defined in (37).The three-objectives optimization is carried out with 250 individuals per population iterated for 100 generations and the required computation time is nearly 150 hours (i.e. more than four times longer than the physically decoupled approach). The two-objectives optimization is instead performed with 180 elements iterated for 100 generations (for a total computational time of 110 hours) being lower the complexity of the objective function.

3.4.5 Optimization results

Figure 59 summarizes the results of both optimization strategies (performed with the multi-objective genetic algorithm NSGA-II) in the average torque – torque ripple plane with the stress factor shown by means of a coloured scale. For each optimization at least 3 runs have been carried out in order to evaluate the repeatability of the results and in the following only the most important results are shown for the sake of clarity. The Pareto front obtained after the first step of the physically decoupled design approach (i.e. torque-ripple optimization) is shown with black dots since the mechanical performances are not evaluated at this stage. All these solutions are structurally unfeasible due to the absence of radial ribs. In the same figure the Pareto fronts of the physically coupled design approach are reported: the coloured stars represent the front of the 3-objective optimization (torque, ripple, stress factor) while the black crosses are the front of the 2-objective optimization (torque-ripple with the constraint on the maximum stress FE evaluated). Considering the physically decoupled optimization, one solution (highlighted with a yellow circle) is selected from the Pareto front torque-ripple and mechanically optimized. Figure 60 shows the stress factor evolutions during the best and the worst structural optimization run; the electromagnetic performance of these two extreme solutions are reported in Figure 59 using coloured dot. It has to be underlined that these two extreme final solutions obtained with the structural optimizations present really different stress factors (248 and 978 MPa); the best

solution structural wise (i.e. the one with SF=248 MPa) produce an average torque 6% higher than the worst solution (i.e. the one with SF=978 MPa).

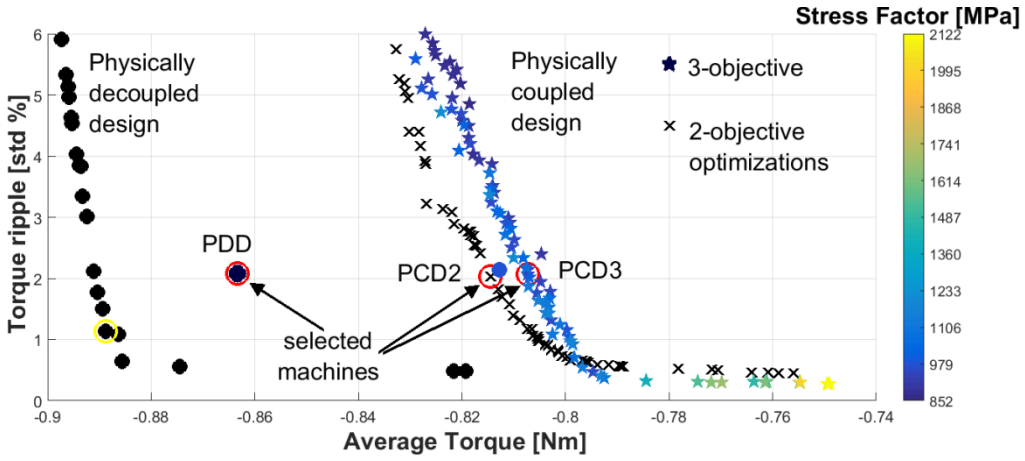


Figure 59: Optimization results: physically decoupled approach (black dots is the Pareto front of the electromagnetic optimization while the colored dot is the final solution after the structural optimization), physically coupled approach (colored stars is the Pareto front of the 3-objective optimization while the black crosses is the front of the 2-objective optimization)

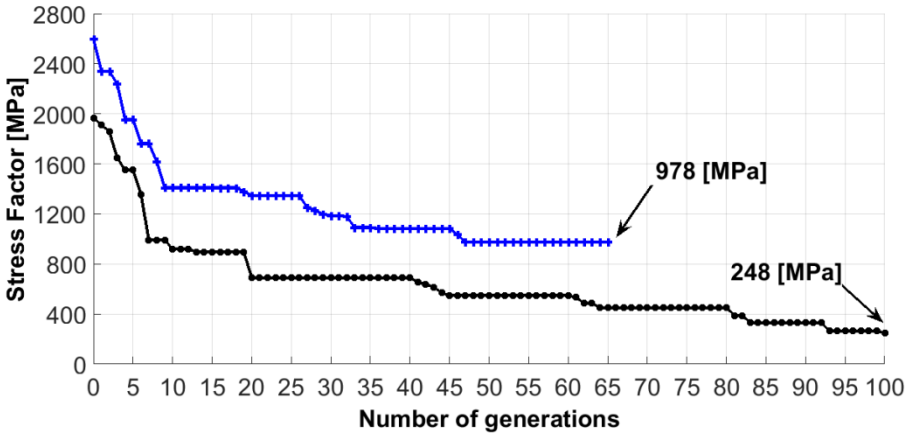


Figure 60: Stress factor evolutions during the structural optimization (i.e. second stage of the physically decoupled approach). The best and the worst runs are reported.[1]

Regarding the 3-objective physically coupled optimization and its Pareto front (coloured stars in Figure 59), it can be noticed that the stress factor decreases as the average torque increases. This trend can be generically justified since a

[1] The improvement obtained in the last generation of the best optimization run is negligible (also considering a higher number of functional evaluations).

lower stress factor implies that all the iron bridges experience a von Mises stress closer to the stress target, which means that the bridges' widths are minimized. Therefore, a better mechanical exploitation of the rotor iron and the torque maximization are pursued at the same time. The Pareto front obtained with the 2-objective physically coupled optimization (black crosses in Figure 59), is almost overlapped with the front achieved with the 3-objective optimization. However the stress factors shown by the optimal solutions obtained with the multi-physics 2-objective optimization (evaluated in post processing) are higher than the ones achieved with the 3-objective optimization as reported in Figure 61. It can be stated that the two physically coupled optimizations produce comparable electromagnetic performance but they must lead to different rotor geometries as will be reported in the next paragraph.

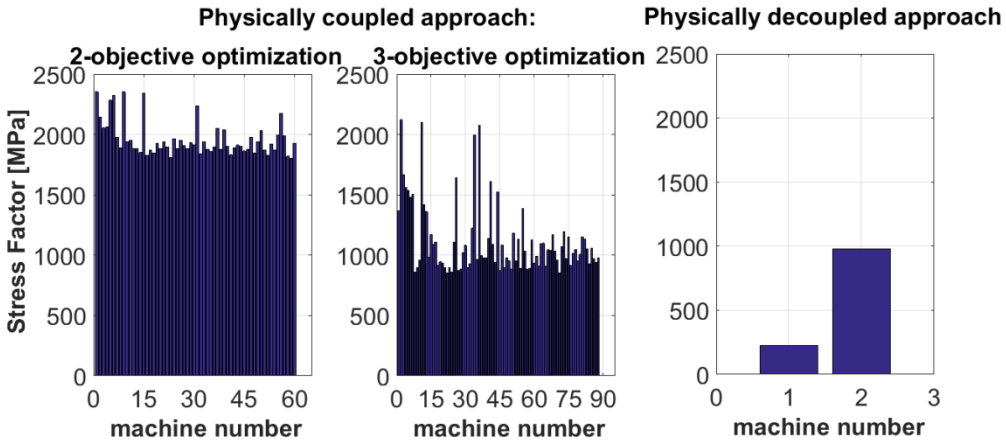


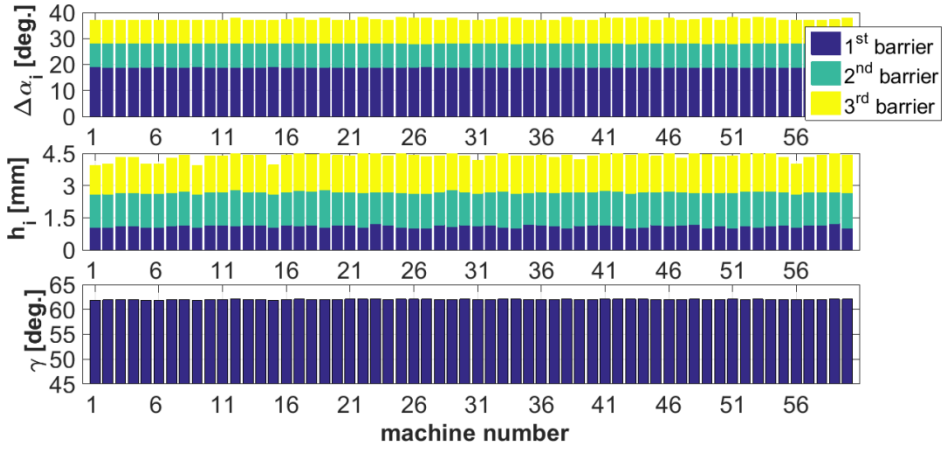
Figure 61: Stress factors of the optimal solutions of the two design strategies, i.e. the multi-physics approach (2 and 3 objective optimizations) and physically decoupled approach

Comparing the two design approaches, it is clear that the best physically decoupled design allows an improvement of almost 10% in terms of average torque and at least 400% in terms of stress factor compared with the solutions

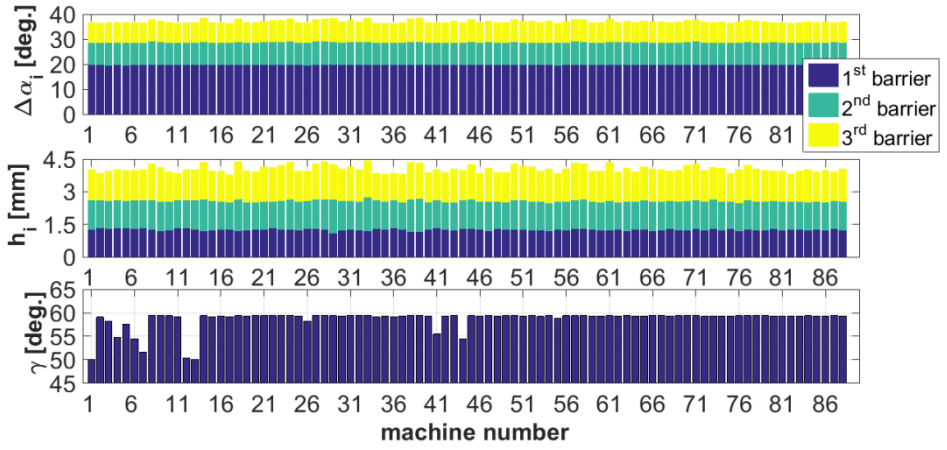
having the same torque ripple obtained with the multi-physics optimizations (both 2 and 3-objective runs). On the other hand, the worst solution of the physically decoupled approach has comparable performance to the one obtained with the multi-physics design approach.

3.4.6 Analysis of the optimized machines

Even if the two multi-physics optimizations produce structurally feasible rotors having comparable electromagnetic performance, their optimal geometries are quite different, as reported in Figure 62 and 63. In particular the 2-objective multi-physics optimization produces rotor geometries with flux barriers having bigger thicknesses while the 3-objective one leads to rotor structures having the innermost flux barrier positioned more towards the q-axis (i.e. having a smaller $\Delta\alpha_3$). The other most noticeable difference lies in the complete absence of the lateral bridge on the second barrier in the rotors optimized minimizing also the stress factor as shown in Figure 63. It is worth to underline that the tangential rib thickness of the optimal rotors (of both multi-physics approaches) constitute a relevant portion of the total bridge of each barrier (especially for the outermost one). With the aim of comparing more in detail the optimal geometries obtained with the two design approaches, one solution has been selected from each optimization run.



a)



b)

Figure 62: Airgap angular positions $\Delta\alpha_i$ and heights h_i of the flux barriers and current phase angle $\gamma$of the Pareto optimal solutions of the two multi-physics design approaches a) 2-objective, b) 3-objective optimization. The solutions are numbered from the one showing the smallest torque ripple to the highest.

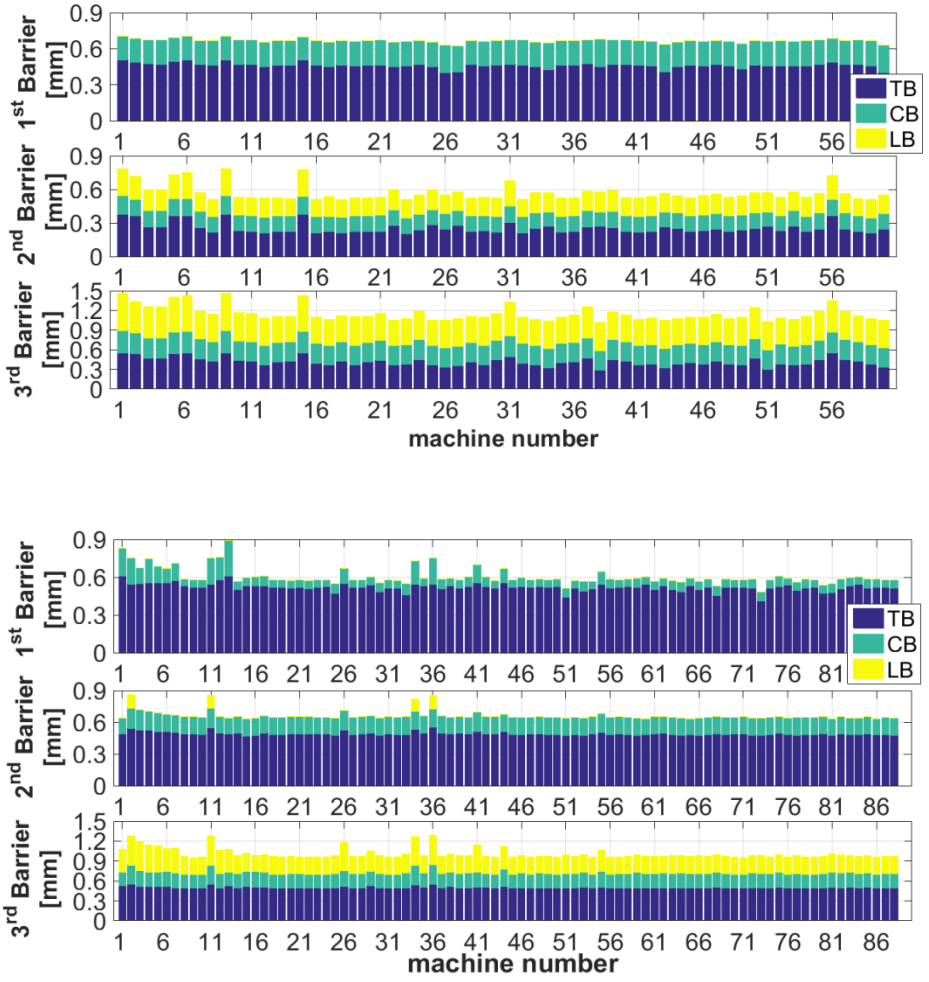


Figure 63: Total iron bridge thickness distributions per barrier of the Pareto optimal solutions of the two multi-physics design approaches a) 2-objective, b) 3-objective optimization. The solutions are numbered from the one showing the smallest torque ripple to the highest.

In particular three machines showing almost the same torque ripple have been considered as reported in Figure 59 (highlighted with the red circles). The three selected rotors (*PDD, PCD3, PCD2*) are shown in Figure 64 while their geometrical parameters are reported in Figure 65. Analyzing the rotor geometries the following observations can be deduced.

- The airgap angular position of the flux barriers of the *PDD* solution respect quite well the constant rotor slot pitch rule while the *PCD* designs assume

different angular distributions of the barrier especially for the outermost and innermost one even if they show almost the same torque ripple level.

- The barrier height increase going from the outermost to the innermost barrier for all the 3 optimal machines; however the *PCD2* solution has a remarkable bigger flux barrier heights respect to the other two solutions.
- The tangential ribs of the *PCD3* rotor are almost constant, while the *PDD* solution has the second barrier with the smallest TB and the first and the third ones with a TB almost doubled with respect to the second one; regarding the *PCD2*, the outermost barrier has the biggest TB while the other two barriers have a TB almost halved respect to the first one.
- The central ribs increase from the most external to the most internal barrier for both *PDD* and *PCD3* designs.
- Both *PDD* and *PCD3* do not have the lateral iron bridge on the middle barrier; this feature is peculiar of the rotors optimized minimizing the *SF*.

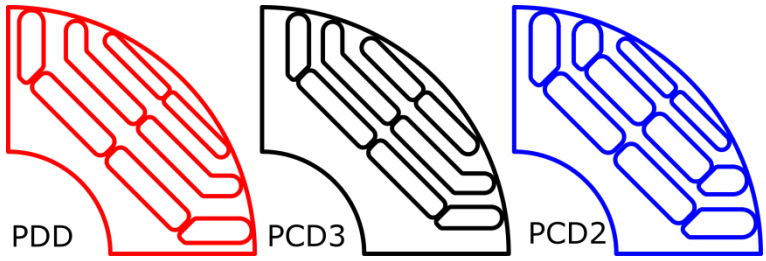


Figure 64: Selected rotor optimized with the physically decoupled design approach (*PDD*), the multi-physics approach carried out with a 3-objective (*PCD3*) and 2-objective (*PCD2*) optimization

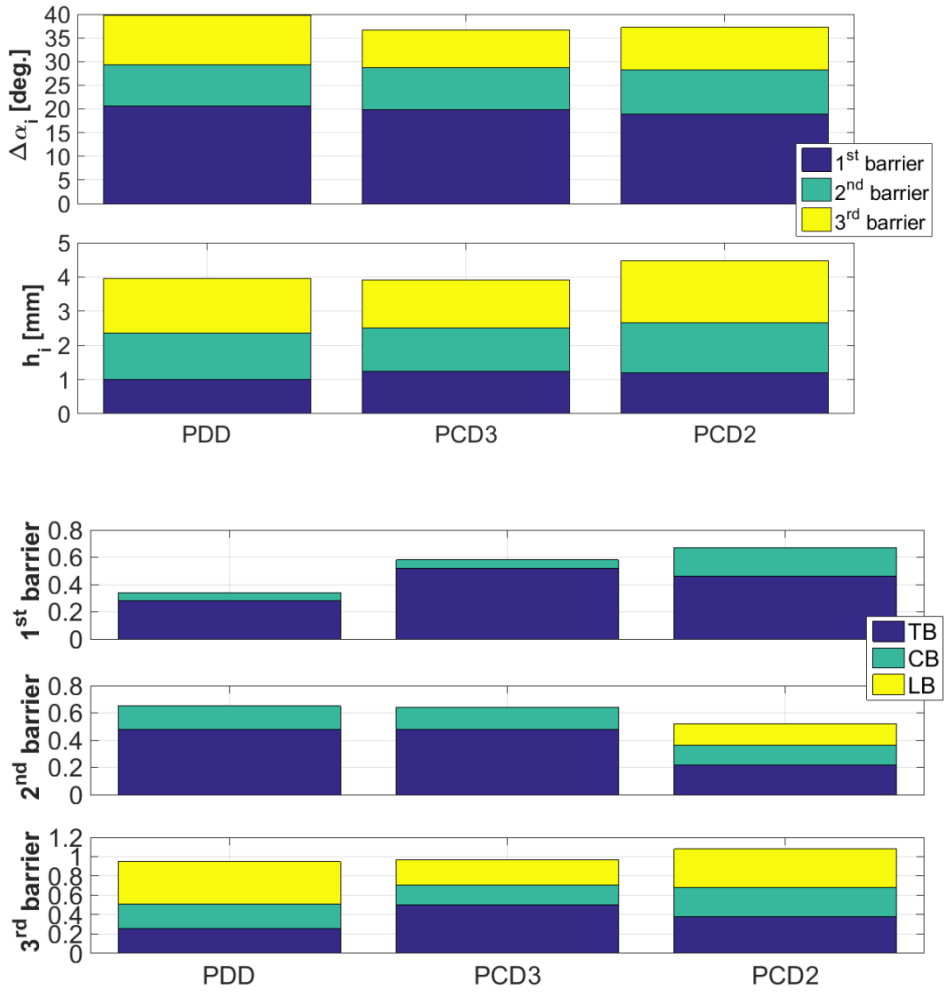


Figure 65: a) Airgap angular positions $\Delta\alpha_i$ and heights h_i of the flux barriers and b) total iron bridge thickness distributions per barrier of the selected rotors

These geometrical differences significantly affect the von Mises stress distribution, shown in Figure 66, and so all the maximum stress in each critical area which define the stress factor, reported in Table 7. As expected the rotor designed with the physically decoupled approach (*PDD*) shows the most uniform stresses distribution for all critical areas since it has the lowest stress factor. In fact the latter implies that the critical stresses have a mean near to the stress target and a low standard deviation. The rotor designed with the multi-physics approach have a much higher stress factor and so a mean critical stress

much different from the stress target and with a higher standard deviation (especially for the rotor obtained with the 2-objective optimization).

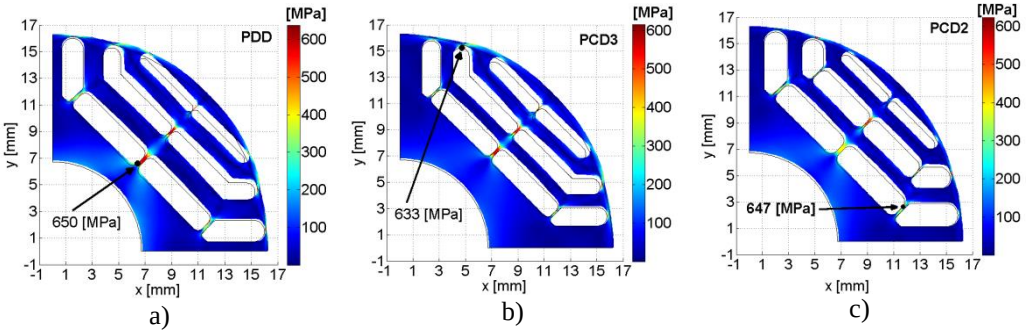


Figure 66: von Mises stress distribution of the selected rotors with a 1:30 scale for the deformation optimized with the a) physically decoupled design approach and the multi-physics design approach carried out with b) a 3–objective and c) a 2-objective optimization

While the torque ripple (at MTPA condition and 150% the rated current) is almost the same for the selected optimal rotors, the average torque produced by the solution optimized with the physically decoupled approach is about 6% higher than the one achievable by the other design approach. This can be mainly due to:

1. the more uniform distribution of the flux barriers of the PDD solution, both in terms of their airgap angular positions and heights, which lead to a slightly lower level of the rotor iron saturation (consequence of the bigger flux guides, especially for the third flux guide) as shown in Figure 67;
2. a smaller thickness of the iron bridge of the most external flux barrier; the other two barriers show almost the same total iron bridge thickness for all the three optimal machine (except for the middle barrier of the *PCD2* rotor).

Table 7: Structural performance (critical von Mises stresses, stress factor, mean and standard deviation of the critical stresses) and electromagnetic performance (torque and ripple) of the selected rotors

	Design				
	PDD	**PCD3**	**PCD2**	**Unit**	
TB_1	633.5	314.8	312.7	MPa	**Maximum stress in each critical region**
TB_2	635.9	632.4	508.1	MPa	
TB_2	625.7	442.9	277.9	MPa	
CB_1	542.3	498.5	149.3	MPa	
CB_2	627.7	575	513.3	MPa	
CB_3	650.4	603.9	432.3	MPa	
LB_2	-	-	527.8	MPa	
LB_3	631.1	603.4	640.7	MPa	
SF	248	945	1898	MPa	**Overall structural performance**
Mean Stress	620.9	524.4	420.3	MPa	
Std Stress	35.6	114.0	161.2	MPa	
T_m	0.863	0.807	0.814	Nm	**Electromagnetic performance**
T_{rip}	2.08	2.07	2.03	Std %	

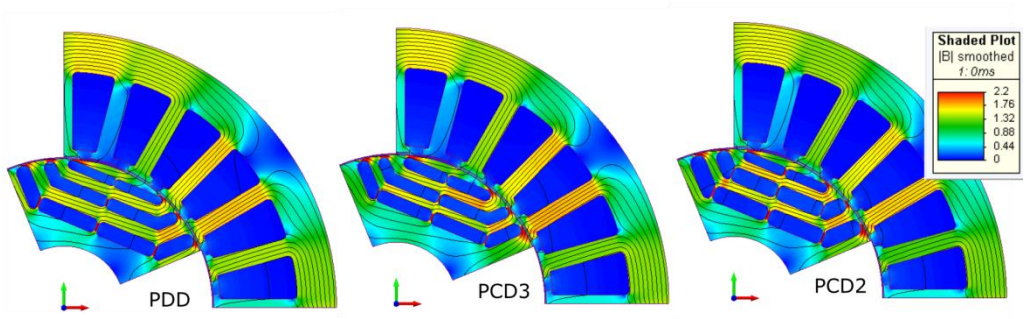


Figure 67: Flux density distributions (at MTPA with 150% the rated current) of the selected rotors optimized with the PDD) physically decoupled design approach and the multi-physics design approach carried out with PCD3) a 3–objective and PCD2) a 2-objective optimization

3.4.7 Design strategy comparison

The physically coupled design strategy allows considering the interaction of magnetic and structural design choices. In other words, since all the parameters are addressed at the same time during the optimization, the OA is allowed to explore regions of the research space that are otherwise ignored (as during the standard design procedure or the physically decoupled approach). Such possibility tends the OA to produce unconventional rotor solutions both in the case of the 2- and 3-objective optimizations. The first one leads to rotor structures with bigger flux barrier heights, while the second one produces geometries with the third flux barrier nearer to the second one. By doing so, the thicknesses of the flux guides are smaller and so the maximum stress is relieved and possibly also the iron bridges are minimized. These areas of the research space cannot be explored during the physically decoupled design approach. However the latter produces better results for the following reasons.

1. The mechanical objective function (stress factor) is highly nonlinear and presents several local optima. In fact different structural optimizations (reported in Table 8), carried out with the same setting, produce a wide range of results, both in terms of stress factors, and does not evaluate all the allowed generations. This means that most of the time the OA is trapped in local optimum.
2. The research space dimension of the physically coupled approach (i.e. 15) is doubled compared to the one of the physically decoupled strategy (7 and 8 respectively for the electromagnetic and structural optimization), therefore more iterations are required to obtain performance comparable with the one obtained with the physically decoupled methodology.
3. During both design approaches, the rotors showing a maximum stress higher than the stress limit are penalized by means of a static penalty (i.e. the objective functions is multiplied by a constant factor). This approach has the drawback of not fully exploiting any information from the penalized solutions that might be generated by the algorithm to guide the search [108]. Therefore the optimization process could stagnate because of all the penalized solutions show comparable performance.

Table 8: Final results and evaluated generations of 10 structural optimizations carried out with the same setting, i.e. 80 elements per population for 100 maximum generations.

Run	**1**	**2**	**3**	**4**	**5**	**6**	**7**	**8**	**9**	**10**
SF [MPa]	279	679	248	534	633	818	459	904	267	475
Generation	99	53	100	66	81	65	58	52	73	58

The physically decoupled design strategy requires about a fourth of the time needed to guarantee final performances at least comparable with those obtained with the 3-objective multi-physics approach. Reducing the number of cost function from 3 to 2, i.e. not considering the minimization of the stress factor as objective, allows obtaining the same results in terms of torque performance respect to the more complex 3-objective problem with a 25% reduction of the computational time; however the final solutions of the two multi-physics optimization are quite different. Even considering the 2-objective multi-physics strategy, the physically decouple approach provides better results in about a third of the computational time. Clearly, the performance of the multi-physics approach could be improved by further increasing the population size and the number of iterations at the expenses of computational time. Considering that the results shown here were achieved after 150 hours of calculations (for the 3-objective problem and 110 for the 2-objective one), it appears at least a not practical approach unless the calculations can be distributed over a cluster of microprocessors. For most designers who can count on a single workstation for their simulations, the two step design approach is currently the best choice.

3.5 Conclusion

In this chapter, the rotor design challenges of a HS-SyR machine are analysed in details. These challenges are mainly due to two issues, namely 1) the high number of geometrical degrees of freedom involved during the design, and 2) the long computational time required evaluating the electromagnetic and structural performance both by means of FEAs. The latter is needed in order to properly evaluate the electromagnetic and structural non-linearities and to consider the influence of all geometrical parameters. These two characteristics lay the further problem of selecting the most effective design strategy which correctly balances the performance of the final design and computational time required to achieve this solution. In order to properly evaluate the trade-off between the quality of the final design and the related computational burden, a comparative study of two design approaches has been presented. The proposed design procedures differ according to whether the electromagnetic and the structural design aspects are truly coupled or not. Both design strategies adopt the same objective functions, i.e. average torque, torque ripple and an innovative structural figure of merit with which the rotor's von Mises stress distribution can be described. Better results in term of average torque and von Mises stress distribution are obtained with a reduced computational time, by adopting a physically decoupled optimization in which a proper mechanical optimization follows the electromagnetic optimization. The physically coupled approach, that optimizes the whole geometry executing both electromagnetic

and structural finite element analysis for each rotor candidate, addresses better the interaction of the magnetic and structural design aspects. This leads to rotor geometries slightly different from the one obtained with the physically decoupled approach. However the decoupled approach does produce better results because dividing the research space in two subspaces makes the optimizations shorter and more focused on the aspect under consideration. From this work, it can be concluded that unless a powerful computational cluster is available, the physically decoupled approach is the more appropriate choice. It has to be underlined that the physically decoupled design approach provides a better result also when compared to the standard design methodology presented in the paragraph 3.3. Although the average torque improvement is only about few per cent (4-5% in the best case), performing a structural optimization instead of a parametric study (aimed at redistributing the analytical estimated ribs) drastically reduces the risk of obtaining a sub-optimal solution and avoids the need of preliminary assuming the tangential bridge thickness (and/or the mechanical safety factors).

Chapter 4
Structural design optimization of HS-SyR machine

The aims of this chapter are three.

- Investigate the reasons of the low repeatability of the structural optimization results presented in the previous chapter as a part of the physically decoupled design strategy.
- Explore the trade-off between the rotor geometrical complexity and electromagnetic performance by means of a comparative study of several structural optimizations carried out on different rotor geometries.
- Quantify the influence on the structural and electromagnetic performance of the rotor-shaft coupling assured by the well-known method of the interference fitting.

4.1 Alternative structural performance indexes

The structural optimization shown in the previous chapter as the second step of the physically decoupled design strategy provides a wide variety of results in terms of performance index as reported in Table 8. Most of the time the OA is trapped in local optimum because does not evaluate all the allowed generations (the OA stops because the rate of improvement of the cost function is smaller than a certain threshold). This essentially means that the result of the structural optimization is unreliable since it does not lead to the same solution both in terms of stress factor and rotor geometry. With the aim of improving the repeatability of the results, another stochastic OA has been adopted, i.e. a differential evolution algorithm (DE). The latter definitely gives better results in terms of objective function, being the standard deviation of the final stress factors (*std(SF)*) of 10 optimization runs lower with respect to the one obtained with the GA (and the same number evaluations), as shown in Table 9. Although the obtained stress factors improve when adopting a DE algorithm, the latter provides a wider variety of optimal rotor geometries. A possible index describing how much different the final rotor solutions are respect to each other is the difference between the Euclidean distance (*ED*) of the farthest (*max(ED)*) and the nearest (*min(ED)*) solutions with respect to the average solution or the standard deviation of such set of Euclidean distances. These figures of merit are also reported in Table 9 where it is clear that the DE algorithm gives a wider spectrum of final rotor geometries with respect to the

results obtained with the GA algorithm even if a higher number of functional evaluations is adopted.

Table 9: Analysis of the results of 10 structural optimizations performed with GA and DE with 80 element per population and 100 (or 150) generations: std(SF) standard deviations of the final stress factors, max(ED) – min(ED) difference between the maximum and minimum Euclidean distances calculated respect to the average solution and std(ED) standard deviation of the same set of distances. In round bracket the same figures of merit are reported calculated respect to the best solution. The column marked with the asterisk (*) reports the results obtained calculating the stress factor considering the average of the stress for each critical region and not its maximum value

	GA 80x100	**DE 80x100**	**DE 80x150**	**DE 80x150 (*)**	
mean(SF)	547.3	543.7	385.7	-	
std(SF)	39.6	25.9	25.3	11.0	%
max(ED) – min(ED)	0.125 (0.36)	0.45 (0.74)	0.26 (0.51)	0.27 (0.68)	mm
std(ED)	0.05 (0.12)	0.13 (0.23)	0.09 (0.18)	0.09 (0.17)	mm

The reason behind the difficulties of the OA to produce a reliable result could lie in the characteristics of the objective function and how it is calculated. In fact, the evaluation of the stress factor is definitely affected by the mesh size of the FE solution. Consequently similar rotor geometries can be described with two really different stress factors. However even if the stress factor is calculated considering an average stress for each critical region of the rotor instead of the maximum stress, the results improves in terms of objective function (the *std(SF)* is lower) but the rotor geometries are still too much different (*std(ED)* does not decrease) as shown in Table 9. It can be then concluded that the high non-linearity of the structural objective function and the lack of univocal relationship between the geometry and the stress factor

prevent the OA to provide reliable results. The fact that really different rotor geometries can be described with the same stress factor should not be a problem as long as solutions with a lower stress factor produce a higher average torque. In fact, it has to be underlined that the physically decoupled design approach is valid if the considered structural design criterion explicitly or implicitly leads to the minimization of the iron bridge thicknesses and so the maximization of the electromagnetic torque (and possibly not changing the torque ripple). Unfortunately the produced torque does not increase as the stress factor decreases as shown in Figure 68a; in this figure, the stress factors and the average torques of the 10 optimal machines obtained minimizing the stress factor are represented. The same figure (subplot b) proves that there is neither a clear relationship between the stress factor and the average total bridge per flux barrier (*ATB*) calculated as:

$$ATB = \frac{1}{n}\sum_{i=1}^{n}(2 \cdot TB_i + 2 \cdot LB_i + CB_i) \tag{38}$$

where n is the number of barrier and TB_i, CB_i and LB_i are the respectively the thickness of the tangential, central and lateral iron bridge of the *i-th* barrier. However plotting on the same graph the average total bridge and the produced torque of the 10 optimized machines, it is evident the direct relationship between this two indexes. This correlation is obvious, smaller *ATBs* correspond a general reduction of the thicknesses of the iron bridges and so an increment of the electromagnetic torque. The direct consequence of this observation is the

possibility of using the average total bridge per barrier as cost function to be minimized during the structural optimization instead of the stress factor.

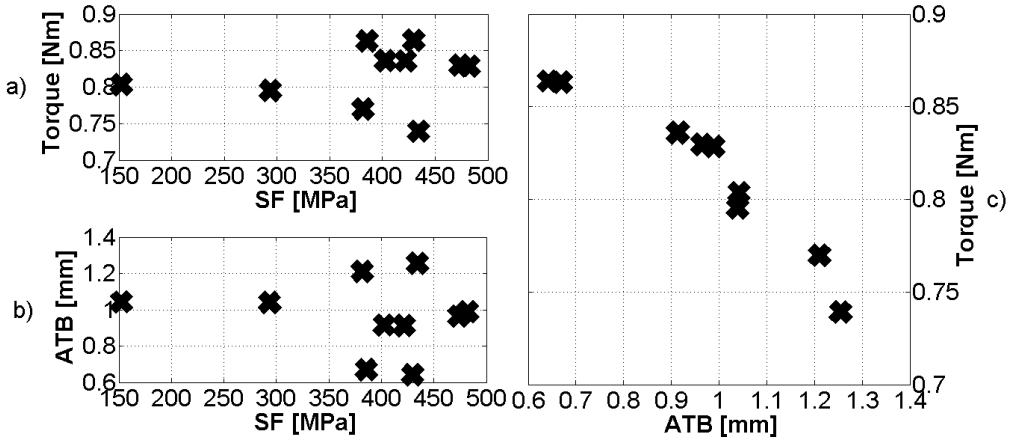


Figure 68: Analysis of the results of 10 structural optimization runs carried out with a DE algorithm (80 elements per population for 150 generations) minimizing the stress factor. a) torque – stress factor, b) average total bridge (*ATB*) – stress factor, c) torque – *ATB*

The adoption of this new structural objective function lies on the weak hypothesis that the decrement of the average torque (*dT*) caused by the increment of an iron bridge thickness (*dB*) is independent from the real position of the rib's increment. In other words, wherever *dB* is allocated, such as on the tangential, lateral or central rib and whatever the position of the lateral one is, the loss of torque *dT* should remain the same. If this conjecture is verified, as it will be in the next paragraph, the minimization of the average total bridge (*ATB*) subject to the constraint on the maximum stress will lead to rotor structure with the highest average torque for a given maximum stress limit. In order to evaluate the repeatability of the results obtained minimizing this alternative structural performance index, 10 mechanical optimizations have been carried out adopting the DE algorithm with 80 element per population iterated for 150 generations. Table 10 summarizes the analysis of the results

obtained minimizing the stress factor and the average total bridge with the same OA and number of functional evaluations.

Table 10: Analysis of the results of 10 structural optimizations both performed with the DE algorithm (with 80 element per population and 150 generations) minimizing the stress factor or the average total bridge per barrier: *std(SF)* standard deviations of the final stress factors, *max(ED) – min(ED)* difference between the maximum and minimum Euclidean distances calculated respect to the average solution and *std(ED)* standard deviation of the same set of distances. In round bracket the same figures of merit are reported calculated respect to the best solution.

	DE 80x150		
Cost function	**SF**	**ATB**	
std(cost function)	25.3	2.2	%
max(ED) – min(ED)	0.26 (0.51)	0.09 (0.1)	mm
std(ED)	0.09 (0.18)	0.05 (0.03)	mm

It is clear that minimizing the *ATB* leads to much more reliable results both in terms of objective function and rotor geometries. In fact, the standard deviation of the cost function is drastically reduced when the *ATB* is considered as objective; in addition the obtained final geometries are much more similar to each other since both *max(ED) – min(ED)* and *std(ED)* decrease.

4.2 Proposed comparative study

The comparative study between the two radically different design approaches presented in the previous chapter has been performed on a rotor geometry described with 15 parameters. The choice of the geometrical variables to

include in the optimizations has been carried out without having a clear knowledge of the effect of all the geometrical variables on the overall performance. In particular, the selection of the variables describing the iron bridge thicknesses and positions along the barrier could have been different since the advantage and disadvantages of considering a complex iron bridge parameterization are not completely clear. The study presented in the paragraph 3.3.3 gives a general understanding of the influence of some of these design factors on the torque profile and maximum von Mises stress. However such results have a limited generality since the analysis is based on certain assumptions in order to decrease the number of combinations of design factor to evaluate (and so the computational time). In order to investigate the compromise between obtainable electromagnetic performance and number of variables and thus computational time, several rotors showing different geometrical degrees of freedom (*GDOF*) in terms of iron bridge thicknesses and distributions have been structurally optimized considering the same OA and cost function. In other words, only the second step of the physically decoupled design approach will be implemented since this strategy provides better results with a reduced computational time. However, the minimization of the average total bridge per barrier (and not of the stress factor) has been adopted as objective function, since it yields to more reliable results as proved in the previous paragraph. It is worth to repeat that the adoption of the physically decoupled design approach is based on the assumption of the weak influence of the electromagnetic design choice on the structural performance and vice versa. In particular, ideally the final solution obtained with the

structural optimization should modify as little as possible the torque profile. Figure 69 shows the maximum number of variables that can describe the iron bridges of one flux barrier. Five rotors having an iron bridge parameterization described by an increasing number of variables have been optimized obviously keeping the airgap angular position and heights of the flux barriers equal to the optimal values obtained with the electromagnetic optimization.

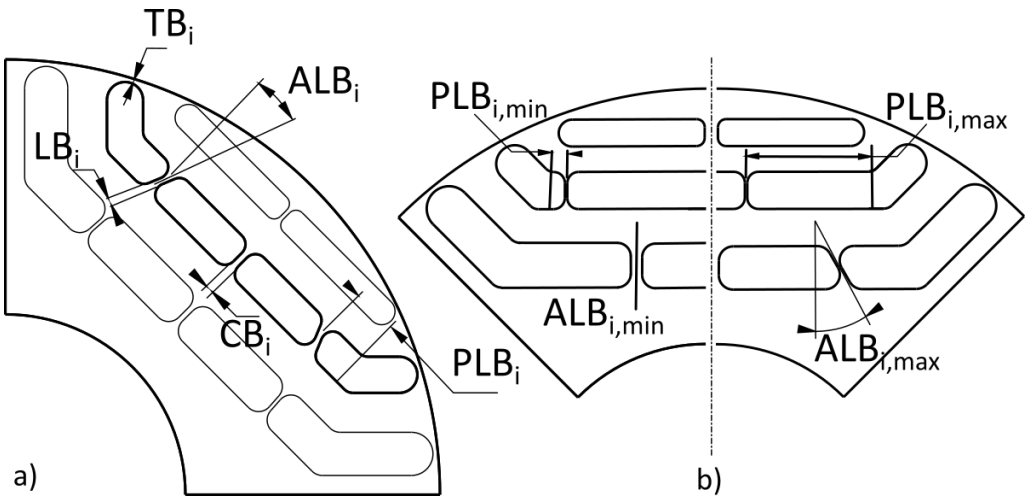


Figure 69: a) iron bridge parameterization, b) upper and lower limits of the position and bending angle of the lateral rib

In particular, the five considered iron bridges parameterizations are described in the following:

- 4 *GDOF* has equal tangential bridge thicknesses TB for all the flux barrier, different central ribs CB_i and do not present the lateral posts LB_i on the second and third barriers; this is the simplest parameterization with only 4 geometrical degrees of freedom;
- 6 *GDOF* features equal tangential bridge thicknesses TB, different central and lateral ribs CB_i, LB_i but the position PLB_i and the bending angle ALB_i of the latter are set to zero; this means that the lateral radial ribs will be

parallel to the q-axis and positioned at the extreme end of the straight part of the barrier;

- 8 *GDOF* can assume whatever value inside the boundaries of the tangential, central and lateral bridges TB_i, CB_i, LB_i, but the position PLB_i and the bending angle ALB_i of the latter are still set to zero; this parameterization correspond to the one used in the previous chapter;
- 10 *GDOF* respect to the previous, has the further possibility of varying the positions of the lateral posts PLB_i inside the defined bounds;
- 12 *GDOF* can additionally present a bending angle of the lateral rib ALB_i bigger than zero and lower than 30 degrees.

The boundaries of the research space are shown in Table 11. The lower boundaries of the radial ribs thicknesses are zero; however they are not inserted in the corresponding barrier if their thickness, generated by the OA, is lower than the minimum iron thickness (0.1 mm). By doing so, only rotor structures that can be easily manufactured are considered during the optimization as it has been done also for the comparative study presented in the previous chapter. Particular care needs to be paid to the selection of the upper limit of the angular position of the lateral iron bridge to be used during the structural optimization. In fact, an extremely high upper bound of such variable would cause the complete loss of proportionality between the average total bridge (*ATB*) and the produced torque as shown with the parametric study presented in the paragraph 3.3.3. The latter analysis has been carried out keeping constant the thickness of the radial ribs therefore the potential reduction of the same rib due

to the relieved value of the maximum stress has not been explored. In order to exploit such possibility without completely losing the proportionality between the average total bridge (*ATB*) and the average torque, an upper limit of the bending angles of 30 degrees has been considered. This value causes a loss of torque of about 2% if the thicknesses of LBs are considered constant as shown in the paragraph 3.3.3. Such value obviously depends also from the considered radius fillet of the barrier's corners. In fact if a smaller value of this radius is adopted, a higher upper bound of ALB can be considered during the optimization.

Table 11: Boundaries of the research space of the structural optimizations

Parameter	**Lower**	**Upper**	**Unit**
$\boldsymbol{TB_{1,2,3}}$	0.1	0.7	mm
$\boldsymbol{CB_{1,2,3} - LB_{2,3}}$	0	0.7	mm
$\boldsymbol{PLB_{2,3}}$	0	1	p.u.
$\boldsymbol{ALB_{2,3}}$	0	30	deg.

Each rotor structure has been optimized carrying out 10 optimization runs (with the DE algorithm) in order to evaluate the repeatability of the results. As the *GDOF* increases, the number of performed functional evaluations has been incremented allowing the algorithm to converge as it will be discussed in the next paragraph. The FE evaluation of the von Mises stress distribution needed to extrapolate the maximum stress and the computation of the objective

function *ATB* requires 8 seconds per rotor (on an Intel Core i7, 3.6 GHz, 16GB RAM).

4.3 Optimization results

The *ATB* evolutions during the optimization of all rotor structures are shown in Figure 70. For each considered rotor geometry, the best and the worst runs have been reported. Analysing the optimization evolutions, the following considerations regarding the trade-off between obtainable performance index (*ATB*) and required functional evaluations can be drawn.

- When moving from a 4 to 6 *GDOF* rotor, it is always possible to achieve a substantial reduction (35-40%) of the *ATB* even with the same functional evaluations. Therefore splitting the radial ribs into two parts placed in the middle and at the extreme end of the straight part of the barrier allows obtaining a lower performance index.
- Comparing 6 with 8 *GDOF* rotors, then to obtain a reduction of 5% or less of the optimization goal, the functional evaluations have to be almost doubled (from 5400 to 10000). Consequently it can be stated that considering tangential ribs with different thicknesses can lead to a weak improvement of the *ATB* at the cost of remarkable increase of the functional evaluations and so of the computational time.
- Going from 8 to 10 *GDOF* rotors, then to assure an additional improvement of 5% (in the best case), the evaluation calls have to be at least increased by

35%; this small improvement can be achieved optimizing also the positions of the lateral ribs.

- A further increment (35%) of the number of functional evaluations, going from 10 to 12 *GDOF* rotors will not result in any improvement. It can be then concluded that optimizing the bending angle of the lateral rib does not lead to any benefit.

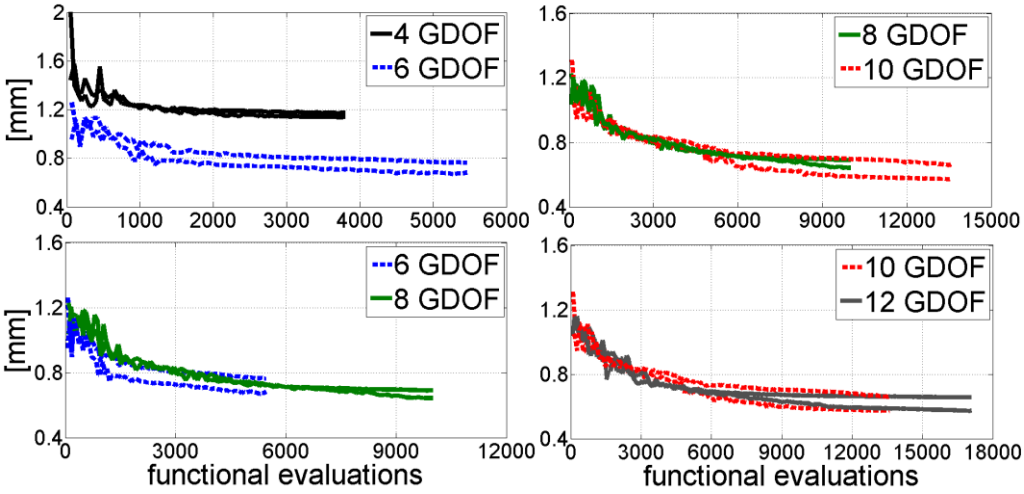


Figure 70: Average total bridge evolutions during the structural optimizations of the 5 considered rotor geometries

It can also be argued that the optimizations of the rotor having 12 *GDOF* could achieve better performance if the number of functional evaluations is increased. However, it has to be considered that one optimization run (of the 12 *GDOF* rotor) shown here was obtained after 38 hours of calculations and the increment of the functional evaluations would have made the computational time impracticable. In addition, it is worth to mention that the results obtainable with the most complex parameterization of the iron bridge do not improve if the lateral bridges are allowed to rotate in a bigger range. For example, if the maximum bending angle is doubled (from 30 to 60 deg.) and

the radius fillet of the barrier corners is properly reduced (from 1/3 to 1/5 of the barrier height) in order to preserve the proportionality between *ATB* and average torque, the range of variation of the optimal average total bridges remains equal to the one obtained with a smaller upper limit of ALB.

4.4 Analysis of the optimized rotor geometries

The improvements of the average torque ΔT (calculated at 150% the rated current) caused by the reduction of the average total bridge ΔATB with respect to the simplest rotor as function of the *GDOF* are shown in Figure 71. Also in this graph the final results of the best and worst optimization runs are reported. Considering the best case scenario for each *GDOF*, it can be deduced that passing from rotor geometries comprising:

- 4 to 6 *GDOF*, then the 41% reduction of *ATB* causes the increment of the mean torque of about 8.6%;
- 6 to 8 *GDOF*, then the additional 5.1% *ATB* decrement leads to another 1.5% torque improvement;
- 8 to 10 *GDOF*, then the extra 9.8% decrement of the *ATB* induces the production of 1.8% more torque;
- 10 to 12 *GDOF*, then there is no change in *ATB* and therefore in the average torque.

Even when considering the worst optimization runs, these considerations are still valid, in fact the improvements of the average torque is remarkable at the

beginning (4 to 6 *GDOF*) and tends to weaken as the *GDOF* increases, until it becomes null for the most complicated rotor structure. Table 12 reports the iron bridge dimensions and the electromagnetic performances for the optimal rotors of each best optimization run while Figure 72 shows their von Mises stress distributions.

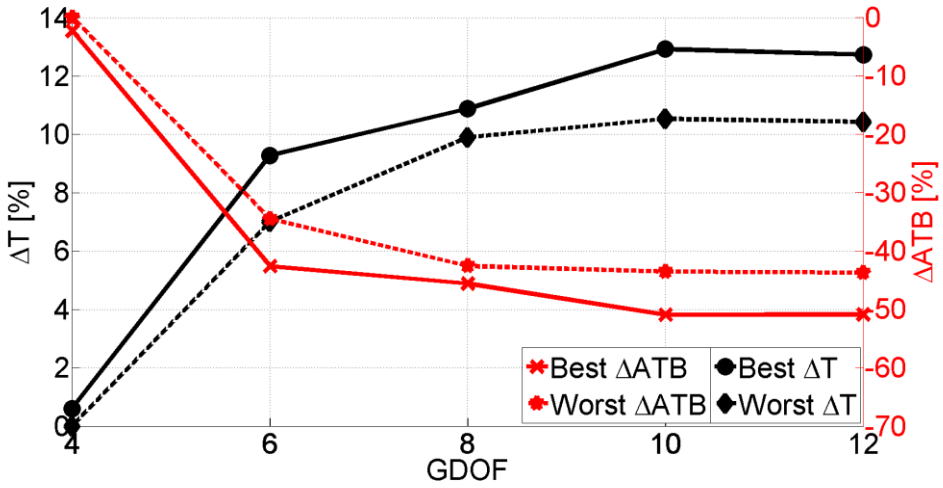


Figure 71: Average total bridge and average torque as function of the geometrical degrees of freedom (*GDOF*) for the best (continuous line) and worst (dashed line) optimization runs

It is worth to underline that passing from rotor with 6 to 8, 10 or 12 *GDOF*, the number of radial bridges (*NRB*) decreases from 7 to 5. In particular, comparing the rotor with 6 and 8 *GDOF*, the latter does not have the lateral ribs on the second barrier but has a bigger tangential bridge (TB_2); furthermore the dimension of LB_3 is remarkably reduced. These changes simplify the rotor construction, especially in case of small rotor bore diameter, because it is preferable to have a reduced number of iron bridges with a larger thickness than more thinner ribs. However this advantage comes at the price of an increased torque ripple with respect to the initial machine.

Table 12: Geometrical parameters and electromagnetic performance of the optimal rotors

	4 *GDOF*	**6 *GDOF***	**8 *GDOF***	**10 *GDOF***	**12 *GDOF***	**Unit**
TB_1	0.48	0.11	0.12	0.11	0.11	mm
TB_2	=	=	0.22	0.10	0.20	mm
TB_3	=	=	0.12	0.15	0.13	mm
CB_1	0.1	0.12	0.12	0.18	0.13	mm
CB_2	0.14	0.13	0.19	0	0.22	mm
CB_3	0.29	0.25	0.28	0	0.25	mm
LB_2	-	0.11	0	0.15	0	mm
LB_3	-	0.33	0.2	0.26	0.12	mm
PLB_2	-	-	-	0.52	0.43	p.u.
PLB_3	-	-	-	0.65	0.08	p.u.
ALB_2	-	-	-	-	11.6	deg.
ALB_3	-	-	-	-	5.2	deg.
ATB	1.14	0.67	0.63	0.57	0.57	mm
NRB	3	7	5	5	5	-
T_m	0.785	0.852	0.865	0.881	0.879	Nm
T_{rip}	1.67	1.37	1.94	1.15	2.5	std %

In fact the torque ripple of the machine without any radial bridges (and all TBs equal to 0.3 mm), which is the output of the electromagnetic design stage, is 1.14% (in standard deviation, std). The more the tangential bridge thicknesses vary from the initial value (0.3 mm), and/or more they differ respect to each other, more the torque ripple changes, as it is for the rotors with 8 and 12 *GDOF* (see Table 12). Differently from the other geometries, the rotors with 8 and 12 *GDOF* do not present tangential bridge thicknesses which increase from the outermost to the innermost barrier. All the optimized rotor share instead increasing central and lateral rib widths going from the outermost to the inner most barrier. Analysing the geometry featuring 10 *GDOF*, it has to be highlighted that the optimal positions of the lateral iron ribs are at 52% and 65% of the respective barrier lengths.

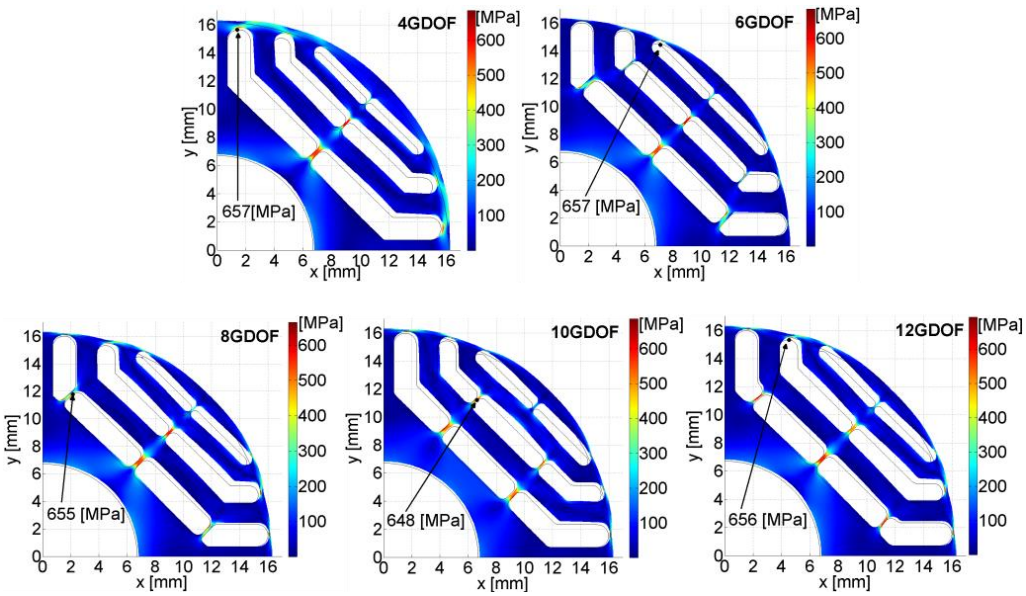


Figure 72: von Mises stress distributions of the optimized rotor geometries with a 1:30 scale for the deformation

This distribution achieves the best performance in terms of average total bridge and therefore electromagnetic torque. Comparing rotors showing 10 and 12 *GDOF*, since they have the same *ATBs* and so electromagnetic torque, it can be deduced more than one optimal geometry exists for a given value of average total bridge per flux barrier. This indicates that the solution of the structural optimization problem, as it has been conceived here, for the rotor having 10 and 12 *GDOF* is not unique. This is also proved by the observation that the optimizations of the rotors with 10 and 12 *GDOF* are more likely to provide a different final geometry, when compared to the optimizations of the rotors having 4, 6 and 8 *GDOF* as it is shown in Table 13.

Table 13: Analysis of the results of 10 structural optimizations performed on the 5different rotor geometries minimizing the average total bridge per barrier: *mean(ATB)* mean of the final *ATBs*, *std(ATB)* standard deviations of the optimal *ATBs*, *max(ED) – min(ED)* difference between the maximum and minimum Euclidean distances calculated respect to the average solution and *std(ED)* standard deviation of the same set of distances.

	GDOF					
	4	**6**	**8**	**10**	**12**	**Unit**
mean(ATB)	1.15	0.7	0.66	0.62	0.62	mm
std(ATB)	0.72	4.7	2.2	5.12	3.75	%
max(ED) – min(ED)	0.067	0.073	0.088	0.407	0.382	mm
std(ED)	0.02	0.024	0.025	0.11	0.11	mm

In fact, even if the standard deviation of the final *ATBs* remains quite low for all the 5 sets of optimizations, the standard deviation of the Euclidean distances (*std(ED),* as also *max(ED) – min(ED)*), which clearly represents how much

different are the optimal rotors, is much bigger for the rotor with 10 and 12 *GDOF* than the others with less degrees of freedom.

All the above lead to the following conclusions.

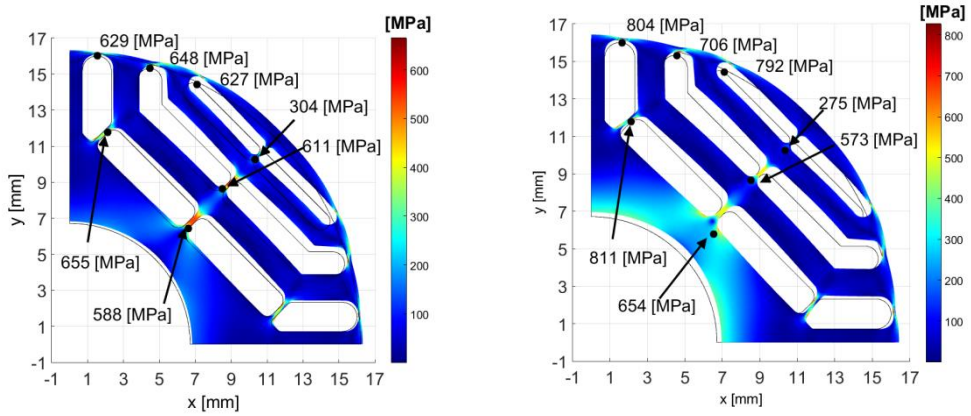
- The best compromise between obtainable performance and required computational time is achieved adopting the geometry with 6 *GDOF*.
- The rotor having 8 *GDOF* is the best trade-off among computational time, performance and manufacturability since it allows the reduction of the number of radial iron bridges.
- The highest electromagnetic torque is given by the rotor having 10 *GDOF*.
- Adopting the geometry with 12 *GDOF* does not bring any further advantages.
- If the positions and the bending angles of the lateral ribs are considered during the structural design, at a given average total bridge corresponds more than one rotor geometry.

4.5 Rotor-shaft coupling influence

Once the rotor geometry has been identified accurately considering both structural and electromagnetic aspects by FEAs, two other issues need to be faced before proceeding with the manufacturing. In particular, the effects on the overall performance of the manufacturing tolerance and the rotor-shaft coupling have to be analysed in detail. An attempt to address the first problem will be presented in Chapter 5 while the second one is investigated in the following. A proper rotor-shaft coupling is required to guarantee the

transmission of the torque and to avoid that the two assembled parts separate from each other at the maximum operating speed [12]. In this case study, the coupling is assured by the well-known method of interference fit which of course causes an additional stress at the mating surface (called interference or contact pressure). This pressure negatively affects the rotor von Mises stress distribution and so the maximum stress; its influence becomes significant as the maximum operating speed increases. In fact, the contact pressure depends on the interference, temperature, dimensions and materials properties of the assembled components. In turn the amount of interference, required to avoid the separation of the rotor from the shaft, increases as the maximum speed rises. It is clear that adopting the interference fit, the maximum stress experienced in the rotor will increase, therefore the dimension of the iron bridges have to be redesigned. The increase of the stresses, due to the interference pressure, in the critical regions of the rotor is not uniform as shown in Figure 73. The latter shows the von Mises stress distribution (and the maximum stress in each rib region) of the optimal solution with 8 GDOF obtained with and without considering the contact pressure. It is evident that the iron ribs of the innermost barrier are more affected by the contact pressure respect to the others. Although the modifications of the iron bridge thickness aimed at bringing the maximum stress below the limit can be done manually (e.g. incrementing all the ribs thickness by a fixed amount or only the ones belonging to the innermost barrier), the final obtained solution might not be optimal anymore. In order to identify the influence on the rotor design due to the interference fit and reduce the risk of obtaining a suboptimal solution,

several structural optimizations have been carried out considering the geometries having 8 and 12 *GDOF* taking into account the contact pressure.



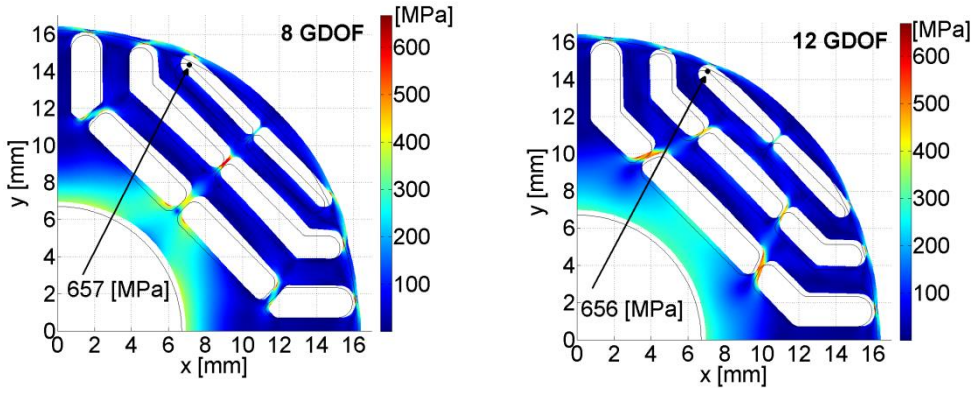
a) b)

Figure 73: von Mises stress distribution of the optimal rotor geometry with *8 GDOF* obtained with b) without a) considering the interference pressure

The calculation of the needed interference and the resulting pressure can be done analytically for simple cylindrical parts [107] while it requires a set of FE simulations in case of non-standard geometry. In this study the interference pressure used during the optimizations has been analytically estimated approximating the rotor as a cylindrical component (i.e. without flux barrier) and then verified by FE for one rotor geometry. It has to be underlined that the amount of interference and so the related pressure can lie with a certain range defined by the imposed manufacturing tolerance of the inner rotor bore and outer shaft diameter. The pressure (calculated at the maximum speed) considered during the optimizations (50 MPa) corresponds to the worst case scenario in terms of interference (so maximum interference). Table 14 reports the iron bridge dimensions and the electromagnetic performances of the best optimized rotor while Figure 74 shows their von Mises stress distributions.

Table 14: Geometrical parameters and electromagnetic performance of the rotors with 8 and 12 *GDOF* optimized with and without considering the interference pressure

	With interference pressure		**Without interference pressure**		
	8 *GDOF*	**12 *GDOF***	**8 *GDOF***	**12 *GDOF***	**Unit**
TB_1	0.17	0.12	0.12	0.11	mm
TB_2	0.26	0.15	0.22	0.20	mm
TB_3	0.18	0.19	0.12	0.13	mm
CB_1	0.11	0.1	0.12	0.13	mm
CB_2	0.15	0	0.19	0.22	mm
CB_3	0.31	0	0.28	0.25	mm
LB_2	0	0.15	0	0	mm
LB_3	0.4	0.28	0.2	0.12	mm
PLB_2	-	0.6	-	0.43	p.u.
PLB_3	-	0.53	-	0.08	p.u.
ALB_2	-	9.6	-	11.6	deg.
ALB_3	-	19.2	-	5.2	deg.
ATB	0.86	0.63	0.63	0.57	mm
NRB	5	5	5	5	-
T_m	0.768	0.813	0.865	0.879	Nm
T_{rip}	1.64	1.28	1.94	2.5	std %



a) b)

Figure 74: von Mises stress distribution of the rotor geometry with a) *8 GDOF* and b) 12 *GDOF* optimized considering the interference pressure

In this case, increasing the number of *GDOF* (from 8 to 12) leads to an improvement in terms of average total bridge per barrier of about 26% which implies an increment of the torque of 6%. Obviously the better electromagnetic performance comes at the price of an increased computational effort. Comparing the final geometries obtained with and without considering the contact pressure during the structural optimization, it can be deduced that optimizing also the positions and the bending angles of the lateral iron bridges allows a remarkable advantage. In fact, the average total bridge of the rotor with 8 *GDOF* is incremented of about 35% while the geometry with 12 *GDOF* requires an *ATB* increment of only 10% in order to sustain the interference pressure and keep the maximum stress at the same level. In particular the optimal position and the bending angles of the lateral ribs of the best rotor structure are respectively 60% and 9.6 deg. for the central barrier and 53% and 19.2 deg. for the most internal one. It is worth to notice that the iron bridge of the optimal rotors obtained considering the contact pressure during the

optimization are completely different respect to the respective solution obtained neglecting the interference pressure. Consequently any attempts to modify the rotor optimized without taking into account the rotor-shaft coupling in order to bring the maximum stress below the limit would most probably lead to a suboptimal solution. Also in this case the repeatability of the optimization results of the rotor featuring 8 *GDOF* is much higher than the geometry having 12 *GDOF* as shown in Table 15.

Table 15: Analysis of the results of 10 structural optimizations performed on the rotor geometries featuring 8 and 12 *GDOF* minimizing the average total bridge per barrier: *mean(ATB)* mean of the final *ATBs*, *std(ATB)* standard deviations of the optimal *ATBs*, *max(ED) – min(ED)* difference between the maximum and minimum Euclidean distances calculated respect to the average solution and *std(ED)* standard deviation of the same set of distances.

	8 *GDOF*	**12 *GDOF***	**Unit**
mean(ATB)	0.88	0.67	mm
std(ATB)	1.67	7.3	%
max(ED) – min(ED)	0.07	0.47	mm
std(ED)	0.02	0.13	mm

In conclusion, considering the effect of the interference fit during the structural optimization, the relationship between the number of geometrical degrees of freedom and the improvement of the average total bridge per barrier is monotonically increasing. It can be therefore stated that better electromagnetic performance can be obtained at the cost of an increased computational time.

4.6 Conclusion

In this chapter it has been shown that the minimization of the average total bridge per flux barrier subject to the constraint on the FE evaluated maximum stress leads to the rotor structure with the highest average torque for a give stress limit. This alternative structural performance index allows achieving a more reliable result when compared to the minimization of the stress factor introduced in the previous chapter. With the aim of evaluating the trade-off between performance and number of geometrical variables (and so computational time), several rotor geometries showing different *GDOF* (in terms of iron bridge thicknesses and distributions) have been optimized, neglecting and considering the rotor shaft coupling influence. Neglecting the interference pressure during the design, as it is normally done in low-medium speed range applications[2], the following conclusion can be drawn.

- As the geometrical complexity (*GDOF*) grows, the improvements of the mean torque is remarkable at the beginning (from 4 to 6 *GDOF*), then tends to weaken (from 6 to 10 *GDOF*) till to becomes null for the most complicated rotor structure.
- The best compromise between obtainable performance and required computational time is obtained adopting the geometry with 6 GDOF which features equals tangential bridge, increasing central ribs from the outermost

[2] In these applications, the transmission of the torque is usually guaranteed by means of rotor-shaft keys configuration or knurling the shaft.

to the innermost barrier and the lateral ones positioned at the extreme end of the straight part of the barrier.

- Adding the possibility of having different tangential bridge widths (i.e. with the 8 *GDOF*) allows reducing the number of radial iron bridges which makes the rotor manufacturing easier especially in case of small rotor OD. However having different tangential rib per barrier negatively affects the torque ripple.
- The highest electromagnetic torque is given by the rotor in which even the placements of the lateral ribs along the straight part of the barrier are optimized.
- If the positions and the bending angles of the lateral ribs are considered during the structural design, at a given average total bridge corresponds more than one rotor geometry. Consequently the solution of the structural optimization problem, as it has been conceived here, is not unique anymore.

When the interference pressure is considered during the structural optimization:

- as the *GDOF* rises, the average total bridge decreases therefore better average torque can be obtained at the cost of an increased computational effort;
- the position and the bending angle of the lateral iron ribs play a fundamental role in the reduction of the maximum stress and so in the minimization of ATB.

According to the comparative study presented in this chapter, the rotor geometry featuring 12 *GDOF* optimized considering the rotor-shaft coupling by interference fit has been selected for the prototyping as it is the best solution both electromagnetic and structural wise. In the next two chapters, an in deep analysis of the performance of the selected solution will be presented. In particular, in Chapter 5 an attempt to analyse the effect of the manufacturing tolerance on the overall performance will be outlined, while Chapter 6 will provide a complete electromagnetic and thermal analysis of the final machine.

Chapter 5
Manufacturing tolerance influences on the machine performance

This chapter aims at analysing the overall performance modifications of the optimized machine caused by phenomena related with the manufacturing processes. These alterations can be ascribed to two main reasons. The first one is related with the geometrical manufacturing tolerances while the second is associated with the change of the magnetic properties of the stator and rotor materials. The latter in turn depends on two factors: the lamination cutting method and its settings and the different mechanical stress condition in which the materials operate when the machine is assembled. All these subjects have been addressed in specialized literature and thus in the following only the problem of evaluating the influence of the geometrical manufacturing tolerances on the performance of a SyR machine is addressed. In Chapter 7, the influence of different mechanical stress conditions on the magnetic properties will be measured with a custom built test setup.

5.1 Introduction

The influence of the geometrical manufacturing tolerances on the performance of an electrical machine depends on the machine topology, its dimensions and obviously the value of these tolerances. The performance indexes to be considered during the evaluation of such influences are determined by the specific design problem and application. The most common electromagnetic measure considered during such analysis is the quality of the voltage waveform for generator applications and the quality of the torque for the motor ones. The dimensions of the machine under investigation, which is mainly defined by the rated torque, indirectly affect this issue. In fact, high speed machines have smaller dimensions compared to lower speed machines rated at the same power. Therefore it can be generically stated that they are more affected by the manufacturing tolerance respect to low speed machine (if the construction tolerance remains constant). The tolerance obviously depends on the adopted manufacturing method. Laminations are traditionally produced by punching or by electrical discharge machining (EDM) or laser cutting. The process settings of the selected procedure (e.g. number of refinement cuts during the EDM, etc.) play a very important role. The minimum tolerances that can be achieved by means of an EDM or by laser cutting lies within the range of $\pm 50\ \mu m$ (the punching method usually provides a wider bound, i.e. much less accuracy). The difficulty of evaluating the manufacturing tolerance influence most of the time is related with the high number of variables needed to describe the machine geometry and the long computational time related with the FE

evaluation of the considered performance indexes. The consequent impressive overall computational time needed to carry out such analysis is the most important practical limiting factor, similar to the multi-physics FE-based optimization described in the last two chapters. There are several approaches with which the manufacturing tolerance influences can be evaluated; they can be discriminated according to the following aspects.

- *How such influence is measured.*

  In fact the robustness of each solution, i.e. its capability to have performance relatively invariant with respect to parameters change, can be defined in different ways. The first measure of the robustness has been introduced by Taguchi [109] which consists in the signal to noise ratio of the objective function calculated for different design factors perturbation combinations chosen using the design of experiment theory. Other measures describing the robustness of the solution comprise the variance of the objective functions or the worst objective function (always calculated on a particularly chosen subset of variables perturbations) or the maximum ratio between the difference of the best and worst objective functions and the distance between these two solutions in terms of design factors [110, 111].

- *How the set of combinations of design variables to evaluate is selected.*

  Since it is computationally impossible to evaluate all the geometrical variables combinations therefore another selection criterion has to be chosen. As mentioned in Chapter 3, one can perform 1) a parametric study addressing the influence of certain design factors or 2) a statistical analysis on the results of a parametric study carried out on a particularly defined

subset of variables. The first one provides more intuitive results having a limited generality while the second gives a more complete understanding of the effects and mutual effects of the design variables.

- *How the design variables are treated.*

  The design factors can be treated as deterministic variables or more correctly as random variables obeying to a certain distribution function reflecting the knowledge about the uncertainties (related with the manufacturing tolerances). By considering the uncertainties of each variable during the analysis ensures that the designed system will perform within the prescribed margin with certain reliability (i.e. with a certain robustness index).

- *When such measurement is carried out during the design process.*

  Once the combinations of design variable to evaluate have been chosen, the calculation of the robustness can be carried out a-posteriori or during the design procedure. In the first case, once the final optimal solutions are obtained, the calculation of the robustness of each design allows selecting the candidate with the best user-defined trade-off among the optimized objectives with a clear knowledge about the robustness of such solution. In the second case, the robustness is not only evaluated but also optimized during the design procedure. Several robust optimization algorithms, i.e. methods considering the uncertainties of each design factor during the optimization, have been presented in literature. This topic is very wide and out of the scope of this work however interested reader may refer to a quite complete overviews presented in [112, 113].

From all the above considerations, it is clear that the problem of evaluating the possible influence of the manufacturing tolerances on the performance of an electrical machine can be faced in various ways and several works have been presented in literature. For example, in [114, 115] the influence of the rotor manufacturing tolerance on the cogging torque and bemf of a permanent magnet synchronous machine is analysed via the design of experiment and robustness index introduced by Taguchi. An interesting attempt aimed at investigating the influence of small geometrical variations on the torque ripple of SyR machines has been presented in [84]. The authors perform a stochastic optimization of a three flux barriers rotor geometry minimizing the torque ripple by acting only on the airgap angular position of the barriers. Once the final set of optimal solutions is obtained, a sensitivity analysis is carried out directly from the data generated from the optimization process without requiring any additional functional evaluations (and so no further computational cost).

5.2 Proposed sensitivity analysis

In the following paragraph, the results of two analyses will be presented. The first one consists of a simplified FE parametric study that independently addresses the effect of each design factor on the structural and electromagnetic performance of the optimal geometry. In particular the influence on the torque profile and on the maximum stress of the variation of iron bridge thicknesses

and flux barrier heights due to the manufacturing tolerances will be investigated. This analysis is useful to verify the need of any final modification of the rotor geometry before the real manufacturing in order to be on the safe side in the worst possible condition. The second one comprises a more comprehensive sensitivity analysis carried out generalising the approach presented in [84]. In particular the evaluation of a robustness index is performed on the results obtained from the two-objective multi-physics optimization presented in Chapter 3. Although this approach is not the completely exact [111], it gives a satisfactory notion of the sensitivity of the evaluated solutions to small geometrical variations. It has to be underlined that the manufactured rotor has not been designed applying the two-objective multi-physics approach whose results are used here to implement the sensitivity analysis. In addition the manufactured rotor geometry is described by a higher number of geometrical parameters compared to the one optimized with the multi-objective approach. Even though the results of the sensitivity analysis are not directly applicable to the built rotor, they are useful to draw general conclusions about how small perturbation of the geometry can affect the torque profile and the maximum stress.

5.3 Sensitivity analysis carried out by a simplified parametric study

Starting from the rotor designed with the physically decoupled approach considering the interference pressure, a simple sensitivity analysis on the

dimension of the iron ribs and barrier thicknesses is carried out with the aim of identifying the maximum impacts on the performance of their possible deviations due to the manufacturing tolerance. To do so, the analysis is performed by varying the iron bridges and the barrier radial thickness in positive or negative directions of a quantity equal to the tolerance (i.e. 50 [μm]). The deviations of the iron bridge thickness are implemented first on all tangential ribs, then on all radial ones and finally on both of them in order to assess a possible different effect on the structural and electromagnetic performance. Figure 75 reports the variations of the maximum stress, average torque and torque ripple (calculated in the rated current condition at MTPA) for ribs deviations in the range $-50 \div 100$ [μm].

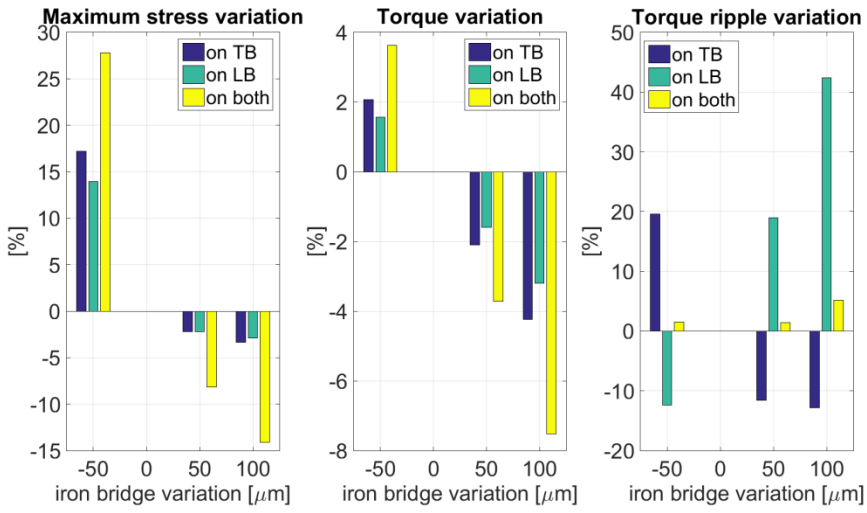


Figure 75: Maximum Von Mises stress, average torque and torque ripple variations (respect to the optimized machine performance) due to positive and negative deviations of the iron bridge dimensions

From the structural point of view, a certain iron bridge deviation produces the same changes of the maximum stress wherever the deviation is allocated on the tangential (*TB*) or on the radial (*LB*) rib (obviously this observation may

change according to the selected optimal solution). However the same deviation of iron ribs produces different changes on the maximum stress whether it is a reduction or an increment. In particular a reduction of the iron bridges causes a stress modification more than three times respect to an increment of the same amount (this behaviour tends to remain the same for all the optimal solutions). The influence of the iron ribs variation on the average torque is linear, symmetric and almost independent whether the variation is allocated on tangential (*TB*) or lateral ribs (*LB*). In fact, a positive or a negative deviation of all the iron bridges of 50 [μm] cause an average torque change of about 4%. The torque variations caused by the deviation of the iron bridge thicknesses are (obviously) mainly due to the change in the d-axis flux linkage as reported in Figure 76. The latter outlines also the deviation of the q-axis flux linkage which is clearly much lower than the d-axis one.

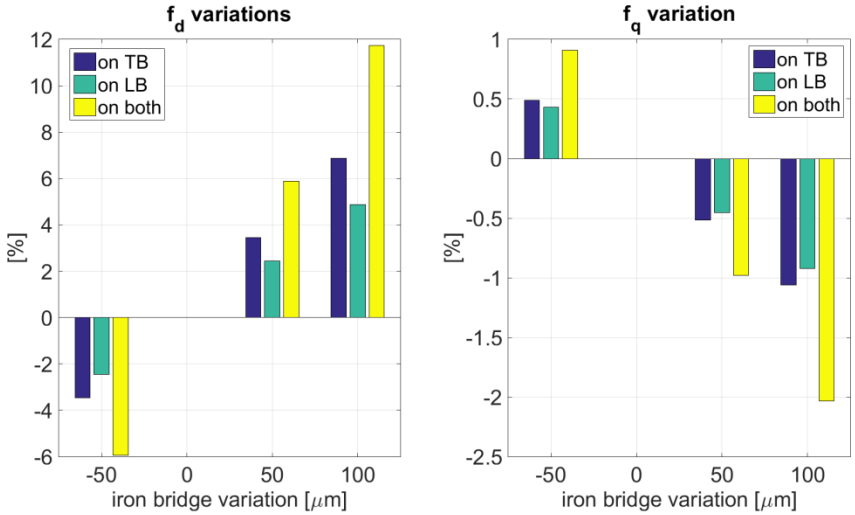


Figure 76: d- and q-axis flux linkage variations (respect to the optimized machine performance) due to positive and negative deviations of the iron bridge dimensions

The torque ripple is more affected by the alterations of the iron bridge as shown in the rightmost graph of Figure 75. In particular, deviations of the tangential and radial ribs or both of them cause a different torque ripple changes. Such change is also potentially much higher than the average torque one.

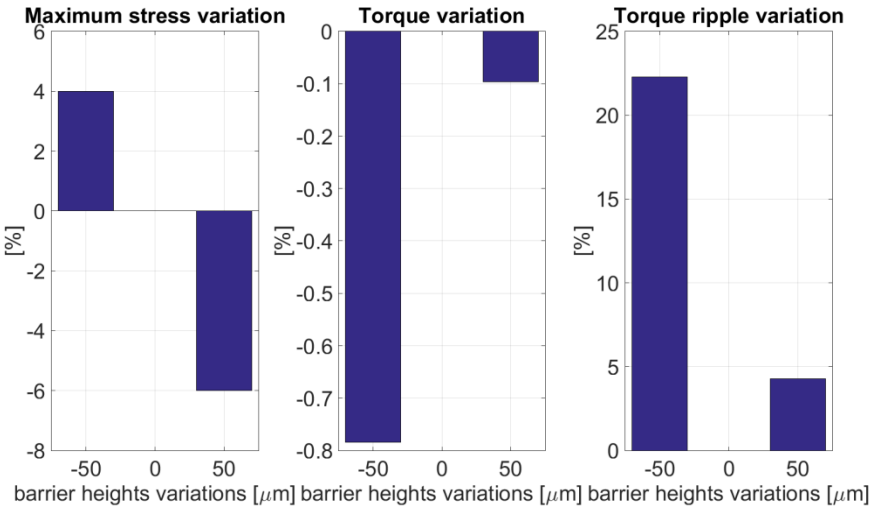


Figure 77: Maximum Von Mises stress, average torque and torque ripple variations (respect to the optimized machine performance) due to positive and negative deviations of the barrier thicknesses

Figure 77 illustrates the structural and electromagnetic performance changes caused by the positive and negative barrier thickness deviations of 50 [μm]. It is clear that the average torque is almost not affected by such deviations while the torque ripple is much more influenced being its change of about 20% in case of 50 [μm] decrement of the barrier thickness. Figure 78 reports the variations of the d- and q-axis flux linkages due to the deviations of the barrier heights; at the MTPA and rated current condition, a barrier thickness change influences more the d-axis flux than the q-axis one.

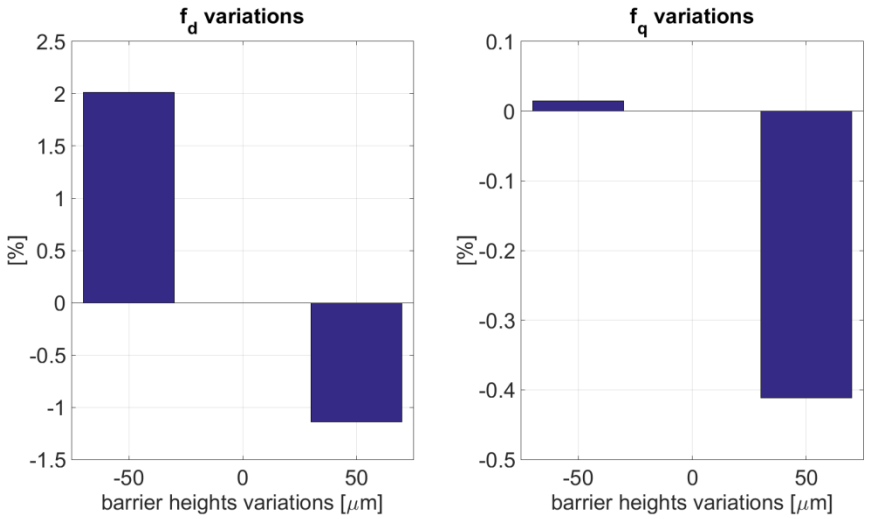


Figure 78: d- and q-axis flux linkage variations (respect to the optimized machine performance) due to positive and negative deviations of the barrier thicknesses

The maximum stress is affected less by small barrier heights variation respect to the same modification of the iron bridges. All the above considerations lead to the need of incrementing all the iron bridge thicknesses of an amount equal to the manufacturing tolerance ($50\,[\mu m]$) when the selected rotor is prototyped. Such final adjustment is necessary in order to not exceed the maximum stress limit (i.e. 80% of the yield strength of the rotor material) also in the worst case. The latter obviously consists in an unlikely reduction of all iron bridges of $50\,[\mu m]$ which would cause an increment of about 25% of the maximum stress. Incrementing all the iron bridge dimensions of the built rotor understandably cause a decrement of the rated performance of about 4% in terms of average torque.

5.4 Sensitivity analysis carried out on the multi-physics optimization results

The aim of the multi-objective stochastic optimization algorithm (MOOA) is to individuate the Pareto optimal solutions among all the individuals generated during the search as explained in Chapter 3. If the MOOA does not prematurely converge to suboptimal solutions, the part of the research space having the best objective functions is properly represented in the whole set of individuals evaluated during the optimization. This essentially means that the part of the objective space where the Pareto front is located is particularly dense, so it is reasonable to use this data to carry out a sensitivity analysis assessing the robustness of each solution to small perturbations of the design variables. Figure 79 reports the objective functions of all rotor candidates evaluated during the multi-physics rotor optimization in which average torque and torque ripple have been optimized with a constraint on the upper limit on the FE evaluated maximum Von Mises stress. It is clear that the region surrounding the Pareto front is much denser than the other part of the fitness space. Therefore part of these data (shown in the inset of the same figure) will be used to carry out a sensitivity analysis having the aim of addressing how torque ripple, average torque and maximum stress are affected by small geometrical variations.

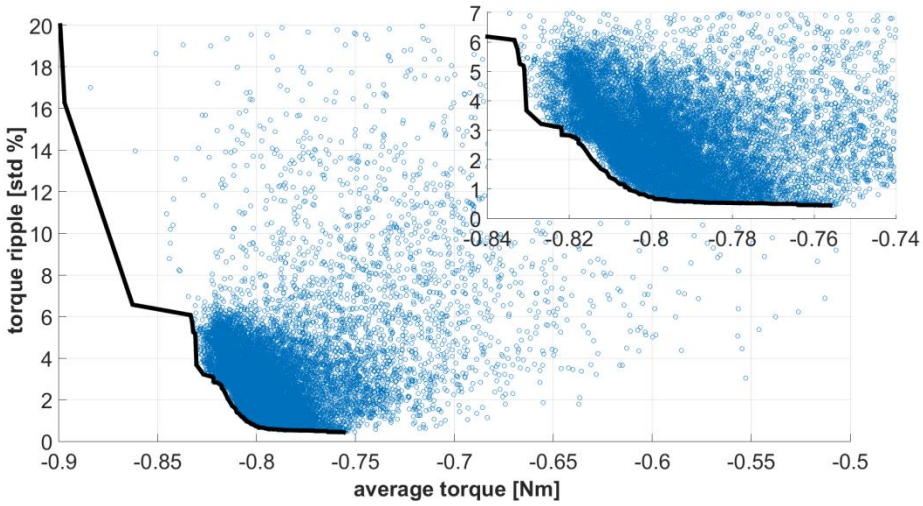


Figure 79: Objective functions of all the evaluated candidates during the multi-physics optimization of the rotor geometry (in which average torque and oscillation are optimized with the upper constraint on the FE calculated maximum Von Mises stress)

Each solution is described by 14 geometrical parameters (3 airgap angular positions and 3 heights of the barriers and 8 iron bridge thicknesses) defining the vector $\overrightarrow{x_i}$, its fitness function $\overrightarrow{y_i}$ (torque and ripple), and the value of the constraint g_i (i.e. the maximum von Mises stress). The first step of the sensitivity analysis consists in searching for each $\overrightarrow{x_i}$ solution its neighbours, i.e. all the solutions $\overrightarrow{x_j}$ whose components deviate from the relative components of the solution $\overrightarrow{x_i}$ for a maximum value defined by the manufacturing tolerances. Although this approach is the most correct from the practical point of view, it does not allow quantifying the distance between two solutions. There are several metrics that can be used to describe the distance between two generic n-dimensional vectors [116]. The most obvious one is the generalized n-dimensional version of the Euclidean distance, defined as:

$$ED(\overrightarrow{x_i}, \overrightarrow{x_j}) = \sqrt{\sum_{k=1}^{n} [x_i(k) - x_j(k)]^2} \tag{39}$$

where $\overrightarrow{x_i}$ and $\overrightarrow{x_j}$ are two generic solutions. However the components of $\overrightarrow{x_i}$ are on a completely different scale of measurements (some are angles in degrees and some other are thicknesses in mm), therefore the bigger values will dominate in the calculation of the distance. To overcome this problem, some form of standardization is necessary to balance all the contributions; the conventional way of doing it is to transform the components of $\overrightarrow{x_i}$ so they have all the same variance equal to one. To do so, each component difference is weighted by the inverse of the standard deviation calculated for each pair of respective component; the consequent standardized Euclidean distance is:

$$SED(x_i, x_j) = \sqrt{\sum_{k=1}^{n} \frac{[x_i(k) - x_j(k)]^2}{std([x_i(k); x_j(k)])^2}} \tag{40}$$

In the following, the neighbours of each solution $\overrightarrow{x_i}$ are calculated according to the standardized Euclidean distance which allows removing the effect of having components with different scale. In particular, for a given vector $\overrightarrow{x_i}$, the solutions having a SED respect to $\overrightarrow{x_i}$ lower than a fixed threshold SED_{lim} are considered neighbours; this limit is proportional to the maximum deviations caused by the manufacturing tolerances. Once the neighbours of each i-th solution are identified, the neighbour having the biggest rate of change of the performance under consideration y (in this case average torque or torque ripple

or maximum stress) can be individuated; consequently one way of defining the sensitivity of the i-th solution considering only the worst case scenario is:

$$S_y(x_i) = max\left(\frac{y_j - y_i}{y_i}\right) \cdot 100, \forall\, j \mid SED\left(\overrightarrow{x_i}, \overrightarrow{x_j}\right) < SED_{lim} \qquad (41)$$

Figure 80, 81 and 82 report the torque ripple, average torque and maximum stress sensitivity calculated according to (41) using part of the solutions evaluated during the multi-physics optimization and an upper limit of the standard Euclidean distance SED_{lim} approximately equal to the manufacturing tolerance. In particular each figure includes the sensitivity shown by the coloured scale of all solutions in the average torque – torque ripple plane and the distribution of the sensitivity for discrete range of the torque ripple and average torque. The sensitivity of the torque ripple clearly tends to dramatically increases as the torque ripple decreases as shown in Figure 80a. In fact the number of solutions more robust to small parameter variation decreases as the torque ripple decreases while the one less robust increases as reported also Figure 80b.

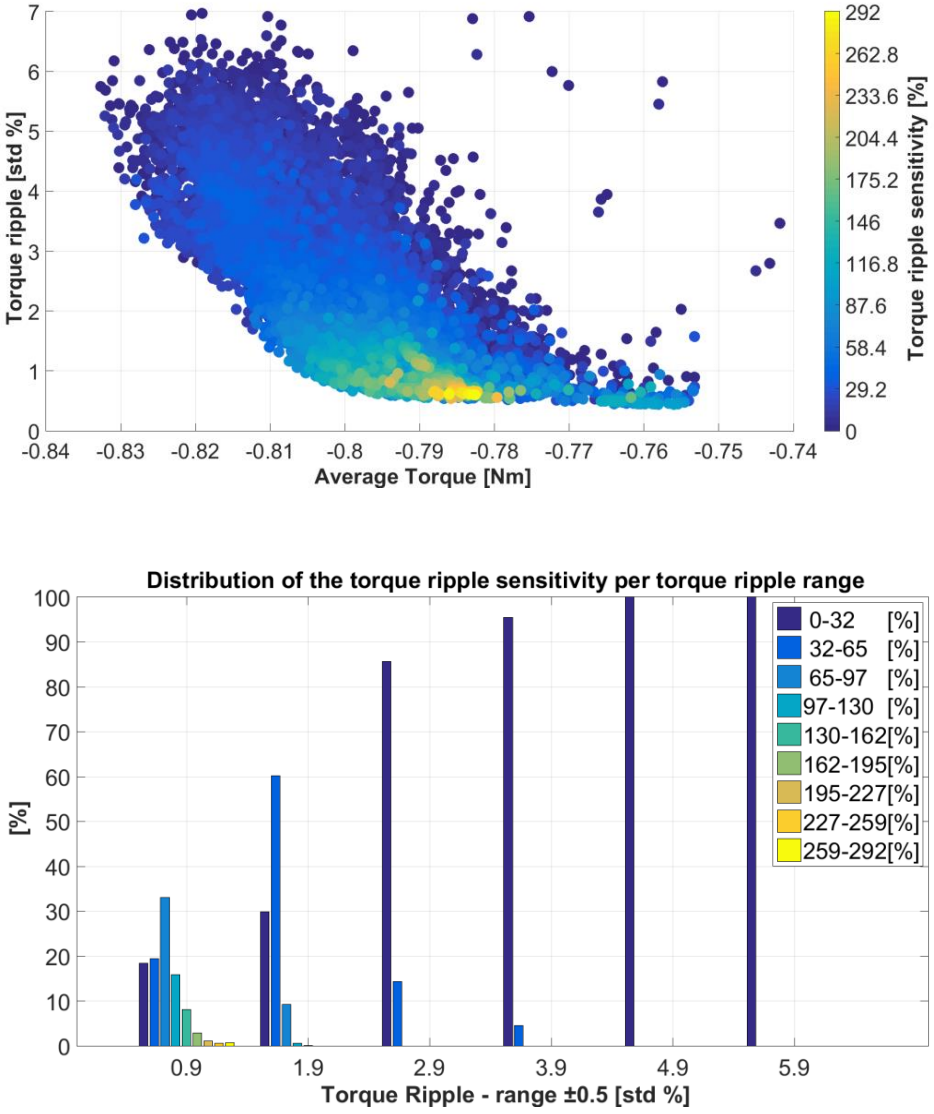


Figure 80: Torque ripple sensitivity a) in the average torque - torque ripple plane and b) its distribution for discrete range of torque ripple

This result generalizes and confirms the considerations reported in [84], that is the optimal solution torque ripple wise is more likely to be less robust to small deviation of the geometrical parameters. In the worst case scenario the torque ripple can become almost three times the expected value. The sensitivity of the average torque presents a similar behaviour, i.e. the solutions having the

highest torque are more likely to be less robust to small parameters variations caused by the manufacturing uncertainties as shown in Figure 81.

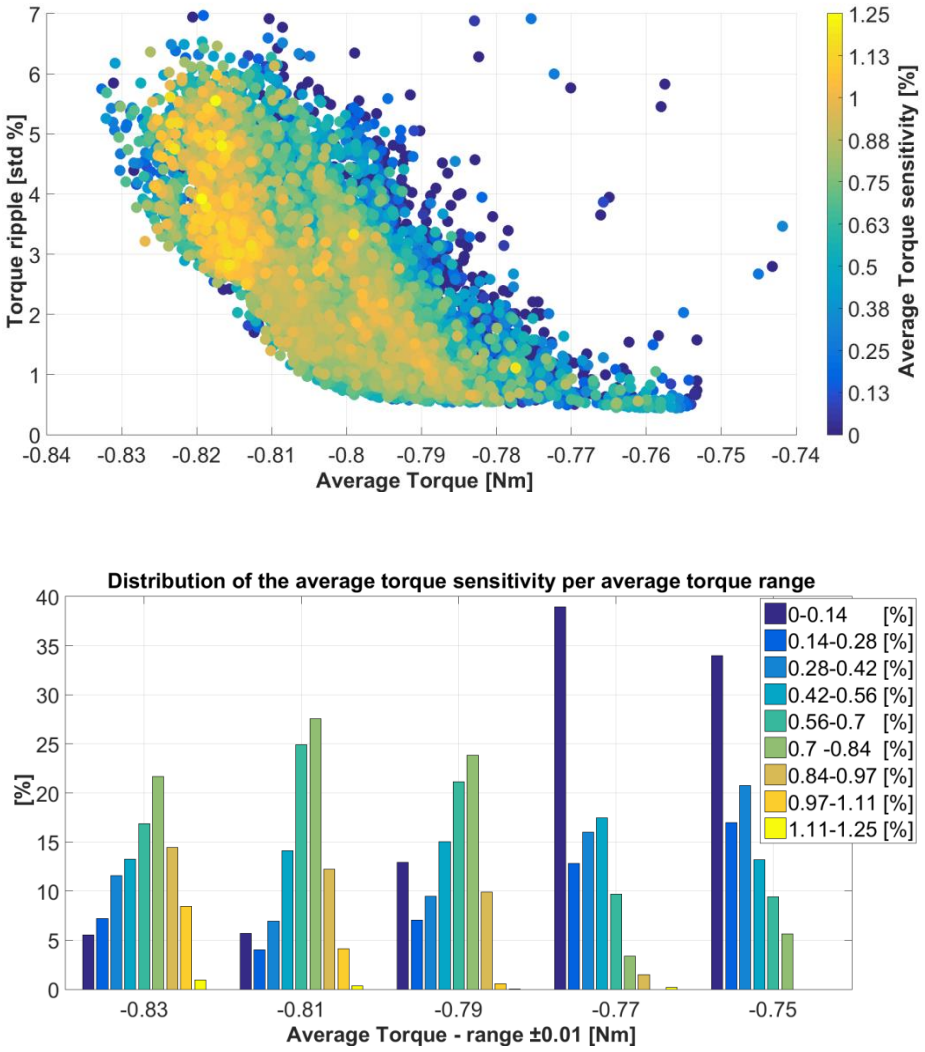


Figure 81: Average torque sensitivity a) in the average torque - torque ripple plane and b) its distribution for discrete range of average torque

However the average torque in the worst case decreases of about 1.25% which is more than two orders lower than the worst torque ripple change. The sensitivity of the maximum stress shows the same behaviour of the average torque one, i.e. solutions having the highest torque are more prone to be less

structural wise robust respect with candidates with a lower torque as reported in Figure 82.

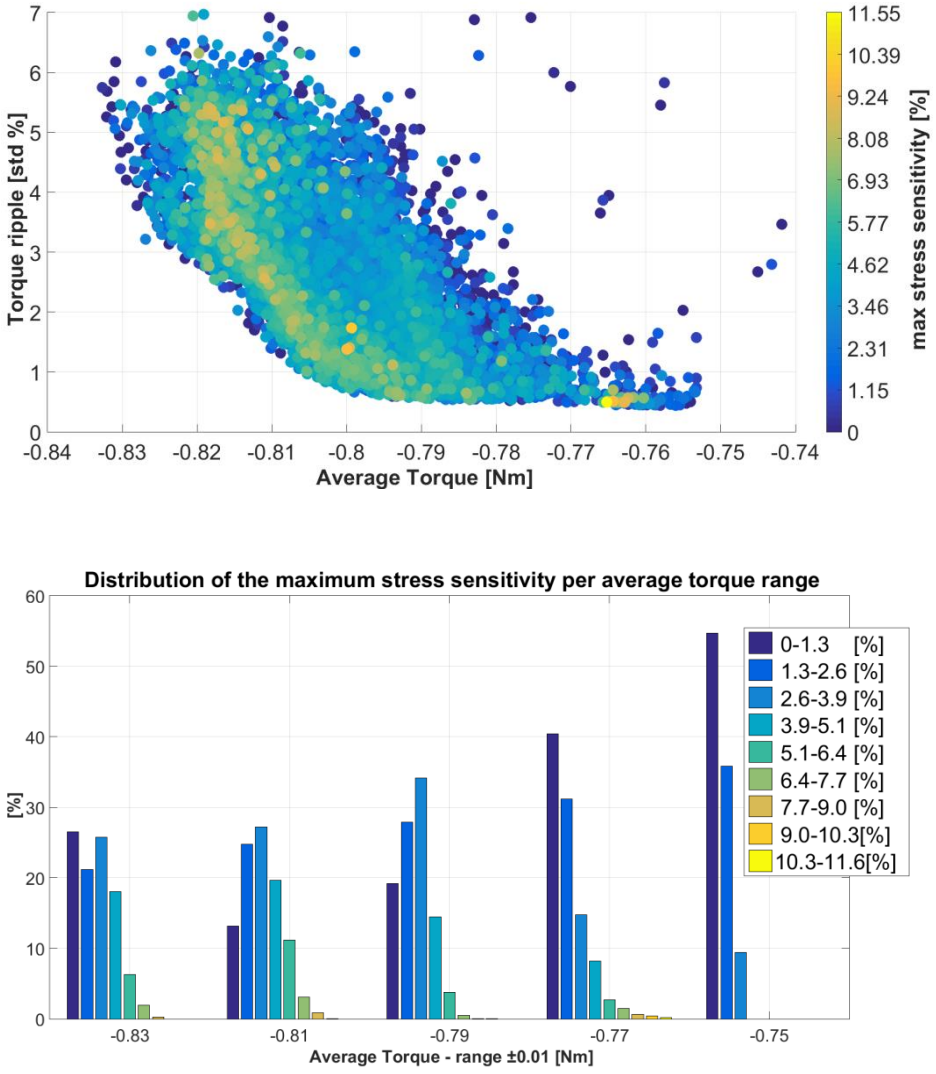


Figure 82: Maximum stress sensitivity a) in the average torque - torque ripple plane and b) its distribution for discrete range of average torque

This can be intuitively explained by the fact that rotors with the highest torque most probably have thinner iron bridges which are more sensible to small deviations. In the worst case scenario the maximum stress increment is about 11%. Considering all the above it can be concluded that:

- the most affected performance index by small geometrical deviations is the torque ripple;
- the maximum stress increment in the worst case scenario is an order lower than the ripple one;
- while the average torque is the performance index less influenced.

These observations are also confirmed if a different upper limit of the standardized Euclidean distance SED_{lim} is considered as shown in Figure 83. This threshold distance also corresponds to the radius of the hypersphere which contains all the neighbours of the solution located at the centre of the hypersphere. The latter figure reports the sensitivity of torque, ripple and maximum stress as such radius increases. As just mentioned the torque ripple is much more affected by small deviations of the optimal geometry while the average torque is influenced much less.

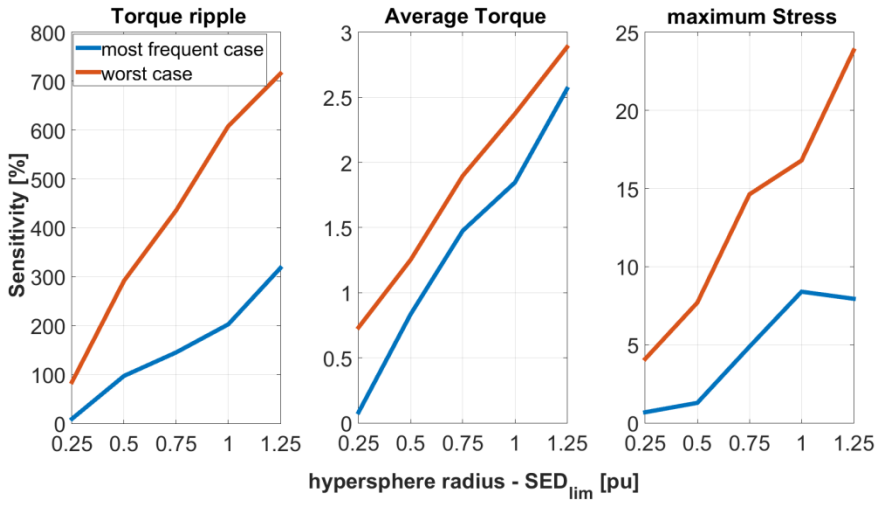


Figure 83: Sensitivity of the torque ripple, average torque and maximum stress as the limit of the standardized Euclidean distance defining the neighbours of each solution increases. The most frequent and worst cases are reported in the lowest torque ripple range. The previous three figures correspond to a $SED_{lim} = 0.5\ [pu]$

5.5 Conclusion

The analyses presented in this chapter clearly prove that the geometrical manufacturing tolerances can heavily affect the torque ripple while the average torque is the least affected performance index. In particular both analyses show that the average torque variations lie within the range of few percent (maximum 5%) while the torque ripple deviations can reach also 300% in the worst case scenario. Regarding the maximum stress, its percentage worsening is intermediate between the torque ripple and the average torque one (i.e. ~10%). The sensitivity analysis carried out on the results of the two-objective multi-physics optimization shows that whatever *p* performance index is considered (e.g. torque, ripple, and stress) if an optimal solution *p*-wise is selected then the *p* performance of such solution is more likely to be the least robust to small deviation of the geometrical parameters. Namely the optimal solution *p*-wise does not correspond to the most robust solution *p*-wise. Considering what it has been shown in this chapter regarding the worsening of the performance due to the manufacturing tolerances, it is clear that the selected optimal solution has to be slightly modified before the real manufacturing. In particular the iron bridge thicknesses have to be incremented by an amount equal to the maximum possible deviation due to cutting tolerances. Such modifications are needed in order to not exceed the maximum stress limit also in the worst and unlikely case scenario of maximum decrement of all the iron bridge thicknesses. The next chapter will give an in-detail

analysis of the electromagnetic and thermal performance of the optimal machine having all the iron bridge dimensions incremented by 50 [μm].

Chapter 6
Performance of the optimized machine

Following the electromagnetic and structural design presented in the previous chapters, in the following an in-detail analysis of the thermal and electromagnetic performance will be given. First the calculation of the several loss components is outlined and then the temperature distribution of the optimized machine in steady state condition will be estimated using a lumped parameter thermal network. The identification of the maximum temperature is required to determine the minimum flow rate of the cooling liquid and to establish the thermal limitation of the optimal machine for a given cooling and winding insulation systems. The last paragraph summaries the overall thermal and electromagnetic performance of the optimal machine.

6.1 Power losses calculation

In the following subparagraph the calculations of the copper losses both dc and ac components, the iron losses and the airgap friction losses are described in details. Both copper and airgap friction losses are function of the temperature of the related components (copper and airgap air); however in the next paragraphs all of them are shown at room temperature. The obtained losses constitute the initial values used in the lumped parameter thermal network which estimates the temperature distribution and update the losses value to the correct temperature with an iterative procedure.

6.1.1 Copper losses

The winding details are defined according to classical electromagnetic consideration [79]. In particular, the number of turns of the adopted winding configuration (24 slots/4 poles with a short pitch of 5/6) has been chosen considering a DC link voltage of 540 V (with a maximum fundamental voltage obtained without any third harmonic injection). The base speed has been selected equal to the maximum operating speed therefore the designed machine will always operate in the constant torque region. Once the winding details are defined, it is a common practice to subdivide each conductor into a number of smaller parallel connected sub-conductors (also called strands). This approach is essentially adopted in order to limit the skin and proximity losses caused by

the uneven current density distribution within each conductor in the slots while keeping a high slot fill factor. However the adoption of stranded conductors could potentially lead to an uneven distribution of the currents between the strands; this phenomenon, called circulating currents effect, causes an additional component of the AC copper losses. This component is highly dependent on the positions of the strands inside the slot which for random-wound winding cannot be controlled. Several measures can be implemented with the aim of limiting the circulating current losses such as the transposition of the conductors (carried out within the slot or in the end winding region) and the adoption of Litz-type wires. Both these solutions allow decreasing the circulating current losses but also slightly compromise the performance at lower frequency due to the increased winding length and lower slot fill factor. The calculation of the skin and proximity component of the AC copper losses can be addressed by analytical means as reported in numerous books [79, 117, 118]. On the other hand the determination of the circulating current component of the AC copper losses requires more effort as this phenomena is strictly related to the real positions of the strands inside the slot. Several works have been recently presented in literature which try to calculate the circulating currents both by analytical method (essentially based on circuital approach) and brute-force FE study [119-121] mainly focusing on concentrated winding configuration. However only the study reported in [122] provides the circulating current losses as function of the frequency with a certain degree of variation due to the random positions of the strands within the slot for a distributed winding configuration. In the following, a simple FE simulation of

the final winding arrangement (featuring 14 conductors per slot and 15 strands per conductor) has been carried out in order to estimate the dependence of the copper losses with the frequency. The results of this kind of FE study obviously depends on the simulated positions of the strands within the slots which do not take into account the real random strands locations; therefore the following results can only provide a general understanding of the phenomena. Figure 84a reports the FE model used to estimate the AC copper losses and the first strand of each conductor of the phase A are highlighted. Figure 84b shows the current density distribution obtained considering the strand as solid components so to simulate the "real" scenario. In fact, it can be noticed the uneven distribution of the current density within each strand and between strands; therefore both skin/proximity and circulating current loss components are present.

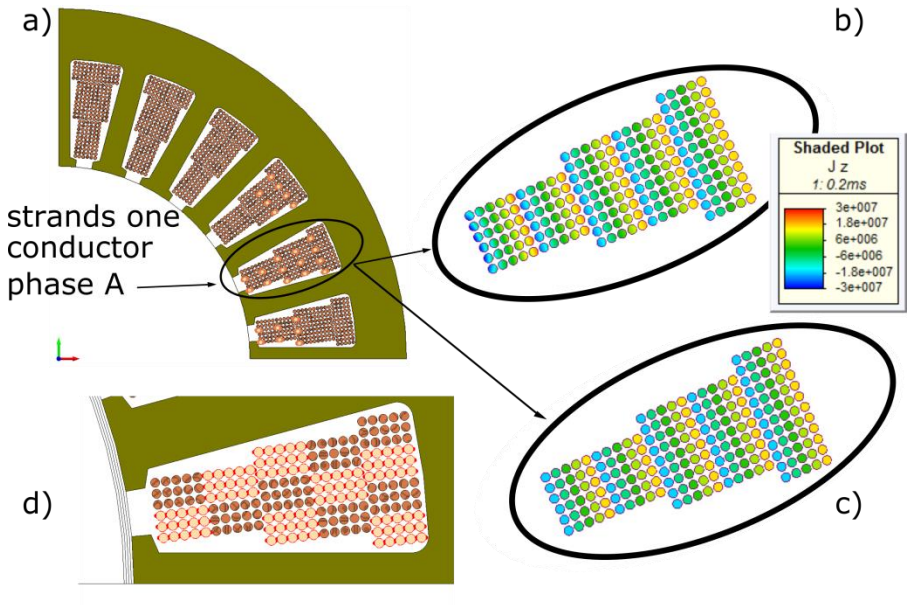
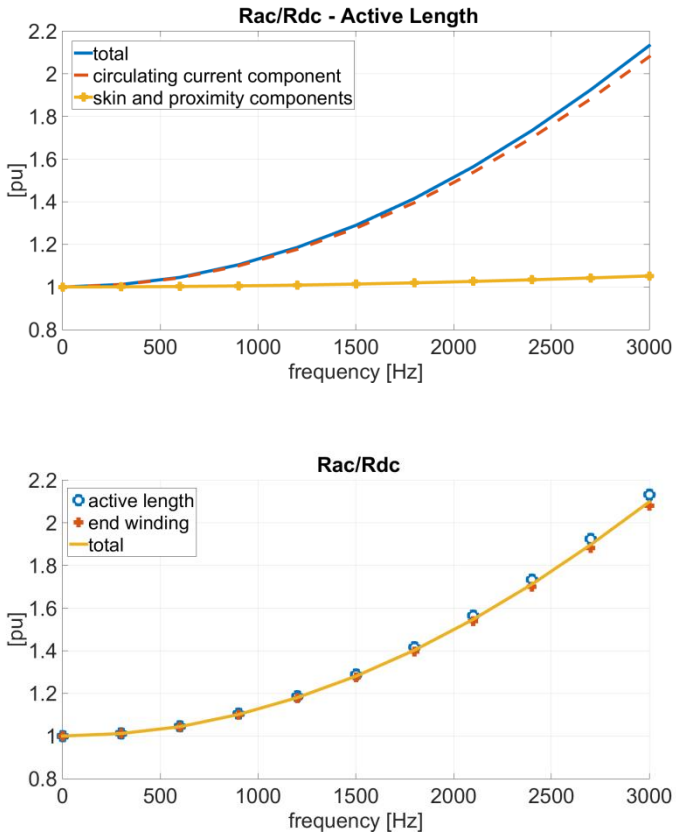


Figure 84: a) FE model implemented to estimate the AC copper losses, b) current density distribution with a phase current of 12 A_{pk} and 2500Hz, c) detailed current density distribution within the conductor of one slot, d) placement of the bundles

The inset c reports the current density distribution obtained considering each strand not as a solid conductor therefore neglecting the skin/proximity loss component (in fact note that the current density within each strand is constant). Figure 85 outlines how the ratio between the AC and DC resistance (called resistance factor R_{ac}/R_{dc}) of the winding portion included in the lamination stack varies with the frequency due to both AC copper loss components. As previously mentioned the subdivision of each conductor into several strands drastically reduces the skin and proximity losses but can also remarkably increase the circulating current loss.



a)

b)

Figure 85: Resistance factors components as function of the frequency: related to a) winding portion included in the lamination stack (active length) and b) the whole phase winding (i.e. including the end winding part)

The proximity and skin effect in the end winding can be definitely considerable negligible while the circulating current loss obviously takes place also in that region [117]. For this reason the total resistance factor lies between the resistance ratio of the active length and the one related with the end winding (which is simply considered equal to the component in the stack due to the circulating current). Figure 86 reports the constant loci of the copper losses in the speed-torque plane. This graph has been realized using the resistance factor calculated with the above mentioned study and considering for each current its maximum obtainable torque (so in MTPA condition).

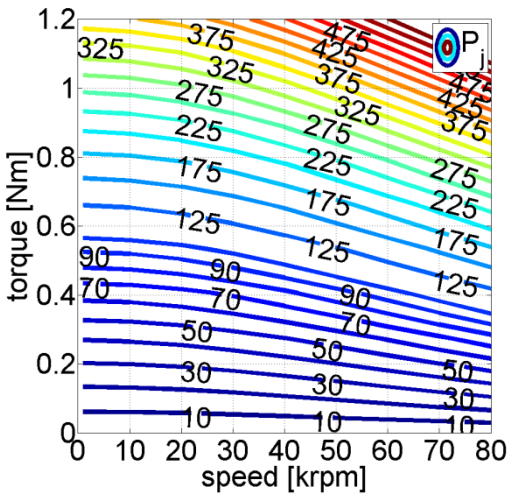


Figure 86: Constant copper loss loci [W] in the speed-torque plane

6.1.2 Iron losses

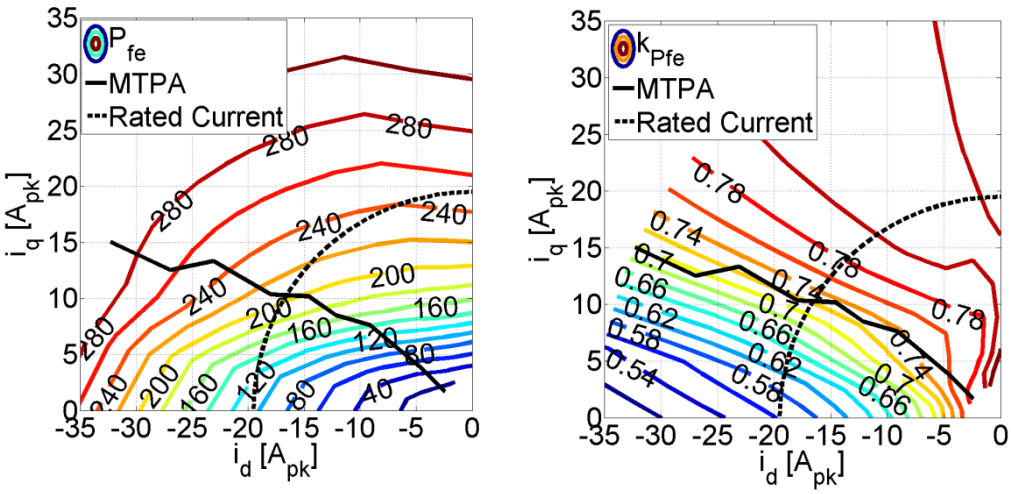
Most electromagnetic FE software neglect the hysteresis phenomena during the evaluation of the field distribution, i.e. they use a single BH curve for both

magnetization and demagnetization phases of the magnetic material. A direct consequence of this ploy, needed to simplify the FE implementation, is the difficulty of estimating the iron losses being the area enclosed by the implemented BH curve equal to zero. With the aim of evaluating the iron losses, most of the software carry out the fast Fourier transformation of the flux density in each FE mesh element (obviously function of the time). The peak values of the flux densities for each frequency are then used to estimate the iron losses of each FE element by means of a closed form expression. Several formulations of the iron losses as function of the frequency and field density have been proposed in literature [123]. The most common one is the modified Steinmetz equation; the latter has two terms: the first one represents the hysteretic and excess iron losses components p_h while the second one includes the eddy current phenomena p_{edd}:

$$p_{fe} = p_h + p_{edd} = k_h \cdot f^{\alpha} \cdot B^{\beta} + k_e (f \cdot B)^2 \; [W/kg] \qquad (42)$$

The values of the coefficients k_h, k_e, α, β are determined fitting the measured data provided by the manufacturer in the form of losses-frequency diagram for different peak flux densities B. It is clear that the accuracy of this method in the evaluation of the iron losses is strictly related with the considered input data. These measurements are usually obtained under sinusoidal flux density and ideal mechanical conditions. Consequently the losses estimated with this approach differ from the real ones for several reasons, such as non-sinusoidal flux density variation, mechanical condition different from the one in which the measurement has been carried out, influence of the cutting and assembling

process, etc. For these reasons, it is a common practice to multiply the obtained iron losses by a factor bigger than two in order to cope with its possible deviation from the expected value (in this study a factor of 2 has been adopted). The iron losses have been calculated at the maximum operating speed (80 krpm) over a grid in the d-q current plane[3] as reported in Figure 87a in which also the MTPA trajectory and the rated current circle are highlighted. Figure 87b shows the distribution ratio between stator and rotor losses at the same speed ($k_{fe} = Pfe_{stator}/Pfe_{total}$).



a) b)

Figure 87: a) Constant total iron losses loci [W] at 80 krpm in the d-q current plane, b) constant loci of the ratio between stator and total losses in the d-q current plane

[3] **It is opportune to mention that in this chapter and in the next one a different d-q axis convention has been adopted respect to the results shown in Chapter 2. In particular, the convention of the axis positions usually adopted for non-salient synchronous machine is considered; the two reference systems are just rotated respect to each other of 90 degrees.**

At the MTPA condition the stator iron losses constitute almost the 75% of the total iron losses while in the flux weakening zone (so near the d-axis) the weight of the rotor iron losses becomes more important. In order to extrapolate the losses at all speeds, a simplified model presented in [124, 125] has been implemented. The latter makes the assumption that the frequency of the flux density variations in the different part of the machine is proportional to the synchronous speed. With this statement in mind, being f_0 the simulated frequency, the iron losses at the generic frequency f can be calculated as:

$$P_{fe}(f) = P_h(f_0)\left(\frac{f}{f_0}\right)^{\alpha} + P_{edd}(f_0)\left(\frac{f}{f_0}\right)^{2} \tag{43}$$

It has to be underlined that in the case under study, the equation (43) has been independently applied for stator and rotor iron losses being their material different from each other (and obviously their Steinmetz coefficients). Figure 88 shows the constant loci of the iron losses at the MTPA condition in the speed-torque plane.

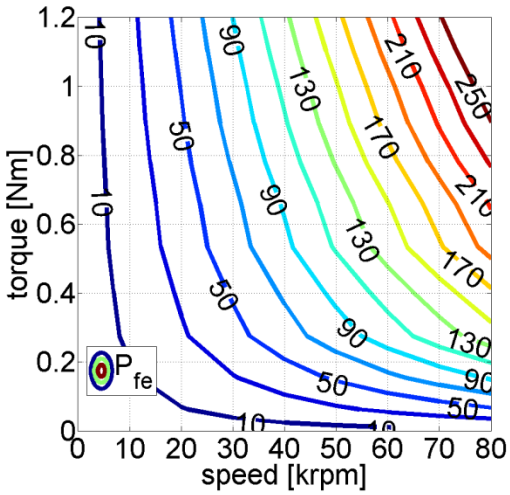


Figure 88: Constant iron losses loci [W] at MTPA condition in the speed-torque plane

6.1.3 Airgap friction losses

The loss resulting from the gas friction in the airgap has been estimated using the formulation based on the measurements first reported in [126] and also adopted by other authors [127, 128]. The friction losses obviously occur in the airgap and in the rotor end region (i.e. the space between the rotor end cap and the bearing housing); both can be estimated using the following relationship:

$$P_{friction} = k_{surface} \cdot k_{friction} \cdot \rho \cdot \pi \cdot \omega^3 \cdot r^4 \cdot L \qquad (44)$$

where $k_{surface}$ is the surface roughness coefficient (here considered 2.5 being the stator surface axially slotted), $k_{friction}$ is the friction coefficient, ρ is the density of the air, ω is the shaft speed in rad/s, r is the rotor radius and L is the lamination stack length. The friction coefficient depends on the flow regime which can be discriminated according to the value of the Couette-Reynolds number $R_{e\delta}$:

$$k_{friction} = 5 \cdot \frac{(g/r)^{0.3}}{R_{e\delta}} \qquad R_{e\delta} \leq 64 \qquad (45a)$$

$$k_{friction} = \frac{(g/r)^{0.3}}{R_{e\delta}{}^{0.6}} \qquad 64 < R_{e\delta} \leq 500 \qquad (45b)$$

$$k_{friction} = 0.515 \cdot \frac{(g/r)^{0.3}}{R_{e\delta}{}^{0.5}} \qquad 500 < R_{e\delta} \leq 10^4 \qquad (45c)$$

$$k_{friction} = 0.0325 \cdot \frac{(g/r)^{0.3}}{R_{e\delta}{}^{0.2}} \qquad R_{e\delta} > 10^4 \qquad (45d)$$

where the $R_{e\delta}$ is calculated according to the following relationship:

$$R_{e\delta} = \frac{\rho \cdot v_t \cdot g}{\mu} \qquad (46)$$

being v_t the tangential speed of the rotor, g the airgap length and μ the dynamic viscosity of the air. The reported formulation allows estimating the airgap friction losses without considering the loss component due to the axial flow through the airgap. Figure 89 reports the friction loss as function of the speed neglecting the loss component due to the friction in the end region.

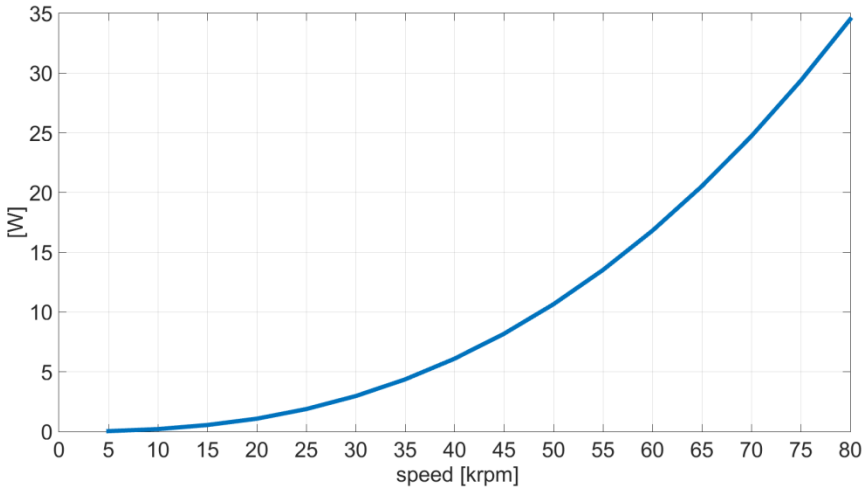


Figure 89: Friction losses in the airgap as function of the speed.

6.2 Thermal modelling

A lumped parameter thermal network has been implemented in order to estimate the temperatures in the most salient points of the optimized machine and possibly identify its hotspots. After a brief explanation of the adopted network and the used heat transfer coefficients, such model is used to determine the minimum coolant flow rate and to establish the thermal limit of the machine for a given winding insulation system and cooling scenario. With the aim of validating the developed thermal network highlighting its benefits and limitations, the temperature distribution will be compared with the one obtained with a commercial thermal analysis software (MotorCAD). Other approaches can be obviously applied in order to predict the thermal performance of an electrical machine, such as thermal FEA and more complex computational fluid dynamic (CFD) simulations. The choice of a lumped parameter network approach allows a fast estimation of the bulk temperatures without providing the temperature distribution within each component. The latter can be calculated (for solid component) by a thermal FEA at the expense of an increased computational effort. However the difficulties of predicting the real values of the heat convection coefficients and the contact resistances heavily affect the accuracy of both lumped parameter networks and FEAs. CFD has the advantages of predicting the fluid flow in complex geometries, such as the end winding region, but it is very demanding in terms of model setup and computational time [129].

6.2.1 Lumped parameters network

6.2.1.1 Model description

The thermal modelling of a high speed electrical machine is not a trivial task since several complex phenomena are involved in the heat transfer mechanisms. A consistent amount of literature have addressed this issue and the results of the most relevant works (mainly assessing the heat transfer coefficients calculation and the identification of the most important heat paths) have been used in order to implement a meaningful thermal model. In fact a thermal network has to consider the most influent heat paths but at the same time it should not exceed in term of complexity (mainly defined by the number of nodes). In particular, a thermal network with 12 nodes, similar to the one reported in [127, 130], has been developed as shown in Figure 90. The adopted model considers the most important radial and axial heat transfer mechanisms. In fact, the heat transfers between the main sources of the losses (copper and iron losses) and the coolant fluid, the airgap medium and the external ambient are taken into account. Although it is considered in a really simplified way, also the heat paths between the end winding and the end space regions are taken into account. Analysing the network in details, it is clear that the modelling of the rotor does not include the presence of the flux barrier. This simplification along with the fact that other axial components are neglected (bearings and end caps) lead to the obvious conclusion that the adopted

network will not be able to accurately predict the rotor and shaft temperature. This statement will be proved in the next sub-paragraph where the thermal performance estimated with MotorCAD will be compared with the one predicted with the built network. The temperature rises in the different nodes have been determined applying the classic nodal analysis to the thermal circuit, i.e. solving the following matrix equation [127, 128]:

$$\Delta T = \left(G + G_{fluid}\right)^{-1} \cdot P \tag{47}$$

where P is the vector containing the losses injected in each node, ΔT is the temperature rise vector, G is the thermal conductance matrix and G_{fluid} is the cooling matrix which models the heating of the coolant fluid. The elements of the matrix G are defined as:

$$g_{ii} = \sum_{k \in i} \frac{1}{R_k}; g_{lm} = -\frac{1}{R_{lm}} \tag{48}$$

that is the diagonal element ii is the sum of the thermal conductances connected to the node i, while the extra diagonal element lm is the negative conductance between the nodes l and m. The cooling matrix G_{fluid} defines the temperature rise of the cooling fluid flow passing in each node and between nodes as function of the injected powers; its elements are defined as:

$$g_{fluid\_ii} = \frac{1}{R_{q\_ii}}; g_{fluid\_lm} = \frac{1}{R_{q\_lm}}; R_q = \frac{1}{\rho \cdot q_v \cdot c_p} \tag{49}$$

where ρ, q_v, c_p are respectively the mass density, the volume flow rate passing the node i, and the specific heat of the cooling fluid. It has to be underlined that the matrix equation (47) defining the temperature rise vector has to be calculated iteratively updating the loss components dependent from the related temperature (mainly the dc copper loss due to its obvious dependence from the temperature and the windage loss due to its indirect dependence from the airgap medium temperature which affects its properties).

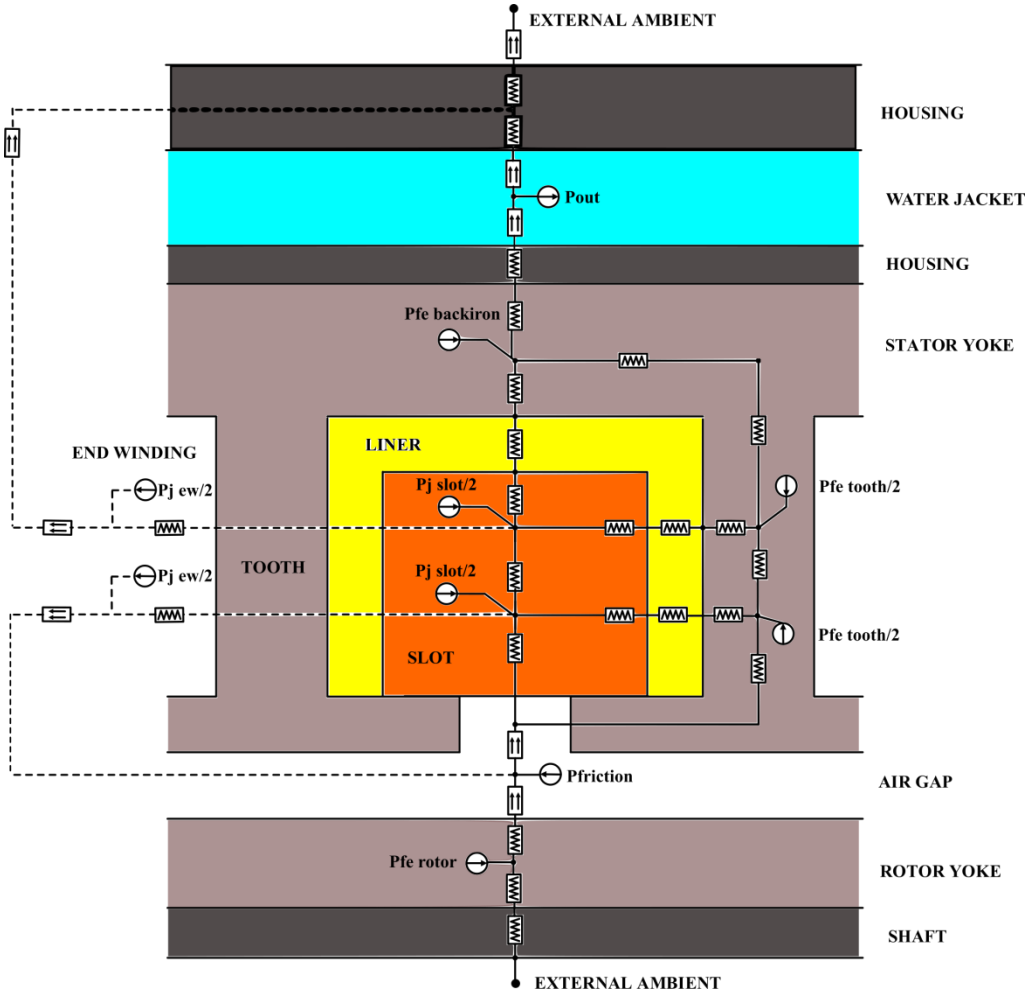


Figure 90: Lumped parameters thermal network

The thermal resistances defining the heat transfer by conduction in the solid components have been calculated by following the relationships (in Cartesian or polar coordinates according to the specific component):

$$R_{conduction} = \frac{L}{k \cdot A} \; ; R_{conduction} = \frac{1}{k \cdot L \cdot \beta} \cdot \log(\frac{r_{out}}{r_{in}}) \qquad (50)$$

where L is the length of the component in the direction of the heat flow, A is the surface of the component normal to the heat flow, r_{out}, r_{in} are the outer and inner radius of the sector (having an angular span of β) of the hollow cylinder. On the other hand the thermal resistance governing the heat transfer by convention is defined with obvious meaning of the symbols as:

$$R_{convection} = \frac{1}{h \cdot A} \qquad (51)$$

6.2.1.2 Adopted heat transfer correlations

As previously mentioned the difficulties of defining a thermal network which faithfully approximate the real behaviour of the machine are related not only with the complexity of the network but also with the issue of identifying the correct heat transfer coefficients (k for conduction and h for convection). Regarding the heat conduction mechanism the difficulties mainly lie in the evaluation of 1) the equivalent conductivity of composite component (mainly the slots area) and 2) the contact resistance between the constituent parts of the

machine. Several approach have been proposed to face the first issue as reported in [129, 131, 132]; some of them are derived from curve fitting the experimental data while others are the results of more theoretical approach (e.g. layered winding model [133]). In the following, the suggested equivalent conductivity range reported in [129] has been adopted (i.e. $k_{eq\_slot} = 2 - 3\ W/m \cdot °C$). The contact resistance between the stator lamination and the housing is usually modelled with an equivalent interface gap [131] derived from specific test campaign. Such resistance is a complex function of the materials hardness, interference pressure and smoothness of the surfaces. In the following the contact resistance as function of the interference pressure reported in [134, 135] have been used to estimate such complex phenomena for the case under study. The convection heat transfer coefficients are usually calculated adopting formulations, derived from fitting experimental data, expressed in terms of dimensionless numbers. There is a conspicuous amount of literature [136] reporting such empirical formulations which correlate the Nusselt number as function of the Grashof Gr and Prandtl Pr numbers for the natural convection mechanism, ($Nu = f(Gr, Pr)$), and in terms of Reynolds Re and Prandtl for the forced convection one ($Nu = g(Re, Pr)$). The Nusselt number defines the ratio between the convective to conductive heat transfer. Once Nu is calculated applying the correct empirical formulation, the convective heat transfer coefficient can be then easily calculated. The Reynolds number is used to discriminate the laminar from the turbulent flow in forced convection system; in a similar fashion, the product Grashof and Prandtl

numbers is used in natural convection scenario. In natural convection mechanism, flow is induced by the buoyancy forces due to the different fluid densities caused by the temperature variation between the solid surface and the fluid. On the other hand forced convection is essentially a function of the fluid velocity and its properties and indirectly depends on the fluid temperature (because the fluid properties depend in turn from the temperature). All the mentioned dimensionless numbers are defined by the following relationships [137]:

$$Re = \rho \cdot v \cdot L_c/\mu \tag{52a}$$

$$Gr = \beta \cdot g \cdot \Delta T \cdot \rho^2 \cdot L_c^3/\mu^2 \tag{52b}$$

$$Pr = c_p \cdot \mu/k \tag{52c}$$

$$Nu = \frac{h \cdot L_c}{k} \tag{52d}$$

where v is the velocity of the fluid, L_c is the characteristic length (generically defined as the dimension which lies perpendicular to the direction of growth of the boundary layer), μ is the fluid dynamic viscosity, β the fluid coefficient cubical expansion, g is the gravitational force of attraction, ΔT is the temperature difference between the surface and the fluid, and finally k is the fluid thermal conductivity. In the following the correlation used for determining the heat convection coefficient at the external surface of the housing, in the water jacket, in the airgap and in the end winding regions are briefly described.

- The natural convection heat transfer coefficient between the external surface of the housing (which in this case is a simple cylinder) and the ambient can be easily calculated applying the basic relationship reported in [137]:

$$Nu = 0.525 \cdot (Gr \cdot Pr)^{0.25} \qquad 10^4 < Gr \cdot Pr \leq 10^9 \qquad \text{(53a)}$$

$$Nu = 0.129 \cdot (Gr \cdot Pr)^{0.33} \qquad 10^9 < Gr \cdot Pr \leq 10^{12} \qquad \text{(53b)}$$

where the flow regime (laminar or turbulent) is discriminated according to the value of the product of the Grashof and Prandtl number (also called Rayleigh number).

- Due to the short active axial length of the machine (30 mm), a spiral water jacket configuration with a unique channel has been considered in order to simplify the manufacturing of the housing. Assuming a highly turbulent flow, that is a fluid having a Reynolds number bigger than 10000, the Nusselt number has been estimated adopting the correlation quoted in [137]:

$$Nu = \frac{(f/8) \cdot (Re - 1000) \cdot Pr}{1 + 12.7 \cdot (f/8)^{1/2}(Pr^{2/3} - 1)} \qquad \text{(54)}$$

$$\text{where } f = (0.79 \cdot \log(Re) - 1.67)^{-2}$$

Re is calculated considering the characteristic length equal to the hydraulic diameter of the channel $(2 \cdot h_{ch} \cdot w_{ch})/(h_{ch} + w_{ch})$, being h_{ch} and w_{ch} the height and the width of the channel. In the case of Reynolds number below the turbulent flow threshold, other empirical formulation has to be used as reported always in [137].

- Several studies have been conduct in order to examine the heat transfer mechanism in the airgap of concentric and rotating cylinders [138, 139]. Such investigations have shown that three different flow regimes can be established in such configuration, namely laminar shear flow, laminar with vortex and fully turbulent. With the aim of discerning the flow regime, another dimensionless number is usually used, named Taylor number Ta, defined as:

$$Ta = Re\sqrt{g/R_r} \tag{55}$$

where g in this case is the airgap length, R_r is the rotor radius and the Reynolds number (calculated considering the airgap thickness as characteristic length). Once the Taylor number is determined, the correlations defining the Nusselt number for the different flow regimes are [137]:

$$Nu = 2 \qquad Ta \leq 41 \tag{56a}$$

$$Nu = 0.212 \cdot Ta^{0.63} \cdot Pr^{0.27} \qquad 41 < Ta \leq 100 \tag{56b}$$

$$Nu = 0.386 \cdot Ta^{0.5} \cdot Pr^{0.27} \qquad Ta > 100 \tag{56c}$$

It has to be noted that the influence of the slot presence is completely neglected in this formulation; few studies have addressed this issue however none of them reports equations to quantify the phenomena (decrease of Nu in the laminar region and its increase in the fully turbulent one).

- The challenge of evaluating the heat transfer convection coefficient in the end winding regions lies in the complex end winding geometry, its surface finish and the difficulty of estimating the local fluid velocities in the different parts of the end region cavity. Given the topology of the considered thermal network, the end winding cavity has been divided into two parts: the outer one connects the outermost side of the end winding with the inner surface of the housing while the inner one connects the inner side of the end winding with the airgap node. Several authors have faced this issue and a wide overview of the topic is proposed in [140, 141]; almost all of them propose the following formulation to estimate the convection heat transfer coefficient in this peculiar configuration:

$$h = k_1(1 + k_2 \cdot {v_{fluid}}^{k_3}) \tag{57}$$

where k_1, k_2, k_3 are curve fit coefficients (in this case study 15, 0.4, 0.9 have been respectively adopted). The local fluid velocity in the inner part of the end winding cavity has been assumed equal to the average tangential speed calculated at the rotor and shaft diameter as reported in the following being Ω the rotor angular speed:

$$v_{fluid\_inner} = \Omega \cdot \frac{R_r + R_{shaft}}{2} \tag{58a}$$

$$v_{fluid\_outer} = 0.2 \cdot v_{fluid\_inner} \tag{58b}$$

The fluid velocity in the outer part of the end winding region has been simply supposed equal to the 20% of the inner fluid velocity.

6.2.2 Thermal performance

Once the assumptions of the thermal model have been detailed along with the calculation of the power losses, the developed network has been used to estimate the minimum coolant flow rate in order to not exceed the maximum winding temperature (i.e. 180°C corresponding to the class H of the insulation system). Figure 91 reports the maximum winding temperature rise (located in the innermost end winding node of the network) as function of the water flow rate in the rated current condition and the maximum speed. Given the numerous uncertainties of the developed model due to inevitable simplifications and assumptions on which the modelling is based, a conservative choice of the minimum coolant flow rate has been implemented. In particular a flow rate of 15 l/min has been selected as the minimum value leading to a maximum winding temperature rise around 110 °C which is well below the maximum limit dictated from the selected insulation system. With such conservative choice the maximum winding temperature would lie within the safe range also in the worst case scenario of inaccuracy of the underestimated thermal performance of about 50%.

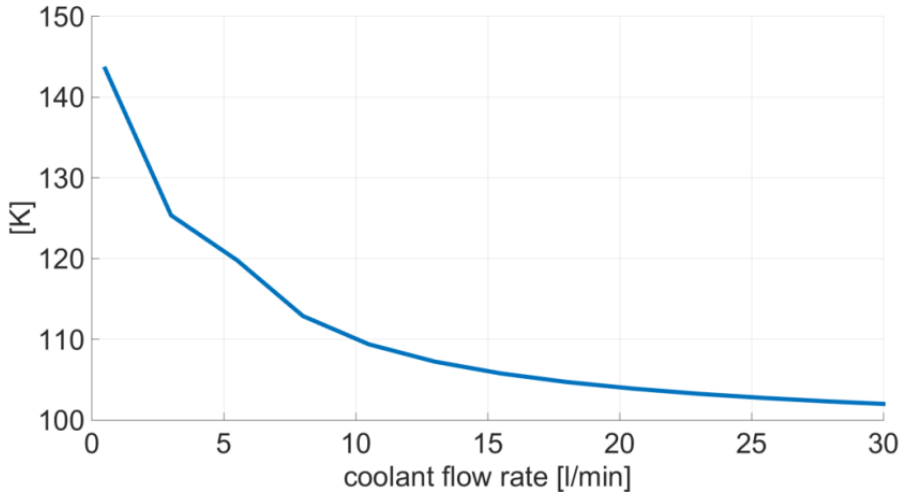


Figure 91: maximum winding temperature rise as function of the coolant flow rate for the rated current (17Apk) and the maximum speed (80 krpm)

Figure 92 outlines the estimated temperature rises in the most salient nodes of the developed network. The hotspot is located in the inner node of the end winding region, while the coolest part results the one nearer to the water jacket as obviously expected.

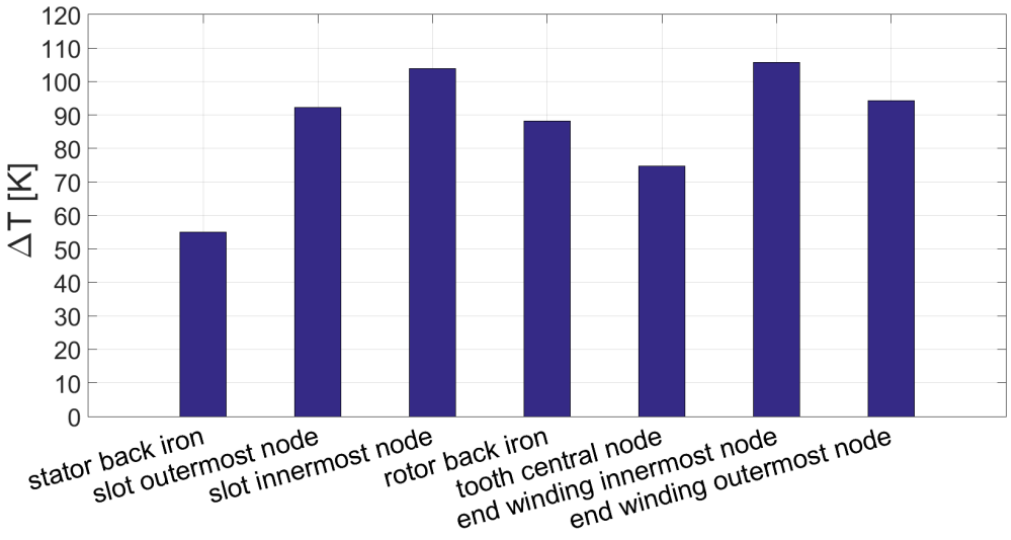
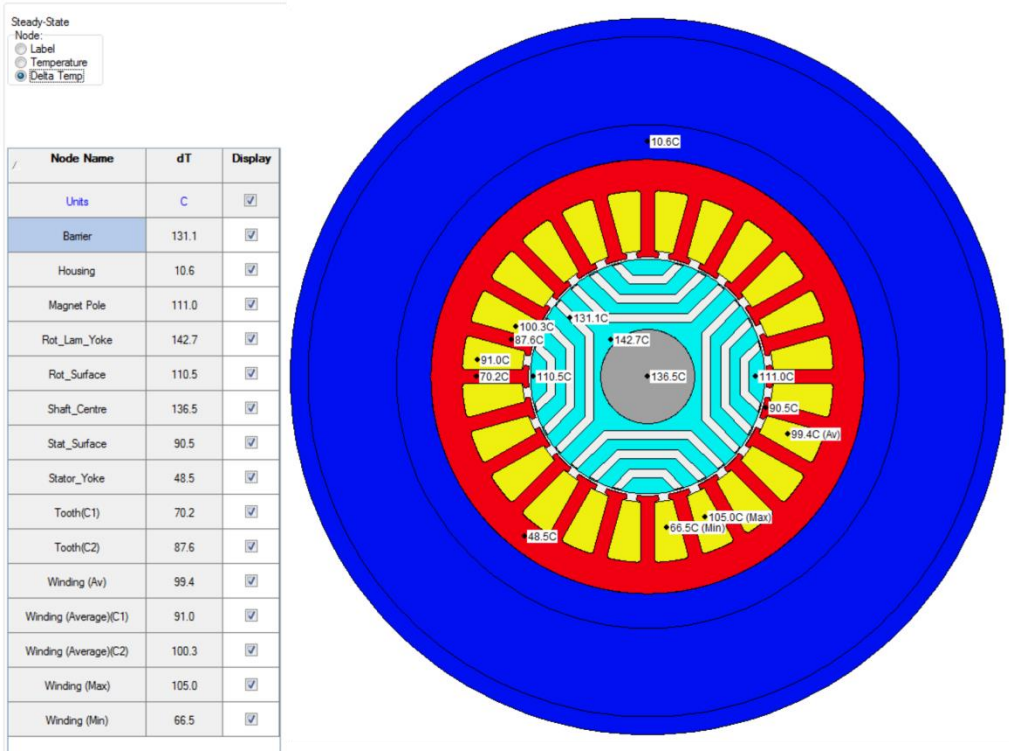


Figure 92: Estimated bulk temperatures with coolant flow rate of 15 l/min in the rated current condition (19Apk) and maximum speed (80 krpm)

With the aim of validating the developed thermal network, an off-the-shelf thermal analysis software has been used to compare the temperature distributions. In particular, the selected software (MotorCAD) implements a highly detailed thermal network with a number of nodes two orders higher than the one implemented in-house; in addition it also gives the possibility of performing a thermal FEA of the stator and rotor geometry. Obviously the model built with the commercial software is implemented with identical materials properties, coolant flow rate and losses. Both models produce results in close agreement in terms of winding temperature with a maximum deviation of about 15% as shown in the Figure 93. However, large discrepancy between the two models can be noted in the evaluation of the rotor temperature. In particular the developed model underestimates the rotor temperature of about 30% (if an average of the rotor temperatures calculated by MotorCAD is considered as a reference). This difference is due to the drastic simplification of completely neglecting the flux barriers whose presence obviously limits the conduction heat transfer within the rotor. Figure 94 reports the FE calculated temperature distribution in the slot and in the rotor geometry by MotorCAD. The temperature hotspots for clear reasons are located near the airgap for within the slot and towards the shaft within the rotor. It is worth to notice that estimated FE temperature distribution within the rotor corresponds to the worst case scenario in terms of iron losses (since a building factor of 2 has been considered).



Node Name	dT	Display
Units	C	☑
Barrier	131.1	☑
Housing	10.6	☑
Magnet Pole	111.0	☑
Rot_Lam_Yoke	142.7	☑
Rot_Surface	110.5	☑
Shaft_Centre	136.5	☑
Stat_Surface	90.5	☑
Stator_Yoke	48.5	☑
Tooth(C1)	70.2	☑
Tooth(C2)	87.6	☑
Winding (Av)	99.4	☑
Winding (Average)(C1)	91.0	☑
Winding (Average)(C2)	100.3	☑
Winding (Max)	105.0	☑
Winding (Min)	66.5	☑

Figure 93: Radial temperatures rise with coolant flow rate of 15 l/min in the rated current condition (19Apk) and maximum speed (80 krpm) estimated with MotorCAD

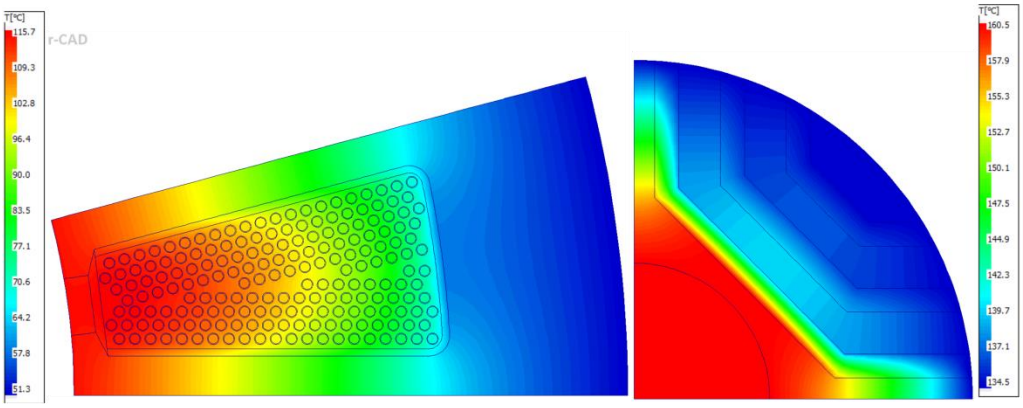


Figure 94: Radial temperatures distribution in the rotor (b) and in the slot (a) with coolant flow rate of 15 l/min in the rated current condition (19Apk) and maximum speed (80 krpm) estimated with the FE tool of MotorCAD

6.3 Overall performance

This section outlines the electromagnetic and thermal performance of the optimized machine in the d-q axis current plane and in the torque-speed plane at MTPA condition. Figure 95 shows the d- and q-axis flux linkages versus the respective axis current. For a given current, the q-axis flux is clearly higher respect to the d-axis flux linkage. The iron saturation limits the q-axis flux linkage while the d-axis flux remains almost linear except for current close to zero. In that range the d-axis flux current curve change its slope due to the saturation of the iron bridges. The same figure reports the cross saturation effect, i.e. how each flux is affected also by the other current component. Let's underline that both axis inductances are not constant as the current increases and the apparent and incremental inductances are different. This constitutes one of the main issues of the control of this machine topology.

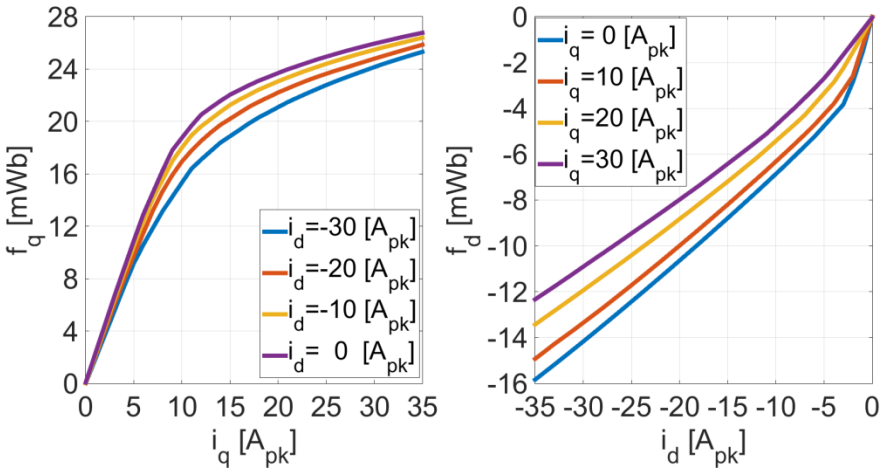


Figure 95: q- and d-axis flux linkage as function of the respective axis current

Figure 96 reports the flux densities contour plots in the salient point of the machine in the d-q axis current plane, i.e. the stator tooth, the stator yoke and the central rotor flux guide. The increment of the iron exploitation along the MTPA trajectory is clear for all the considered points of the machine

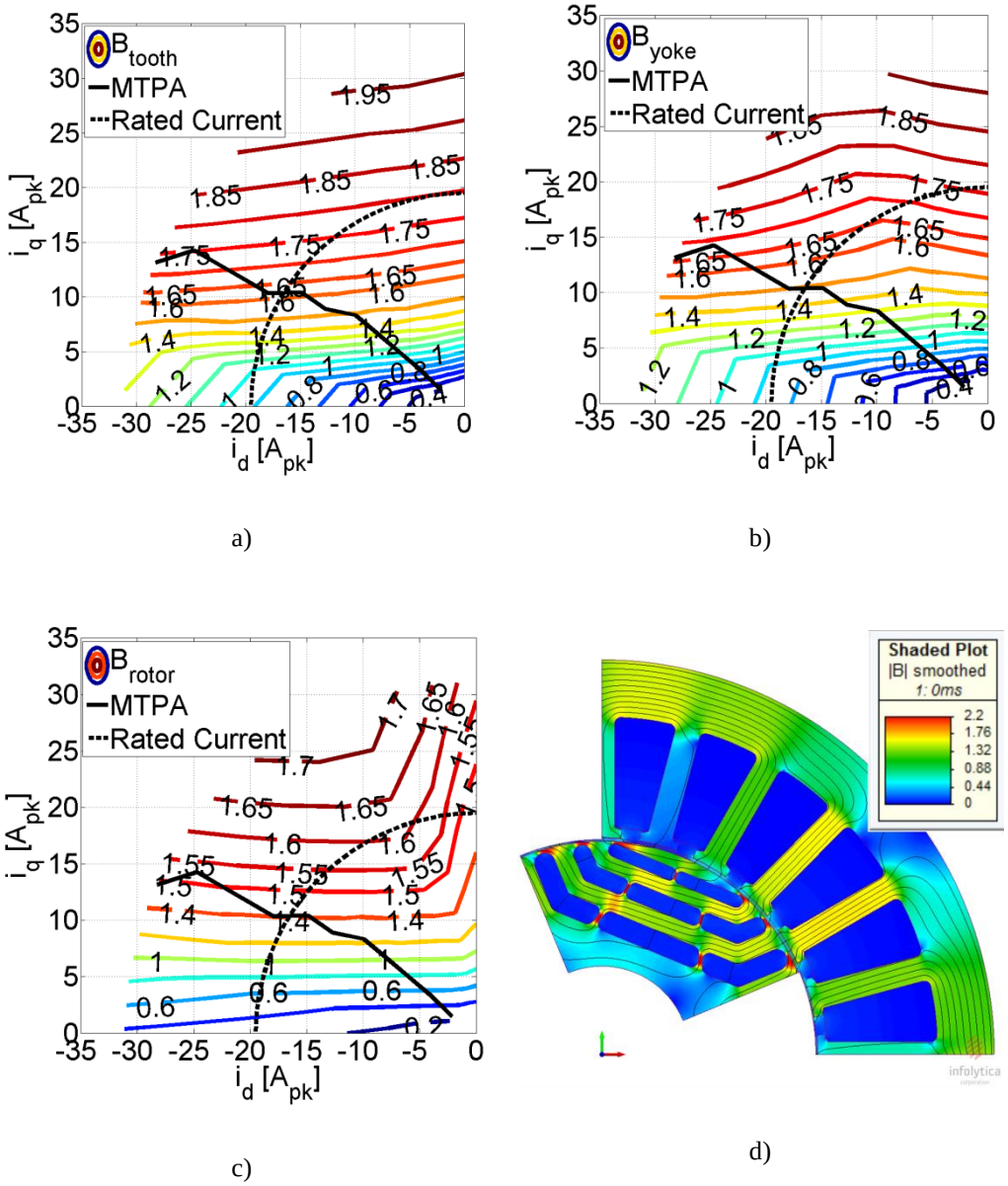
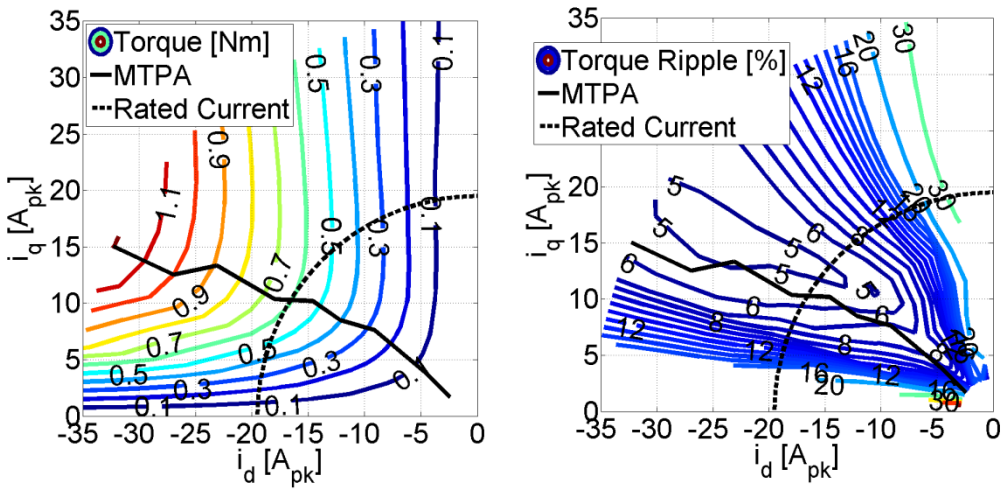


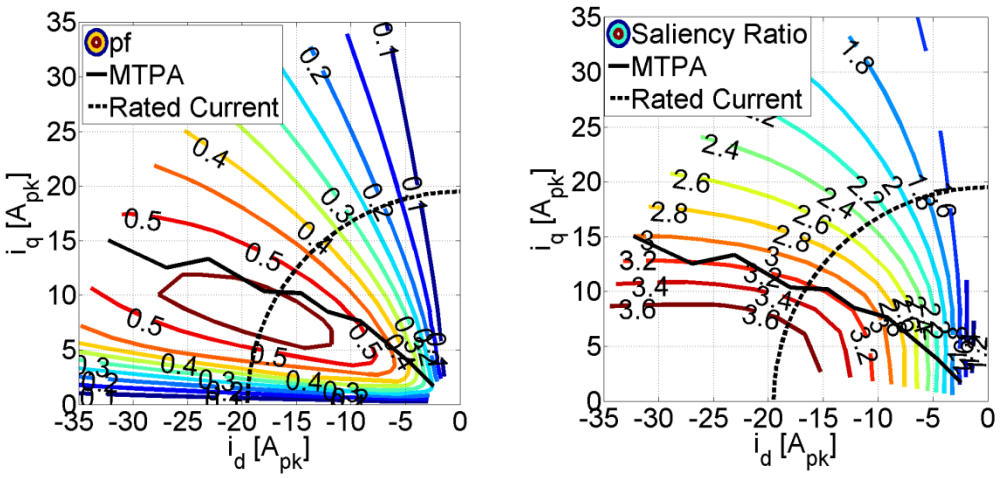
Figure 96: Constant loci in the d-q axis current plane of the maximum flux densities in t5he salient points of the machine: a) stator tooth, b) stator yoke, c) central rotor flux guide; d) flux density distribution of the optimal machine in the rated condition.

It can be observed that in the same operating condition (as usual), the stator tooth is more loaded respect to the stator yoke while the rotor flux density is slightly lower compared to the two previous values because the rotor material has a lower flux density saturation level. For a given current amplitude, the considered iron flux densities obviously decrease as the absolute value of $i_d$increases being the total flux also decreasing in the same direction. Figure 96d also illustrates the flux density distribution in the rated condition of the optimal machine. Figure 97, 96 show the constant loci in the d-q axis current plane of the average torque, torque ripple (calculated as $(T_{max} - T_{min})/T_{average} \cdot 100$), power factor and saliency ratio. Figure 99 outlines the first three mentioned performance indexes as function of the current amplitude at MTPA condition. Along the MTPA trajectory and for current amplitude higher than half the rated value (19 A_{pk}) the torque ripple remains always below the 8%.



a) b)

Figure 97: Average torque and torque ripple constant loci in the d-q axis current plane



a) b)

Figure 98: a) Internal power factor and b) saliency ratio constant loci in the d-q axis current plane

This behaviour is mainly due to the fact that the rotor geometry has been electromagnetically optimized with a current amplitude higher than the rated value (about 150%) as addressed in chapter 3. As described by analytical means in Chapter two, the power factor of a high speed synchronous reluctance machine is definitely low compared to alternative synchronous machine topologies whose torque production mechanism essentially rely on the permanent magnets. In fact in the rated current condition the optimal machine shows a power factor of 0.55 (while the ipf is about 0.52). However its value remains quite stable also in overload condition as clearly reported in Figure 99. The saliency ratio along the MTPA trajectory and for current amplitude higher than half of the rated value is always above 3 as shown in Figure 98b. The FE calculated average torque and internal power factor are in close agreement with the analytically estimated ones reported in Chapter 2 (the discrepancies are within 15% for both performance indexes).

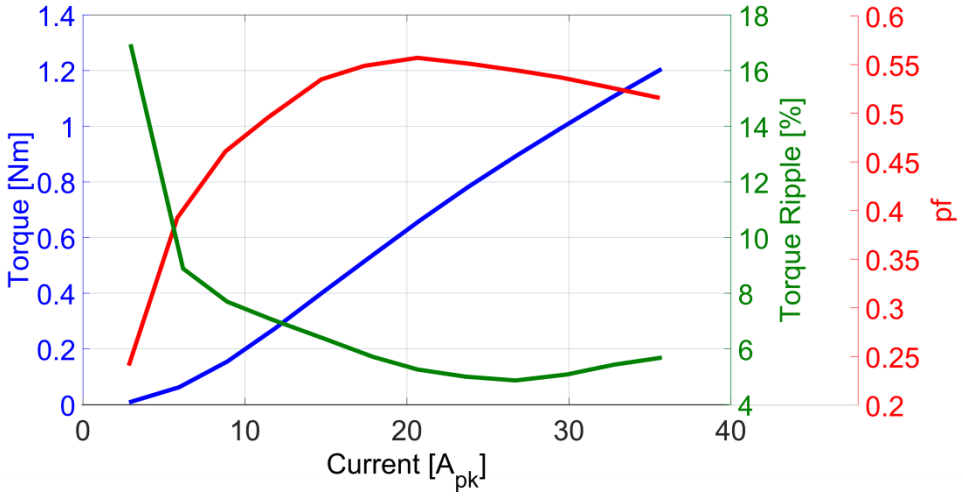
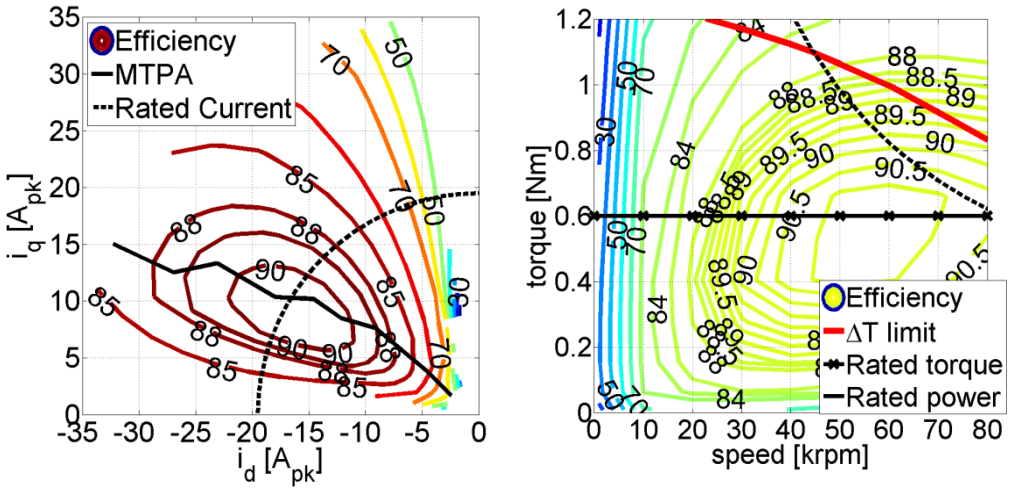


Figure 99: Average torque, torque ripple and internal power factor at the MTPA condition as function of the current amplitude

In the following the efficiency of the optimal machine is calculated considering the copper losses updated at the correct winding temperature. The latter has been estimated with the thermal model presented in the previous chapter considering the losses in the respective operating condition. Figure 100a shows the efficiency at the maximum operating speed (80 krpm) in the d-q axis current plane. At the maximum speed along the MTPA trajectory the efficiency is always above the 90% for current amplitude higher than half of the rated value. The efficiency map in the torque-speed plane assuming MTPA as control strategy is reported in Figure 100b. The efficiency is always above the 85% in the region of practical interest (i.e. speed and torque higher than 10 krpm and 0.1 Nm respectively). The constant loci of the rated torque (line marked with x) and rated power (dashed line) are also reported in the same graph. As the speed increases at the rated torque level, the efficiency tends to sharply increases (between 0-20 krpm), then its rate of increment drastically decrease (between 20-60 krpm) and finally slightly decreases for higher speed

operation. Analysing the rated constant power loci it is clear that as the speed increase the efficiency tends to increases of about 4%.



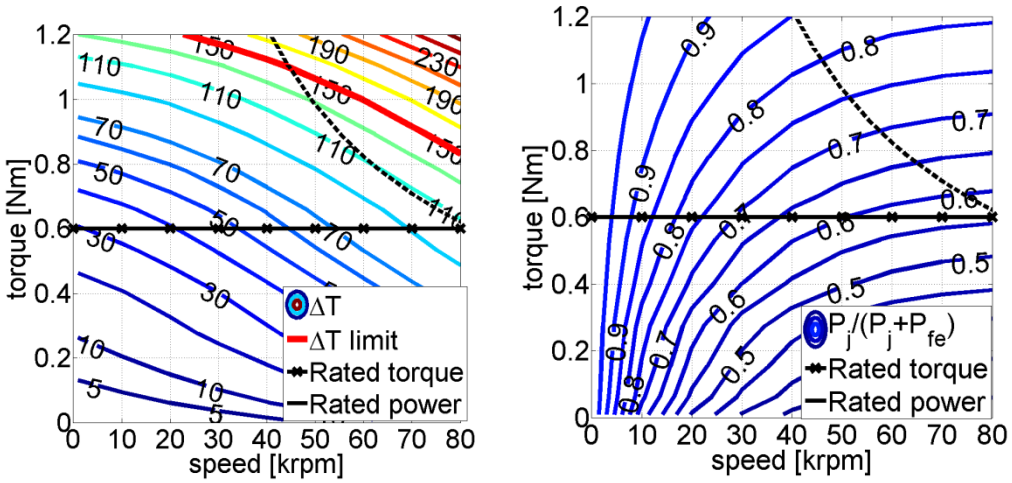
a) b)

Figure 100: Constant efficiency loci a) in the d-q axis current plane at the maximum speed (80 krpm) and b) in the speed-torque plane at MTPA condition.

In the same figure it is also shown the thermal limit of the machine, that is the locus above which the maximum temperature rise is higher than the limit imposed by the selected winding insulation system (i.e. $\Delta T_{max} = 150\,°C$ being $T_{max} = 180\,°C$ and supposing $T_{ambient} = 30\,°C$)[4]. In fact, once all the losses components are known, the lumped parameter thermal model presented in the previous paragraph can be used to estimate the winding temperature rise ΔT. Figure 101a shows constant the temperature rise contour in the torque-speed plane with the iron losses calculated always assuming MTPA as control strategy. It is clear that the winding temperature is dominated by the copper losses being the shape of the constant loci of these two variables really similar

[4] It is worth to notice that the reference node of the thermal network is the external ambient node.

as it can be seen comparing Figure 86 with Figure 101a. The relative weight of the copper losses compared to the total electromagnetic losses decreases as the speed increases as shown in Figure 101b. The latter reports the ratio between the copper and the total losses in the torque-speed plane. It is opportune to note that the copper losses influence in the high speed region depends also on the torque levels. In particular for high operational speeds the copper losses weight increases as the torque increases mainly due to the additional contribution of the AC copper losses.



a) b)

Figure 101: Constant loci of a) the maximum winding temperature rise and b) the electromagnetic loss distribution in the speed-torque plane at MTPA condition.

6.4 Conclusion

An in-depth analysis of the electromagnetic performance of the final optimal machine has been given taking into consideration its thermal limitation. In

particular the challenges of calculating the loss components of a HS-SyR (common to all HS machines) have been outlined. The copper and iron losses have been FE evaluated while the airgap friction loss has been estimated by analytical mean. After the calculation of the loss components, the temperature distribution has been predicted implementing a lumped parameter thermal network. The results of the latter have been compared with the one obtained by an off-the-shelf thermal analysis software; a close agreement has been found in terms of winding temperature. Once validated, this model has been employed to identify the minimum coolant flow rate and to establish the thermal limitation of the optimal machine for given cooling system characteristics. In the last subsection an overview of the electromagnetic performance (mainly torque, ripple, power factor, efficiency and loss distribution) has been presented in terms of contour plots in the d-q axis current plane and torque-speed plane taking into account also the upper temperature constraint dictated by the selected winding insulation system.

It is worth to underline that the reported efficiency should correspond to the worst case scenario for the two following reasons.

1. The additional copper loss due to circulating current effect has been estimated supposing a certain position of the strands inside each slot. Clearly the real value could be different from estimated one.
2. The thermal model overestimates the winding temperature if compared with the MotorCAD results.
3. The iron losses have been calculated considering a building factor of two.

4. The bearing loss component has been neglected. Anyway they should be of the same order of the airgap friction losses therefore a small portion of the total one.

All the mentioned approximations and uncertainties are other possible sources of discrepancy between the estimated performance and the measured one which will be shown in the next Chapter.

Chapter 7
Experimental results

This chapter first introduces the work undertaken to build and test the prototype whose designs and analysis have been reported in the previous chapters. After a brief description of the built machine and the test set up, the experimental results will be shown. In particular, first the measured magnetic model is compared with the FE calculated one both in terms of flux-current relationships and produced torque. The measured magnetic model was used to build the required look-up tables needed for the vector control of the machine. The experimental results are presented and compared to the predicted results, and considerations on the discrepancies with the expected performance are discussed.

7.1 The built prototype

The electromagnetic, structural and thermal design considerations described in the previous chapters provide some of the information needed to enable the manufacturing of the prototype. The inter-bearing distance and the bearing selection follow the rotor dynamic analysis carried out by the industrial partner of the project (Cummins). The majority of the components were machined using the available in-house expertise and equipment. Figure 102 shows a section view of the built prototype highlighting the main components. The geometry of the drive end (DE) side of the main housing (as the peak connecting shaft) follows the details of the bracket of the used high speed rig (which will be described in the next paragraph). The selected bearings (SKF 7000 CE/HCP4A) were inserted into their seats insuring the right amount of clearance fit specified by the bearing manufacturer. The bearing housings, also shown in Figure 102, feature the inlet and outlet channels required for the air-oil mist lubrication system of the bearings. The axial position of the NDE (non-drive end) bearing was kept "fixed" while the one on the DE was kept "floating" and the required preload was applied by means of a spring-washer (with the proper elastic constant guaranteeing the required preload in all temperature conditions). Both stator and rotor laminations were cut using the EDM method. Once the rotor stack was manufactured (see Figure 103a-b), the shaft was interference fitted into the rotor.

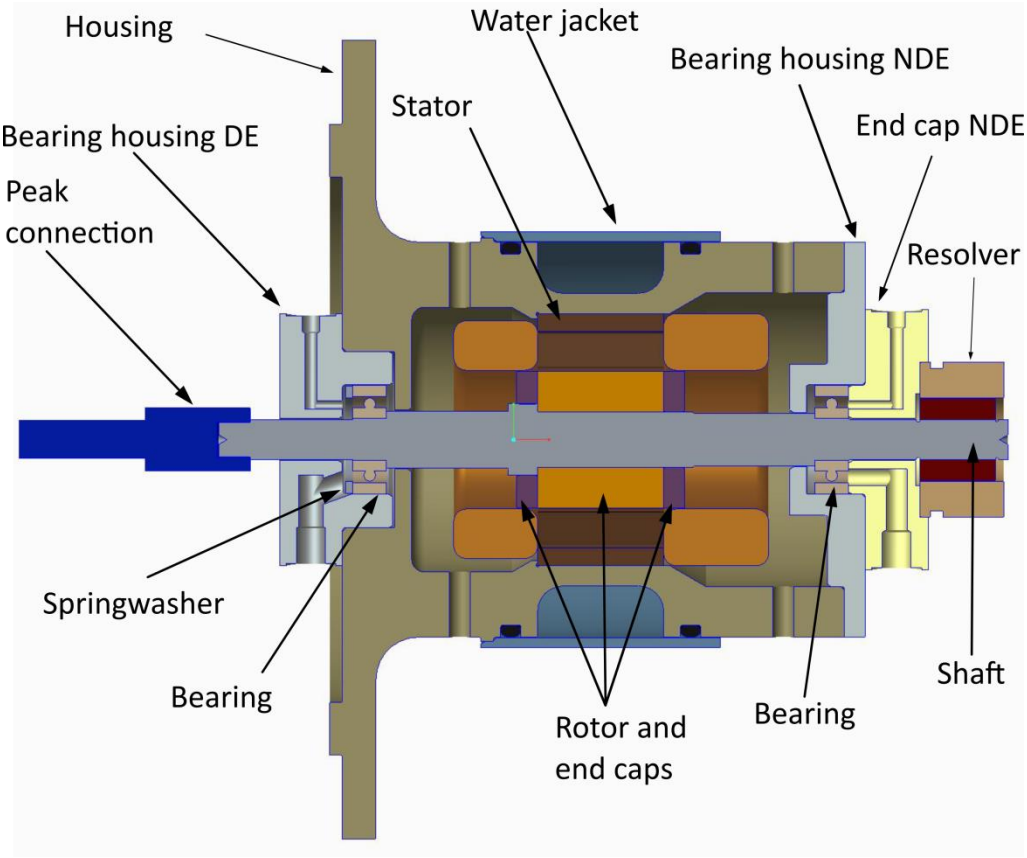
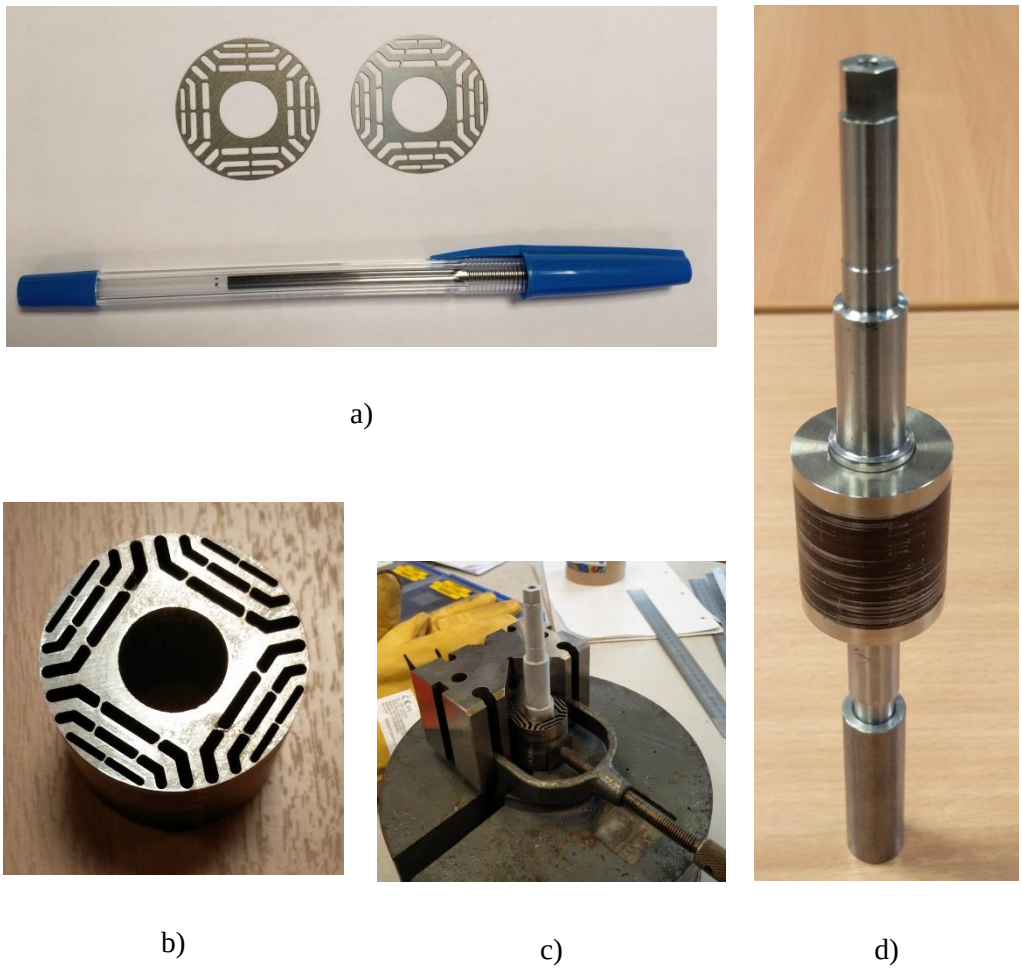


Figure 102: Section view of the built prototype showing the most important components

In particular, the shaft was shrunk by its immersion in a bath of liquid nitrogen (at a temperature of -196 °C) allowing its insertion without the need of using any press as shown in Figure 103c. The end caps of the rotor were assembled on the shaft in a similar way; the final assembled rotor is reported in Figure 103d. Once assembled, the rotor was balanced[5] to an ISO 1940 quality grade of G1 at a service speed of 100 krpm which corresponds to a permissible residual unbalance of 0.035 gmm for the two planes of balancing being the rotor mass equal to 325 g.

[5] It has to be noticed that the rotor assembly was balanced without the bearings and the rotor resolver since once the latter are fitted on the shaft it is not possible to insert the rotor system into the housing.

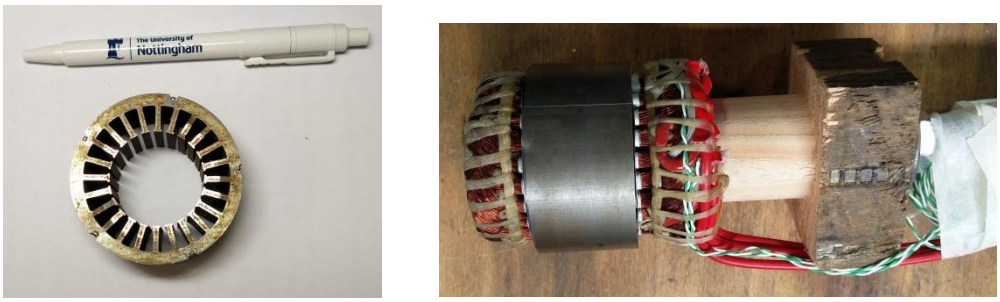


a) b) c) d)

Figure 103: a) Prototyped rotor lamination (the one on the right)[6], b) rotor stack before shaft insertion, c) shaft insertion phase and d) complete rotor assembly.

The used correction planes were the retention end caps of the rotor laminations. Figure 104 shows the stator lamination stack before and after the winding and the insertion of the thermocouples needed to monitor the winding temperatures. The complete stator was then interference fitted into the main housing increasing the housing temperature of about 200 °C thus allowing a smooth insertion without applying any external force.

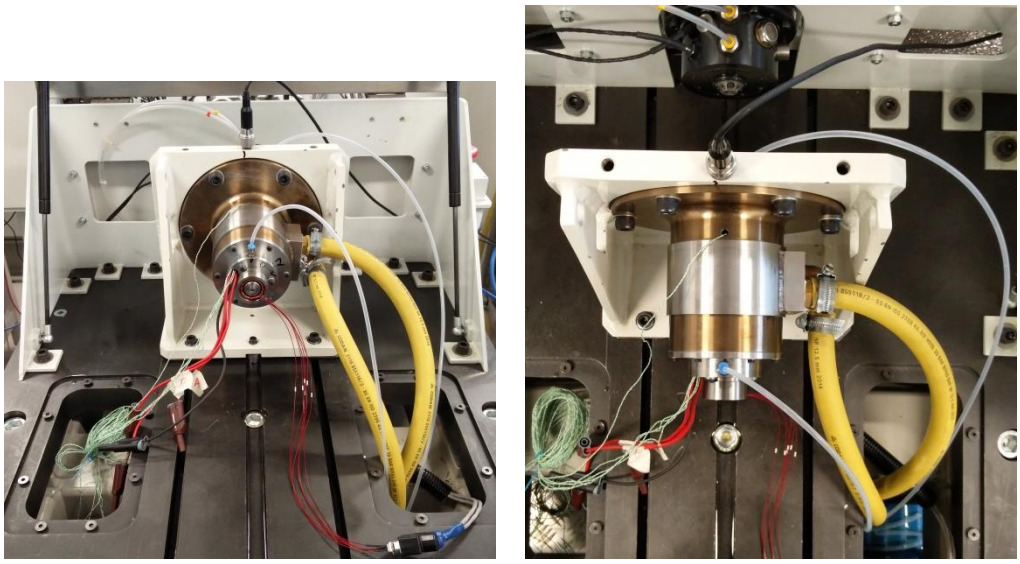
[6] The one on the left is the rotor geometry of the permanent magnet assisted version of the target machine whose design has not been described in this thesis.



a) b)

Figure 104: a) Stator lamination stack before winding, b) Stator with windings before the insertion in the housing.

The NDE bearing seat was positioned on the shaft and the respective bearing interference fitted (increasing its temperature to about 100 °C). After the rotor-shaft-NDE-bearing-seat assembly was placed into the stator-housing for the final interference fitting of the DE bearing. Then the mounting of the DE bearing housing and NDE end cap was carried out. As a final step, the rotor resolver was interference fitted on the NDE side of the shaft while its stator simply pressed fit on the appositely designed inset of the NDE end cap. The resolver (ADMOTEC RO3620-K) was obviously used for the rotor position measurement needed for the vector control of the built HS-SyR machine. Figure 105 illustrates the complete machine mounted on the loading test bracket. The water cooling of the prototyped machine is provided by an external unit able to measure the outlet temperature of the coolant. The flow rate was confirmed once during the set-up of the cooling system, by an external flowmeter and the measurements lie in the expected range 15-20 l/min.



a) b)

Figure 105: Complete machine mounted on the bracket of the test rig: a) rear view, b) top view.

7.2 Experimental rig layout

- *Test rig*

The manufactured prototyped was coupled with the loading rig via a connecting shaft, made of Peek, whose dimensions follow the recommendations of the test-rig manufacturer. The most important components of the loading rig, shown in Figure 106, are:

- 37.7 kW-20krpm induction motor (OSWALD),
- speed increasing gearbox with a ratio 1:5.975 (Torquemeters Ltd),
- 3 Nm torquemeter (Torquemeters Ltd type ET0044),
- 4 quadrant regenerative drive (Control Techniques, Unidrive/SP4403),
- auxiliaries (gearbox and torquemeters lubrication systems, motor air-cooling unit).

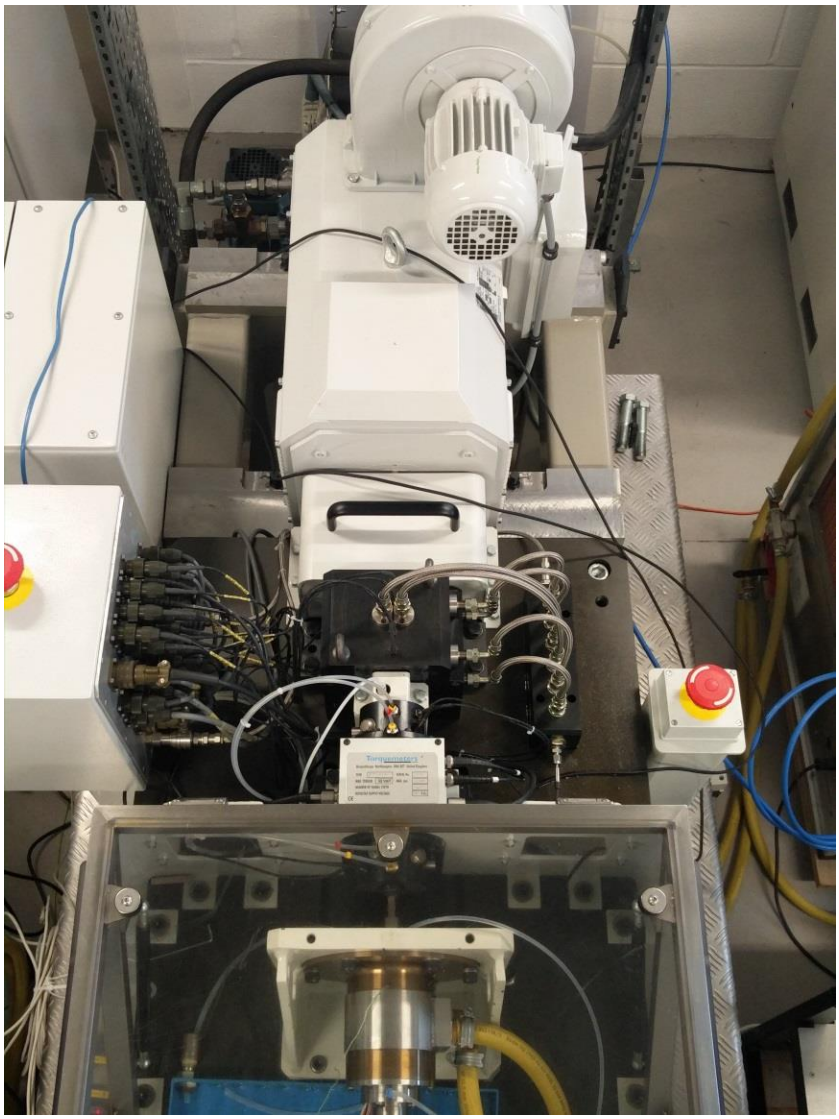


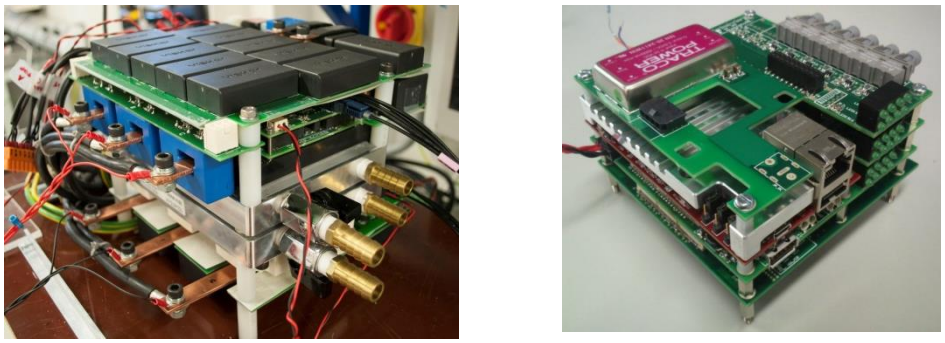
Figure 106: Layout of the loading rig

- *Converter and control platform*

The power electronic converter used to supply the prototyped HS-SyR machine was an available, 50kW SiC three phase bridge converter built and designed in-house[7]. Figure 107a shows the mentioned converter featuring three ROHM 1.2kV 180A half bridge full SiC power modules, mixed ceramic and MKP film

[7] In particular, it was designed and built by another member of the group (Giovanni Lo Calzo).

dc-link capacitors, liquid cooled cold plate and custom made gate drivers able to drive the switches up to 60 kHz switching frequency. Clearly the converter was not designed for the power rating of the HS-SyR developed during in this work; however it has allowed reaching the required value of switching frequency enabling the high speed operation of the built machine. During the test the switching frequency was set to 40 kHz guaranteeing an enough high ratio between the switching and the fundamental frequency over the whole operating speed range. Figure 107b reports the control platform used during the test for acquiring the currents and rotor measurements, to implement the control algorithm and to generate the required control signals for the gate drivers. The control platform is based on Xilinx Zynq7020 SoC and features 24 fibre optics channels, 16 14bit 1Msps ADCs channels, communication interfaces, resolver and encoder interface. Similar to the SiC-based converter described above, the control platform has been designed and programmed in-house by other members of the PEMC group[8].



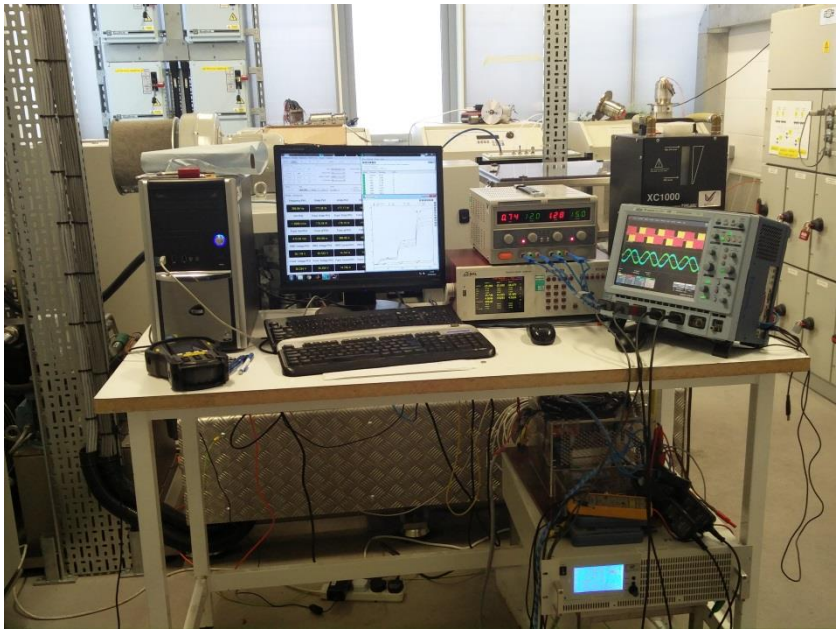
a) b)

Figure 107: a) power electronic converter, b) control platform

[8] Respectively by Giovanni Lo Calzo and Andrea Formentini



a)



b)

Figure 108: a) top view of the experimental layout, b) view of some of the measurement instrumentations (power analyser and oscilloscope), power electronic converter with its cooling, and dc power supply

- *Power supplies and instrumentations*

The converter was supplied by a 15kW dc power supply (ETPS LAB/HP 0-600V/0-25A) while the gate driver board by another external smaller power

supply. Several measurement systems have been used to monitor the most salient electrical, thermal and mechanical variables. The mechanical power at the rig shaft was recorded thorough the rig torquemeter while the electrical power by means of a power analyser (Newtons4th Ltd, PPA5500). Phase currents and voltage were also monitored with an oscilloscope (Lecroy Waverunner 64Xi); the winding temperatures were recorded with a thermocouple data logger (Pico TC-08) while the vibrations level was measured by a SKF Microlog MX system. An overview of the described set up is given in Figure 108.

7.3 Magnetic model identification at constant speed

The need to identify the magnetic model of a salient synchronous machine, i.e. the flux-current relationships in the d-q reference frame, is twofold: validate the FE calculated performance and perform an accurate vector control.

7.3.1 Vector control scheme

The majority of the vector control schemes rely on the knowledge of the magnetic parameters. If the latter (used in the control) differ from the real ones, the control becomes in the best case scenario non-efficient and in the worst case unstable. Although there are several algorithms which can be applied for

the control of a SyR machine [49, 70], the experimental tests in this work have been carried out with the "standard" vector control scheme featuring the PI current controllers on both d-q axis and an external PI speed controller [142]. The d- and q- axis current references are provided by two lookup tables whose input is obviously the output of the speed controller. The decoupling between the two axes is insured by adding two terms to the reference voltages which need the knowledge of the axis inductances. Also these two values are selected from two look-up tables according to the measured d- and q-axis currents. Such look-up tables provide both current references and inductances in the d-q reference frame along the MTPA trajectory (in the constant torque region). It is clear that the adopted control scheme needs the knowledge of four[9] look-up tables; the latter can be derived from the FE study or more precisely by an experimental identification as previously mentioned.

7.3.2 Magnetic model identification procedure

Several magnetic model identification procedures have been presented in literature and a good overview has been recently given in [58, 143]. In the following the identification approach presented in [144] has been implemented for the following reasons:

[9] The look up tables can be reduced to three if the speed PI provides the q-axis reference current instead of the torque reference; then d-axis reference current is obtained with a single look-up table in which the locus of the both axis currents at MTPA is stored.

- it does not rely on the knowledge of the stator resistance which varies with the winding temperature;
- the voltage used for the flux estimation can be the reference voltage and so the voltage measurement is not necessary;
- it does not need to perform any inverter non-linearities compensation.

This procedure performs the identifications of the fluxes for every point in the d-q axis current plane via a sequence of tests carried at constant speed. The speed test needs to be low enough in order to be able to neglect the iron losses equivalent current respect to the magnetizing current and high enough to achieve reasonable voltage levels (in this case the test is performed at 5000 rpm). The ploy used to avoid using the stator resistance during the flux estimation consists in performing two tests for each point of the d-q current plane, namely one in motoring mode and the other in generating mode. In fact two complex conjugate current vectors produce two complex conjugate flux linkage vectors (equation 59a); therefore from the vector voltage equations in the two operating conditions (equation 59b) the two relationships allowing the flux estimation (equation 59c) can be easily derived after some manipulations[10] (with ω representing the electric frequency):

$$\begin{cases} \overrightarrow{I_m} = i_d + j \cdot i_q \\ \overrightarrow{I_g} = i_d - j \cdot i_q \end{cases} \Rightarrow \begin{cases} \overrightarrow{\lambda_m} = \lambda_d + j \cdot \lambda_q \\ \overrightarrow{\lambda_g} = \lambda_d - j \cdot \lambda_q \end{cases} \tag{59a}$$

[10] In particular, they are respectively derived starting from the quantities $(\overrightarrow{V_m} + \overrightarrow{V_g})/2$ and $(\overrightarrow{V_m} - \overrightarrow{V_g})/2$.

$$\begin{cases} \overrightarrow{V_m} = v_{dm} + j \cdot v_{qm} = R_s \cdot \overrightarrow{I_m} + j \cdot \omega \cdot \overrightarrow{\lambda_m} \\ \overrightarrow{V_g} = v_{dg} + j \cdot v_{qg} = R_s \cdot \overrightarrow{I_g} + j \cdot \omega \cdot \overrightarrow{\lambda_g} \end{cases} \quad (59b)$$

$$\begin{cases} \lambda_d = \dfrac{v_{qm} + v_{qg}}{2 \cdot \omega} \\ \lambda_q = -\dfrac{v_{dm} - v_{dg}}{2 \cdot \omega} \end{cases} \quad (59c)$$

The application of equation 59c is based on the hypothesis that the shaft speed and the stator resistance do not vary in the two operating modes[11]. A small resistance/temperature variation is obtained if the period of the two operating modes is as lower as possible; however the latter needs to be long enough to let the speed reach the steady state condition after the unavoidable speed transient (which depends on the speed PI parameters of the loading drive). As previously mentioned the voltage references can be used for the flux estimation in equation 59c (instead of the real voltages whose measurement is not trivial) without any loss of accuracy. In fact the combination of the motoring and generating modes compensates the inverter errors (i.e. the difference between the reference and the real voltage), as elegantly shown by a vector diagram in [58], if all signals are averaged over at least one sixth of the electrical period (being 1/6th the period of the inverter dead time distortion). In general it is a good practice to average both voltage and current signals used in the flux estimations over a wider time span. In particular averaging over at least one mechanical period allows 1) extracting only the fundamental components of

[11] It is worth to notice that the winding temperature and so the stator resistance can change during the mapping of the d-q current plane. This does not affect the flux estimation as long as the winding temperature in the two operating conditions of each point of the plane can be considered constant. This is obviously true only for machine without PMs.

the variables 2) compensating the influence of all harmonic effects having a periodicity equal to a multiple of the rotor mechanical frequency (m.m.f harmonic, inverter non-linearities, rotor eccentricity, etc.) and 3) removing the current noise measurement. Figure 109 shows the currents, voltages, speed and torque time-dependent behaviours (in both motoring and the generating modes) recorded with the control platform during the experimental identification of one point of the d-q current plane. The variables used to estimate the flux linkages have been averaged over the time window placed in the last period of each operating mode (always reported in the same figure). It is worth to underline that the current references have been smoothed with a first order filter with the aim of avoiding a sharp torque change which could damage the several peak shafts present between the components of the loading rig and between the latter and the machine under test.

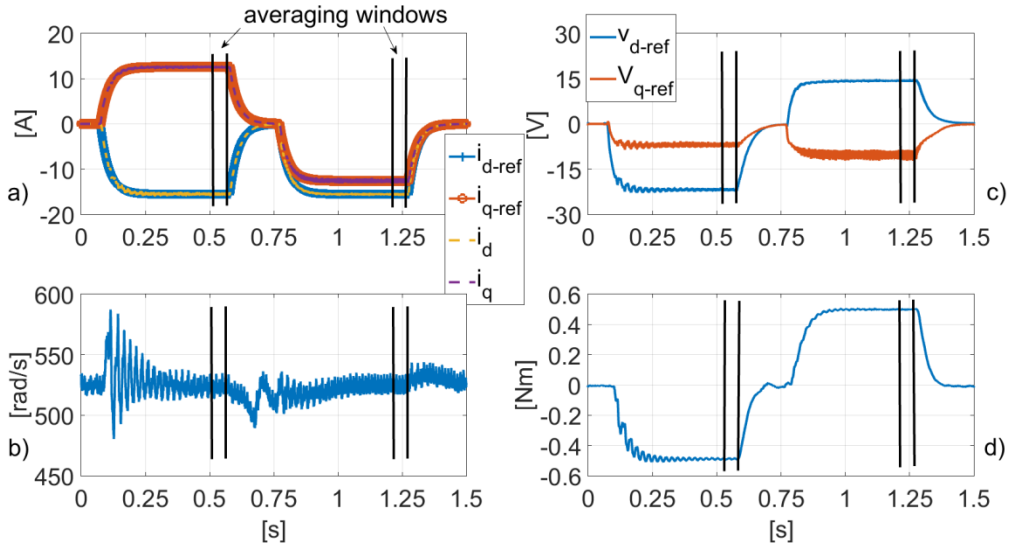


Figure 109: Example of the salient variables time-behaviour during the identification test of one point of the d-q current plane: a) reference and measured currents, b) shaft speed transient, c) reference voltages, d) torque transient.

Figure 110 reports an example of the phase currents recorded with the oscilloscope during the experimental flux identification.

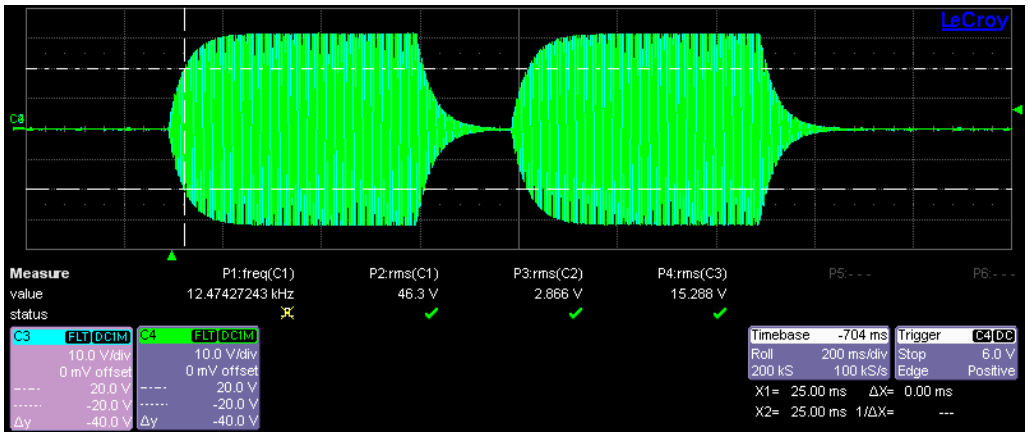


Figure 110: Example of the two current phase behaviours during the experimental magnetic model identification of one point of the d-q current plane.

7.3.2 Comparison between the measured and the FE magnetic model

The identification method described in the previous paragraph has been implemented (in an automatic way on the control platform and in matlab) in order to estimate the flux linkage on a quite dense grid in the 2nd quadrant of the d-q axis current plane. Figure 111 and 112 compare the measured d- and q-axis fluxes and the FE-calculated ones as function of the homonymous axis current and having the heteronymous axis current as parameter. The same figures also report the error between the measured and the FE values. The measured q-axis flux is lower than the FE-calculated one over all the considered i_d and i_q range. Analysing Figure 111 it can be notice that the difference between the measured and the expected λ_q is particularly high in the

non-linear region of the q-axis flux-current curve being almost 15% (i.e. the knee of the curve). As i_q increases the discrepancy between the FE and the measured value decreases till 5% in the most saturated point; in addition the error slightly worsen when i_d increases. The difference between the FE-evaluated and the measured value of the d-axis flux is definitely lower as depicted in Figure 112 with respect to the discrepancy of the q-axis flux linkage.

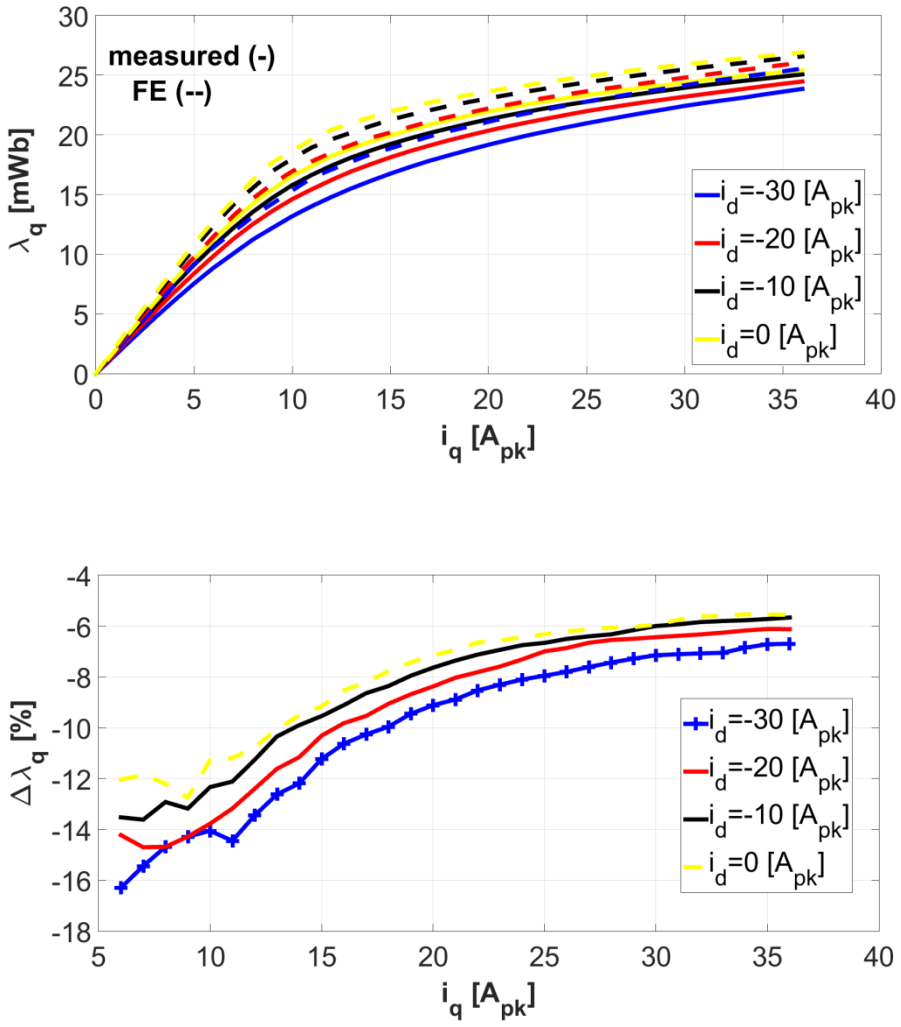
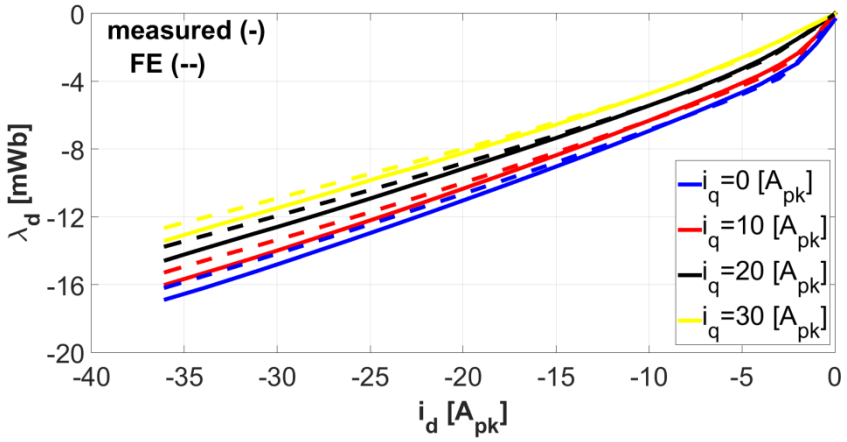
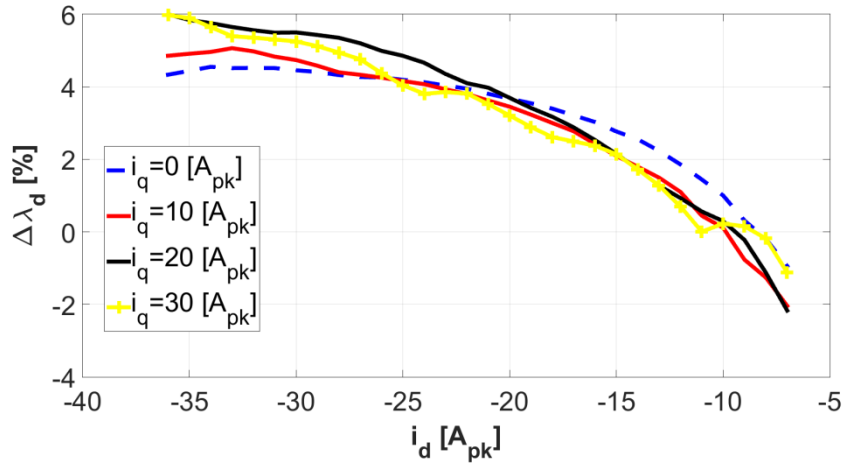


Figure 111: FE-calculated and experimental estimated flux linkages a) q-axis and b) d-axis

In fact, the measured λ_d is still higher (and so worsens) than the expected value over all the considered current range, but their difference is about 6% in the worst condition. Differently than the discrepancy of the q-axis flux, in this case the error tends to increase as the both axes currents increase. Figure 113 reports the measured and the FE d- and q-axis fluxes as function of the current amplitude in the MTPA condition. As mentioned above, it is clear that the discrepancy of λ_d is much lower than that of λ_q.



a)



b)

Figure 112: Relative difference between the FE-calculated and experimental estimated flux linkages a) q-axis and b) d-axis

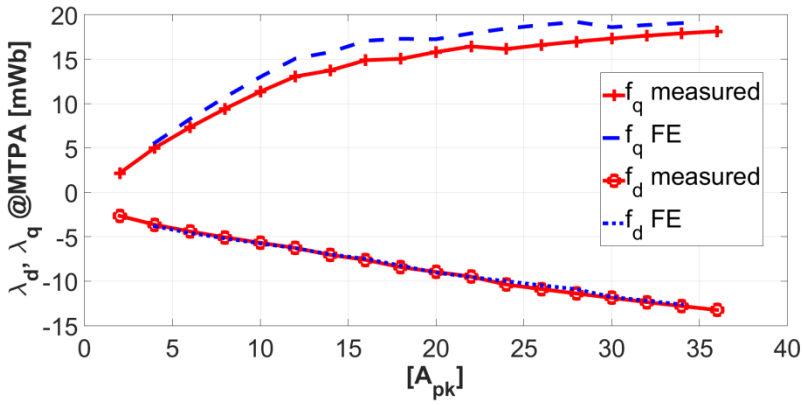
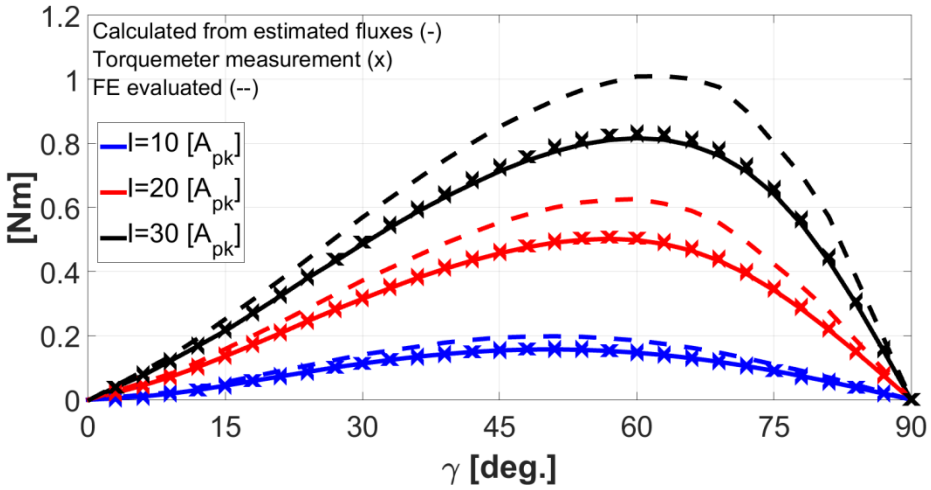


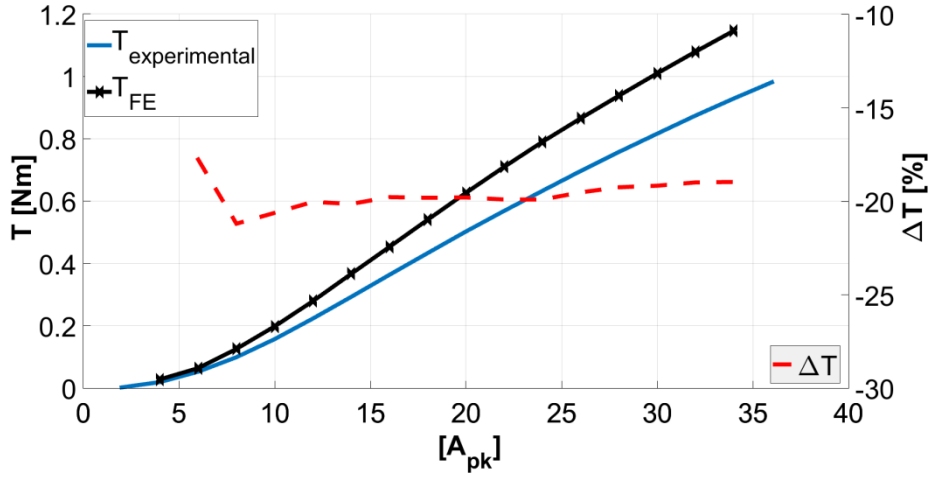
Figure 113: Measured and FE-calculated d- and q-axis fluxes as function of current module at the MTPA condition.

The error between the measured and the FE calculated d-axis flux in the rated current and MTPA condition lies within the maximum deviation due to the manufacturing tolerances (6%). The latter have been calculated in Chapter 5 for both deviations of the iron bridge thickness (Figure 76) and barrier heights (Figure 78). The discrepancy of the q-axis flux cannot be ascribed to the manufacturing tolerance. In fact in the rated condition the error of λ_q is much higher (almost 10%) than the deviation calculated in Chapter 5 due to the possible change in the dimensions of the all the iron bridge thickness and barrier heights (2%). Figure 114a reports the torque as function of the current phase angle calculated by the FE solver, calculated from the estimated flux and measured by the torquemeter. The validity of the implemented flux identification method is clearly proved by the almost null difference between the torque calculated by the measured flux and the one measured with the torquemeter. The obvious consequence of the dissimilarity between the expected fluxes and the real one is the reduction of the produced torque. Figure 114b shows the torque at MTPA condition as function of the current module

experimentally and FE evaluated. The reduction of the torque is constantly 20% over all the considered current module range. Considering the real torque-current curve, the current needed to achieve the rated torque (0.6 Nm) has to be incremented of 15% respect to the expected rated current.



a)



b)

Figure 114: a) Torque as function of the current phase angle: FE-evaluated, measured by the torquemeter and calculated from the estimated flux; b) torque at MTPA as function of the current estimated from flux and FE-evaluated and their percentage difference.

With the aim of investigating the reasons behind the difference between the expected and the measured performance, the magnetic properties of both stator

and rotor materials have been measured in different mechanical stress conditions with a specially designed test setup. The results of the materials properties characterizations along with some specifications of the test setup will be reported in the next paragraph.

7.4 Magnetic material properties characterizations

7.4.1 Introduction

The in-house experimental setup for the magnetic properties characterization is shown in Figure 115 and it mainly comprises a linear power amplifier, measurement interface, temperature control module, a fluxmeter and the real time computer interface. Several methods of measuring the iron losses are available: an Epstein frame, a single sheet tester and a toroidal core measurement. For all of them, the iron losses are evaluated by the wattmeter method (starting from the current of the primary coil and the voltage of the secondary coil, the power is calculated and then the copper losses at the real temperature are subtracted). This available test setup provides the capability to test electrical steel samples of standard geometries in electromagnetic, mechanical and thermal conditions which replicate as much as possible the ones in which the material is subject in the real scenario. In particular, it is possible to measure the one dimensional iron losses using sinusoidal and non-sinusoidal flux excitations up to 20 kHz in soft magnetic material when subject

to tensile and compressive stress (respectively up to 500 MPa and 150MPa)[12]. An in-detail description of the outlined experimental setup as well as a good overview of the several iron losses mechanisms can be found in [145].



Figure 115: Control rack of the magnetic properties characterization facility available in-house and single sheet tester used for measurements under tension and compression

[12] The facility is also able to measure 1) the magnetostriction under 1D excitation under different thermal and stress condition, 2) the 2D iron losses under sinusoidal and non-sinusoidal excitation up to 20 kHz and 3) the iron losses of hard magnet materials when subject to compressive and thermal stress.

For the rest of this section, the normalized DC magnetization curve and the iron losses under sinusoidal excitation of the stator and rotor materials are measured with the single sheet tester under different mechanical conditions.

7.4.2 Stator material

As mentioned in Chapter 2 the stator material is the JHNF600 (which is 0.1mm thick) and it has been tested in the unstressed condition and under compressive stress. The first test is obviously needed to compare the magnetic data provided by the manufacturer and used in the FE solver to predict the performance with the real data. The second test emulates the mechanical stress scenario which the material experiences when inserted in the housing. In fact, as mentioned in the first paragraph of this chapter, the stator lamination stack once manufactured has been interference fitted into the housing; to such interference corresponds a compressive pressure in the range of 25-75 MPa[13]. Figure 116a shows the datasheet and the measured BH curve and their percentage difference (dashed line).

[13] The range obviously depends on the imposed manufacturing tolerances of the stator bore diameter and the housing inner bore.

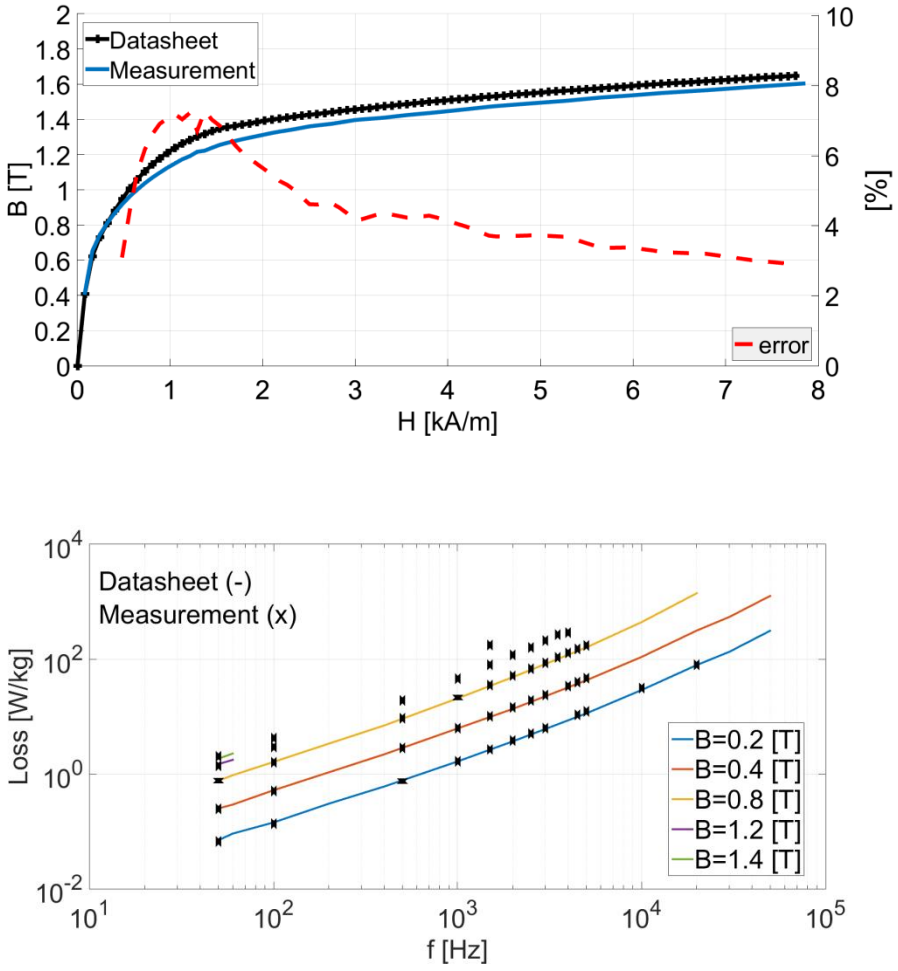
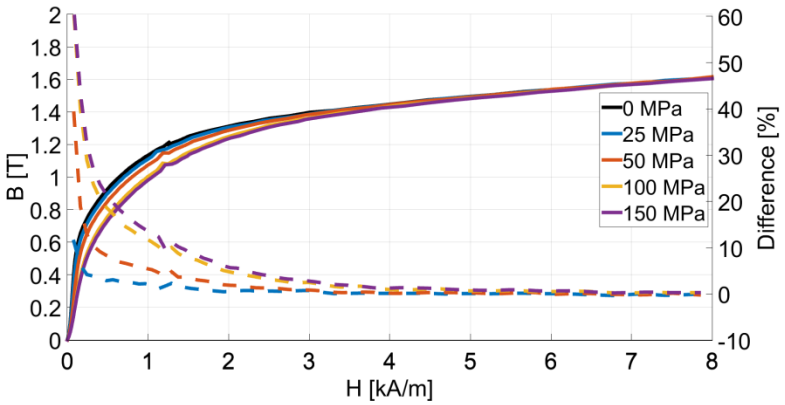


Figure 116: Datasheet and measured characteristics of the JNHF600 a) DC magnetization curves and their percentage difference and b) specific iron losses

The BH curve implemented in the FE software is higher than the measured one over the entire considered H field range. In particular their difference is higher in the knee region reaching a maximum of 8% and it reduce up to 3% in the high saturation region. Despite the discrepancy of the DC magnetization curve, the measured iron losses show a good agreement with the data provided by the manufacturer for all the considered frequencies and flux densities as reported in Figure 116b. When the compressive stress is applied to the material only the knee region of the BH curve is affected as it can be seen in Figure 117a. The

difference increases as the compressive stress increase and it reaches almost the 15% for the highest stress (150 MPa) in the middle of the curve-knee (i.e. at 1 kA/m). The permeability rapidly decreases even when a small compressive stress is applied and then the rate of change reduces as the stress increases; these results are similar to the one reported in [146, 147]. Figure 117b reports the measured iron losses when the material is in the unstressed condition and subject to the maximum compressive stress (150 MPa). For all the considered frequency and flux density values the iron losses when the material is subject to the compressive stress increase respect to the unstressed condition[14]. The rate of increment of the specific iron losses is high for small stress value and then decreases till to become almost zero for the highest stress range; also this trend has been reported in [146]. It is worth to underline that the iron losses at low flux densities are more affected by the compressive stress respect to the higher values (this feature is also related with the microscopic material properties, i.e. grain size) and they tend to slightly increase with the frequency.



a)

[14] Note that the same figure shows also some outliers of the measurements which have not been removed.

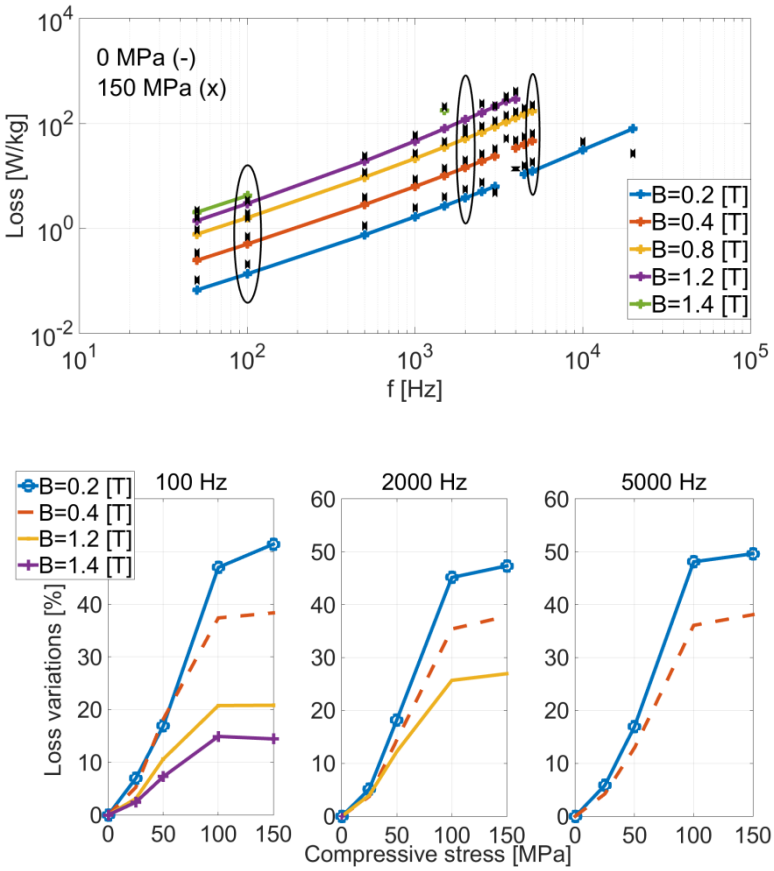


Figure 117: Measured characteristics of the JNHF600 material when subject to different compressive stress: a) DC magnetization curves and their differences respect to the unstressed condition, b) specific iron losses with the material unstressed and subject to the compressive stress of 150 MPa, c) percentage variations of the specific iron losses as function of the compressive stress for different frequencies and flux densities

7.4.3 Rotor material

Figure 118a reports the datasheet and the measured dc magnetization curve in the unstressed condition and their percentage difference of the rotor material[15] (35HXT780T whose lamination is 0.35 mm thick). Differently than the stator material, the curve provided by the manufacturer is always lower than the measured one over the entire H field range.

[15] The rotor material has been kindly provided free of charge by Nippon Steel and Sumitomo Metal.

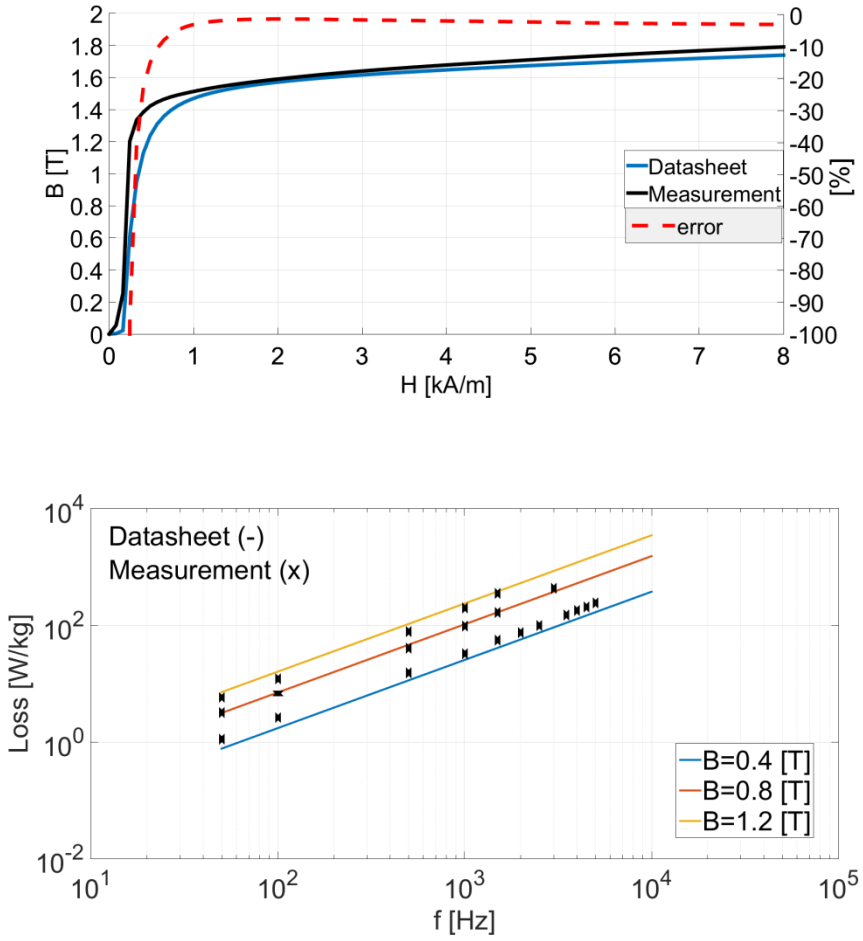
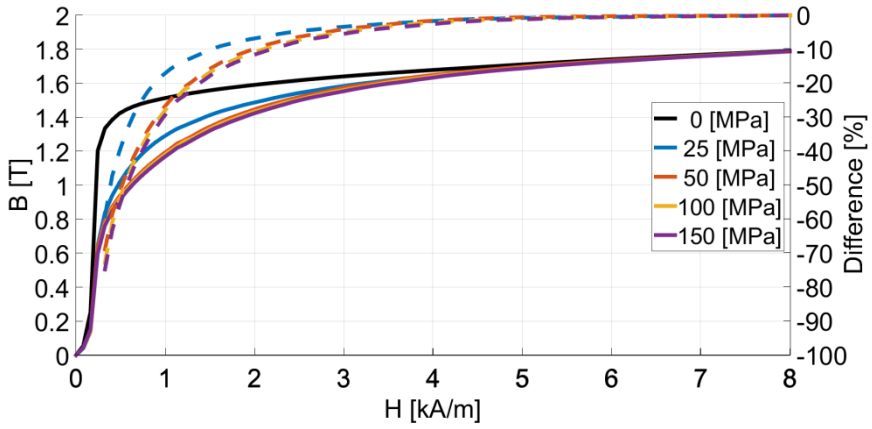


Figure 118: Datasheet and measured characteristics of the 35HXT780T a) DC magnetization curves and their percentage difference and b) specific iron losses



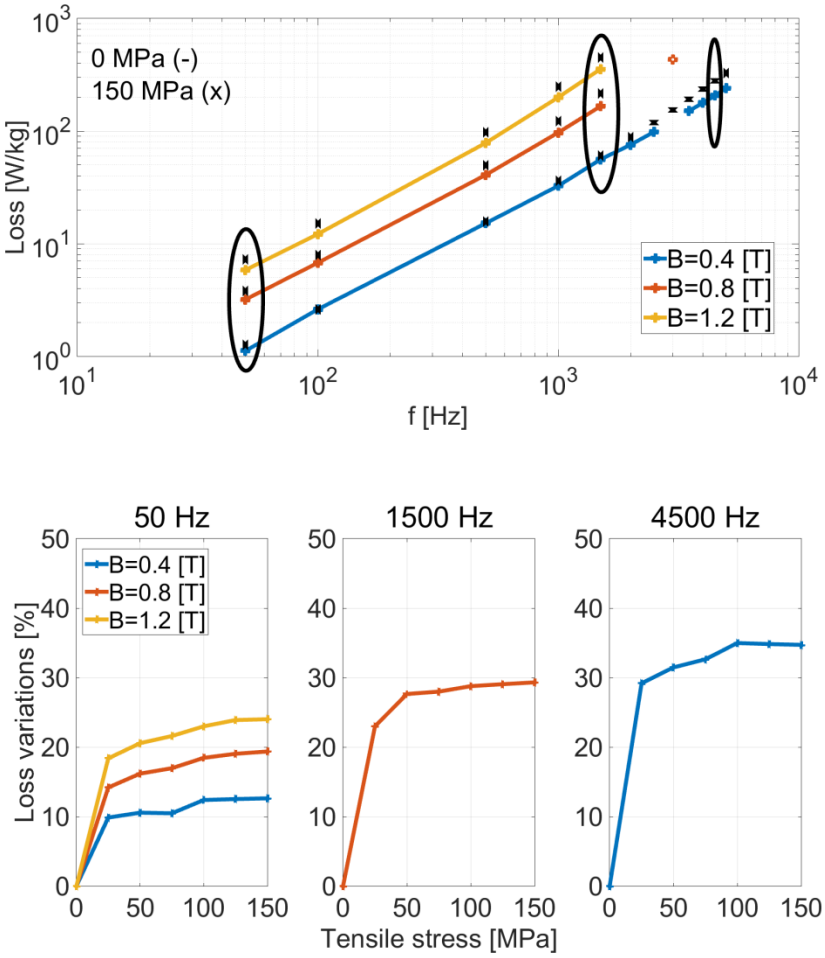


Figure 119: Measured characteristics of the 35HXT780T material when subject to different tensile stress: a) DC magnetization curves, b) specific iron losses with the material unstressed and subject to the tensile stress of 150 MPa, c) percentage variations of the specific iron losses as function of the tensile stress for different frequencies and flux densities

The error is higher in the knee-region of the curve and tends to decrease up to 3% for deep saturation levels. The measured iron losses (shown in Figure 118b) are quite different with respect to the datasheet values being their difference about 75% in the worst case area. In particular, the loss data provided by the manufacturer are lower than the measured ones for the low flux density values and conversely they are too high for higher flux densities. Figure 119a outlines the dc magnetization curves when the material is subject

to different tensile stresses. Also in this case the knee region of the BH curve is the most affected and the rate of change of the permeability in that region is extremely high even for low stress values and then decreases towards zero for the highest considered tensile stress. The maximum deviation at 150 MPa and 1 kA/m is about 20%. Also the iron losses increase as the tensile stress increases as shown in Figure 119b and c. The rate of increment of the iron losses is very high for small value of stress and then also converges towards zero. Differently from the stator material, the percentage iron loss variation seems to be bigger for high flux densities (for a given stress) and they always tends to increase with the frequency. A test campaign of the rotor material under compressive stress is still on going at the moment of writing and thus it cannot be included in this work.

7.4.4 Considerations on the discrepancy between the expected and measured performance

The measured dc magnetization characteristics of the constituent materials of the built machine (in the unstressed condition) show a conspicuous differences respect to the data provided by the manufacturers and used in the FE-solver to predict the electromagnetic performance. Such discrepancies regard both the knee of the BH curve and the high saturation region. In particular the data implemented in the FE software for the stator material overestimates the real curve of at least 3% over the entire range of H field reaching a maximum

deviation of 8% in the knee. Regarding the rotor material, the data employed in the FE solver underestimates the real curve of about 3% over the whole H range reaching a peak of discrepancy of 20%. In addition it has been shown that the stator laminations when subjects to compressive stress similar to the one experienced in the real assembling (due to the interference with the housing) worsen only in the knee region of the BH curve of about 10%. Also the measurements of the rotor material under tensile stress have revealed a reduction of the knee part of the magnetization curve of about 20%. All the above mentioned discrepancies are possible reasons for the 10% reduction of the measured q-axis flux of the built machine respect to the expected FE-evaluated trends. The re-evaluation of the electromagnetic performance of the prototyped machine with the measured magnetic properties in unstressed mechanical condition has not been carried out yet simply due to time constraints[16]. In addition, the exact FE calculation of the of the electromagnetic performance when the stator and the rotor cores are shrink fitted respectively in the housing and on the shaft was out of the scope of this work (as well as the exact FE-evaluation of modified rotor material properties due to the centrifugal stress).

[16] The additional time required for such analysis would have span beyond the PhD project time frame.

7.5 Motoring no load test

With the aim of implementing an accurate vector control of the built machine, the measured magnetic model has been used to build the look-up tables expressing the torque and the inductances along the MTPA trajectory. In fact, as mentioned in the paragraph 7.3, the prototyped HS-SyR machine operates always in the constant torque region along the MTPA trajectory. Figure 120 reports the contours of the measured torque and d- and q-axis inductances highlighting the mentioned locus.

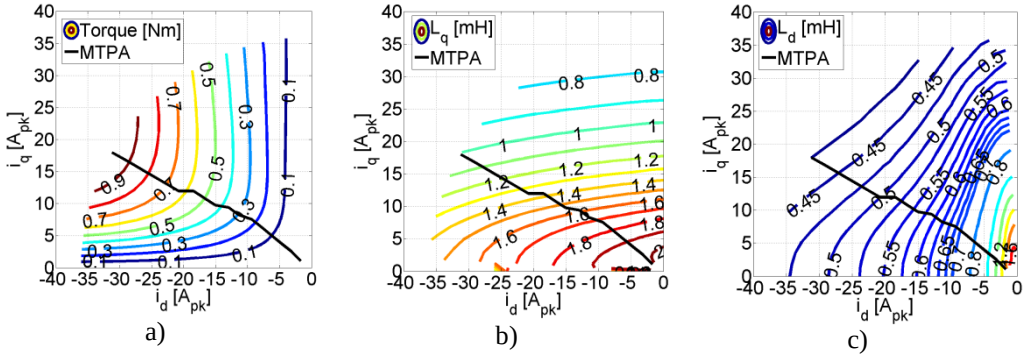


Figure 120: Measured torque, q- and d-axis apparent inductances contours with the MTPA locus used to build the look-up tables needed for the vector control

The measured inductances have been also used to re-tune the proportional and integral coefficients of the current PIs. In fact, in the first stage the latter have been determined imposing for both axes a bandwidth of 800Hz based on the rated inductances obtained by the FE analysis. Once measured, the real inductances have been used to update the PI coefficients. The speed PI controller was tuned (carrying out several trial and error tentative) imposing a bandwidth more than 10 times lower than the one of the current loops. Once

the coefficients of the speed and current PIs have been tuned, several motoring no-load tests have been carried out. In particular, the first set of tests aimed at verifying the integrity of the prototype; to do so a series of ramp shaped reference speeds have been imposed having a step of 2000 rpm and a slope of 500 rpm/s. With this approach the maximum speed of 30000 rpm has been successfully reached without measuring any relevant vibrations (which were monitored by an accelerometer on the top of one bearing seat). Figure 121a shows the transient behaviour of the speed, voltage and currents (in the d-q reference frame) acquired on the host PC from the control platform during the last step, i.e. from 28 to 30 krpm. The same figure also reports the steady state phase currents, dc link voltage and duty cycles; it is worth to underline that such tests have been carried out with a dc link voltage halved respect to the rated one. A snapshot of two phase currents measured by the oscilloscope at 30000 rpm is reported in Figure 121b. Figure 122a and b show the speed, voltage and current acquisitions during a test in which a trapezoidal speed reference has been imposed reaching a maximum speed of 35 krpm.

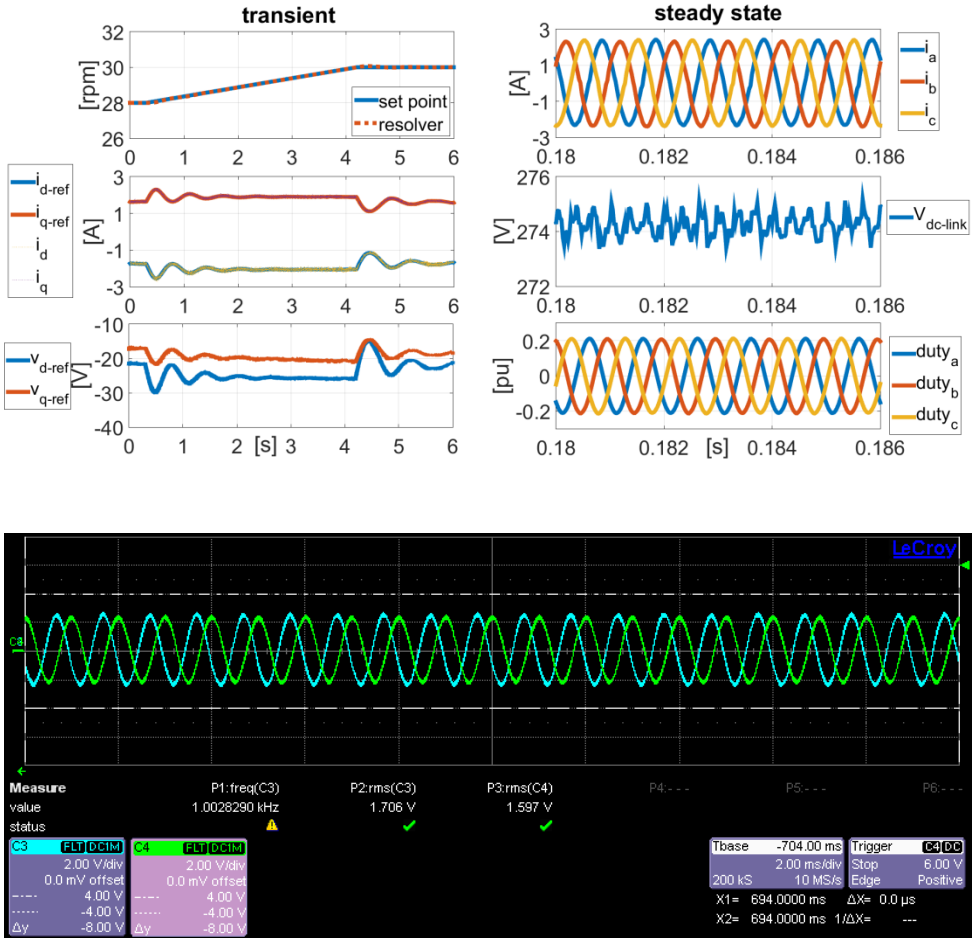


Figure 121: a) Transient and steady state acquisitions during the no-load motoring tests in which the speed increases from 28 to 30 krpm, b) snapshot of two phase currents measured by the oscilloscope at 30 krpm

The experimental tests are limited to 35 krpm due to unforeseen difficulties with test-rig vibrations. In order to investigate the reasons of such vibrations a bearing and bearing-housing inspection need to be carried out to check for the incurred wear (possible also due to unprecise bearings assembling) and replace the bearings as required. However time constraints limited the effort of doing such activities.

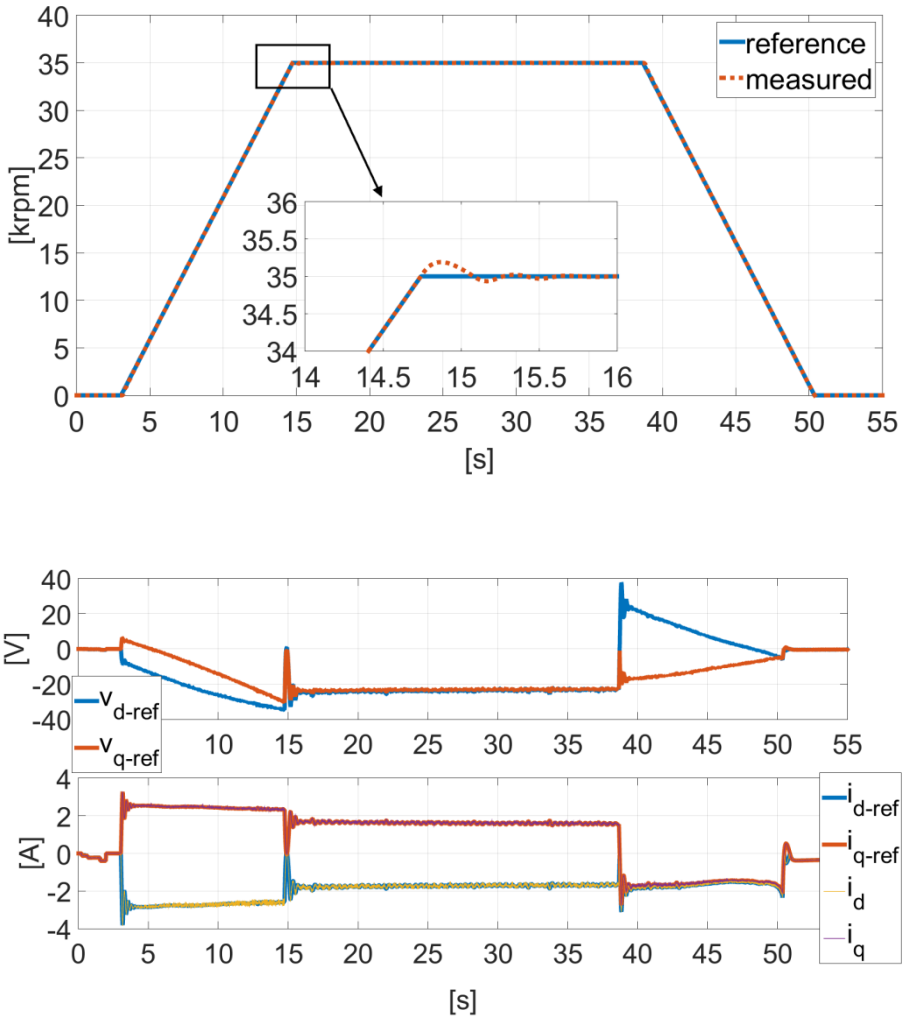
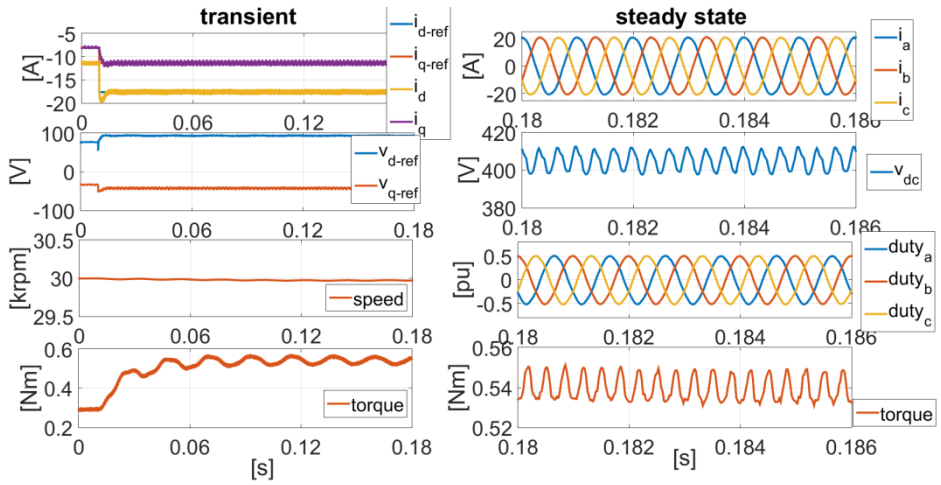


Figure 122: Measurements during a transient motoring no-load speed test up to 35krpm: a) Reference and measured mechanical speed, b) reference d/q voltage/current and measured current

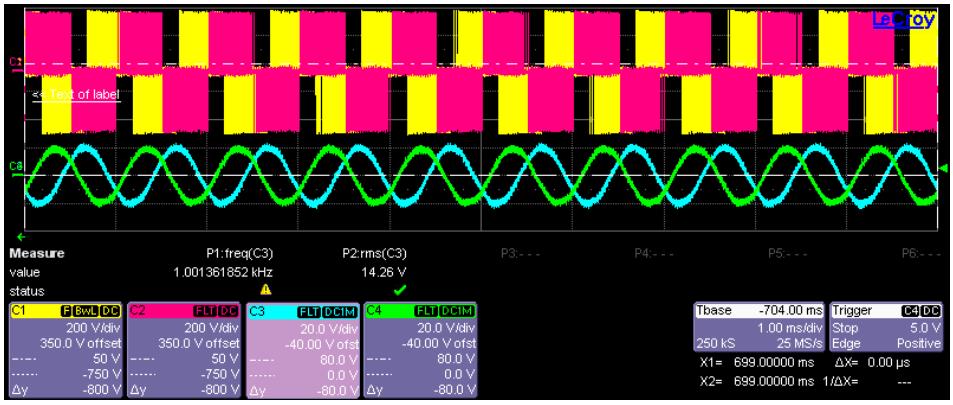
7.6 Generating load test

Several load tests have been performed in generating mode. Motoring mode was not feasible due to limitations introduced by the commercial loading drive which made it impossible to obtain an accurate control of the torque in all the

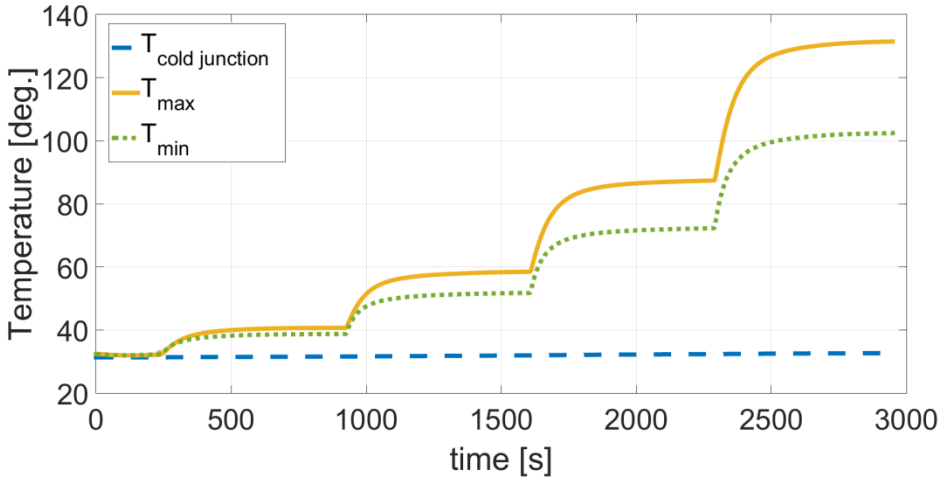
range of interest. The reasons behind this behaviour are two: the rating of the loading drive is much bigger than the machine under test (as well as its inertia) and the PI coefficients of the loading drive were set for the rated conditions (much higher than the range of interest). In order to carry out the load tests a resistance, appropriately scaled for each test (according to the used dc-link voltage and speed) was inserted across the dc-link with the aim of dissipating the produced power. Adopting this approach several load tests have been performed at different speeds (which were imposed by the loading drive) and different current amplitudes. For each current module the imposed d- and q-axis components were obtained from the experimental evaluated MTPA look-up tables. For every considered speed and load, the tests were carried out reaching the thermal steady state and acquiring at regular time sample several electrical, mechanical and thermal variables. The input mechanical power was calculated from the torquemeter and resolver readings (acquired using the control platform) while the output electric power was measured with the power analyser. In particular 20 load tests have been carried out reaching 30 krpm and 28 A_{pk} by means of five speed steps of 6 krpm and four current steps of 7 $A_{pk.}$ Figure 123a shows the transient behaviour of the speed, torque, voltage and currents (in the d-q reference frame) during the current step between 17 and 21 A_{pk}; the same figure also reports the steady state phase currents, dc link voltage, duty cycles and torque. Figure 123b reports the snapshot of two phase currents and phase to phase voltage measured with the oscilloscope in the same operating condition (i.e. 30 krpm and 21 A_{pk}).



a)



b)



c)

Figure 123: Transient and steady state acquisitions during the load generating test at 30krpm in which the current module increases from 14 to 21 A_{pk}, b) snapshot of two phase currents and two phase to phase voltages measured by the oscilloscope at steady state at 30 krpm and with a current module of 21 $A_{pk,}$ c) measured minimum and maximum winding temperatures during the load test at 30 krpm

The last subgraph of the same figure outlines the measured minimum and maximum temperatures experienced by the winding during the load tests at 30 krpm. In the following two sub-paragraphs the results of such set of load tests are compared with the predicted performance shown in Chapter 6.

7.6.1 Comparison between the measured and estimated temperatures

Figure 124a compares the measured maximum steady state winding temperature rises with the ones predicted by the developed thermal network as function of both speed and current amplitude. The estimated trends are quite in line with the measured ones (<5%) for the lowest speed (i.e. 6 krpm). However, as the speed increases, the error between the expected and the measured temperatures increase as also shown in Figure 124b. In particular, the thermal network overestimates the maximum temperature of about 40% in the worst condition, i.e. the highest speed and the lowest current amplitude. The trends of the error between the expected and measured temperature rises can be justified by the following considerations.

The measured stator phase resistance (in dc at ambient temperature) is very similar to the calculated value used during the performance evaluation shown in Chapter 6 (the measured[17] value was 0.173 Ω, 5% lower than the predicted one). This fact (along with the accuracy of the developed thermal model) explains the good agreement between the estimated and the measured temperature rises for the lowest speed. In fact, the dc copper loss is the biggest

[17] The four wires method has been used to measure the dc stator phase resistance.

component of the overall losses in the low speed range (almost the 90% as reported see Figure 101b) therefore the contribution of the iron, windage and ac-copper losses to the temperature rise can be neglected.

The increment of the observed discrepancies as the speed increases can be ascribed to two reasons.

1. One is the possible overestimation of the iron losses and ac-copper losses whose influence obviously increases with the speed. It is important to note that as mentioned in Chapter 6 the evaluation of both iron and copper losses contain several uncertainties and simplifications.

   Regarding the iron losses, their FE-estimated values have been multiplied by a building factor of two in order to cater for their possible increment due to the manufacturing processes. The measurements reported in the paragraph 7.4 show that the iron losses increment of the constituent materials when subject to compressive and tensile stress is not higher than 50% in the worst case scenario. However, this phenomenon is not the only one which can contribute to the iron losses worsening. Other effects must be considered such as the lamination cutting method and its setting (interesting readers may refer to [145, 148, 149]). Considering all these effects, the use of an iron losses multiplying factor of two can be considered reasonable.

   Concerning the ac-copper losses, its calculation is not devoid from inaccuracy as explained in paragraph 6.1. This value was achieved from FE simulations, but as the actual value depends on the actual positions of the strands inside the slot, something which cannot be represented 100% accurately in the simulations, then there is always a level of discrepancy. In

addition the dependence of the ac-copper losses on the temperature has been neglected during the evaluation of the copper losses updated at the estimated winding temperature. Specialized literature [150, 151] has shown that for particular winding layouts (concentrated configuration) the resistance factor (R_{ac}/R_{dc}) decreases as the temperature increases. These facts along with the inaccuracy of the selected evaluation method of the circulating current losses are possible explanations of the overestimation of the winding temperature in the high speed range.

2. The second is obviously associated with the thermal model. In fact, the simplifications (related with the network topology) and uncertainties (related with the calculations of the heat transfer coefficients) inevitably lead to the perceived inaccuracies. An a-posteriori calibration of the thermal model would probably lead to a more precise estimation of the temperatures distribution; however the latter was out of the scope of this work.

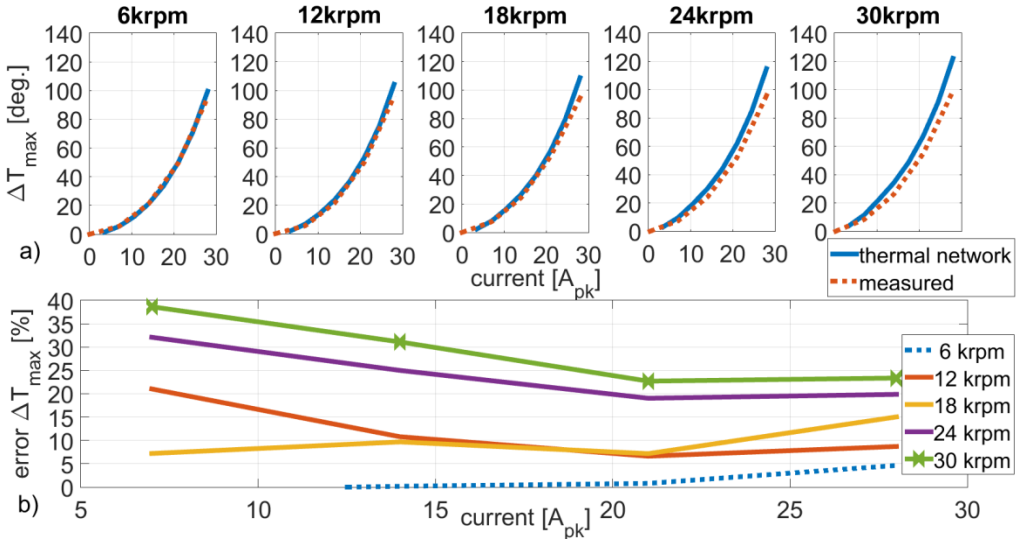


Figure 124: a) Measured and estimated maximum winding temperatures as function the current amplitude for different speeds, b) percentage error between the estimated and the measured temperature

7.6.2 Comparison between the measured and estimated efficiency and power factor

Figure 125a reports the measured efficiency map in the torque-speed plane. Analysing these constant loci, the same trends found in the respective constant loci of the FE-evaluated efficiency reported in Figure 100b can be observed.

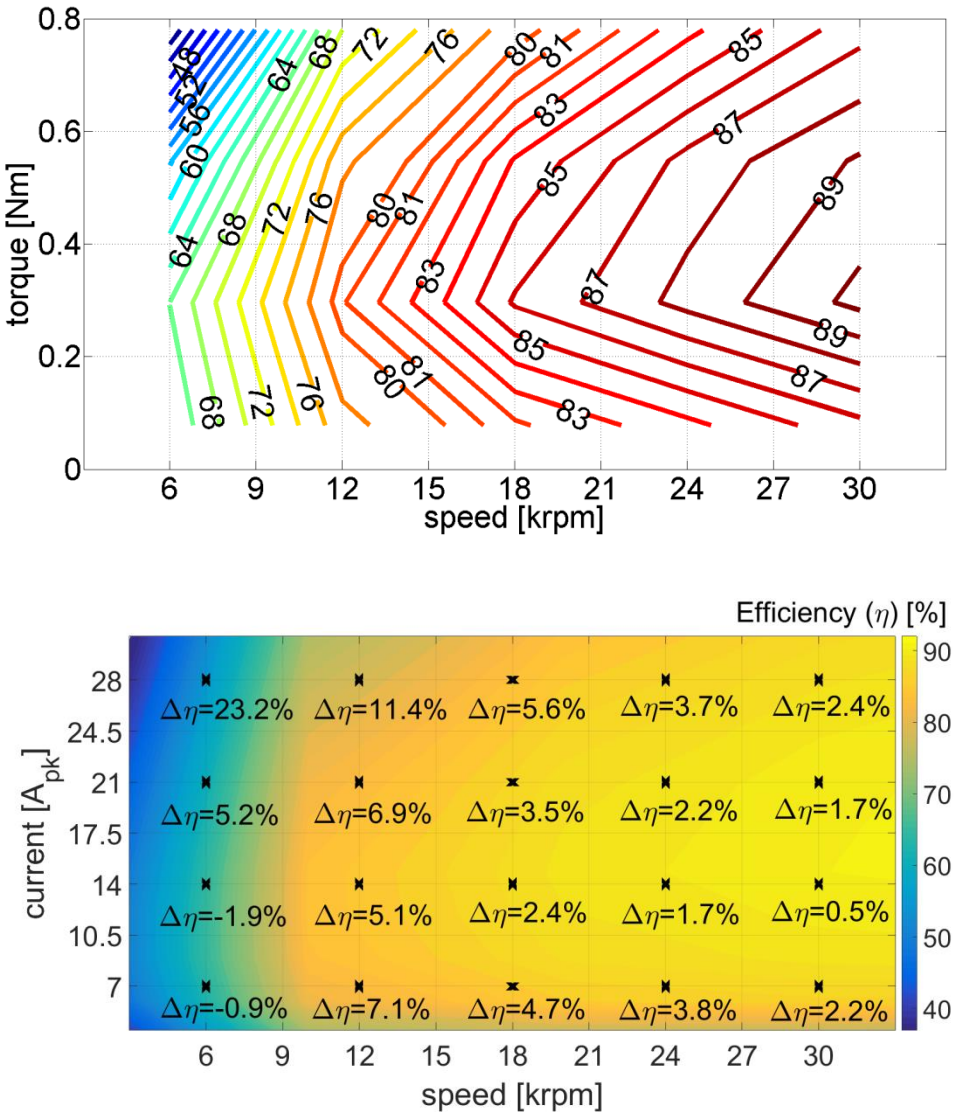


Figure 125: a) Measured efficiency constant loci in the torque-speed plane, b) Coloured contour of the initial estimated efficiency in the current-speed plane and error between the estimated and the measured efficiencies

In fact, for a given speed the efficiency first increases and then decreases with a low rate of change. While for a given torque, the efficiency sharply increases, and then tends to remain almost constant; the decreasing part of the curve cannot be seen in the measured efficiency being the maximum speed tested only 30 krpm. Although the measured efficiency (in the speed range 0-30 krpm) trends are similar to the one FE-estimated, the measured values should be lower than the expected ones of about 20% being the latter equal to the decrement of the developed torque respect to the FE one. This statement would have been true if the overall estimated losses were correct. However, this is not the case as reported in Figure 125b. The latter shows the FE-estimated efficiency map in the current-speed plane with the percentage error respect to the measured values (i.e. $\Delta\eta = 100 \cdot (\eta_{FE} - \eta_{meas})/\eta_{FE}$). It is clear that the FE-estimated efficiency is not constantly higher than the measured one of about 20%. In particular, smaller discrepancies can be observed for higher values of the speed. This observation confirms the conclusion that the overall electromagnetic losses in the higher speed range have been overestimated[18]. Figure 126 outlines the measured and predicted trends of the power factor as function of the current amplitude. As obviously expected the measured power factor is lower than the FE-calculated one of about 15-20% over all the considered current range. The measured power factor at the rated torque condition is 0.46.

[18] It is worth to underline that the measured efficiencies can also contain errors. Such measurement errors usually increase as the power factor of the system under investigation decreases.

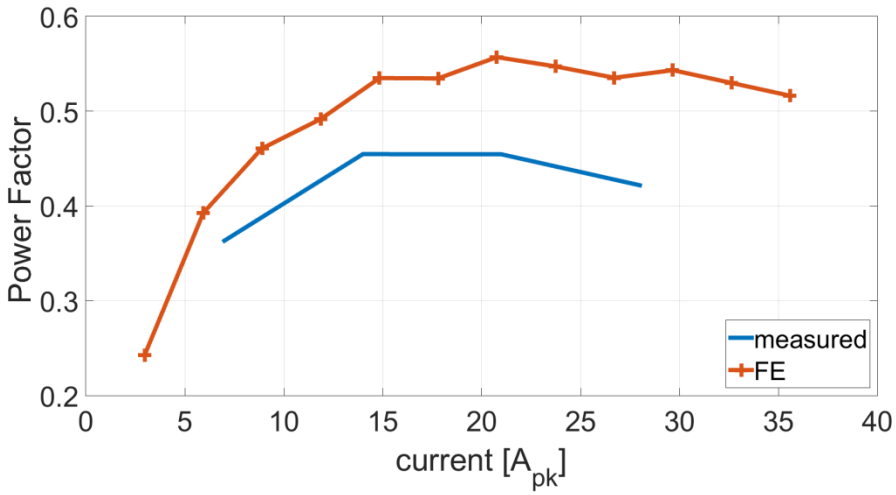


Figure 126: measured and FE-estimated power factor as function of the current amplitude

7.7 Conclusion

In conclusion, the magnetic model of the designed and prototyped machine was first identified and compared with the expected FE-performance. In order to justify the found discrepancy between the measured and estimated performance, a set of tests aimed at fully characterizing the magnetic properties of the constituent materials have been carried out. These measurements have shown a relevant difference between the real dc magnetization curve of the constituent materials and the ones implemented in the FE-solver to predict the performance. The discrepancies between the real and initially-used magnetization curve along with the performance deviation due to the manufacturing tolerances justify the difference between the expected and measured performance. Once the magnetic model has been identified, the machine was successfully tested up to 30 krpm and up to 130% rated torque

showing a measured efficiency of 89% at 30 krpm and the rated torque (0.6 Nm). Some considerations about the differences between the expected and measured temperatures and efficiencies have been carried out revealing a possible overestimation of the electromagnetic losses during the design stage. The main conclusions of the whole multi-physics work developed in designing, analysing and testing the HS-SyR will be reported in next conclusive chapter.

Chapter 8
Conclusion

8.1 Summary of the undertaken work

This thesis has described the work done during the several stages of the design, analyse, manufacture and testing of a high speed synchronous reluctance machine capable of delivering 5 kW at 80 krpm. The study started with a detailed investigation of the analytical design equations of a low speed SyR machine. Then, the speed dependent limitation factors have been included in the design equations with the twofold aims of:

- evaluating the effects of the not-negligible increments of the iron losses and thickness of the structural bridges on the machine performance;
- carrying out the preliminary analytical design of the target machine including some considerations regarding the lamination material selection.

This preliminary design has constituted the base for the following FE design refinements needed to consider the non-linearities of the structural and electromagnetic performance and the influence of all the geometrical parameters. The high number of geometrical degrees of freedom and the long computational time required for the FE evaluation of the electromagnetic and structural performance are the main challenges of the rotor design of a HS-SyR machine. These two challenges project the further problem of selecting the most effective design strategy which correctly balances the performance of the final design and computational time required to achieve such solution. In order to properly evaluate the above mentioned trade-off, a comparative study of two design approaches has been presented. The proposed design procedures, both

based on stochastic optimization algorithms, differ according to whether the electromagnetic and the structural design aspects are truly coupled or not. Both design strategies adopt the same objective functions, i.e. average torque, torque ripple and an innovative structural figure of merit. The latter, called stress factor, essentially describes the mechanical exploitation of the most critical regions of the rotor. Better machine performances are obtained with a reduced computational time, by adopting a physically decoupled optimization in which a proper mechanical optimization follows the electromagnetic optimization. Indeed dividing the research space into two subspaces makes the optimizations shorter and more focused on the physic under consideration. Once the most effective design strategy has been identified, an alternative structural performance index, which allows achieving a more reliable result (compared to the minimization of the stress factor), has been then introduced. Such design criterion simply consists in the minimization of the average total bridge per flux barrier subject to the constraint on the FE evaluated maximum stress. The last step of the design stage has been a comparative study in which several rotor geometries showing different geometrical degrees of freedom (in terms of iron bridge thicknesses and distributions) have been structurally optimized. Through this study, the trade-off between the number of variables describing the iron bridges (and so computational burden) and the final machine performance has been properly investigated. According to this comparative analysis, the best rotor geometry (both electromagnetic and structural wise) has been selected for prototyping.

Once the optimal machine geometry has been selected, before starting its manufacturing, three different analyses have been performed with the following purposes.

1. Evaluate the influence of the geometrical rotor manufacturing tolerances on the machine performance and deduce some considerations about the robustness of the optimal solution. Such analysis has revealed the need of introducing some geometrical modifications of the final design aimed at keeping the maximum stress within the limit also in the worst case scenario introduced by the cutting tolerances.
2. After the calculation of the several loss components, the temperature distribution within the machine has been estimated by means of an in-house developed lumped parameter thermal network. Such analysis has had the aims of establishing the minimum cooling requirements and the thermal limitations of the machine for a given cooling arrangement and winding insulation system.
3. Once all the loss components have been calculated, the complete electromagnetic analysis of the final machine has been carried out considering each loss iteratively updated at the respective temperature calculated from the thermal model. By doing so, an estimation of the machine efficiency has been obtained along with the main performance in both torque-speed and d-q current planes.

During the final stage of the project, the selected final machine has been prototyped and the performance measured carrying out several experimental

tests. The comparison between the measured and FE-calculated magnetic model revealed a 20% discrepancy in terms of the produced torque which was not justifiable by the performance deviations ascribable to the manufacturing tolerance. With the aim of investigating the reasons behind these differences, the magnetic properties of both stator and rotor materials have been measured in different mechanical stress conditions with a specially designed test setup available in-house. The measured dc magnetization curves of the constituent materials of the built machine (in the unstressed condition) show a conspicuous differences respect to the data provided by the manufacturers and used in the FE-solver to predict the electromagnetic performance. Such discrepancies regard both the knee of the BH curve and the high saturation region. The knee of such curve is the only affected region when the materials are subject to compressive and tensile stress. The discrepancies between the real and initial used magnetization curve along with the performance deviation due to the manufacturing tolerances justify the difference between the expected and measured performance. Once the magnetic model has been identified, the machine was successfully tested up to 35 krpm at no-load and up to 30 krpm at load. Tests beyond such speeds were not possible due to the relevant measured machine vibrations. The measured efficiency was 89% at 30 krpm and the rated torque (0.6 Nm). Some considerations about the differences between the expected and measured temperatures and efficiencies have been carried out revealing a possible overestimation of the electromagnetic losses during the design stage and the need of a fine re-calibration of the thermal model.

8.2 Scientific contributions

8.2.1 Specific conclusion

The attempt of providing general design guidelines of high speed synchronous reluctance machine can be considered the truly original scientific contribution of this thesis. This consists in the identification of the most effective design strategy in terms of computational effort and quality of the final design and the introduction of two innovative structural design criteria capable of indirectly considering also the electromagnetic aspect.

In particular, it has been shown that if a FE-based electromagnetic and structural optimization is adopted as rotor design approach, then better machine performance can be obtained with a reduced computational time, by implementing a physically decoupled design approach. In fact, properly dividing the set of the rotor geometrical variables into two subsets, one mainly affecting the electromagnetic performance and the other primarily influencing the structural behaviour, allows the optimization to focus more on the aspect under consideration. Although this conclusion depends on 1) the selected optimization algorithm and its settings, and 2) the chosen rotor parametrization, it can be considered general. In fact, 1) the applications of other optimization algorithms or algorithms with specifically tuned settings would not drastically change this conclusion, and 2) the selected rotor parametrization allows achieving a good compromise between machine performance and

computational time, as proven with the comparative study reported in Chapter 4.

With the aim of performing a structural design, two different mechanical performance indexes have been introduced. One describes the exploitation of the most critical region of the rotor, while the second describes the average dimension of the structural iron bridges. The minimization of one of these indexes (preferably the second one) via a FE-based structural optimization, which act only on a certain subset of rotor variables, allows obtaining rotor geometries with the best average torque (without its direct evaluation during the optimization).

Other innovative aspects of this thesis include:

- the analytical analysis aimed at assessing the influences of the speed dependent limiting factors on the machine performance (Chapter 2);
- the evaluation of the compromise between the rotor geometrical complexity (in terms of iron bridge parametrization) and final performance, (Chapter 4);
- the analysis intended to measure the influence of the manufacturing tolerances on the machine performance (Chapter 5).

Despite the prototyped machine has not been tested up to the maximum speed, the carried out experimental measurements essentially validate the proposed design approach and considerations.

8.2.2 General conclusion

Although a detailed comparison of the proposed design with other machine topologies is out of the scope of this work, it can be generally stated that the HS-SyR machine do not achieve comparable power density obtainable with the more common SPMSM, if the same thermal loading is considered. In addition, the power factor provided by the HS-SyR machine is definitely lower. Where the application does not allow the use high energy permanent magnets, SyR technology is offering a good alternative to SPMSM with the clear drawbacks of a higher electrical loading (and so more complex thermal management) needed to obtain comparable performance. Instead, if compared to IM and SRM, the overall performance can be comparable or superior even with the same current loading with the advantages of the possibility of improving the power factor by inserting PMs inside the rotor structure and using a standard three-phase converter to drive the machine (with reference to the SRM that needs an asymmetrical bridge converter).

8.3 List of published papers

- M. Di Nardo, M. Galea, C. Gerada, M. Palmieri, and F. Cupertino. Multi-physics optimization strategies for high speed synchronous reluctance

machines. In Energy Conversion Congress and Exposition (ECCE), 2015 IEEE, pages 2813–2820.

- M. Di Nardo, M. Galea, C. Gerada, M. Palmieri, F. Cupertino, and S. Mebarki. Comparison of multi-physics optimization methods for high speed synchronous reluctance machines. In Industrial Electronics Society, IECON 2015 - 41st Annual Conference of the IEEE, pages 002771–002776, Nov 2015.
- M. Di Nardo, M. Degano, M. Galea, C. Gerada, M. Palmieri, F. Cupertino, N. Bianchi, and D. Gerada. End barrier shape optimizations and sensitivity analysis of synchronous reluctance machines. In Industrial Electronics Society, IECON 2015 - 41st Annual Conference of the IEEE, pages 002914–002919, Nov 2015.
- M. D. Nardo, G. L. Calzo, M. Galea, and C. Gerada, "Structural design optimization of a high speed synchronous reluctance machine," in 2016 XXII International Conference on Electrical Machines (ICEM), 2016, pp. 2073-2079.
- M. Degano, M. Di Nardo, M. Galea, C. Gerada, and D. Gerada, "Global design optimization strategy of a synchronous reluctance machine for light electric vehicles," in 8th IET International Conference on Power Electronics, Machines and Drives (PEMD 2016), 2016, pp. 1-5.
- R. Abebe, M. Di Nardo, D. Gerada, G. Lo Calzo, L. Papini, C. Gerada . High Speed Drives Review: Machines, Converters and Applications. In Industrial Electronics Society, IECON 2016 - 42st Annual Conference of the IEEE.

8.4 Possible future works

The presented work opens the possibility of carrying out several further investigations. Some of the latter are listed in the following subdividing them in specific and general future works.

Specific future works

- The magnetic material properties characterization aimed at investigating the discrepancy between the measured and FE performance revealed a clear difference between the measured and the adopted dc magnetization curve. Therefore the first obvious step would be to import the measured BH curves in the unstressed condition into the FE models and re-evaluate the machine performance when implemented with the more accurate data. The comparison between the updated FE-performance and the measured one will reveal a smaller level of discrepancy. The latter can be then surely ascribed to the manufacturing and assembling processes (both geometrical tolerance and change in the magnetic properties when the materials are subject to different mechanical stress).
- With respect to the incurred machine vibrations at speeds higher than 35 krpm, an inspection of the general test-rig alignment, and the bearing and bearing-housing needs to be carried out in order to check possible wear and replace the bearings if required. After such inspections, tests above the mentioned speed could be performed.

- A better understating of the efficiency behaviour in the torque-speed plane can be achieved segregating the machine losses into each constituent component by means of dedicated measurements and a fine recalibration of the developed thermal model.

General future works

- Both analytical and FE analysis as well as the measurement on the built prototype have undoubtedly shown the low power factor of this machine topology. As described in Chapter 2, this is mainly due to the incremented iron bridge thicknesses required to assure the structural integrity. A possible solution to overcome this clear disadvantage is the introduction of permanent magnets inside the rotor flux barriers. The design criterion of the amount of PMs needs to consider both electromagnetic and structural performance. In fact, the PM assistance enhances both torque and power factor but its insertions increase the minimum iron bridge thicknesses required to guarantee the same rotor mechanical exploitation.
- The rotor structural design presented in this thesis has been performed assessing only the static load; however a fatigue analysis is definitely needed to evaluate the rotor structure life time resulting from the application of cyclic time-variant loads. Fatigue failures are obviously expected to initiate in the iron bridge areas of the rotor, i.e. where there are the relevant stress concentrations. Several criteria can be applied for the evaluation of the fatigue failure limit; the selection of such criteria heavily depends on the geometry of the iron bridges which define the notch effect as reported in

[97]. Although the latter report a detailed analysis, it is difficult to draw general conclusions about the safety factor to adopt in order to consider also this kind of load during the structural design.

- Small inaccuracies during the rotor assembling could lead to small static and dynamic eccentricity. The latter can cause radial forces [152] (higher respect to SPM) and so machine vibrations. Therefore an in-deep analysis of the radial forces caused by rotor eccentricities can also justify the measured machine vibrations.

[1] J. F. Gieras, *Advancements in Electric Machines*: Springer Netherlands, 2008.

[2] A. Binder and T. Schneider, "High-speed inverter-fed AC drives," in *2007 International Aegean Conference on Electrical Machines and Power Electronics*, 2007, pp. 9-16.

[3] D. Gerada, A. Mebarki, N. L. Brown, C. Gerada, A. Cavagnino, and A. Boglietti, "High-Speed Electrical Machines: Technologies, Trends, and Developments," *IEEE Transactions on Industrial Electronics*, vol. 61, pp. 2946-2959, 2014.

[4] R. R. Moghaddam, "High speed operation of electrical machines, a review on technology, benefits and challenges," in *2014 IEEE Energy Conversion Congress and Exposition (ECCE)*, 2014, pp. 5539-5546.

[5] COMMISSION REGULATION (EC) No 640/2009 of 22 July 2009 implementing Directive 2005/32/EC of the European Parliament and of the Council with regard to ecodesign requirements for electric motors [Online].

[6] I. Tanaka and H. Yashiki, "Magnetic and Mechanical Properties of Newly Developed High-Strength Nonoriented Electrical Steel," *IEEE Transactions on Magnetics*, vol. 46, pp. 290-293, 2010.

[7] J. B. Bartolo, H. Zhang, D. Gerada, L. D. Lillo, and C. Gerada, "High speed electrical generators, application, materials and design," in *2013 IEEE Workshop on Electrical Machines Design, Control and Diagnosis (WEMDCD)*, 2013, pp. 47-59.

[8] A. Tenconi, S. Vaschetto, and A. Vigliani, "Electrical Machines for High-Speed Applications: Design Considerations and Tradeoffs," *IEEE Transactions on Industrial Electronics*, vol. 61, pp. 3022-3029, 2014.

[9] M. v. d. Geest, H. Polinder, J. A. Ferreira, and M. Christmann, "Power Density Limits and Design Trends of High-Speed Permanent Magnet Synchronous Machines," *IEEE Transactions on Transportation Electrification*, vol. 1, pp. 266-276, 2015.

[10] J. D. v. M. R. D. van Millingen, "Phase shift torquemeters for gas turbine development and monitoring," *Proc. Int. Gas Turbine Aeroengine Congr. Expo*, pp. 1-10, Jun. 1991.

[11] A. Borisavljevi´c, "Limits, Modeling and Design of High-Speed Permanent Magnet Machines," *PhD Thesis*, 2011.

[12] W. Tong, *Mechanical Design of Electric Motors*: Taylor & Francis, 2014.

[13] J. D. Ede, Z. Q. Zhu, and D. Howe, "Rotor resonances of high-speed permanent-magnet brushless machines," *IEEE Transactions on Industry Applications*, vol. 38, pp. 1542-1548, 2002.

[14] NSK. *Super Precision Bearings*.

[15] R. F. Schiferl and T. A. Lipo, "Power capability of salient pole permanent magnet synchronous motors in variable speed drive applications," *IEEE Transactions on Industry Applications*, vol. 26, pp. 115-123, 1990.

[16] W. L. Soong and T. J. E. Miller, "Field-weakening performance of brushless synchronous AC motor drives," *IEE Proceedings - Electric Power Applications*, vol. 141, pp. 331-340, 1994.

[17] V. N., "High Saturation, High Strength Iron Cobalt Alloy for Electrical Machines," *CWIEME 2012 - Berlin*.

[18] J. R. Bumby, E. S. Spooner, J. Carter, H. Tennant, G. G. Mego, G. Dellora, *et al.*, "Electrical machines for use in electrically assisted turbochargers," in *Second International Conference on Power Electronics, Machines and Drives (PEMD 2004)*. 2004, pp. 344-349 Vol.1.

[19] A. Boglietti, A. Cavagnino, A. Tenconi, and S. Vaschetto, "Key design aspects of electrical machines for high-speed spindle applications," in *IECON 2010 - 36th Annual Conference on IEEE Industrial Electronics Society*, 2010, pp. 1735-1740.

[20] C. Zwyssig, J. W. Kolar, and S. D. Round, "Megaspeed Drive Systems: Pushing Beyond 1 Million r/min," *IEEE/ASME Transactions on Mechatronics*, vol. 14, pp. 564-574, 2009.

[21] D. Krahenbuhl, C. Zwyssig, H. Weser, and J. W. Kolar, "A Miniature 500 000-r/min Electrically Driven Turbocompressor," *IEEE Transactions on Industry Applications*, vol. 46, pp. 2459-2466, 2010.

[22] W. L. Soong, G. B. Kliman, R. N. Johnson, R. A. White, and J. E. Miller, "Novel high-speed induction motor for a commercial centrifugal compressor," *IEEE Transactions on Industry Applications*, vol. 36, pp. 706-713, 2000.

[23] H. B. Goldstein L., Knowles D., Freedman S., Woods R., Schweizer R. , "Gas-Fired Distributed Energy Resource Technology Characterizations," *Report National Renewable Energy Laboratory, US Department of Energy and the Gas Research Institute*, 2003.

[24] J. Peralez, P. Tona, O. Lepreux, A. Sciarretta, L. Voise, P. Dufour, *et al.*, "Improving the control performance of an Organic Rankine Cycle system for waste heat recovery from a heavy-duty diesel engine using a model-based approach," in *52nd IEEE Conference on Decision and Control*, 2013, pp. 6830-6836.

[25] M. A. Awadallah and B. Venkatesh, "Energy Storage in Flywheels: An Overview," *Canadian Journal of Electrical and Computer Engineering*, vol. 38, pp. 183-193, 2015.

[26] http://www.magnetimarelli.com/excellence/technological-excellences/kers. last access 03 May 2017 [Online].

[27] http://www.torotrak.com/products-partners/products/flybrid/. last access 03 May 2017 [Online].

[28] X. Ma, R. Su, J. Tseng King, S. Wang, X. Zhang, V. Vaiyapuri, *et al.*, "Review of high speed electrical machines in gas turbine electrical power generation," in *TENCON 2015 - 2015 IEEE Region 10 Conference*, 2015, pp. 1-9.

[29] Z. Kolondzovski, A. Arkkio, J. Larjola, and P. Sallinen, "Power Limits of High-Speed Permanent-Magnet Electrical Machines for Compressor Applications," *IEEE Transactions on Energy Conversion*, vol. 26, pp. 73-82, 2011.

[30] N. Bianchi, S. Bolognani, and F. Luise, "Potentials and limits of high-speed PM motors," *IEEE Transactions on Industry Applications*, vol. 40, pp. 1570-1578, 2004.

[31] J. F. Gieras, "Design of permanent magnet brushless motors for high speed applications," in *2014 17th International Conference on Electrical Machines and Systems (ICEMS)*, 2014, pp. 1-16.

[32] F. Luise, A. Tessarolo, S. Pieri, P. Raffin, M. D. Chiara, F. Agnolet, *et al.*, "Design and technology solutions for high-efficiency high-speed motors," in *2012 XXth International Conference on Electrical Machines*, 2012, pp. 157-163.

[33] L. Papini, C. Gerada, D. Gerada, and A. Mebarki, "High speed solid rotor induction machine: Analysis and performances," in *2014 17th International Conference on Electrical Machines and Systems (ICEMS)*, 2014, pp. 2759-2765.

[34] S. L. Ho, S. Niu, and W. N. Fu, "A Novel Solid-Rotor Induction Motor With Skewed Slits in Radial and Axial Directions and Its Performance Analysis Using Finite Element Method," *IEEE Transactions on Applied Superconductivity*, vol. 20, pp. 1089-1092, 2010.

[35] D. Gerada, A. Mebarki, N. L. Brown, K. J. Bradley, and C. Gerada, "Design Aspects of High-Speed High-Power-Density Laminated-Rotor Induction Machines," *IEEE Transactions on Industrial Electronics*, vol. 58, pp. 4039-4047, 2011.

[36] J. B. Bartolo, M. Degano, J. Espina, and C. Gerada, "Design and Initial Testing of a High Speed 45 kW Switched Reluctance Drive for Aerospace Application," *IEEE Transactions on Industrial Electronics*, vol. PP, pp. 1-1, 2016.

[37] A. T. d. Almeida, F. J. T. E. Ferreira, and G. Baoming, "Beyond induction motors — Technology trends to move up efficiency," in *49th IEEE/IAS Industrial & Commercial Power Systems Technical Conference*, 2013, pp. 1-13.

[38] D. G. Dorrell, "The challenges of meeting IE4 efficiency standards for induction and other machines," in *2014 IEEE International Conference on Industrial Technology (ICIT)*, 2014, pp. 213-218.

[39] J. Ikäheimo, J. Kolehmainen, T. Känsäkangas, V. Kivelä, and R. R. Moghaddam, "Synchronous High-Speed Reluctance Machine With Novel Rotor Construction," *IEEE Transactions on Industrial Electronics*, vol. 61, pp. 2969-2975, 2014.

[40] H. Hofmann and S. R. Sanders, "High-speed synchronous reluctance machine with minimized rotor losses," *IEEE Transactions on Industry Applications*, vol. 36, pp. 531-539, 2000.

[41] M. E. H. Zaim, "High-Speed Solid Rotor Synchronous Reluctance Machine Design and Optimization," *IEEE Transactions on Magnetics*, vol. 45, pp. 1796-1799, 2009.

[42] I. Tanaka, H. Nitomi, K. Imanishi, K. Okamura, and H. Yashiki, "Application of High-Strength Nonoriented Electrical Steel to Interior Permanent Magnet

Synchronous Motor," *IEEE Transactions on Magnetics,* vol. 49, pp. 2997-3001, 2013.

[43] M. Palmieri, M. Perta, and F. Cupertino, "Design of a 50.000-r/min Synchronous Reluctance Machine for an Aeronautic Diesel Engine Compressor," *IEEE Transactions on Industry Applications,* vol. 52, pp. 3831-3838, 2016.

[44] A. M. E.-. Refaie, R. Manzke, and T. M. Jahns, "Application of bi-state magnetic material to automotive offset-coupled IPM starter/alternator machine," *IEEE Transactions on Industry Applications,* vol. 40, pp. 717-725, 2004.

[45] P. B. Reddy, A. El-Refaie, S. Galioto, and J. P. Alexander, "Design of synchronous reluctance motor utilizing dual-phase material for traction applications," in *2015 IEEE Energy Conversion Congress and Exposition (ECCE)*, 2015, pp. 4812-4819.

[46] P. B. Reddy, K. Grace, and A. El-Refaie, "Conceptual design of sleeve rotor synchronous reluctance motor for traction applications," *IET Electric Power Applications,* vol. 10, pp. 368-374, 2016.

[47] A. Vagati, G. Franceschini, I. Marongiu, and G. P. Troglia, "Design criteria of high performance synchronous reluctance motors," in *Conference Record of the 1992 IEEE Industry Applications Society Annual Meeting*, 1992, pp. 66-73 vol.1.

[48] I. I. A. S. A. Meeting, A. Vagati, T. A. Lipo, and I. I. D. Committee, *Synchronous Reluctance Motors and Drives: A New Alternative*: IEEE, 1994.

[49] N. Bianchi and T. M. Jahns, *Design, Analysis, and Control of Interior PM Synchronous Machines: Tutorial Course Notes ; Seattle, Oct. 5, 2004*: CLEUP, 2004.

[50] A. Blondel, C. O. Mailloux, and C. A. Adams, *Synchronous Motors and Converters: Theory and Methods of Calculation and Testing*: McGraw-Hill Book Company, 1913.

[51] R. E. Doherty and C. A. Nickle, "Synchronous machines I-an extension of blondel's two-reaction theory," *Transactions of the American Institute of Electrical Engineers,* vol. XLV, pp. 912-947, 1926.

[52] P. J. Lawrenson and L. A. Agu, "Theory and performance of polyphase reluctance machines," *Electrical Engineers, Proceedings of the Institution of,* vol. 111, pp. 1435-1445, 1964.

[53] J. K. Kostko, "Polyphase reaction synchronous motors," *Journal of the American Institute of Electrical Engineers,* vol. 42, pp. 1162-1168, 1923.

[54] J. F. H. Douglas, "Pull-in criterion for reluctance motors," *Transactions of the American Institute of Electrical Engineers, Part II: Applications and Industry,* vol. 79, pp. 139-142, 1960.

[55] P. J. Lawrenson and R. M. Mathur, "Pull-in criterion for reluctance motors," *Electrical Engineers, Proceedings of the Institution of,* vol. 120, pp. 982-986, 1973.

[56] V. B. Honsinger, "The Inductances Ld and Lq of Reluctance Machines," *IEEE Transactions on Power Apparatus and Systems,* vol. PAS-90, pp. 298-304, 1971.

[57] I. Marongiu and A. Vagati, "Improved modelling of a distributed anisotropy synchronous reluctance machine," in *Conference Record of the 1991 IEEE Industry Applications Society Annual Meeting*, 1991, pp. 238-243 vol.1.

[58] G. Pellegrino, T. M. Jahns, N. Bianchi, W. Soong, and F. Cupertino, *The Rediscovery of Synchronous Reluctance and Ferrite Permanent Magnet Motors: Tutorial Course Notes*: Springer International Publishing, 2016.

[59] A. Vagati, M. Pastorelli, G. Francheschini, and S. C. Petrache, "Design of low-torque-ripple synchronous reluctance motors," *IEEE Transactions on Industry Applications,* vol. 34, pp. 758-765, 1998.

[60] A. Fratta, G. P. Toglia, A. Vagati, and F. Villata, "Ripple evaluation of high-performance synchronous reluctance machines," *IEEE Industry Applications Magazine,* vol. 1, pp. 14-22, 1995.

[61] D. A. Staton, T. J. E. Miller, and S. E. Wood, "Maximising the saliency ratio of the synchronous reluctance motor," *IEE Proceedings B - Electric Power Applications,* vol. 140, pp. 249-259, 1993.

[62] M. J. Kamper and A. F. Volsdhenk, "Effect of rotor dimensions and cross magnetisation on L_d and L_q inductances of reluctance synchronous machine with cageless flux barrier rotor," *IEE Proceedings - Electric Power Applications,* vol. 141, pp. 213-220, 1994.

[63] N. Bianchi, "Synchronous reluctance and interior permanent magnet motors," in *2013 IEEE Workshop on Electrical Machines Design, Control and Diagnosis (WEMDCD)*, 2013, pp. 75-84.

[64] I. Boldea, *Reluctance Synchronous Machines and Drives*: Clarendon Press, 1996.

[65] N. Bianchi, H. Mahmoud, and S. Bolognani, "Fast synthesis of permanent magnet assisted synchronous reluctance motors," *IET Electric Power Applications,* vol. 10, pp. 312-318, 2016.

[66] M. Ferrari, N. Bianchi, A. Doria, and E. Fornasiero, "Design of Synchronous Reluctance Motor for Hybrid Electric Vehicles," *IEEE Transactions on Industry Applications,* vol. 51, pp. 3030-3040, 2015.

[67] M. Ferrari, N. Bianchi, and E. Fornasiero, "Analysis of Rotor Saturation in Synchronous Reluctance and PM-Assisted Reluctance Motors," *IEEE Transactions on Industry Applications,* vol. 51, pp. 169-177, 2015.

[68] R. R. Moghaddam, *Synchronous Reluctance Machine (SynRM) in Variable Speed Drives (VSD) Applications*: Electrical Engineering, KTH Royal Institute of Technology, 2011.

[69] A. Vagati, M. Pastorelli, F. Scapino, and G. Franceschini, "Impact of cross saturation in synchronous reluctance motors of the transverse-laminated type," *IEEE Transactions on Industry Applications,* vol. 36, pp. 1039-1046, 2000.

[70] A. Vagati, M. Pastorelli, and G. Franceschini, "High-performance control of synchronous reluctance motors," *IEEE Transactions on Industry Applications,* vol. 33, pp. 983-991, 1997.

[71] T. Lubin, H. Razik, and A. Rezzoug, "Magnetic saturation effects on the control of a synchronous reluctance machine," *IEEE Transactions on Energy Conversion*, vol. 17, pp. 356-362, 2002.

[72] A. Tessarolo, "Modeling and Analysis of Synchronous Reluctance Machines With Circular Flux Barriers Through Conformal Mapping," *IEEE Transactions on Magnetics*, vol. 51, pp. 1-11, 2015.

[73] H. Mahmoud and N. Bianchi, "An improved analytical model of eccentric synchronous reluctance machines considering the iron saturation and slotting effect," in *2016 XXII International Conference on Electrical Machines (ICEM)*, 2016, pp. 107-113.

[74] M. Degano, H. Mahmoud, N. Bianchi, and C. Gerada, "Synchronous reluctance machine analytical model optimization and validation through finite element analysis," in *2016 XXII International Conference on Electrical Machines (ICEM)*, 2016, pp. 585-591.

[75] F. Cupertino, G. Pellegrino, and C. Gerada, "Design of Synchronous Reluctance Motors With Multiobjective Optimization Algorithms," *IEEE Transactions on Industry Applications*, vol. 50, pp. 3617-3627, 2014.

[76] F. Cupertino, G. M. Pellegrino, E. Armando, and C. Gerada, "A SyR and IPM machine design methodology assisted by optimization algorithms," in *2012 IEEE Energy Conversion Congress and Exposition (ECCE)*, 2012, pp. 3686-3691.

[77] G. Pellegrino, F. Cupertino, and C. Gerada, "Automatic Design of Synchronous Reluctance Motors Focusing on Barrier Shape Optimization," *IEEE Transactions on Industry Applications*, vol. 51, pp. 1465-1474, 2015.

[78] M. H. Mohammadi, T. Rahman, R. Silva, M. Li, and D. A. Lowther, "A Computationally Efficient Algorithm for Rotor Design Optimization of Synchronous Reluctance Machines," *IEEE Transactions on Magnetics*, vol. 52, pp. 1-4, 2016.

[79] J. Pyrhonen, T. Jokinen, and V. Hrabovcova, *Design of Rotating Electrical Machines*: Wiley, 2009.

[80] E. Lovelace, "Optimization of a magnetically saturable interior permanent-magnet synchronous machine drive," *PhD thesis*, 2000.

[81] B. Boazzo, A. Vagati, G. Pellegrino, E. Armando, and P. Guglielmi, "Multipolar Ferrite-Assisted Synchronous Reluctance Machines: A General Design Approach," *IEEE Transactions on Industrial Electronics*, vol. 62, pp. 832-845, 2015.

[82] A. Vagati, B. Boazzo, P. Guglielmi, and G. Pellegrino, "Design of Ferrite-Assisted Synchronous Reluctance Machines Robust Toward Demagnetization," *IEEE Transactions on Industry Applications*, vol. 50, pp. 1768-1779, 2014.

[83] B. Boazzo, "Reduced cost Permanent Magnet motor drives: a comprehensive design procedure and a universal approach to the magnetiic model identification and control," *pPhD thesis*, 2014.

[84] N. Bianchi, M. Degano, and E. Fornasiero, "Sensitivity Analysis of Torque Ripple Reduction of Synchronous Reluctance and Interior PM Motors," *IEEE Transactions on Industry Applications*, vol. 51, pp. 187-195, 2015.

[85] E. Howard, M. J. Kamper, and S. Gerber, "Asymmetric Flux Barrier and Skew Design Optimization of Reluctance Synchronous Machines," *IEEE Transactions on Industry Applications,* vol. 51, pp. 3751-3760, 2015.

[86] M. Sanada, K. Hiramoto, S. Morimoto, and Y. Takeda, "Torque ripple improvement for synchronous reluctance motor using an asymmetric flux barrier arrangement," *IEEE Transactions on Industry Applications,* vol. 40, pp. 1076-1082, 2004.

[87] N. Bianchi, S. Bolognani, D. Bon, and M. D. Pre, "Rotor Flux-Barrier Design for Torque Ripple Reduction in Synchronous Reluctance and PM-Assisted Synchronous Reluctance Motors," *IEEE Transactions on Industry Applications,* vol. 45, pp. 921-928, 2009.

[88] N. Bianchi, S. Bolognani, D. Bon, and M. D. Pr, "Torque Harmonic Compensation in a Synchronous Reluctance Motor," *IEEE Transactions on Energy Conversion,* vol. 23, pp. 466-473, 2008.

[89] S. Yammine, C. Henaux, M. Fadel, S. Desharnais, and L. Calégari, "Synchronous reluctance machine flux barrier design based on the flux line patterns in a solid rotor," in *2014 International Conference on Electrical Machines (ICEM)*, 2014, pp. 297-302.

[90] Y. Wang, G. Bacco, and N. Bianchi, "Geometry analysis and optimization of PM-assisted reluctance motors," in *2016 XXII International Conference on Electrical Machines (ICEM)*, 2016, pp. 1756-1762.

[91] M. Gamba, G. Pellegrino, and F. Cupertino, "Optimal number of rotor parameters for the automatic design of Synchronous Reluctance machines," in *2014 International Conference on Electrical Machines (ICEM)*, 2014, pp. 1334-1340.

[92] G. Pellegrino, F. Cupertino, and C. Gerada, "Barriers shapes and minimum set of rotor parameters in the automated design of Synchronous Reluctance machines," in *2013 International Electric Machines & Drives Conference*, 2013, pp. 1204-1210.

[93] G. Pellegrino, P. Guglielmi, A. Vagati, and F. Villata, "Core Losses and Torque Ripple in IPM Machines: Dedicated Modeling and Design Tradeoff," *IEEE Transactions on Industry Applications,* vol. 46, pp. 2381-2391, 2010.

[94] M. Barcaro, N. Bianchi, and F. Magnussen, "Rotor Flux-Barrier Geometry Design to Reduce Stator Iron Losses in Synchronous IPM Motors Under FW Operations," *IEEE Transactions on Industry Applications,* vol. 46, pp. 1950-1958, 2010.

[95] S. H. Han, T. M. Jahns, and Z. Q. Zhu, "Design Tradeoffs Between Stator Core Loss and Torque Ripple in IPM Machines," *IEEE Transactions on Industry Applications,* vol. 46, pp. 187-195, 2010.

[96] R. Krishnan, *Electric Motor Drives: Modeling, Analysis, and Control*: Prentice Hall, 2001.

[97] M. Barcaro, G. Meneghetti, and N. Bianchi, "Structural Analysis of the Interior PM Rotor Considering Both Static and Fatigue Loading," *IEEE Transactions on Industry Applications,* vol. 50, pp. 253-260, 2014.

[98] D. C. Montgomery, *Design and Analysis of Experiments*: Wiley, 2000.

[99] S. Wiak and E. N. Juszczak, *Computational Methods for the Innovative Design of Electrical Devices*: Springer Berlin Heidelberg, 2010.

[100] D. H. Wolpert and W. G. Macready, "No free lunch theorems for optimization," *IEEE Transactions on Evolutionary Computation,* vol. 1, pp. 67-82, 1997.

[101] K. Deb, *Multi-Objective Optimization Using Evolutionary Algorithms*: Wiley, 2001.

[102] A. E. Eiben and C. A. Schippers, "On evolutionary exploration and exploitation," *Fundam. Inf.,* vol. 35, pp. 35-50, 1998.

[103] S.-H. L. Matej Crepinsek, Marjan Mernik, "Exploration and exploitation in evolutionary algorithms: A survey," *ACM Comput. Surv.,* vol. 45, pp. 1-33, 2013.

[104] M. Palmieri, M. Perta, F. Cupertino, and G. Pellegrino, "High-speed scalability of synchronous reluctance machines considering different lamination materials," in *IECON 2014 - 40th Annual Conference of the IEEE Industrial Electronics Society*, 2014, pp. 614-620.

[105] G. Pellegrino and F. Cupertino, "IPM motor rotor design by means of FEA-based multi-objective optimization," in *2010 IEEE International Symposium on Industrial Electronics*, 2010, pp. 1340-1346.

[106] G. Pellegrino and F. Cupertino, "FEA-based multi-objective optimization of IPM motor design including rotor losses," in *2010 IEEE Energy Conversion Congress and Exposition*, 2010, pp. 3659-3666.

[107] J. A. Collins, H. R. Busby, and G. H. Staab, *Mechanical Design of Machine Elements and Machines: A Failure Prevention Perspective*: Wiley, 2010.

[108] C. A. Coello Coello, "Theoretical and numerical constraint-handling techniques used with evolutionary algorithms: a survey of the state of the art," *Computer Methods in Applied Mechanics and Engineering,* vol. 191, pp. 1245-1287, 1/4/ 2002.

[109] G. Taguchi and A. P. Organization, *Introduction to quality engineering: designing quality into products and processes*: The Organization, 1986.

[110] P. Di Barba, *Multiobjective Shape Design in Electricity and Magnetism*: Springer Netherlands, 2009.

[111] S. L. Avila, A. C. Lisboa, L. Krahenbuhl, W. P. Carpes, J. A. Vasconcelos, R. R. Saldanha, *et al.*, "Sensitivity analysis applied to decision making in multiobjective evolutionary optimization," *IEEE Transactions on Magnetics,* vol. 42, pp. 1103-1106, 2006.

[112] B. S. Hans-Georg Beyer, "Robust optimization – A comprehensive survey " *Computer Methods in Applied Mechanics and Engineering,* vol. Vol. 196, No. 33-34, pp. pp. 3190-3218, 2007.

[113] G. I. Schuëller and H. A. Jensen, "Computational methods in optimization considering uncertainties – An overview," *Computer Methods in Applied Mechanics and Engineering,* vol. 198, pp. 2-13, 11/15/ 2008.

[114] M. A. Khan, I. Husain, M. R. Islam, and J. T. Klass, "Design of Experiments to Address Manufacturing Tolerances and Process Variations Influencing Cogging Torque and Back EMF in the Mass Production of the Permanent-

Magnet Synchronous Motors," *IEEE Transactions on Industry Applications*, vol. 50, pp. 346-355, 2014.

[115] K. S. Kim, S. J. Lee, S. G. Cho, J. Jang, T. Lee, J. P. Hong, *et al.*, "Multi-response Taguchi robust design of back electromotive force and cogging torque considering the manufacturing tolerance for electric machine," in *2012 13th International Conference on Optimization of Electrical and Electronic Equipment (OPTIM)*, 2012, pp. 379-387.

[116] R. O. Duda, P. E. Hart, and D. G. Stork, *Pattern classification*: Wiley, 2001.

[117] E. Di Pierro, *Costruzioni elettromeccaniche*: Siderea, 1984.

[118] W. Schuisky and G. L. Basile, *Calcolo delle macchine elettriche*: CEA, 1969.

[119] D. Bauer, P. Mamuschkin, H. C. Reuss, and E. Nolle, "Influence of parallel wire placement on the AC copper losses in electrical machines," in *2015 IEEE International Electric Machines & Drives Conference (IEMDC)*, 2015, pp. 1247-1253.

[120] M. v. d. Geest, H. Polinder, J. A. Ferreira, and D. Zeilstra, "Current Sharing Analysis of Parallel Strands in Low-Voltage High-Speed Machines," *IEEE Transactions on Industrial Electronics*, vol. 61, pp. 3064-3070, 2014.

[121] P. B. Reddy and T. M. Jahns, "Analysis of bundle losses in high speed machines," in *The 2010 International Power Electronics Conference - ECCE ASIA -*, 2010, pp. 2181-2188.

[122] A. Lehikoinen, N. Chiodetto, E. Lantto, A. Arkkio, and A. Belahcen, "Monte Carlo Analysis of Circulating Currents in Random-Wound Electrical Machines," *IEEE Transactions on Magnetics*, vol. 52, pp. 1-12, 2016.

[123] P. Pillay, "Improved Design of Motors for Increased Efficiency in Residential and Commercial Buildings," *U. S. Department of Energy - Building Technologies Program Topical Report*, 2008.

[124] G. Pellegrino, A. Vagati, B. Boazzo, and P. Guglielmi, "Comparison of Induction and PM Synchronous Motor Drives for EV Application Including Design Examples," *IEEE Transactions on Industry Applications*, vol. 48, pp. 2322-2332, 2012.

[125] A. Mahmoudi, W. L. Soong, G. Pellegrino, and E. Armando, "Efficiency maps of electrical machines," in *2015 IEEE Energy Conversion Congress and Exposition (ECCE)*, 2015, pp. 2791-2799.

[126] E. Bilgen and R. Boulos, "Functional Dependence of Torque Coefficient of Coaxial Cylinders on Gap Width and Reynolds Numbers," *Journal of Fluids Engineering*, vol. 95, pp. 122-126, 1973.

[127] J. Nerg, M. Rilla, and J. Pyrhonen, "Thermal Analysis of Radial-Flux Electrical Machines With a High Power Density," *IEEE Transactions on Industrial Electronics*, vol. 55, pp. 3543-3554, 2008.

[128] J. Saari, *Thermal Modelling of High-speed Induction Machines*: Finnish Academy of Technical Sciences, 1995.

[129] A. Boglietti, A. Cavagnino, D. Staton, M. Shanel, M. Mueller, and C. Mejuto, "Evolution and Modern Approaches for Thermal Analysis of Electrical Machines," *IEEE Transactions on Industrial Electronics*, vol. 56, pp. 871-882, 2009.

[130] A. Boglietti, A. Cavagnino, M. Lazzari, and M. Pastorelli, "A simplified thermal model for variable-speed self-cooled industrial induction motor," *IEEE Transactions on Industry Applications,* vol. 39, pp. 945-952, 2003.

[131] D. Staton, A. Boglietti, and A. Cavagnino, "Solving the More Difficult Aspects of Electric Motor Thermal Analysis in Small and Medium Size Industrial Induction Motors," *IEEE Transactions on Energy Conversion,* vol. 20, pp. 620-628, 2005.

[132] A. Boglietti, A. Cavagnino, and D. Staton, "Determination of Critical Parameters in Electrical Machine Thermal Models," *IEEE Transactions on Industry Applications,* vol. 44, pp. 1150-1159, 2008.

[133] A. Boglietti, E. Carpaneto, M. Cossale, S. Vaschetto, M. Popescu, and D. A. Staton, "Stator Winding Thermal Conductivity Evaluation: An Industrial Production Assessment," *IEEE Transactions on Industry Applications,* vol. 52, pp. 3893-3900, 2016.

[134] R. Camilleri, D. A. Howey, and M. D. McCulloch, "Experimental investigation of the thermal contact resistance in shrink fit assemblies with relevance to electrical machines," in *7th IET International Conference on Power Electronics, Machines and Drives (PEMD 2014)*, 2014, pp. 1-9.

[135] D. P. Kulkarni, G. Rupertus, and E. Chen, "Experimental Investigation of Contact Resistance for Water Cooled Jacket for Electric Motors and Generators," *IEEE Transactions on Energy Conversion,* vol. 27, pp. 204-210, 2012.

[136] W. M. Rohsenow, J. P. Hartnett, and Y. I. Cho, *Handbook of heat transfer*: McGraw-Hill, 1998.

[137] D. A. Staton and A. Cavagnino, "Convection Heat Transfer and Flow Calculations Suitable for Electric Machines Thermal Models," *IEEE Transactions on Industrial Electronics,* vol. 55, pp. 3509-3516, 2008.

[138] D. A. Howey, P. R. N. Childs, and A. S. Holmes, "Air-Gap Convection in Rotating Electrical Machines," *IEEE Transactions on Industrial Electronics,* vol. 59, pp. 1367-1375, 2012.

[139] G. I. Taylor, "Distribution of Velocity and Temperature between Concentric Rotating Cylinders," *Proceedings of the Royal Society of London. Series A - Mathematical and Physical Sciences,* vol. 151, pp. 494-512, 1935.

[140] A. Boglietti, A. Cavagnino, D. A. Staton, M. Popescu, C. Cossar, and M. I. McGilp, "End Space Heat Transfer Coefficient Determination for Different Induction Motor Enclosure Types," *IEEE Transactions on Industry Applications,* vol. 45, pp. 929-937, 2009.

[141] A. Boglietti and A. Cavagnino, "Analysis of the Endwinding Cooling Effects in TEFC Induction Motors," *IEEE Transactions on Industry Applications,* vol. 43, pp. 1214-1222, 2007.

[142] P. Vas, *Vector control of AC machines*: Clarendon Press, 1990.

[143] S. A. Odhano, R. Bojoi, M. Popescu, and A. Tenconi, "Parameter identification and self-commissioning of AC permanent magnet machines - A review," in *2015 IEEE Workshop on Electrical Machines Design, Control and Diagnosis (WEMDCD)*, 2015, pp. 195-203.

[144] E. Armando, R. I. Bojoi, P. Guglielmi, G. Pellegrino, and M. Pastorelli, "Experimental Identification of the Magnetic Model of Synchronous Machines," *IEEE Transactions on Industry Applications*, vol. 49, pp. 2116-2125, 2013.

[145] J. B. Bartolo, "A high performance switched reluctance drive for aereospace application," *PhD Thesis - University of Nottingham*, 2016.

[146] D. Miyagi, N. Maeda, Y. Ozeki, K. Miki, and N. Takahashi, "Estimation of Iron Loss in Motor Core With Shrink Fitting Using FEM Analysis," *IEEE Transactions on Magnetics*, vol. 45, pp. 1704-1707, 2009.

[147] P. Rasilo, D. Singh, U. Aydin, F. Martin, R. Kouhia, A. Belahcen, *et al.*, "Modeling of Hysteresis Losses in Ferromagnetic Laminations Under Mechanical Stress," *IEEE Transactions on Magnetics*, vol. 52, pp. 1-4, 2016.

[148] W. M. Arshad, T. Ryckebush, F. Magnussen, H. Lendenmann, J. Soulard, B. Eriksson, *et al.*, "Incorporating Lamination Processing and Component Manufacturing in Electrical Machine Design Tools," in *2007 IEEE Industry Applications Annual Meeting*, 2007, pp. 94-102.

[149] S. Steentjes, G. v. Pfingsten, and K. Hameyer, "An Application-Oriented Approach for Consideration of Material Degradation Effects Due to Cutting on Iron Losses and Magnetizability," *IEEE Transactions on Magnetics*, vol. 50, pp. 1-4, 2014.

[150] R. Wrobel, A. Mlot, and P. H. Mellor, "Contribution of End-Winding Proximity Losses to Temperature Variation in Electromagnetic Devices," *IEEE Transactions on Industrial Electronics*, vol. 59, pp. 848-857, 2012.

[151] R. Wrobel, D. E. Salt, A. Griffo, N. Simpson, and P. H. Mellor, "Derivation and Scaling of AC Copper Loss in Thermal Modeling of Electrical Machines," *IEEE Transactions on Industrial Electronics*, vol. 61, pp. 4412-4420, 2014.

[152] H. Mahmoud and N. Bianchi, "Comparison between synchronous machines with eccentricity: Reluctance and Permanent Magnets," in *2016 International Symposium on Power Electronics, Electrical Drives, Automation and Motion (SPEEDAM)*, 2016, pp. 394-400.